Optical spectroscopy of graphene quantum dots and halide perovskite nanocrystals

Hugo Levy-Falk

université
PARIS-SACLAY

Optical Spectroscopy of Graphene Quantum Dots and Halide Perovskite Nanocrystals

Spectroscopie Optique de Boîtes Quantiques de Graphène et de Nanocristaux de Pérovskites Halogénées

Thèse de doctorat de l'université Paris-Saclay

École doctorale n° 572, ondes et matière (EDOM)
Spécialité de doctorat: Physique
Graduate School : Physique. Référent : ENS Paris-Saclay

Thèse préparée dans l'unité de recherche **LuMIn**
(Université Paris-Saclay, ENS Paris-Saclay, CentraleSupélec, CNRS),
sous la direction de **Emmanuelle Deleporte**, professeure des universités,
la co-direction de **Fabien Bretenaker**, directeur de recherche CNRS,
et le co-encadrement de **Damien Garrot**, maître de conférence.

Thèse soutenue à Paris-Saclay, le 24 Janvier 2024, par

Hugo Levy-Falk

Composition du jury

Membres du jury avec voix délibérative

Julien Barjon Professeur des Universités, Université Versailles Saint-Quentin-en-Yvelines	Président
Dmitry Aldakov Chargé de recherche, CNRS	Rapporteur & Examinateur
Stephanie Reich Professor, Freie Universität Berlin	Rapporteuse & Examinatrice
Hai-Son Nguyen Maître de conférences, École Centrale Lyon	Examinateur

THESE DE DOCTORAT

NNT : 2024UPAS007

université PARIS-SACLAY | ÉCOLE DOCTORALE Ondes et matière (EDOM)

Titre: Spectroscopie Optique de Boîtes Quantiques de Graphène et de Nanocristaux de Pérovskites Halogénées

Mots clés: pérovskites, nanographène, spectroscopie, boîte quantique, molécule unique, nanocristaux

Résumé: Ce travail se concentre sur la spectroscopie optique de deux classes de matériaux en utilisant la microscopie de fluorescence à température ambiante.

Tout d'abord, les pérovskites halogénées, une classe de semi-conducteurs qui ont connu un regain d'intérêt au cours des dix dernières années en raison de leurs propriétés optoélectroniques exceptionnelles, ce qui en fait une plateforme prometteuse pour les applications photovoltaïques, mais aussi pour l'émission de lumière dans les diodes, les lasers et les dispositifs quantiques. Ces matériaux cristallins sont constitués d'octaèdres dont les sommets sont partagés. Un ion métallique est positionné au centre, souvent du plomb, et des ions halogénures aux sommets : Cl, Br ou I. Un cation complète la structure. Il est soit organique, par exemple le méthylammonium (MA) ou le formamidinium, soit inorganique, par exemple le césium. Dans le contexte de l'émission de lumière, les pérovskites halogénées constituent un excellent choix pour résoudre le problème du *green gap*, c'est-à-dire le manque d'émetteurs efficaces dans la région verte du spectre optique, en raison de la possibilité d'ajuster leur bande interdite grâce à un choix éclairé de l'halogénure lors de la synthèse. De plus, comme la synthèse se fait à température ambiante et implique des étapes de chimie simples, ils sont prometteurs pour les applications industrielles. La synthèse et la caractérisation de nanocristaux de $CsPbBr_3$ émettant dans la région verte du spectre optique à l'aide d'une nouvelle méthode basée sur la précipitation est rapportée. En particulier, la calibration élevé et la bonne stabilité des nanocristaux sont mis en évidence.

La deuxième partie de cette étude porte sur les boîtes quantiques de graphène. Ces objets de faible dimension permettent d'ouvrir la bande interdite du graphène, ce qui les rend fluorescents. Ces émetteurs sont prometteurs parce que leur structure atomiquement fine et leur accordabilité les rendent aptes à réaliser des nanocapteurs. En s'appuyant sur la relation structure-propriétés récemment étudiée des boîtes quantiques de graphène rectangulaires, une étude approfondie au niveau de l'objet unique de ces boîtes quantiques hautement fluorescentes avec 96 atomes de carbone sp^2 est rapportée. L'excellente pureté des échantillons a été mise en évidence. L'étude de la dynamique temporelle de ces émetteurs de photons uniques dans une matrice de polystyrène a permis d'estimer les temps caractéristiques de la dynamique transitoire des boîtes quantiques.

Enfin, la troisième partie rapporte l'étude des boîtes quantiques de graphène sur une surface de pérovskite. La surface des pérovskites présente un intérêt particulier pour la réalisation de dispositifs avec ces semiconducteurs, ce qui en fait un terrain de jeu intéressant pour l'utilisation des boîtes quantiques de graphène. À cette fin, les boîtes quantiques ont été déposés sur la surface de monocristaux millimétriques de $MAPbBr_3$.

- En tant que films minces déposés sur la pérovskite, les boîtes quantiques de graphène présentent une photophysique compatible avec la formation d'excimères.
- Lorsque la concentration de boîtes quantiques sur la surface est réduite, des taches limitées par la diffraction sont observées. L'étude de la photoluminescence dans le domaine temporel révèle des sauts entre des états discrets du système.
- L'étude dans le domaine des fréquences de l'intensité de la photoluminescence de ces émetteurs limités par la diffraction est dominée par le bruit en 1/f, ce qui contraste fortement avec la dynamique stable, dominée par le bruit de grenaille, des émetteurs uniques lorsqu'ils sont étudiés dans une matrice de polystyrène.

Title: Optical Spectroscopy of Graphene Quantum Dots and Halide Perovskite Nanocrystals
Keywords: perovskites, nanographenes, spectroscopy, quantum dots, single-molecule, nanocrystals

Abstract: This work focuses on the optical spectroscopy of two classes of materials using fluorescence microscopy at room temperature.

First, halide perovskites, a class of semiconductors that have known a surge in interest in the last ten years because of their outstanding optoelectronic properties, making them a promising platform for photovoltaic applications, but also light emission in diodes, lasers, and quantum devices. These crystalline materials consist of corner-sharing octahedra with a metallic ion at the center, often lead, and halide ions at the corners: Cl, Br, or I. A cation completes the structure. It is either organic, for example, methylammonium (MA) or formamidinium, or inorganic, for example, cesium. In the context of light emission, halide perovskites are an excellent choice to address the problem of the green gap, that is, the lack of efficient emitters in the green region of the optical spectrum, because of the possibility to tune their band gap thanks to an informed choice of the halide during the synthesis. Moreover, because the synthesis is done at room temperature and involves soft chemistry steps, they are promising for industrial applications. The synthesis and characterization of $CsPbBr_3$ nanocrystals emitting in the optical spectrum's green region using a new reprecipitation-based method is reported. In particular, the nanocrystals' high calibration and good stability are highlighted.

The second part of this study is about graphene quantum dots. Those low-dimensional objects allow the opening of the band gap of graphene, making them fluorescent. These emitters are promising because their atomically-thin structure and tunability make them suitable for realizing nano-sensors. Building on the recently studied structure-properties relationship of rod-shaped graphene quantum dots, a thorough single-molecule study of highly fluorescent graphene quantum dots with 96 sp^2 carbon atoms is reported. The excellent purity of the samples was highlighted. The study of the time dynamics of those single-photon emitters in a polystyrene matrix allowed estimating the characteristic times of the transient dynamic of the quantum dots.

Finally, the third part reports the study of the graphene quantum dots on a perovskite surface. The surface of perovskites is of peculiar interest for the realization of devices with these semiconductors, making it an interesting playground to use graphene quantum dots. To that end, the quantum dots were deposited on a millimetric $MAPbBr_3$ single-crystal surface.

- As thin films deposited on the perovskite, the graphene quantum dots present photophysics compatible with the formation of excimers.
- As the concentration of quantum dots on the surface is lowered, diffraction-limited spots are observed. The time-domain study of the photoluminescence reveals jumps between discrete states of the system.
- The frequency-domain investigation of the intensity of photoluminescence of these diffraction-limited emitters is dominated by 1/f noise, which highly contrasts the stable, shot-noise-dominated dynamics of the single emitters when studied in a polystyrene matrix.

Remerciements

En essayant continuellement on finit
par réussir. Donc : plus ça rate,
plus on a de chance que ça marche.
– Jacques Rouxel

En tout premier lieu je veux remercier Emmanuelle Deleporte, qui a dirigé cette thèse. Malgré toutes les difficultés que nous avons rencontrées, le matériel défaillant, le déménagement, et la ré-orientation du sujet de thèse, j'ai toujours trouvé une oreille attentive, une superviseure présente et enjouée, avec qui j'ai pu échanger sur absolument tout, que ce soit les sujets scientifiques, ou extra-scientifiques. Je veux également remercier Jean-Sébastien Lauret, qui a donné un deuxième souffle à ma thèse en me proposant de travailler sur les boîtes quantiques de graphène. J'ai adoré me plonger dans l'étude de ces objets passionants, et j'espère pouvoir poursuivre l'étude d'émetteurs uniques, sous toutes leurs formes, dans le futur. Merci aussi pour ton humour et ton exigence. Bien que nos sujets aient rapidement divergés, j'ai eu la chance d'échanger régulièrement avec Fabien Bretenaker, en sa qualité de directeur du laboratoire, mais également sur l'enseignement. Merci de m'avoir donné la chance d'encadrer tes travaux dirigés d'Optique et Lasers pendant trois années. J'ai au moins autant appris en les donnants que ce que j'ai pu enseigner. Enfin, je souhaite remercier Damien Garrot pour sa participation et ses conseils durant la première année de ma thèse.

Une thèse ne peut être défendue s'il n'y a de jury pour l'examiner. Je veux donc remercier Julien Barjon d'avoir accepté de présider le jury. Je remercie également Stephanie Reich et Dmitry Aldakov pour avoir accepté de rapporter ce manuscrit. Leurs retours détaillés montrent leur intérêt pour mon travail, et le rendent meilleur. Enfin je remercie Hai-Son Nguyen d'avoir accepté d'examiner mon travail.

Durant ma thèse, notre équipe a été hébergée quelques temps à l'ISMO. Je remercie Thomas Pino son directeur pour l'acueil qui nous y a été réservé, ainsi que les équipes de ce laboratoire qui ont veillé à ce que notre séjour là bas se passe le mieux possible. J'ai également pu bénéficier des services (et de la bonne humeur !) des équipes techniques de LuMIn. Merci à Simon L'Horset, Colin Lopez, et Sébastien Rousselot (qui a développé la capacité à lire sur mon visage que j'avais besoin d'une pièce mécanique). Merci également à l'équipe administrative du laboratoire, et en particulier à Céline Fortabat et Isabelle Maurin, qui ont su

régler envers et contre tout (mais surtout contre la direction des affaires financières) mes problèmes administratifs.

Cette thèse a été co-financée par l'Agence Innovation Défense (AID) et l'Université Paris-Saclay. Je remercie ma tutrice AID Sylvie PAOLACCI-RIERA.

Cette thèse a été pour moi l'occasion de travailler avec des collègues talentueux. En particulier Joanna Urban, post-doctorante au sein du groupe lorsque j'ai commencé, m'a formée avec une grande patience à la spectroscopie et à utiliser la manip' de micro-PL. J'ai dû arrêter de compter le nombre de fois où j'ai désaligné le microscope et ai eu besoin de ton aide pour comprendre comment le remettre en état de marche. Merci pour tout ! J'ai ensuite eu la chance de collaborer avec deux talentueuses stagiaires. Tout d'abord Lauren Hurley, qui est arrivée au début du projet sur les hétérostructures GQD/perovskites, et une semaine avant le déménagement de bâtiment ! Merci pour ta bonne humeur et ton travail, en particulier sur le développement des méthodes de synthèses de cristaux de $MAPbBr_3$ et de dépôts de GQDs. Ensuite, un grand merci à Océane Capelle. Merci pour ton travail appliqué, en particulier sur les GQDs en matrice de polystyrène. C'est grâce à toi et tes manip' (que je ne pouvais piloter que de loin pour cause de rédaction !) que certains des résultats les plus intéressants de cette thèse sont là. Enfin, j'ai eu la chance de travailler à la toute fin de ma thèse (et même durant la prolongation) avec Suman Sarkar, post-doctorant au sein du groupe. Merci pour ton efficacité et ta bonne humeur. Grâce à ton travail, j'ai pu présenter à ma soutenance des résultats additionnels qui ne sont pas dans ce manuscrit, mais le complètent très bien.

En élargissant le champ des collaborateurs, j'ai pu travailler avec Cédric Mayer, qui m'a permis de m'initier au développement de synthèses chimiques lorsque nous avons collaboré sur les nanocristaux de $CsPbBr_3$. Tu as su me montrer que même moi je pouvais faire de la chimie ! J'ai également eu la chance de travailler avec Gaëlle Allard, qui m'a appris à me servir du laboratoire de chimie, a évité quelques catastrophes dues à mon inexpérience, et dont la fine connaissance des synthèses de perovskites a mené à la mise au point de la méthode de cristallisation des substrats de $MAPbBr_3$. J'ai eu le grand plaisir d'échanger avec Loïc Rondin, que ce soit sur l'optique (et qui a eu la patience de régler mes problèmes plus compliqués que "en fait j'avais oublié d'allumer le détecteur", même s'il y a eu aussi parfois cela), sur l'enseignement, ou sur la cuisine et mille autres sujets de la vie quotidienne au laboratoire. Enfin, merci à Elsa Cassette, qui m'a fait profiter de sa grande expertise physique.

J'ai également eu l'occasion de travailler avec des collaborateurs extérieurs au laboratoire. Merci à Daniel Medina-Lopez et Stéphane Campidelli pour leur travaux sur la synthèse des GQDs, et à Muriel Bouttemy pour la caractérisation XPS des cristaux de $MAPbBr_3$. Merci également à Quang-Huy Do et Johann Bouclé du laboratoire X-LIM, avec qui nous avons travaillé à la réalisation de LEDs utilisant les nanocristaux de pérovskite.

Je tiens à profiter ici de l'espace que je me suis auto-octroyé pour démentire fermement les rumeurs calomnieuses qui m'attribuent l'identité du *memeur masqué*. Je remercie par ailleurs Damien Raynal et Thomas Liu, mes deux talentueux comparses de thèse qui ont grandement participé à rendre cette expérience si joyeuse. Je vous souhaite de continuer à vous éclater, que ce soit à l'autre bout du monde en Australie ou à Nancy (je vous ai déjà parlé de la Pépinière ?).

Merci également à tous les autres thésards et post-doc avec qui j'ai eu le plaisir d'interragir au laboratoire. Merci à Christine, qui nous a fait découvrir des restaurants Libanais extras, Trang, Maxime, Timothée (Thimhothéeh ?), Ines (qui n'est pas méchante, juste drôle), Sébastien, Alex (ma source de recommandations littéraires), Isis, Florian, Marie-Charlotte (sur qui je me suis abusivement reposé pour gérer les impressions de TD !), Thomas (qui est beaucoup moins une fraude qu'il ne voudrait le laisser croire), Allan, Gauthier, Cassandra et Joseph (partenaires de manif' au top), Duc-Anh, Sonya (à qui je souhaite bon courage pour la rédaction), François, et toutes celles et ceux que je n'ai pas manqué d'oublier !

J'ai la chance d'être entouré de nombreux amis, dont certains depuis le lycée. Merci à Simon, qui n'est jamais avare d'encouragements. Merci également à tous mes amis d'école, dont certains m'ont accompagné à Londres et ont été de nombreuses fois mes colloc'. Merci à Yoann, Joanne (Dr. Tsunami), Alexandre (qui restera toujours mon MJ de cœur), Laouen, Guillaume, Claire, Benjamin, Camille, Victor, Hugo, Nicolas, Christine, et tous les autres. Merci également à Gabriel, et bon courage pour la fin de ta thèse !

Je souhaite de tout cœur remercier ma famille, et en particulier mes parents, Hélène et Philippe, qui m'ont toujours encouragé à faire ce qui me plaisait, ont enduré des exposés scientifiques à tous les repas depuis que j'ai été en âge de regarder *C'est pas Sorcier*, et sont quand même venus assister à ma soutenance.

Enfin je remercie Émilie. Je suis fier et heureux de compter pour toi.

Merci à toutes et tous de m'avoir accordé votre temps,
votre confiance, et même, souvent, votre amitié.

Contents

Preamble

Objects at the scale of the nanometer are of prime interest, both for the study of the fundamental properties of matter and the possible technological applications. The high potential of nanotechnologies has been recently highlighted by the attribution of the Nobel Prize in chemistry to Moungi G. Bawendi, Louis E. Brus, and Aleksey Yekimov for their work on the synthesis of quantum dots [1]. A remarkable property of nano-objects is that their properties do not depend on their composition alone but also on their size and shape. This makes their study a rich field that necessitates the collaboration of chemists and physicists for the synthesis, experimental study, and theoretical description of the material. My thesis is centered around the study of two kinds of materials: halide perovskites and graphene quantum dots.

Halide perovskites are a class of semiconductors that has seen a spectacular surge in interest over the last ten years, notably because of the outstanding promises they hold for solar cell technologies [2, 3]. They are also promising materials for light-emission applications, with demonstrations of perovskite-based LEDs with an efficiency of 20 % [4], and lasers [5]. Moreover, these compounds can be chemically engineered to form 2D structures [6] and quantum dots [7]. Many open questions remain on these materials, notably because of the delicate interplay of the organic and inorganic parts. I studied these compounds in the group of Emmanuelle Deleporte, who has developed earlier expertise in the synthesis and characterization of two-dimensional perovskites, as well as their use in the context of strong light-matter interactions in cavity [8] and for the realization of lasers [9].

Graphene quantum dots bridge two classes of materials. On one hand, graphene is a famous two-dimensional material, with outstanding conduction properties. Since its first experimental realization in 2004 [10], graphene has been seen as a very promising material for applications. However, its lack of bandgap makes it ill-suited for some optoelectronic applications. One route to open the gap of graphene is to reduce its dimensionality, making it 1D (nanoribbons or nanotubes) or 0D (graphene quantum dots). On the other hand, graphene quantum dots can be seen as members of the polycyclic aromatic hydrocarbons, a group of well-known molecules [11] which present many applications, in particular in the domain of quantum technologies [12]. Due to the tunability of the material, graphene quantum dots may be well suited for those kinds of applications. I investigated these objects in collaboration with Jean-Sébastien Lauret, whose group has developed expertise in the study of carbon nano-objects, in particular at the single-molecule level [13, 14].

In **Chapter 1**, I briefly review the key points of solid-state physics used throughout this thesis. In particular, the mechanisms linked to the emission and absorption of light in semiconductors and graphene quantum dots. Then, I give an overview of the context of the study of halide perovskites, particularly the key properties that make them an interesting research topic. Finally, I will review the important properties of graphene quantum dots, particularly the relationships between their geometry and optical properties.

Then, in **Chapter 2**, I present the experimental methods used to obtain the results reported in this manuscript. A specific focus is given to the optical spectroscopy methods and how they are implemented in the context of microscopic studies. Additionally, I present some noteworthy data analysis methods.

The results obtained on halide perovskites are presented in **Chapter 3**. First, I present my study of quasi-2D perovskites in the context of laser emission. Then, in the second part, I report on the synthesis and characterization of highly calibrated and emissive $CsPbBr_3$ nanocrystals in collaboration with Cédric Mayer.

In **Chapter 4**, I first present the family of rod-shaped graphene quantum dots. After presenting their properties in solution, I detail the result of our investigations at the single-molecule level. In particular, the high purity of the samples is assessed through a statistical study, and the characteristic times of the underlying three-level system are estimated.

Chapter 5 is a report on the investigation of rod-shaped graphene quantum dots deposited on a $MAPbBr_3$ perovskite substrate. The quantum dots were first deposited as films on the substrate, and we then tried to reduce the concentration towards single-molecule studies.

The final chapter consists of a general conclusion on the work conducted during my thesis and presents some possible future developments on the object studied here.

1 Introduction

Introduction

The work reported in this manuscript mainly focuses on unveiling the properties of objects belonging to two classes of materials: halide perovskites and graphene quantum dots. In this introductory chapter, I will first give some general insights into the properties of solids and their interaction with light. I will then present halide perovskites and specifically their use in the context of light emission. Finally, I will present graphene quantum dots and their applications in the context of single photon emission.

1.1 Investigating properties of matter optically

1.1.1 Electronic structure

Solids, such as metals or semiconductors, can be described through the behavior of electrons within the medium. In particular, it can be shown that in crystalline materials, the periodicity of the lattice constraints the energies allowed for an electron into bands, as shown in Figure 1.1. Bloch's theorem shows that the solutions to Schrödinger's equation for an electron within a band can be written

$$\psi_{\mathbf{k}}(\mathbf{r}) = u_{\mathbf{k}}(\mathbf{r})\exp(i\mathbf{k}\cdot\mathbf{r}) \tag{1.1}$$

where $u_{\mathbf{k}}(\mathbf{r})$ is a function with the periodicity of the lattice [15]. These Bloch functions depend on the electronic band considered, which justifies the study of the bands to determine the properties of solids. In particular, depending on the occupancy of the highest occupied band at $T = 0\,\mathrm{K}$, one can distinguish two types of materials: metals and insulators. The former corresponds to a higher band not fully occupied by electrons, allowing them to travel within the material with a zero energy threshold, i.e., conduction. The latter, insulators, corresponds to a situation where the highest occupied band, called the valence band, is fully occupied and separated by a bandgap from the lowest unoccupied band, called the conduction band. This means an electron is not able to travel within the medium. When the bandgap is small-enough (typically $\sim 1\,\mathrm{eV}$) that the conduction band can statistically get populated at non-zero temperatures, insulators are called semiconductors. The energy threshold required for the material to become conductive makes them the ideal platform for developing *e.g.* electronic-based logic gates.

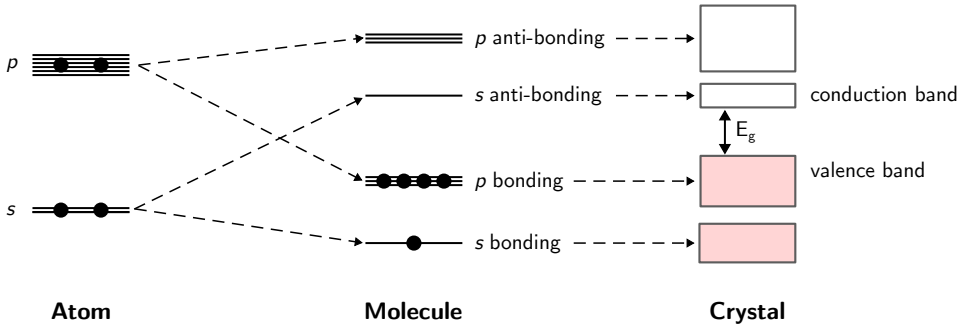

Figure 1.1: Schematic diagram of the electron levels in a covalent crystal made from four-valent atoms. The atoms' s and p states hybridize to form bonding and anti-bonding molecular orbitals, which then evolve into the conduction and valence bands of the semiconductor. Adapted from Ref. [15].

The periodicity of the crystal lattice makes describing the allowed electronic bands of solid in the wavevector space, also called the reciprocal space, suitable. The reciprocal lattice is the Fourier transform of the crystal lattice. The dispersion relations of the bands can be studied within a primitive cell of the reciprocal lattice, corresponding to all the wavevectors of the reciprocal space closer to the origin than to any other point of the reciprocal lattice. That reciprocal primitive cell is called the first Brillouin zone [16]. For example, the zinc-blende structure of GaAs is shown in Figure 1.2a, and the first Brillouin zone in Figure 1.2b. Because of the high degree of symmetry of the reciprocal lattice, one can examine the band structure on lines drawn between points of high symmetry. For GaAs, this yields Figure 1.2c. In particular, one can see that both the maximum of the valence band and the minimum of the conduction band are attained for the same wavevector, here at the Γ point. Such a semiconductor is said to have a direct bandgap and is of peculiar interest for light-matter interactions.

The shape of the conduction band can directly relate to some properties of the material. As can be seen in Figure 1.2c for GaAs, the band structure at the edge of the conduction band can be approximated by a parabola, yielding locally a dispersion relationship in the form $E(k) = E_0 + \frac{\hbar k^2}{2m^*}$, where the effective mass m^* has been introduced and is a measure of the curvature of the band near the gap. By analogy between the latter expression and the free-electron dispersion, one can see that an electron traveling in the medium in this range of energies can be approximated as a free electron with and effective mass m^*. In particular, the Drude model allows writing the mobility μ_e of electrons as $\mu_e = \frac{e\tau}{m^*}$, where e is the elementary charge, τ a relaxation time describing phenomenologically the interactions of the electrons with phonons or defects. The expression of mobility shows that the lighter the effective mass, *i.e.* the more pinched the conduction band around the bandgap, the higher the material's conductivity is.

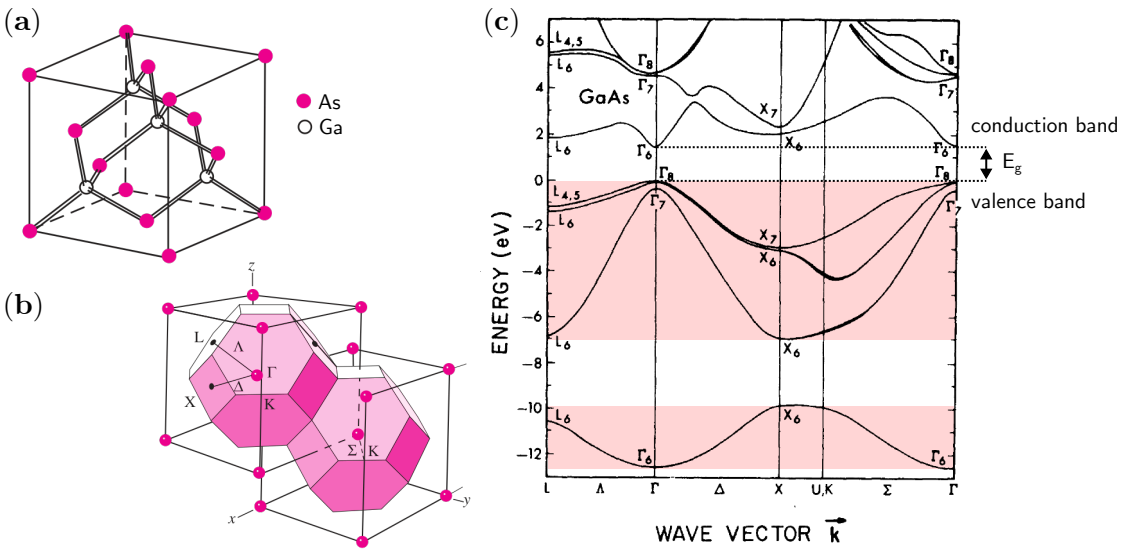

Figure 1.2: (**a**) Real space structure of GaAs. (**b**) Corresponding first Brillouin zone. Both adapted from Ref. [17]. (**c**) Dispersion diagram of GaAs calculated using the pseudopotential method. Adapted from Ref. [18].

So far, I have discussed some properties of solids in a one-electron picture. However, as an electron gets promoted to the conduction band in a semiconductor, the valence band is no longer full. This means the remaining electrons in that band gain some degree of freedom, and a description of the properties of the solid should include them, making the problem an N-body problem. One of the great successes of the twentieth century in solid-state physics was the introduction of the notion of holes. It allows accounting for the dynamics of many electrons in a partially filled band as the dynamics of one positively charged pseudo-particle, called a hole. It is possible to introduce an effective mass of the holes from the curvature of the valence band, and as for the electrons, this effective mass will appear in a semiclassical model of conduction [16]. Notably, one can see *e.g.* for GaAs that the curvature of the top of the valence band is lesser than the curvature of the bottom of the conduction band. This means the mobility of holes is smaller than the mobility of electrons.

Many modeling approaches have been developed to describe the electronic properties of solids. A successful approach is the tight-binding method [16]. This method consists in using a linear combination of the atomic orbitals (LCAO) of the atoms present in the unit cell of the direct lattice. Using the Bloch theorem (coming from the symmetry by translation), the solutions of the crystal Schrödinger equation reads:

$$\psi(\mathbf{r}) = \sum_{\mathbf{R}} e^{i\mathbf{k}\cdot\mathbf{R}} \phi(\mathbf{r} - \mathbf{R}) \tag{1.2}$$

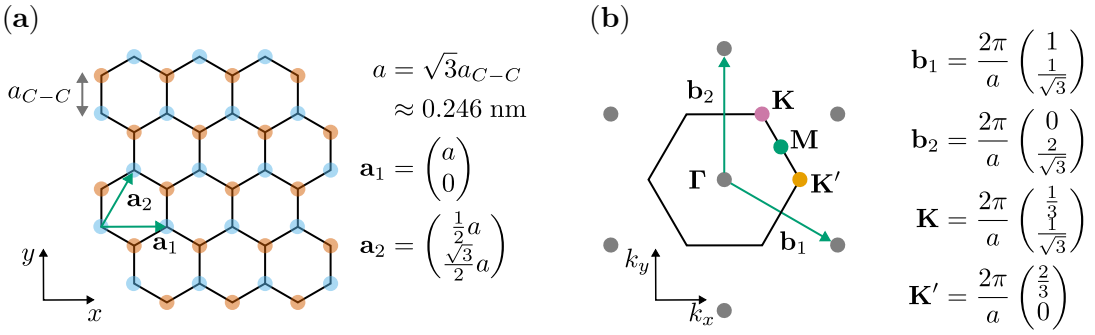

Figure 1.3: (**a**) Hexagonal lattice of graphene, with the two lattice vectors of the primitive cell $\mathbf{a}_1$ and $\mathbf{a}_2$ in green. The primitive cell contains two carbon atoms, in blue and orange, respectively. (**b**) Corresponding first Brillouin zone. The vectors of the reciprocal lattice are denoted $\mathbf{b}_1$ and $\mathbf{b}_2$. Three high symmetry points, $\mathbf{K}$, $\mathbf{K}'$, and $\mathbf{M}$ are highlighted.

where $\phi(\mathbf{r})$ are the linear combination of the atomic orbitals of the atoms of the unit cell and $\mathbf{R}$ are vectors of the direct lattice.

This can be put into practice for calculating the band structure of graphene. This is a two-dimensional material constituted of carbon atoms arranged in a honeycomb lattice, as shown in Figure 1.3a. The honeycomb lattice is a hexagonal lattice with two carbon atoms in the primitive cell (Figure 1.3a: A (orange) and B (blue) type carbons).

Carbon atoms can offer four valence electrons on four orbitals, namely $2s$, $2p_x$, $2p_y$, and $2p_z$. The s-orbitals hybridize with the in-plane p-orbitals to form three σ bonds spaced by 120° [19]. The remaining $2p_z$ orbitals form delocalized π bonds. Restricting to the nearest neighbors interactions, the dispersion relations of the π-bands of graphene are:

$$E(\mathbf{k}) = \pm t\sqrt{1 + 4\cos\frac{ak_x}{2}\cos\frac{\sqrt{3}ak_y}{2} + 4\cos^2\frac{ak_x}{2}} \tag{1.3}$$

where t is the neighbor exchange energy (about 2.8 eV).

The resulting band structure of graphene is plotted in Figure 1.4a on the next page, and a band diagram in Figure 1.4b. The band diagram illustrates the peculiarity of the region around the bandgap. First, the bandgap is vanishing around the K point, which means electrons can be freely promoted to the conduction band. For this reason, graphene is considered a semimetal. Then, the peculiar conical shape of the conduction and the valence band is intriguing. Indeed, the parabolic approximation of the conduction band demonstrated earlier for GaAs cannot work here. Instead, the dispersion relation around the K point reads:

$$E(\mathbf{k} - \mathbf{K}) = \pm v_F\hbar|\mathbf{k} - \mathbf{K}| \tag{1.4}$$

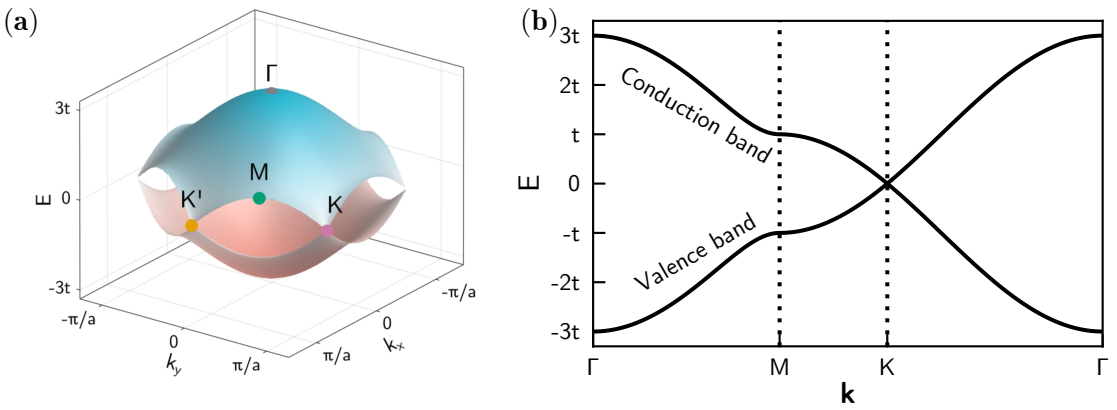

Figure 1.4: (**a**) Band structure of graphene in the first Brillouin zone, accounting for π electrons only. (**b**) Band diagram of graphene along axes of high symmetry of the structure defined in Figure 1.3b.

with v_F the Fermi velocity ($\sim 1 \times 10^6$ m/s). This linear dispersion relationship can be understood as electrons behaving as massless particles, leading to a remarkably high mobility of charges in that medium. This property can be demonstrated, for example in suspended graphene sheets at low temperature [20], with a mobility approaching 200 000 $\mathrm{cm}^2/\mathrm{V/s}$. For comparison, the mobility in gold at low temperatures is typically $\sim 1500\,\mathrm{cm}^2/\mathrm{V/s}$ [21].

Ever since the first isolation of monolayer graphene sheets by Novoselov *et al.* [10], the study of graphene has known a surge in interest. However, the absence of bandgap in its band structure, as shown in Figure 1.4, makes it unfit for some logic and optoelectronic applications. Opening the gap of graphene to use its outstanding properties in those areas has prompted many studies, notably on smaller dimensional graphene-based compounds.

1.1.2 Excitons

I have discussed earlier a possible refinement to the one-electron model in introducing the hole as a pseudo-particle and thus treating a specific band in a one-hole picture. An additional refinement necessary to explain the properties of some materials studied in this manuscript is the concept of exciton. The excitons arise from the Coulomb interaction between a positively charged hole and a negatively charged electron. The electron-hole pair bound by Coulombic attraction can be treated as a quasi-particle named exciton [16].

In the one-electron picture described earlier, the lowest energy required to excite an electron is $E_c - E_v$, with E_c the energy of the minimum of the conduction band and E_v the energy of the maximum of the valence band. Furthermore, because Bloch's theorem states that the wavefunction is periodic, the periodic potential of

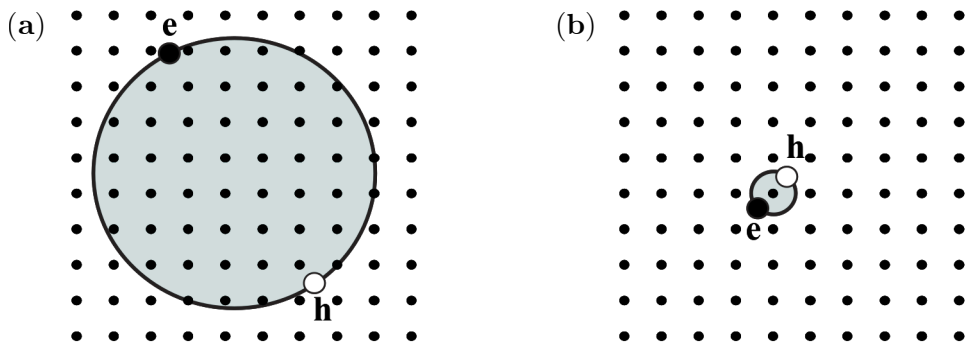

Figure 1.5: (**a**) Wannier-Mott exciton, or free exciton, with a radius larger than the size of the unit cell. (**b**) Frenkel, or tightly-bound exciton, with a radius smaller than the size of the unit cell. Reproduced from Ref. [15].

the crystal is left unaltered by this excitation, as the local change in charge density would be of the order of $1/N$ the charge of an electron, with N the number of cells in the lattice. However, if many energy levels are available near the minimum of the conduction band, the electron can form a wave packet, *i.e.* be localized. The energy of the wave packet $\bar{E}_c$ would be higher than the minimum of the conduction band E_c. If, at the same time, there are enough levels near the maximum of the valence band to form a wavepacket of energy $\bar{E}_v < E_v$, then one can expect that the energy required to excite an electron would be higher than the band-gap, as $\bar{E}_c - \bar{E}_v > E_c - E_v$. However, the Coulombic interaction between the electron and the hole has not been taken into account yet.. The potential resulting from that interaction is negative and can effectively lower the minimum excitation energy required, allowing the creation of bound electron-hole pairs, *i.e.* excitons.

In practice, two classes of excitons are distinguished based on two extreme cases of the localization of the excitons: Wannier excitons and Frenkel excitons, shown in Figure 1.5. The latter was introduced first by Frenkel in 1931 [22], using a tight-binding approach. In this, the electron and hole correspond to occupied or unoccupied orbitals of the same or very close crystal ions. Hence, the Frenkel exciton corresponds to a situation where the electron and the hole are very close to one another, as shown in Figure 1.5b. The exciton can still travel by jumping from cell to cell. The Frenkel exciton is typically found in molecular crystals, such as anthracene. The second extreme case corresponds to an exciton where the average distance between the electron and the hole is much bigger than the typical size of the unit cell, as shown in Figure 1.5a. Wannier showed in 1937 that these excitons can be treated in a hydrogenoïd model [23]. The mean distance between the electron and hole is the Bohr radius, $a_X = \frac{m_0}{\mu\varepsilon_r} a_0$, where a_0 is the Bohr radius of hydrogen (0.529 Å), ε_r is the relative dielectric constant of the medium, m_0 is the mass of the electron in vacuum, and μ the reduced effective mass of the

electron-hole pair. Similar to the hydrogen atom, the excitonic effects induce a series of discrete possible excitation energies below the bandgap:

$$E_{ex}(n) = E_g - \frac{R_X}{n^2} \tag{1.5}$$

Where $R_X = \frac{\mu}{m_0 \varepsilon_r^2} R_H$ is the exciton binding energy, with R_H the Rydberg constant [15]. These excitons can be found in classical semiconductors such as GaAs for temperatures low enough for the thermal energy $k_B T$ to be lower than the binding energy. Indeed, once the carriers gain enough energy to attain the conduction or valence band, the exciton will dissociate, and the carrier will be free to travel within the medium. This is analogous to the ionization of a hydrogen atom. One can then understand that the study of exciton dynamics is of primary importance for applications where the dissociation of the electron-hole pairs is necessary, such as photovoltaic applications.

I have presented here a simplified theoretical argument for the presence of excitons in semiconductors. However, their presence is best highlighted through the material's absorption spectrum.

1.1.3 Probing physical properties: light-matter interactions

Absorption

The first physical process that is of interest to us is absorption. Through the absorption of a photon, an electron can be promoted to a higher energy level whose energy differs from the original energy level of the electron by the energy of the absorbed photon.

Treating the interaction of a monochromatic wave with a two-level system[1] in the framework of the electric-dipole approximation demonstrates that the probability of exciting the system, *i.e.* the probability of absorbing a photon, follows a Lorentzian line shape of the energy of the incoming excitation photons. By comparison with a classical elastically-bound electron, one can introduce the oscillator strength of a transition, which characterizes the strength of the transition [24] and is written

$$f = \frac{2m\omega_0}{\hbar} |\langle 1|\hat{z}|2\rangle|^2 \tag{1.6}$$

Where $\omega_0 = \frac{E_2 - E_1}{\hbar}$ is the pulsation corresponding to the energy of the transition, and $\langle 1|\hat{z}|2\rangle$ is the matrix element of the position of the electron on the z axis for this transition[2]. This quantity could also be linked to the electric dipole moment instead of the displacement.

[1] Which is a suitable approximation when exciting *e.g.* an atom or a molecule close to resonance.
[2] Assuming the dipole oscillates along the z axis.

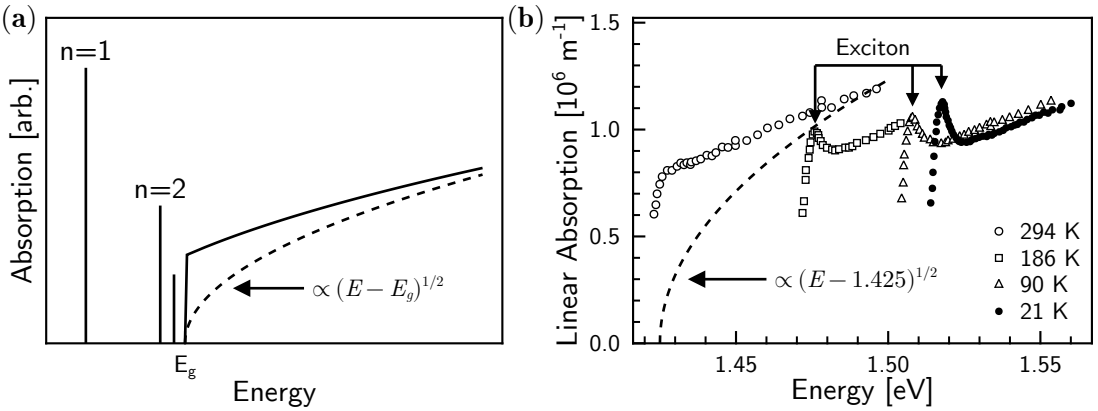

Figure 1.6: (**a**) Schematic view of the theoretical absorption spectrum of a semiconductor with excitonic levels. The absorption without excitonic effects is shown in dashed lines. Reproduced from Ref. [15]. (**b**) Absorption spectrum of GaAs as a function of temperature reported in Ref. [25]. The dashed line shows the expected absorption from the one-electron band theory. Reproduced from Ref. [15].

When dealing with a quasi-continuum of states, one can show that the transition rate $W_{i\to f}$ when exciting an electron from an initial state i to a final state f follows Fermi's golden rule:

$$W_{i\to f} = \frac{2\pi}{\hbar}|M_{i\to f}|^2 g(E) \tag{1.7}$$

where $M_{i\to f}$ is the matrix element for the considered transition and is proportional to the electric dipole moment of the transition. $g(E)$ is the joint density of states[3]. This expression shows that the absorption of a semiconductor is proportional to the joint density of states. In the particular case where the band edge is parabolic, the joint density of states is proportional to the square root of the difference between the energy of the incoming photon and the energy of the bandgap [15], when that energy is above the bandgap. In these conditions, the absorption spectrum near the band edge is written:

$$A(E) \propto \begin{cases} 0 & E < E_g \\ (E-E_g)^{1/2} & E \geq E_g \end{cases} \tag{1.8}$$

If we now also account for the presence of excitons, we expect that discrete atom-like transitions will be visible below the band edge, as shown in Figure 1.6a. This schematic also features an enhanced absorption at the band edge due to electron-hole interaction. This can be accounted for using the more advanced Eliott theory

[3]Fermi's golden rule is usually derived in the case of a single discrete state coupled to a continuum and involves the density of states. In the case of a semiconductor, both the initial and final states lie within a continuum, hence the use of the joint density of states.

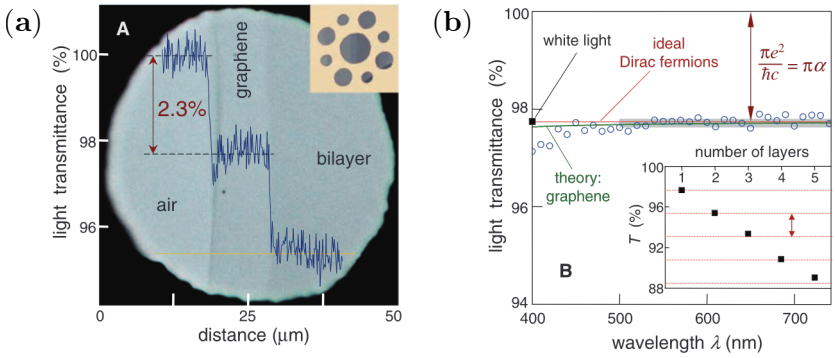

Figure 1.7: (**a**) Suspended membrane of graphene. (**b**) Corresponding transmission spectrum. The inset shows the evolution of transmission as the number of graphene layers increases. Reproduced from Ref. [30].

of Wannier excitons [26]:

$$A(E) \propto \frac{\mu_{\mathrm{cv}}^2}{E}\left[\sum_n \frac{4\pi R_X^{3/2}}{n^3}\delta\left(E - \left[Eg - \frac{R_X}{n^2}\right]\right) + \frac{2\pi R_X^{1/2}}{1 - e^{-2\pi\sqrt{\frac{R_X}{E-E_g}}}}u(E-E_g)\right] \tag{1.9}$$

Where R_X is the exciton binding energy, E_g is the gap energy, μ_{cv} is the transition dipole moment, and $u(E)$ is the Heaviside step function. This model has been applied to classical semiconductors such as GaAs [25] or GaP [27], but also to halide perovskites [28, 29] to determine the gap value and exciton binding energy of those materials. In practice, the visibility of the exciton peak depends on the temperature, and often only the ground state $n = 1$ of the exciton is visible. In particular, the excitonic peak is not visible if the thermal energy $k_B T$ is higher than the exciton binding energy. Figure 1.6b shows the absorption spectra of GaAs as a function of temperature. In particular, the absorption spectrum of GaAs features a characteristic excitonic peak at low temperatures that is not visible at room temperature. Some materials, such as alkali halides, *e.g.* NaCl, have absorption spectra that feature an excitonic peak at 300 K. This shows that the exciton binding energy for these materials is higher than the thermal energy at 300 K.

The absorption spectrum can thus be seen as a fingerprint of the allowed transitions from the ground state through the absorption of a photon. Because this measurement can be performed routinely (see Chapter 2), it is a tool of primary importance for the studies of the properties of solids. The absorption spectrum can even be used as a reference to determine fundamental constants. For example, the absorption of a graphene sheet is constant over the visible spectrum, and the corresponding transmission coefficient is approximately $1 - \pi\alpha \approx 0.975$, with α the

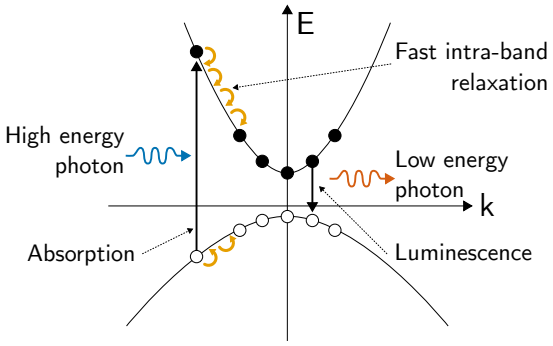

Figure 1.8: Photoluminescence process. A high-energy photon is absorbed to promote an electron to the conduction band. The electron relaxes quickly through vibronic relaxation to the bottom of the conduction band before de-excitation to the valence band through the emission of a photon of low energy.

fine structure constant [30][4]. The transmission spectrum is shown in Figure 1.7b for a suspended membrane such as the one shown in Figure 1.7a.

Luminescence

The second phenomenon of interest to us is the spontaneous emission of light when an electron is de-excited to a lower energy level. This is called luminescence.

As for absorption, we can first look at the case of discrete energy levels. It can be shown [31] that the emission spectrum from an electron's de-excitation is expected to be a Lorentzian function. However, in practice, it will be broadened by thermal effects.

Similarly to the discrete case, a solid can emit light when electrons de-excite from the band edge of the conduction band to the band edge of the valence band. The probability of de-excitation depends on the product of the occupancy of the bands[5], the joint density of states, and the matrix element of the transition. The expected spectrum in the low carrier density regime would thus be a sharply rising function below the gap energy, which then decays exponentially at higher energies [15]. In practice, thermal broadening of the line makes it roughly Gaussian.

In the framework of this thesis, we are interested in photoluminescence, *i.e.* the phenomenon of luminescence after the system has been excited by an external photon. The typical scheme of photoluminescence is illustrated in the dispersion diagram of a typical direct bandgap semiconductor in Figure 1.8. The process takes place in three steps. First, a photon of high energy, *i.e.* whose energy is higher than the bandgap, is absorbed. This results in the promotion of an electron

[4]The supplementary materials of Ref. [30] include a derivation of the absorption spectrum in graphene.

[5]Which can be found through the Fermi-Dirac distribution at thermodynamic equilibrium.

from the valence band towards the conduction band. In the valence band, this is equivalent to the creation of a hole. Light carries a momentum much smaller than the momentum of an electron. Hence, the arrow symbolizing absorption is drawn vertically, and the promoted electron keeps its original momentum. The second part of the process is fast intraband relaxation. The electron is allowed to relax towards the bottom of the conduction band, as long as there are unfilled levels, through the emission of phonons. Similarly, the hole in the valence band can relax towards the top of the valence band. The last part of the process corresponds to the de-excitation of the electron from the conduction band towards the valence band. This is also called the recombination of an electron and a hole. Because the emitted light still has a very small momentum, The arrow symbolizing emission is also vertical. The intraband relaxation is typically much faster than the fluorescence process, $\sim$ 100 fs to a few picoseconds, when the fluorescence process is typically from tens of picoseconds to a few hundreds nanoseconds. This latter process also competes with non-radiative de-excitation processes. For light-emission applications, one wants to maximize the efficiency of the fluorescence process against that of the non-radiative processes.

Because the intraband relaxation processes are very efficient, a bandgap is necessary to produce luminescence. For this reason, graphene does not present any fluorescence. Thus, for all its interesting transport properties and fundamental physics applications, the semi-metallic nature of graphene is not well-suited for logic or fluorescence applications [32]. Several routes to open the gap of graphene are known, such as bilayer-induced gap opening or through confinement of carriers. This latter solution will be discussed in the last section of this chapter.

1.2 Halide perovskites, an emerging class of semiconductors

1.2.1 General context for halide perovskites

Halide perovskites have been studied ever since their first reported synthesis [33] in the twentieth century [34–36]. They have, however, known a surge in interest in the 2010s, when their potential for solar-cell technologies has been highlighted, first as sensitizers for TiO_2-based solar cells, demonstrating a 3.81 % [2] and then 9 % [3] power conversion efficiency. Nowadays, solution-processed perovskite-based solar cells reach 26 % power conversion efficiency [37, 38], making the perovskite based solar cell technologies competitive with technologies studied since the 1970s as shown in the NREL report chart in Figure 1.9 on the following page. Moreover, efficiencies as high as 33.9 % are obtained in tandem solar cells perovskite/silicon [39].

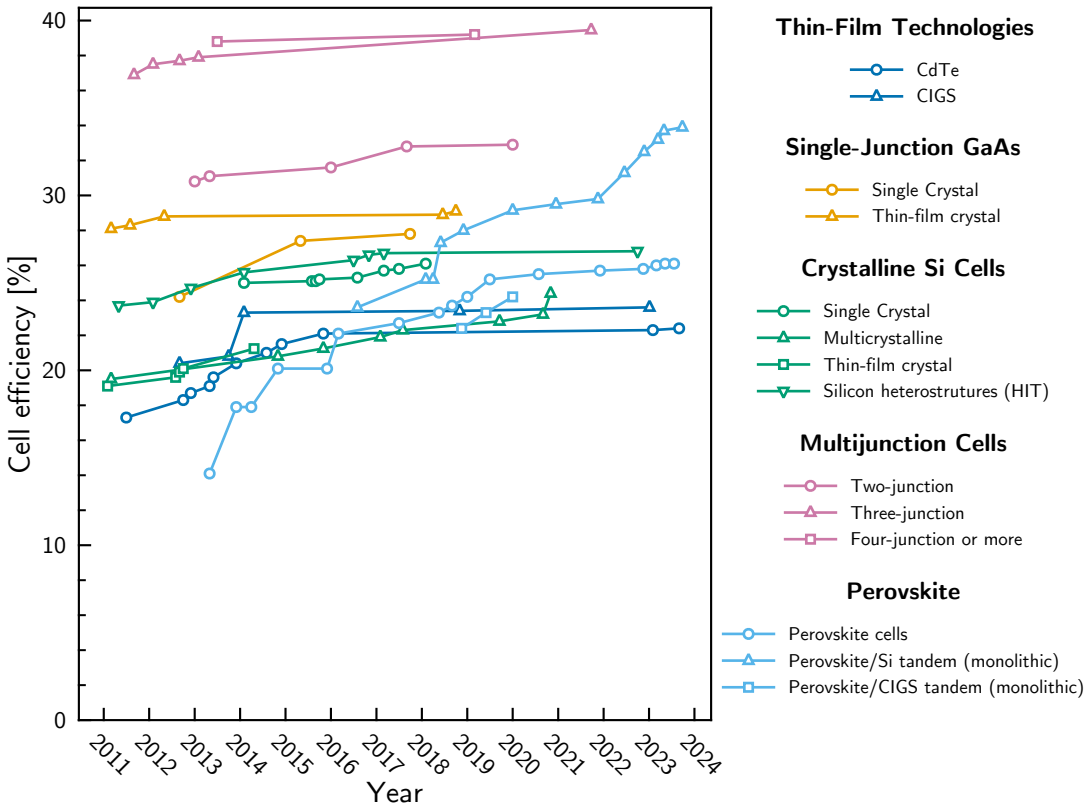

Figure 1.9: Best Research-Cell Efficiency Chart, adapted from the NREL chart [39] by removing concentrator-based and low-efficiency technologies.

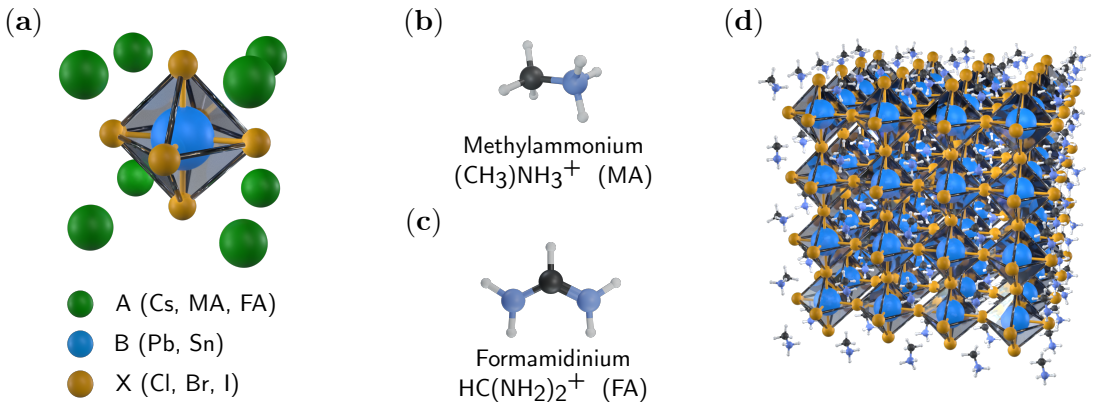

Figure 1.10: (**a**) Defining octahedral structure of halide perovskites, with metal at the center, surrounded by six halide anions and eight cations. The common organic cations are (**b**) methylammonium and (**c**) formamidinium. (**d**) Typical structure for halide perovskite, *e.g.* $MAPbBr_3$, with corner-sharing octahedra forming a cubic structure.

1.2.2 Three dimensional perovskites

Halide perovskite refers to a crystalline structure formed by divalent metallic cations, often lead (Pb), at the center of octahedra and denoted B. The six corners of the octahedra are formed by a halide, which can be chlorine (Cl), bromide (Br), or iodine (I), denoted X. The structure is completed by an organic, generally methylammonium ($CH_3NH_3^+$, MA), or formamidium ($HC(NH_2)_2^+$, FA), or inorganic, generally cesium (Cs^+), cation denoted A. The overall structure is shown in Figure 1.10, which shows the defining corner-sharing octahedra of a perovskite crystal, denoted ABX_3. Variations in the composition of the material exist; notably, considerable research efforts are being put towards the replacement of lead cations by other metals, such as tin (Sn). Mixed-ion perovskites are also widely studied, with perovskites combining several A cations or several halides. In this subsection, I will particularly highlight the properties of $MAPbBr_3$ and $CsPbBr_3$, as they have been at the center of my thesis.

The theoretical determination of the optoelectronic properties of halide perovskites is a challenging task. The structure of perovskites depends on the compounds and the temperature. $MAPbBr_3$ presents a cubic structure at room temperature, but this structure evolves to tetragonal and then orthorhombic as temperature decreases, as shown in Figure 1.11a on the next page. As can be expected from structural changes, the optical properties are affected by these transitions as shown in Figure 1.11b, reflecting evolutions of band structure depending on the crystal structure [40]. $MAPbBr_3$ is usually assigned to a pseudo-cubic structure at room temperature, with a lattice constant $a = b = c \approx 6.18\,\text{Å}$ [44]. Calculation

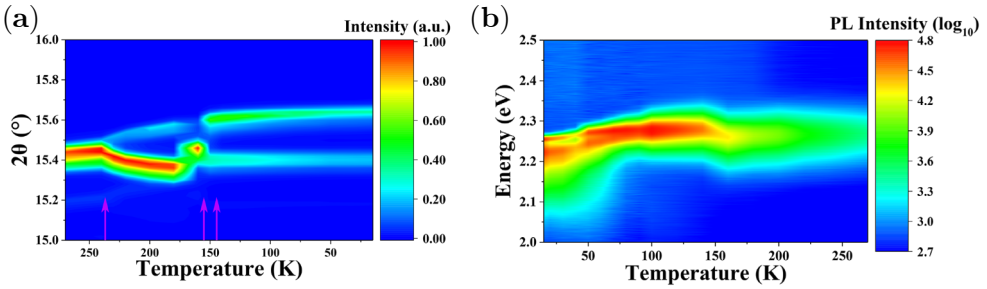

Figure 1.11: (**a**) Detailed X-Rays diffraction spectra of a $MAPbBr_3$ single crystal as a function of temperature. Three phase transition points are identified at $\sim$ 230 K, $\sim$ 160 K, and $\sim$ 150 K, corresponding to transitions from cubic to tetragonal and finally orthorhombic phases. (**b**) Temperature-dependent photoluminescence spectrum of a $MAPbBr_3$ single crystal. Reproduced from Ref. [40]

of the band structure of the material using a pseudo-potential method [41], shown in Figure 1.12a on the facing page, shows a direct bandgap positioned at the R point. The band gap decreases when the halide is switched from chloride to bromide and then to iodide. This is due to the valence band maximum being formed by an anti-bonding Pb s / X p combination while the conduction band minimum is formed by empty Pb p orbitals [42]. The wavefunctions corresponding to the valence band maximum and conduction band minimum of $MAPbI_3$ are illustrated in Figure 1.12b.

The tunability of the gap through halide substitution has been famously illustrated by Protesescu *et al.* [7] in halide perovskite nanocrystals. Figure 1.13 on page 18 illustrates two ways of tuning the gap of perovskites: controlling the halide composition and controlling the confinement of the emitters when the size of the nano-object is inferior to the Bohr radius of the exciton. This latter method will be discussed in the next subsection. It is also possible to use halide mixes to reach intermediary values of the bandgap.

The minimum of the conduction band being formed by lead orbital has important consequences on the properties of halide perovskites. In particular, these heavy atoms present large spin-orbit coupling effects. For example, Figure 1.12c shows the band structure of $MAPbBr_3$ in the orthorhombic phase[6] without and with the spin-orbit coupling [43]. The authors applied the same procedure for room temperature properties of $CsPbX_3$ and $MAPbBr_3$ to show that the conduction band minimum in this family corresponds to 2-fold degenerate spin-orbit split-off states. The band structure in Figure 1.12c that does not account for spin-orbit coupling still matches the experimental bandgap of $MAPbBr_3$ very well. The authors attribute this to error cancellation between the over-estimation brought by the non-accounting of spin-orbit coupling and the natural under-estimation of the

[6] In that case, the gap falls at the Γ point.

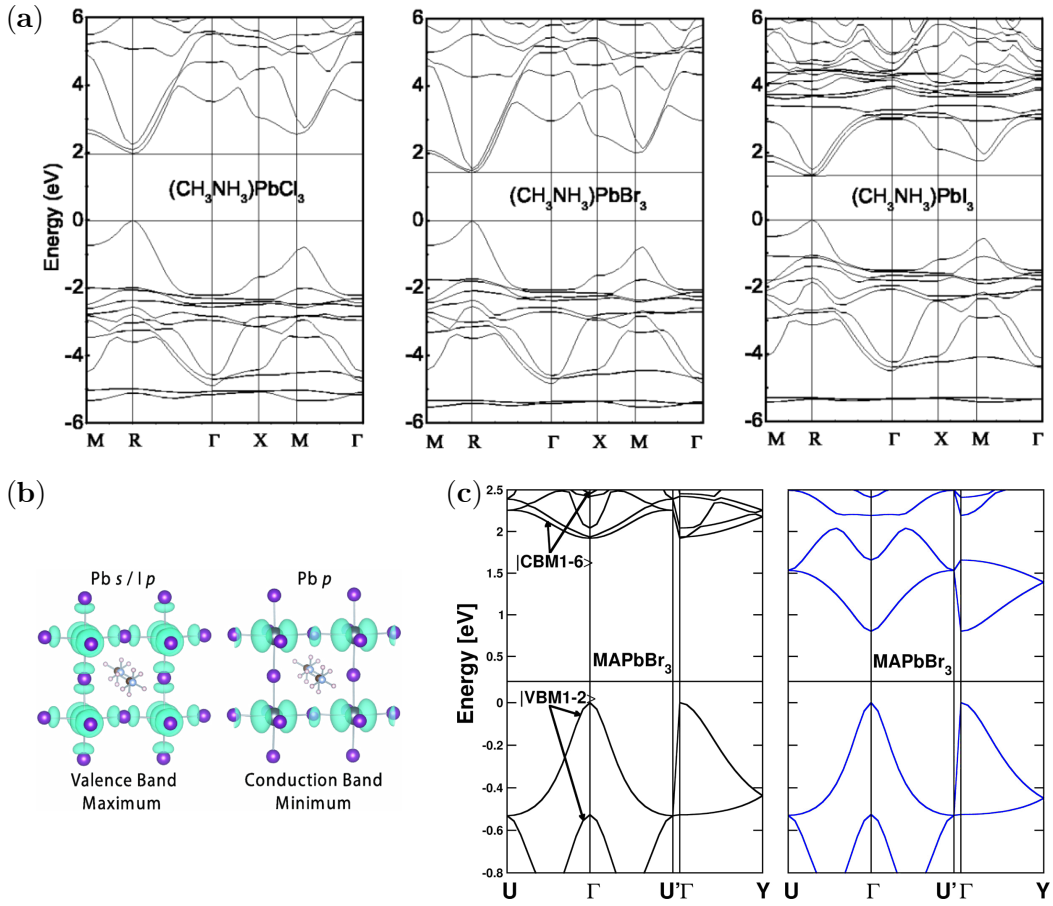

Figure 1.12: (**a**) Calculated band structures of $MAPbCl_3$, $MAPbBr_3$, and $MAPbI_3$ in the cubic phase using first-principles pseudopotential total-energy calculations within the local density approximation. Reproduced from Ref. [41]. (**b**) Isosurface plot of the self-consistent electron density associated with the PBEsol Kohn-Sham wavefunctions of the upper valence and lower conduction bands of $MAPbI_3$. Reproduced from Ref. [42]. (**c**) Density Functional Theory calculations of the structure of $MAPbBr_3$ in the orthorhombic phase without (left) and with (right) the spin-orbit coupling interaction. Reproduced from Ref. [43].

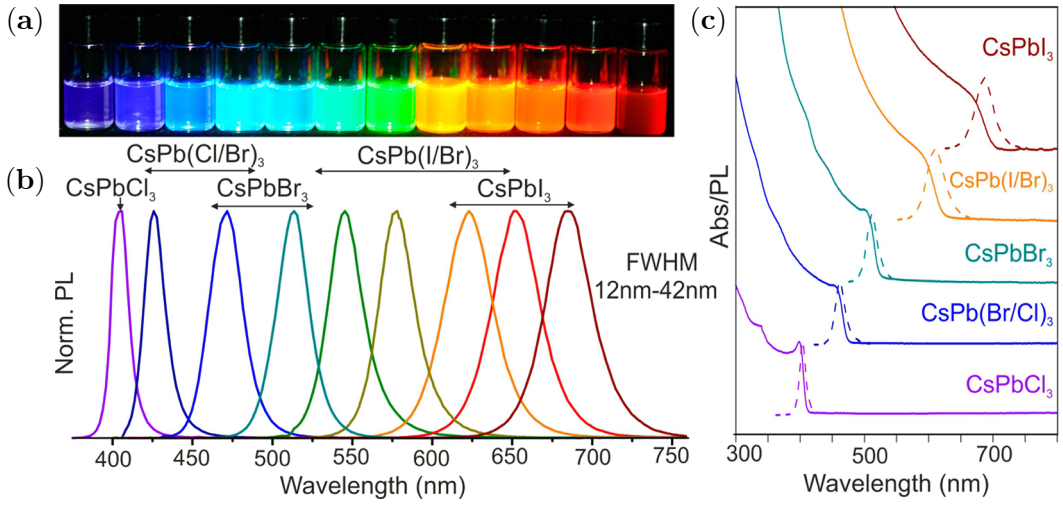

Figure 1.13: (**a**) Colloidal cesium-based perovskite nanocrystals excited by a UV lamp ($\lambda = 365\,\text{nm}$). (**b**) Photoluminescence spectra of the solutions excited at $\lambda = 400\,\text{nm}$, except $CsPbCl_3$ which was excited at $\lambda = 350\,\text{nm}$. (**c**) Superimposed absorption and photoluminescence spectra. Reproduced from Ref.[7].

bandgap by Density Functional Theory (DFT). Halide perovskites are excitonic materials, and the excitons are particularly sensitive to the band-edge spin-orbit coupling effects, as can be shown in the low-temperature absorption spectrum of $MAPbBr_3$ [45] or $CsPbX_3$ perovskites [46].

The last compound of the crystal that hasn't been discussed so far is the cation in cubic sites. It has been shown that MA plays a particular role in the band structure. The electronic levels affected by this compound lie deep within the conduction and valence bands [47], so it does not participate directly to the optoelectronic properties of the perovskite. However, it plays a major role in the formation of the cubic structure of $MAPbBr_3$, and thus indirectly on the bandgap.

The models used to describe perovskites are mostly based on advanced techniques such as Density Functional Theory. It is however also possible to use semi-empirical tight-binding models, whose parameters are derived using experimental and state-of-the-art DFT data [48]. In addition to the lightweight calculations needed for tight-binding compared to DFT, it also helps strengthen the intuition on the microscopic phenomena responsible for halide perovskite properties, particularly the role of p orbitals of lead in the conduction band. This approach, even though simplified, satisfactorily reproduces many experimental properties of the peculiar perovskite studied, here $MAPbI_3$, such as the absorption spectrum over the visible range.

Halide perovskites are known to present Wannier excitons [45]. This is particularly visible in the absorption spectra of the materials, as shown in Figure 1.14 on the facing page, which shows the absorption spectra of $MAPbBr_3$ and $MAPbI_3$ at

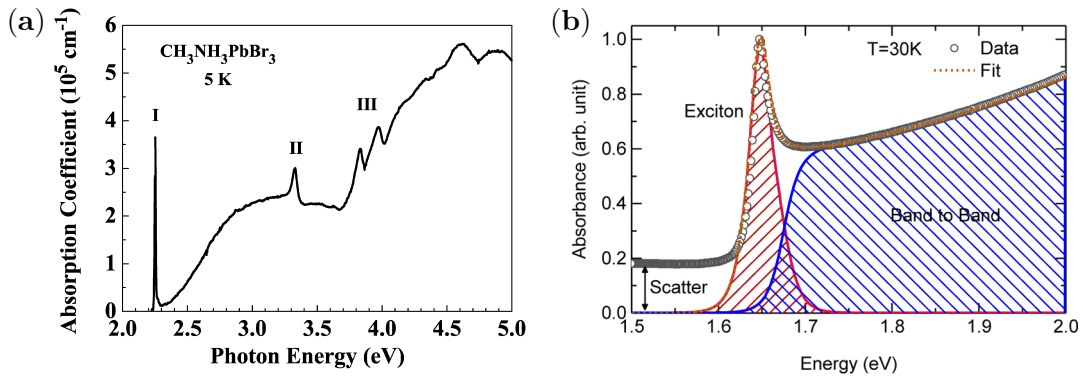

Figure 1.14: (**a**) Optical absorption spectrum of $MAPbBr_3$ at 5 K. Reproduced from Ref. [45]. (**b**) Absorption spectrum of $MAPbI_3$ using Eliott's theory with the excitonic and band-to-band contributions. Reproduced from Ref. [29].

low temperature and features clear excitonic peaks. Although the excitonic peak is not visible in $MAPbI_3$ at room temperature due to the exciton binding energy being of the order or smaller than the thermal energy, excitons still play an important role in that material, as electron-hole correlations induced by Coulomb interaction are non-negligible and the excitonic states increase the oscillator strength of the band-to-band transitions [28]. The exact value of the binding energy in perovskites has been a topic of controversy. For example, for $MAPbI_3$, literature reports range from 50 meV [45] to 2 meV [49]. Some authors attribute these discrepancies to often neglected polaron[7] effects [50]. Including those yields a binding energy of the order of 10 to 15 meV in bulk $MAPbI_3$ and $MAPbBr_3$ at low temperature [51, 52], which is the consensual value given to the exciton binding energy at low temperature nowadays. However, the temperature dependence of the crystalline phase of perovskites makes it difficult to extrapolate the exciton binding energy of the room temperature crystals (cubic phase) from the low-temperature measurements (orthorhombic phase). For example, it has been shown that the exciton binding energy in $MAPbBr_3$ thin films present a temperature dependence around the phase transition at 150 K, switching from $\sim$ 15 meV to $\sim$ 36 meV [53, 54], making the existence of exciton at room temperature plausible.

Halide perovskites present a rich literature on the topic of their synthesis. Depending on the application, they can be synthesized in various forms. Single crystals can be obtained from solution using solution temperature-lowering methods, inverse temperature crystallization methods, slow evaporation crystallization methods, or antisolvent vapor-assisted crystallization methods [6]. They can also be obtained using chemical vapor deposition techniques and from solid phases [55]. Halide perovskites are also frequently synthesized in thin films using spin-coating

[7]The coupling of electronic and longitudinal optical phonon states through the Coulomb interaction between carriers and the ionic lattice.

techniques in the contexts of photovoltaic applications [56] and laser emission [9] for example. Finally, as will be discussed in Chapter 3, halide perovskites can be synthesized as colloidal nanocrystals using *e.g.* hot injection methods [7] or reprecipitation methods [57, 58].

Overall, halide perovskites present many properties that make them enticing for electronics applications, especially photovoltaic and light emission. Notably, their long carrier diffusion length, about 100 nm in $MAPbI_3$ [59] and 1 µm in mixed halide $MAPbI_{3-x}Cl_x$ [60], which greatly outlast the typical 10 nm diffusion length from other types of solution-processed cells. Moreover, their tunability, low-temperature processing, soft crystal lattices, sharp optical absorption edges at energies that are relevant for solar cells, and intrinsic doping through defects while keeping long carrier diffusion lengths, among other interesting properties [61] make this material a rich research topic. Some practical barriers to the industrial application of halide perovskites still need to be lifted, such as addressing the toxicity of lead-based cells and the stability of the material [62].

1.2.3 Low-dimensional perovskites

One important and intriguing property of halide perovskites is the ability to play with the dimensionality of the system, opening a new domain of tunability of the material. For example, it is relatively easy to synthesize quasi-2D layered perovskites using a big organic cation such as phenylethylammonium ($C_6H_5C_2H_4NH_3$, PEA) instead of the A-site cation of the bulk perovskite. In particular, the exciton binding energy is strengthened by the quantum and dielectric confinements in two-dimensional materials [64]. One of the most famous quasi-2D perovskite is $PEA_2MA_{n-1}Pb_nI_{3n+1}$, or PEPI, shown in Figure 1.15a on the next page. The material consists of layers of octahedra separated by PEA. The alternate of octahedra and organic ligand form a multi-quantum-well structure, as shown in Figure 1.15d, in which the width of the quantum wells, and thus the lowest energy state, is defined by the number of octahedra layers n between each organic layer. The organic compound plays the role of an insulator, creating quantum and dielectric confinements. These materials can be synthesized at room temperature to form crystalline thin films of controlled n [65]. In Figure 1.15b, I show crystals of PEPI $n = 1$ to 3 synthesized by the slow cooling method. The crystals' apparent colors change from orange to red and then black, which hints at the change of optical properties as the number of octahedra in the inorganic layers changes. This is shown more rigorously in the photoluminescence spectra of PEPI $n = 1$ to 4 shown in Figure 1.15c. The maximum of photoluminescence shifts from ~ 1.89 eV for $n = 4$ (less confined excitons) to ~ 2.37 eV for $n = 1$ (most confined excitons).

The dimensionality of the perovskite can also be diminished further to form nanowires [66, 67] or, as has been introduced earlier, nanocrystals [7, 57, 58]. The latter are particularly interesting, as playing with the size of nanocrystals allows transitioning from bulk-like unconstrained excitons to confined ones. In particular,

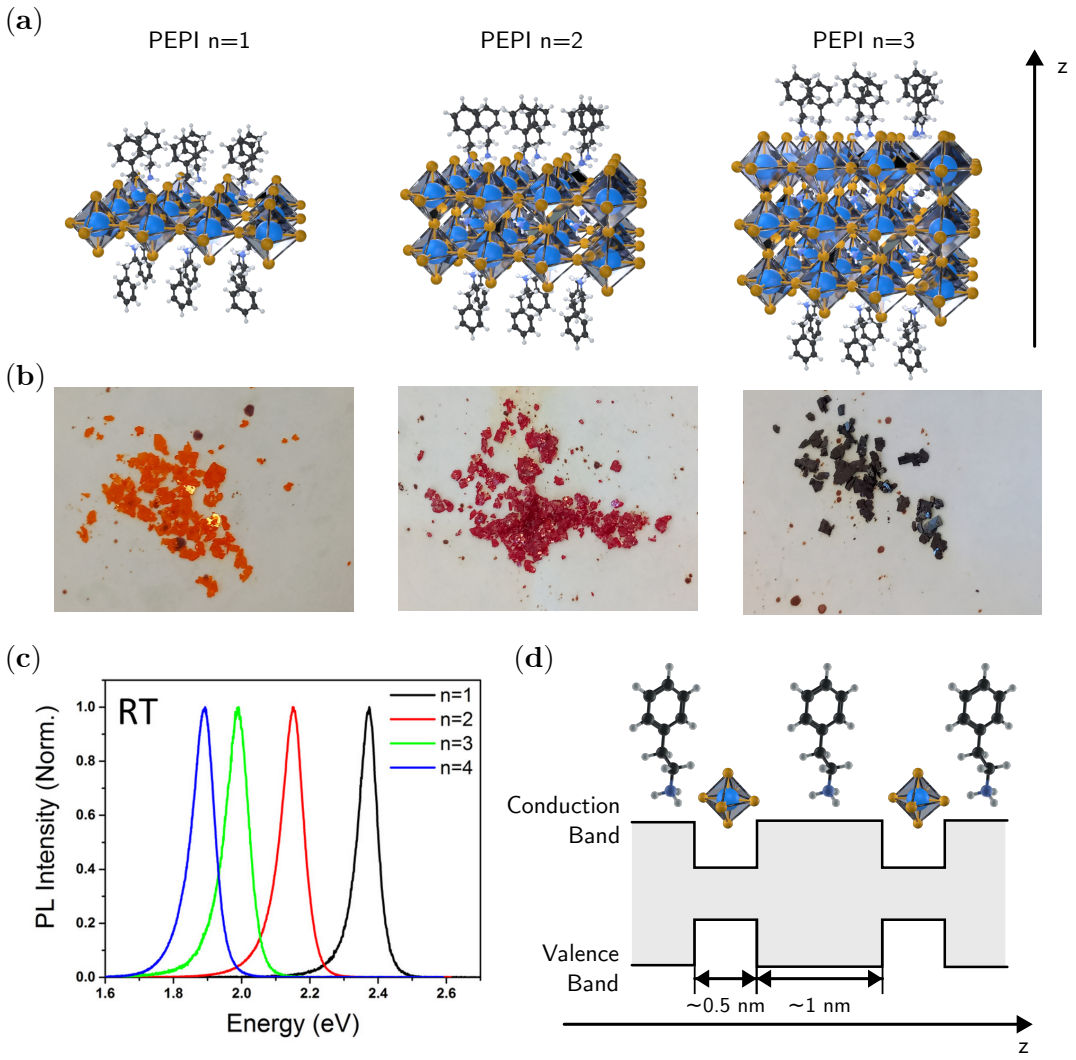

Figure 1.15: (**a**) Schematic representation of $(C_6H_5C_2H_4NH_3)_2(CH_3NH_3)_{n-1}Pb_nI_{3n+1}$ quasi-2D perovskite (PEPI) for $n = 1$ to 3. (**b**) Photograph of PEPI $n = 1$ to 3 crystals synthesized by the slow cooling method. One flake is about 2 mm wide. Courtesy of Gaëlle Allard. (**c**) Photoluminescence spectra of PEPI $n = 1$ to 4. Reproduced from Ref. [63]. (**d**) Schematic representation of the multi-quantum well structure associated with PEPI $n = 1$.

in the weakly confined regime, cesium-based nanocrystals are an ideal platform to explore the fundamental properties of the material, such as the role of bright triplet excitons in the remarkably high emission rate of cesium-based perovskite nanocrystals [46].

An interesting property of low-dimensional halide perovskites is the increased role of the organic part of the material. For example, it has been shown in PEPI that phonon modes of PEA couple to the excitons in inorganic layer and cause vibronic replica to be visible in the absorption spectrum at low temperature [68]. More flexibility for the chemical engineering of the organic part of 2D perovskites allows controlling the transfers between the inorganic and the organic parts of the compound to fine-tune the dynamics of excitons in the inorganic layer [69–71].

1.3 Graphene quantum dots, tailoring single-photon emission

As shown by a simple tight-binding model in Subsection 1.1.1, the band diagram of graphene does not exhibit any bandgap. One way of opening the gap around the K point of the graphene consists in reducing the dimensionality of this 2D material, towards 1D or 0D systems. We are interested in 0D systems, often called Graphene Quantum Dots (GQDs). Two main methods for synthesizing GQDs are the top-down and the bottom-up approaches. The top-down method consists of cutting down a large graphene sheet into smaller pieces. This can be done using lithography or solution treatment and usually presents the advantage of a high production yield but suffers from low control over the final shape and homogeneity of the GQDs. The second approach, the bottom-up method, relies on organic chemistry syntheses. Schematically, it consists of assembling smaller compounds to form the final GQD. Although this approach presents a lower yield than the previous, it can allow for a very high degree of control over the structure and homogeneity of the final GQDs. In this work, we studied bottom-up synthesized GQDs. The synthesis in itself has been developed in the framework of the theses of Medina lopez [72] and Liu [14].

1.3.1 Basic spectroscopic properties of molecules

A GQD can be seen from the molecular physics point of view as a Polycyclic Aromatic Hydrocarbon (PAH). Thus, it is interesting to summarize the basic properties of absorption and emission of molecules.

Molecules are usually studied under the Born-Oppenheimer approximation, which states that the electronic and nuclear motions are independent. This allows drawing the electronic levels as a function of the molecule's configuration, denoted Q. In the case of a diatomic molecule, Q corresponds to the interatomic distance. An example of diagram is shown in Figure 1.16a on the facing page.

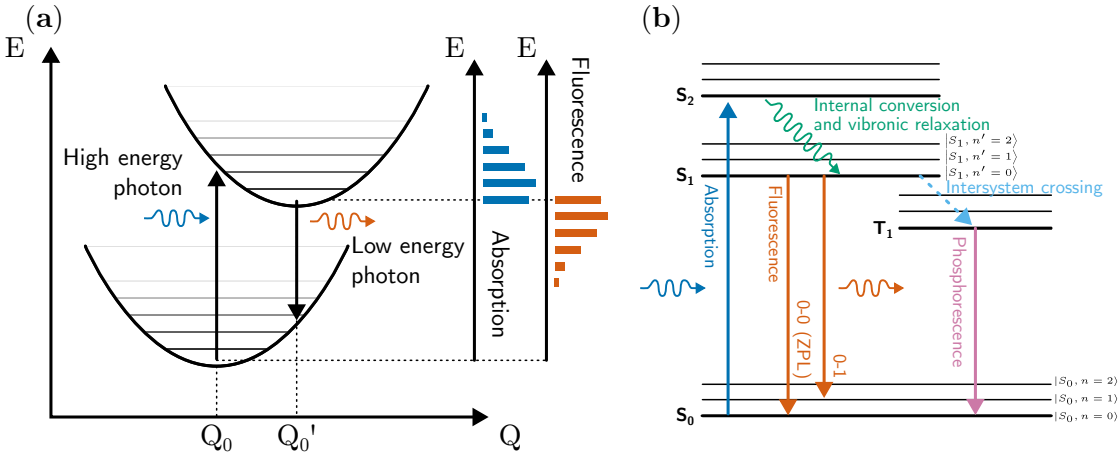

Figure 1.16: (**a**) Schematic configuration diagram for two electronic states in a molecule. Optical transitions are indicated by vertical arrows, and the corresponding schematic absorption and emission spectra are shown on the right-hand side. Adapted from Ref. [15]. (**b**) Jablonski diagram for a typical PAH. Pure electronic states are bold lines, additional vibronic states are lighter. The vibronic quanta for singlet states $\mathbf{S_0}$ and $\mathbf{S_1}$ are denoted n and n' respectively. ZPL: Zero-Phonon Line.

Because the electronic states are expected to be bounded, there is a minimum value of the energy for each electronic state. Moreover, in the Born-Oppenheimer approximation, the vibronic states can be decoupled from the electronic states. Formally, this corresponds to writing the wavefunctions as a product of the electronic and vibronic wavefunctions: $|S_i, n\rangle \approx |S_i\rangle\,|n\rangle$, where S_i labels the electronic states and n the vibronic states [73].

The process of photoluminescence described in Figure 1.16a can be explained through the Franck-Condon principle [15]. This states that an electronic transition happens within a stationary nuclear framework [73]. This is why the absorption and emission of light in Figure 1.16a are vertical. Qualitatively, a fluorescence cycle thus consists of the absorption of a photon, which excites the system from the minimum of the lowest electronic state, *i.e.* the ground state, to an excited electronic state with the same configuration. Then, the system relaxes towards the minimum of the excited state quickly and will eventually de-excite towards the lowest electronic state, emitting a photon. The emission is done while keeping the configuration constant, which means the system will finish the cycle relaxing towards the minimum of the lowest state.

To describe more formally the Franck-Condon principle, we first introduce the typical Jablonski diagram for a molecule, as shown in Figure 1.16b, where the pure electronic states are demarked from the additional vibronic levels. We are interested in the transition rate between a ground state $\langle S_0, n|$ and an excited state

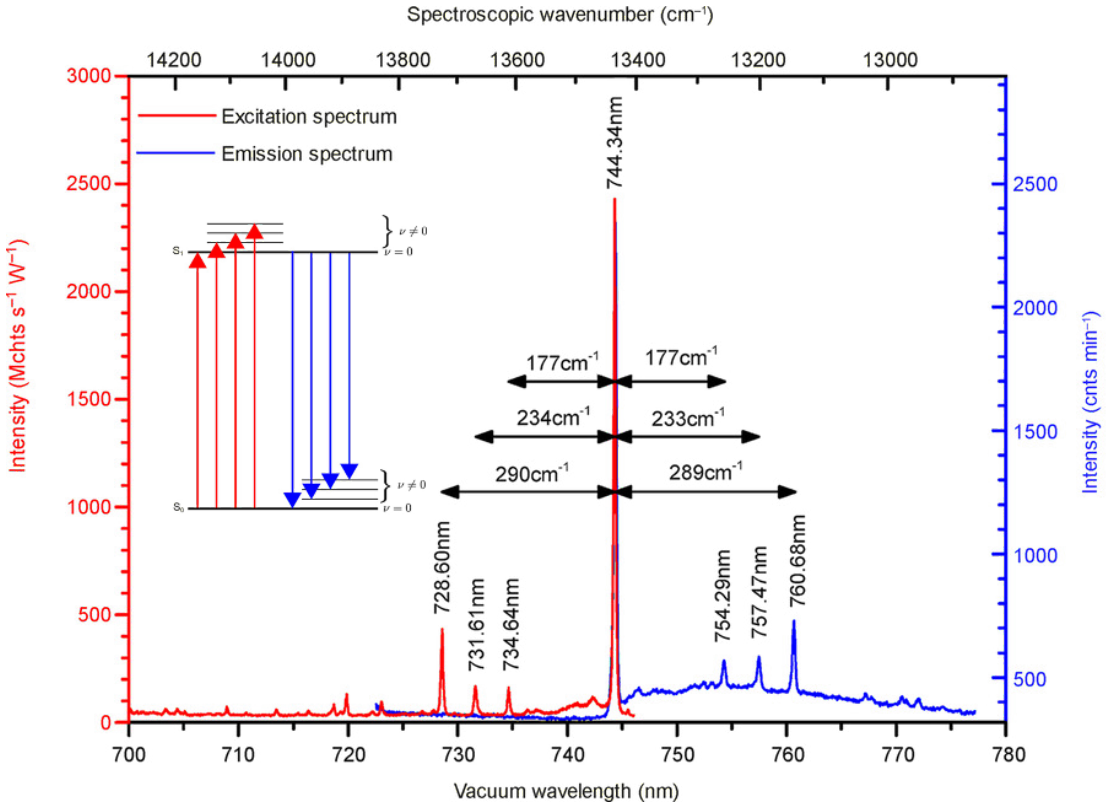

Figure 1.17: Bulk emission and excitation spectra of dibenzoterrylene (DBT) molecules embedded in 1,4-dichlorobenzene at 1.2 K. The emission spectrum features some broad background from the quartz substrate. Reproduced from Ref. [74].

$\langle S_1, n'|$. Within the Born-Oppenheimer approximation, one can show [73] that the dipole transition moment is:

$$\langle S_1, n'|\boldsymbol{\mu}|S_0, n\rangle \approx \boldsymbol{\mu}_{S_1,S_0} \langle n'|n\rangle \tag{1.10}$$

This allows the introduction of the Franck-Condon factor, $F = |\langle n'|n\rangle|^2$, which is proportional to the overlap between the vibronic wave functions. The overlap decreases quickly as n and n' increase, which explains why the transitions occur mainly close to the pure electronic state. Moreover, the Franck-Condon factor is usually non-zero for neighboring vibronic states, which explains why many molecular absorption spectra feature vibronic replicas of the main absorption peaks. Finally, the argument made here for absorption is also valid for the emission of a photon. The first consequence of this is that the emission spectrum can sometimes feature vibronic replicas, corresponding to the transition denoted $0 - 1$ in Figure 1.16b. These are more visible on the experimental emission spectra of very rigid PAHs and GQDs, such as shown in Figure 1.17. Second, the emission and absorption spectra at low energy often share a mirror symmetry, as schematized in Figure 1.16a. The fact that only the low energy part of the absorption spectrum gets mirrored is a consequence of the Franck-Condon principle and is named Kasha's rule [75]. Indeed, the Franck-Condon factor is usually more appreciable when the difference in energy is negligible. This allows internal conversion and vibronic relaxation to de-excite the system to the lowest excited state, as shown in Figure 1.16b. When energy losses occur in the system, the zero-phonon line of the emission spectrum may be shifted from its absorption counterpart. This is the Stokes shift.

The last part of Figure 1.16b that remains uncommented is the long-lived T_1 triplet state lying between the ground state and the first excited state. These states are often present in PAHs and are responsible for the phosphorescence of the system. They arise from the flipping of the spin of an electron in the first excited singlet, resulting in the triplet state. This process is called inter-system crossing and is often unlikely, making the conversion towards the triplet state slow. The triplet is expected to have a lower energy than the excited singlet because of Hund's rule [73]. Briefly, this states that for a given orbital configuration, the term with the maximum spin multiplicity lies at the lowest energy.

1.3.2 Structure-properties relationships in Graphene Quantum Dots

A possible approach to determine the properties of GQDs consists of treating the confinement as a boundary condition applied to the graphene wave functions. Thus, taking the band diagram in Figure 1.4 on page 7, this is equivalent to restricting the allowed values of k to a discrete set of values determined by the characteristic size of the system, k_{restr}. In the region near the K point, an optical

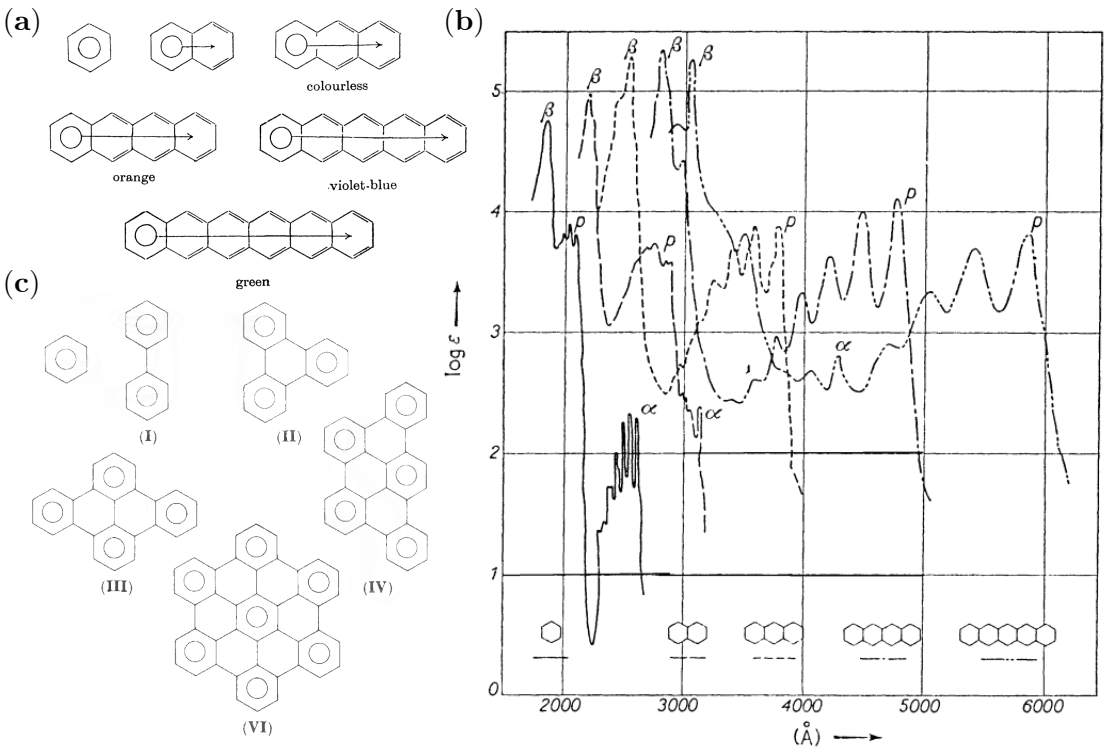

Figure 1.18: (**a**) Clar's representation of the acene series. The migrating π-sextet is represented by a circle and an arrow and is shared over the whole chain. (**b**) Absorption spectra of the acene series. The bands are labelled α, β and p (*para*). The p-bands correspond to the absorption of light polarized in the direction perpendicular to the molecule's long axis. Reproduced from Ref. [11]. (**c**) Clar's representation of fully-benzenoid polycyclic aromatic hydrocarbons. Reproduced from Ref. [76].

transition would correspond to a gap energy of $E_g = 2v_F\hbar k_{\text{restr}}$. The corresponding characteristic length associated is then $L \approx 2\pi/k_{\text{restr}}$ which, for an energy gap of 1 eV corresponds to $L \approx 4.1$ nm. For higher energies, the linear approximation of the dispersion diagram does not hold anymore[8], and this simple approximation breaks down.

Before further discussing graphene quantum dots' properties, it is worth discussing some terminology. From a more chemical point of view, as introduced previously, the graphene quantum dots can be seen as members of the family of polycyclic aromatic hydrocarbons (PAHs), *i.e.* molecules composed of multiple aromatic rings [11], such as naphthalene or anthracene. The absorption spectra for the acene series are shown in Figure 1.18b. These reproduce well the intu-

[8]Due in part to the structure at the M point, but also to other structures coming from next-nearest neighbor jumps that have not been considered in our simplistic treatment of graphene.

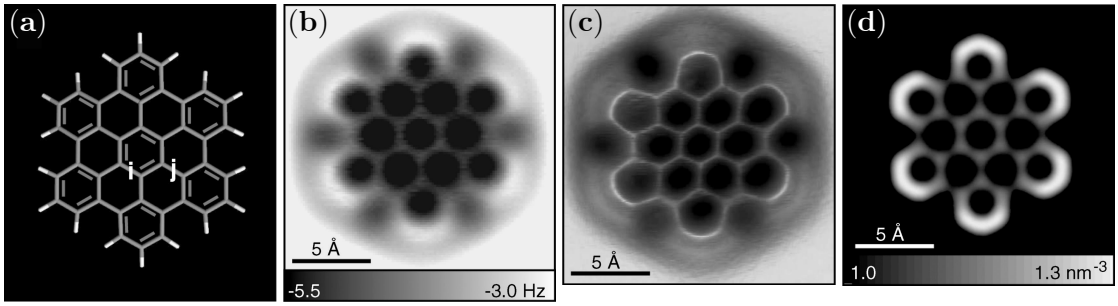

Figure 1.19: Hexabenzocoronene model (**a**) and constant-height AFM measurement on Cu(111) at z=3.7 Å (**b**) and 3.5 Å (**c**) with the local maxima highlighted. (**d**) Calculated electron density at a distance of 2.5 Å above the molecular plane. The bond i is shorter (**c**) and brighter (**b**) than the bond j. Reproduced from Ref. [77].

ition built previously that longer molecules present lower gap energy. The peaks are labeled using Clar's notation, where the prominent peak is usually labeled β, and the lower energy spectra are labeled α and p (*para*). In the acene series, the p-bands correspond to the absorption of light polarized perpendicularly to the long axis of the molecule. The PAHs family usually refers to molecules typically smaller than a GQD, with typically ten to twenty aromatic cycles. Thus, graphene quantum dots are sometimes referred to as large PAHs. Two other denominations are encountered in the literature. The first one is nanographene, which is a larger denomination that also includes graphene-based materials up to a few hundreds of nanometers, such as nanoribbons. The second is carbonaceous dots (or carbon nanodots and other variations). These are usually quantum dots with structures not well controlled and consisting of several layers of graphene sheets. Clar is famously known for his empirical sextet rule [76, 78]. This rule states that the Kekulé resonance structure with the largest number of disjoint aromatic π-sextets (benzene rings) is the most important in determining the properties of the molecule. When several structures with the same number of sextets exist, such as in the acene series in Figure 1.18a, the combination is symbolized by an arrow. In Clar's model, compounds with no lone double bonds, such as in Figure 1.18c, are said to be *fully benzenoid*. Clar's rule, albeit empirical, accounts very well for experimental results [78]. For example, Figure 1.19 shows Atomic Force Microscopy (AFM) measurements performed on a hexabenzocoronene molecule and illustrates the position of the benzene rings as expected from the Clar structure.

The shape of the edges heavily influences the properties of graphene quantum dots. In particular, one distinguishes between "zig-zag", such as the acene series in Figure 1.18a, and "armchair", such as the molecules in Figure 1.18c, edges. In particular, one can convince oneself that a GQD with exclusively armchair edges will be fully benzenoid, leaving no unpaired electrons [79].

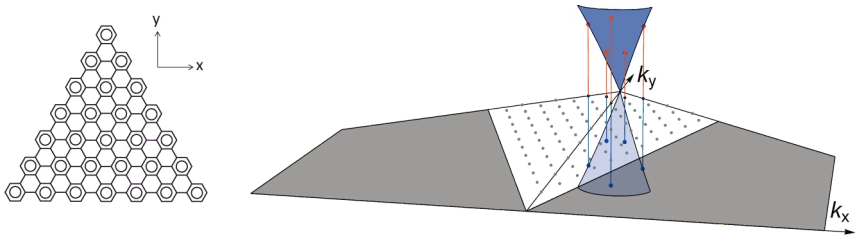

Figure 1.20: Single-particle states in triangular GQDs with armchair edges. The considered GQD consists of $168sp^2$ carbon atoms and is shown on the left. The corresponding restriction of the graphene band structure is shown on the right. Reproduced from Ref. [79], who adapted it from Ref. [80].

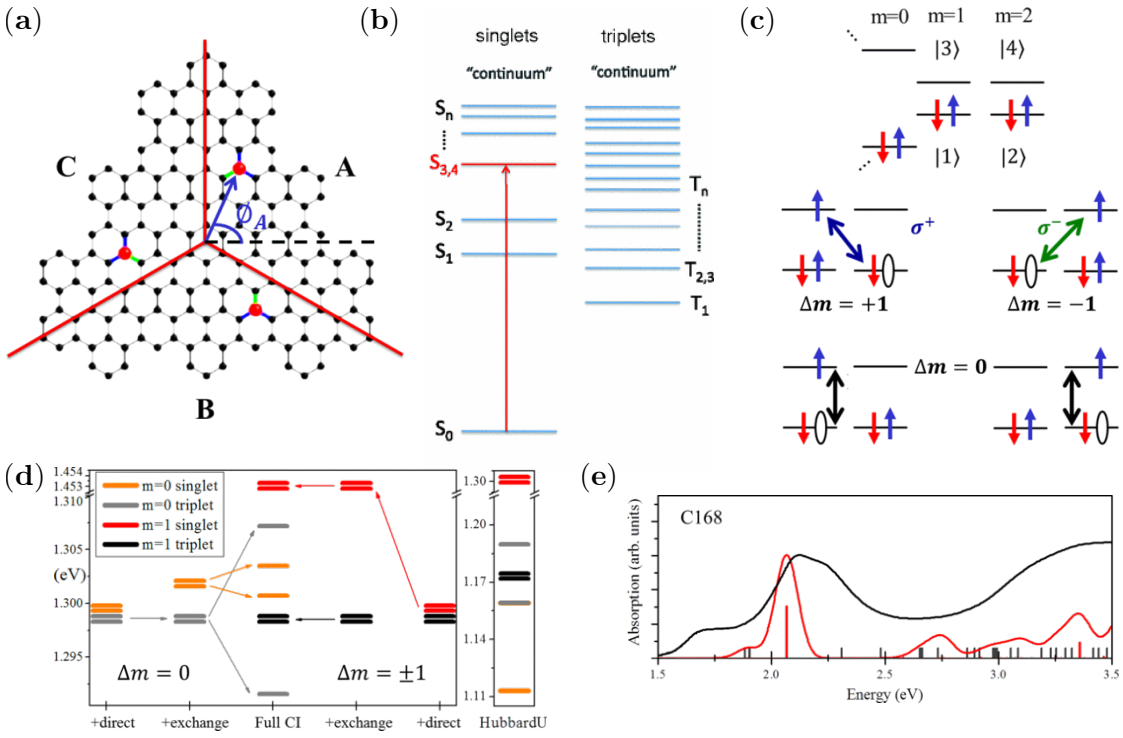

Figure 1.21: (**a**) C_{168} triangular GQD, with symmetry axes in red. From Ref. [81]. (**b**) Illustration of the position of the spectral ordering of the transitions in the GQD, calculated using DFT. From Ref. [82]. (**c**) Ground state of the GQD and allowed transitions depending on the momentum. From Ref. [81]. (**d**) Ordering of transitions using the Hartree-Fock method depending on the various interactions considered. CI: Configuration Interaction. From Ref. [81]. (**e**) Experimental (black) and theoretical (red) absorption spectra of C_{168} triangular GQD, calculated using the Hartree-Fock method and arbitrary broadening of the transitions. From Ref. [81].

For fully-benzenoid structures, it is possible to calculate the solution for a particle in a box in the shape of the GQD and plug the allowed values of the wavevector in the band structure of graphene [80]. Figure 1.20 on the facing page shows the resulting dispersion diagram for such a procedure on a triangular armchair GQD. This is, however, a one-electron picture by necessity of the underlying tight-binding model. More advanced models are required to fully account for the properties of graphene quantum dots. One approach is to use Time-Dependent Density Functional Theory (TD-DFT) to calculate the energy levels. This has been done by Schumacher [82] for triangular GQDs with 168 sp^2 carbon atoms (shown in Figure 1.21a), as well as for a hexagonal GQD with 114 sp^2 carbon atoms. Figure 1.21b shows the two molecules as well as the typical energy levels ordering. In particular, the ground state is a singlet. Moreover, triplet states are expected to lie between the ground state and the first excited singlet. The problem of the modelization of GQDs while accounting for the interaction between electrons has also been tackled using a Hartree-Fock approximation [81, 83]. Both methods highlight the selection rules in polarization, with dark $\Delta m = 0$ momentum transitions and bright $\Delta m = \pm 1$ momentum transitions corresponding to the absorption of a circularly polarized photon, shown in Figure 1.21c. The ordering of the various transitions yields a dark singlet below the first bright excited singlet, as demonstrated in Figure 1.21b and Figure 1.21d. In particular, the Hartree-Fock approach yields a theoretical absorption spectrum compatible with the experimental absorption spectrum (Figure 1.21e).

The selection rules for allowed transitions depend in part on the geometry of the quantum dot and, in particular, on the symmetries of the system. Thus, it is possible to analyze possible transitions allowed by the symmetries of the system *independently of the exact Hamiltonian used to find the eigenstates of that system*, may it arise from simple tight-binding or more advanced approaches, through group theory. An introduction to group theory and its application to quantum mechanics, particularly molecules, is given in Ref. [86]. Briefly, if an operator P corresponding to a symmetry operation, such as a rotation or a reflection, leaves the Hamiltonian H unchanged, *i.e.* commutes with the Hamiltonian, then for any eigenstate $|\phi_n\rangle$ of the Hamiltonian, we have:

$$PH\,|\phi_n\rangle = PE_n\,|\phi_n\rangle \tag{1.11}$$

$$HP\,|\phi_n\rangle = E_nP\,|\phi_n\rangle \tag{1.12}$$

Which is equivalent to saying that a state $P\,|\phi_n\rangle$ obtained by applying a symmetry of the Hamiltonian on an eigenstate of the Hamiltonian will generate another, degenerate, eigenstate of the Hamiltonian[9]. The symmetry operators that leave a Hamiltonian H unchanged form subgroups (in the sense of group theory) that can be classified in irreducible representations[10], and each eigenstate of H belong to

[9] Note that some degenerate state may not be generated by a symmetry operator, and in this case are named *accidental degeneracy*. We do not consider these states here.

[10] Those can be seen here as classes of equivalence for symmetry operations.

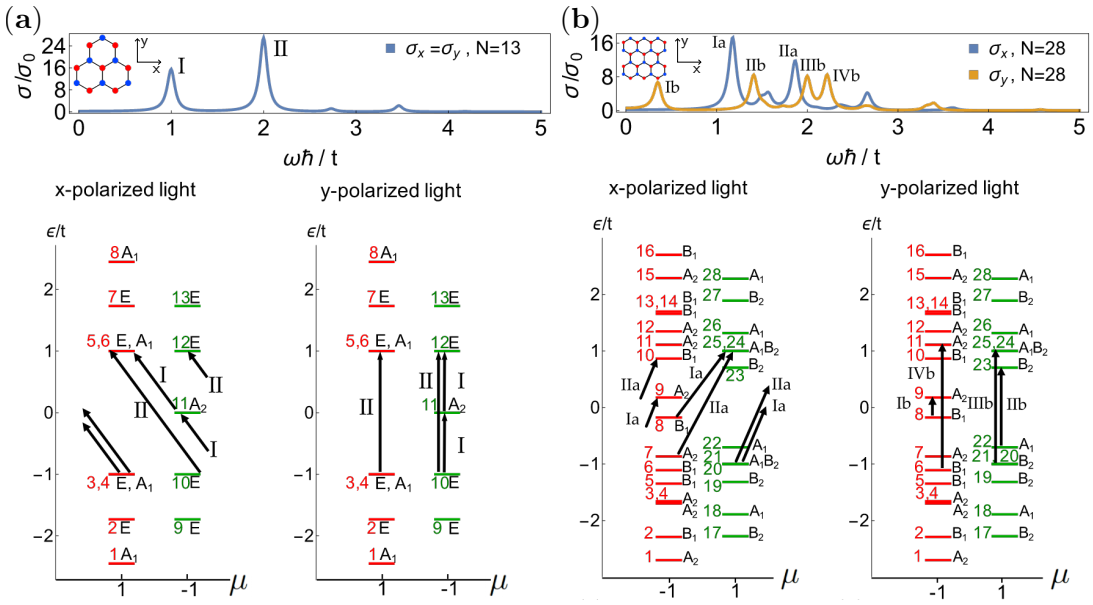

Figure 1.22: Optical selection rules for (**a**) the smallest possible triangular GQD with zigzag edges and (**b**) a rectangular GQD, in linearly polarized light. The optical conductivity $\sigma_\alpha(\omega)$ is calculated with a Lorentzian of FWHM $2\gamma = 0.1t$, with t the exchange energy. The spectrum for each polarization is calculated using a tight-binding model, and the levels are labeled depending on their irreducible representation and eigenvalue under mirror-symmetry on the y axis. Adapted from Ref. [84].

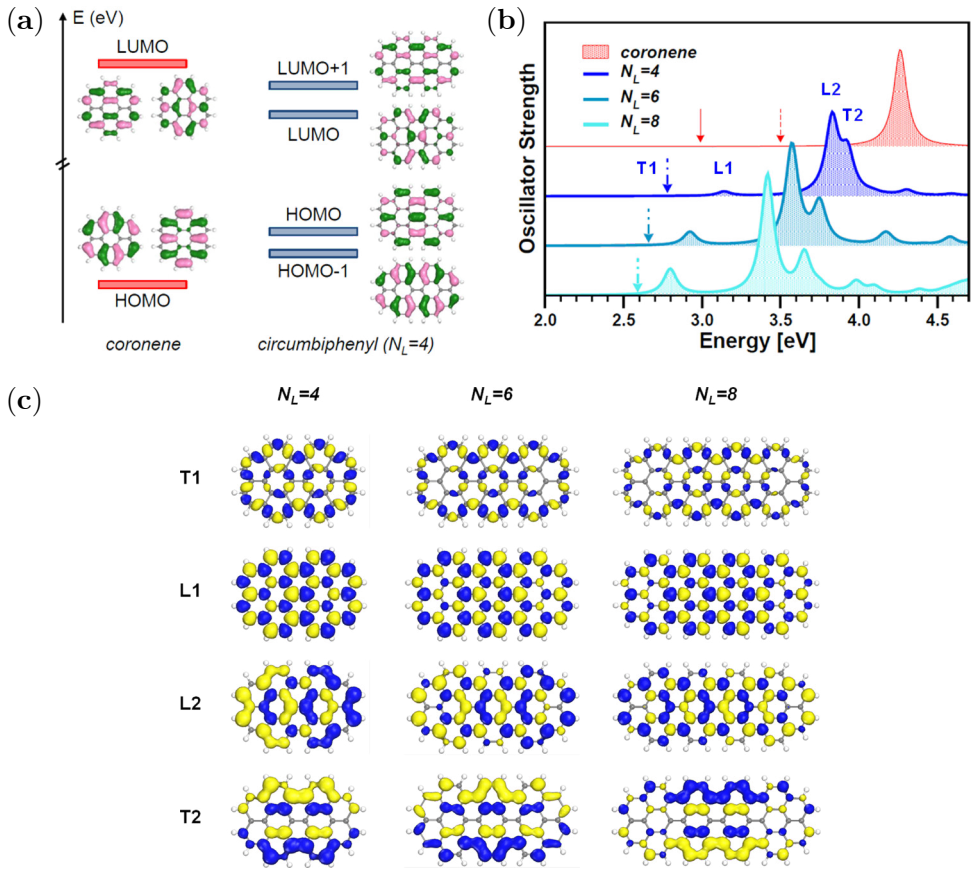

Figure 1.23: (**a**) Isosurfaces of the frontier molecular orbitals of corene and circumbiphenyl. The degeneracy of HOMO and LUMO of coronene is broken in the D_{2h} PAHs. (**b**) Calculated optical absorption spectra of rod-shaped PAHs with fixed width and variable length. The transitions polarized either in the longitudinal (L) or transverse (T) direction are indicated in the spectrum of circumbiphenyl. The dashed-dotted arrows indicate the position of the lowest energy weak excitation T1. The spectrum of Corene is also shown on top. An arbitrary Lorentzian broadening of 110 meV is applied. (**c**) Transition density isosurfaces of the considered species. Reproduced from Ref. [85].

one representation [86]. It can be shown that the matrix elements of an operator H' vanish between functions belonging to different irreducible representations. Thus, if H' represents the perturbed Hamiltonian of the system, one can now see that a transition from state m to n can be allowed only if $|\phi_m\rangle$ and $H'|\phi_n\rangle$ belong to a same representation, *i.e.* have the same symmetries. Using this symmetry-based approach, Pohle *et al.* [84] were able to investigate the selection rules governing the optical transitions of triangular- and rectangular-shaped GQDs. The resulting optical conductivity and eigenstates calculated using a tight-binding model are shown in Figure 1.22a and Figure 1.22b for triangular and rectangular GQDs, respectively. This illustrates how the rectangular GQD because it possesses a simpler symmetry than the triangular GQD, presents a more complex optical response. In particular, the response is polarization-dependent. This has been illustrated by Cocchi *et al.* [85] using a Hartree-Fock method on rod-shaped GQDs, as shown in Figure 1.23 on the previous page. Figure 1.23a and Figure 1.23b show how, starting from the D_{6h} (hexagonal) symmetry of corene, the degeneracy of the lowest transitions corresponding to linearly polarized light get lifted as the symmetry of the molecule is broken to D_{2h} (rectangular) symmetry. This process also renders bright transitions that are forbidden in the hexagonal configuration. The dipole-like character of the transitions is well illustrated by looking at the transition density isosurfaces in Figure 1.23c[11].

Finally, two additional degrees of freedom are available through the edges of the GQDs. First, the shape of the edges, zigzag or armchair, has an influence on the Raman spectrum of the system [88], which means the vibrational picture is affected by the edges. The optical selection rules are heavily influenced by the shape of the edges in graphene nanoribbons [89]. For example, this influence can be retrieved in rectangular GQDs [90]. Moreover, in disordered graphene quantum dots, robust edge states are expected [91]. Then, the functionalization of the edges adds another way to tune the properties of GQDs. In particular, edge functionalization can lead to deformations of the planar structure of GQDs [92], which can then break symmetries and allow new transitions. The effect of functionalization on the transition energy can be experimentally verified, as shown in Figure 1.24a on the facing page for single triangular C_{96} GQDs.

Combining shape-, edge-, and functionalization-tuning of GQDs offers the possibility to choose the optical properties of these objects, as shown in Figure 1.24b and Figure 1.24c. These two figures show the calculated effect of functionalization on the absorption spectra. In particular, it is interesting to see the striking

[11] The transition density isosurface of transition I is defined as $\rho^I(\mathbf{r}) = \sum_{\alpha,\beta} c^I_{\alpha\beta}\phi^*_\beta(\mathbf{r})\phi_\alpha(\mathbf{r})$ where ϕ_α (ϕ_β) indicates the occupied (unoccupied) molecular orbitals and $c^I_{\alpha\beta}$ are the configuration interaction coefficients of the transition I. This relates to the transition dipole moment of transition I as $\mu^I_{0p} = \langle\phi_0|\hat{\mathbf{p}}|\phi_p\rangle = -e\int \mathrm{d}^3r\hat{\mathbf{r}}\rho^I(\mathbf{r})$, with $\hat{\mathbf{p}} = -e\hat{\mathbf{r}}$ the momentum operator, $|\phi_0\rangle$ the ground state Hartree-Fock wave function and $|\phi_p\rangle$ the excited configuration [85]. The transition density isosurface thus provides a visualization of the polarization of the transition.

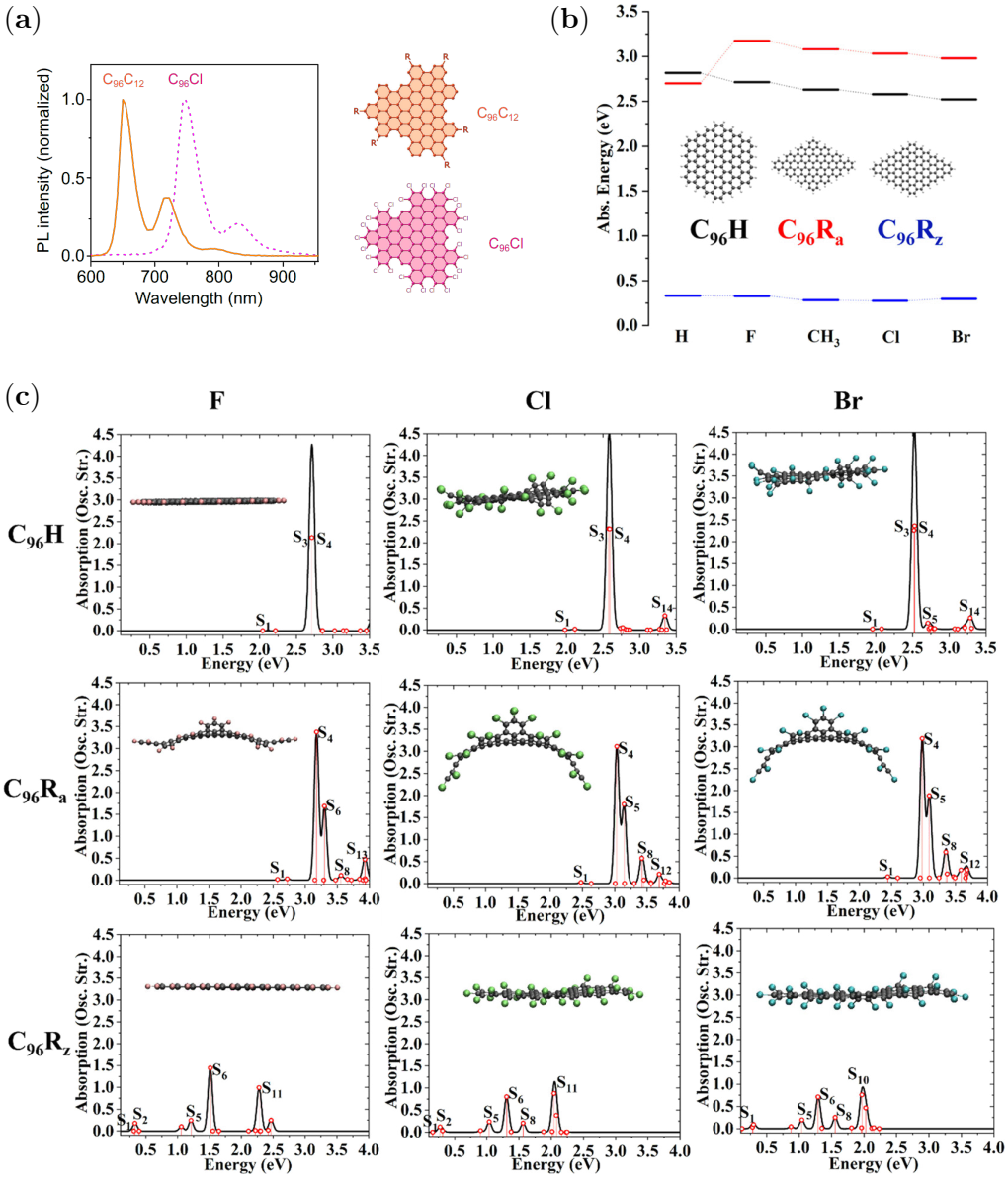

Figure 1.24: (**a**) Emission spectra of GQD with 96 sp^2 carbon atoms functionnalized with dodecyl chains or chlorine atoms. Reproduced from Ref. [13]. (**b**) Schematic of the transition energies of the lowest-energy and bright transitions for the pristine and fully edge-functionalized C_{96} GQDs with CH_3, F, Cl, and Br for various geometries of GQDs (colors). From Ref. [87]. (**c**) Corresponding calculated absorption spectra of the GQDs. The relaxed geometry of the GQD is shown. From Ref. [87].

effect of the edge structure on the lowest bright transition and the rather shape-independent effect of functionalization on the GQD. This also means that it is critical to develop synthesis methods for GQDs that yield highly pure samples. Otherwise, an important in-homogeneous broadening of the ensemble properties is to be expected.

1.3.3 Single-molecule spectroscopy and applications

The field of single-molecule spectroscopy started in the 1990s, with the first optical detection of a single molecule of pentacene in *p*-terphenyl through absorption experiments [93]. The absorption measurement of a single molecule is shown in Figure 1.25a on the next page. Soon after, it became apparent it was in fact possible to use the photoluminescence of the molecules of the same system excited in close resonance [94], as shown in Figure 1.25b, followed by a first measurement of the second-order correlation function [95], shown in Figure 1.25c. In this system, the fluorescent molecules are embedded within a crystal as an impurity. A single molecule is spectrally selected using the inhomogeneous broadening experienced by the molecule within the host matrix, which is possible at low temperatures. One first route explored to produce single-photon emission (see Chapter 2) was the embedding of molecule in a cavity [98]. Another route was the use of near-field spectroscopy [99]. One of the most successful routes to studying single molecules has been using confocal microscopy. This technique allowed the first true display of non-classical light at room temperature from a single emitter [96], as shown in Figure 1.25d. Modern techniques of single-molecule fluorescence microscopy often employ this confocal method. The sample is scanned until a diffraction-limited fluorescence spot is found. Using a specific illumination scheme, this technique allows for example the imaging of the dipole fluorescence pattern of single molecules [97]. In the latter reference, the molecule is embedded in a polymer matrix. This method is often more easily employed for single-molecule fluorescence microscopy, simplifying the sample preparation steps [100].

Single molecules are a platform of choice for nano-sensing applications because of their extreme sensibility to their environment, for example, in biology [101] or material science [102]. Single-molecules such as dibenzoterrylene in anthracene crystals have been proposed as a nanoprobe, *e.g.* for sensing current in molecular crystals [103] or serving as a thermometer at low temperature [104]. This molecule, in particular, is known to be stable at room temperature [105, 106]. Since early in the study of single molecules in the solid state, it has been known that those could experience the Stark effect when put in an electric field [107]. The use of Stark effect can be used nowadays to tune the resonant energy of a single molecule, for example, embedded between 2D materials [108], in 2,3-dibromonaphthalene nanocrystals to experience linear Stark shift [109], or in anthracene nanocrystals, where a local Stark shift can be induced using a laser to tune individual molecules [110]. The fine-tuning of the transitions of a single molecule is an ex-

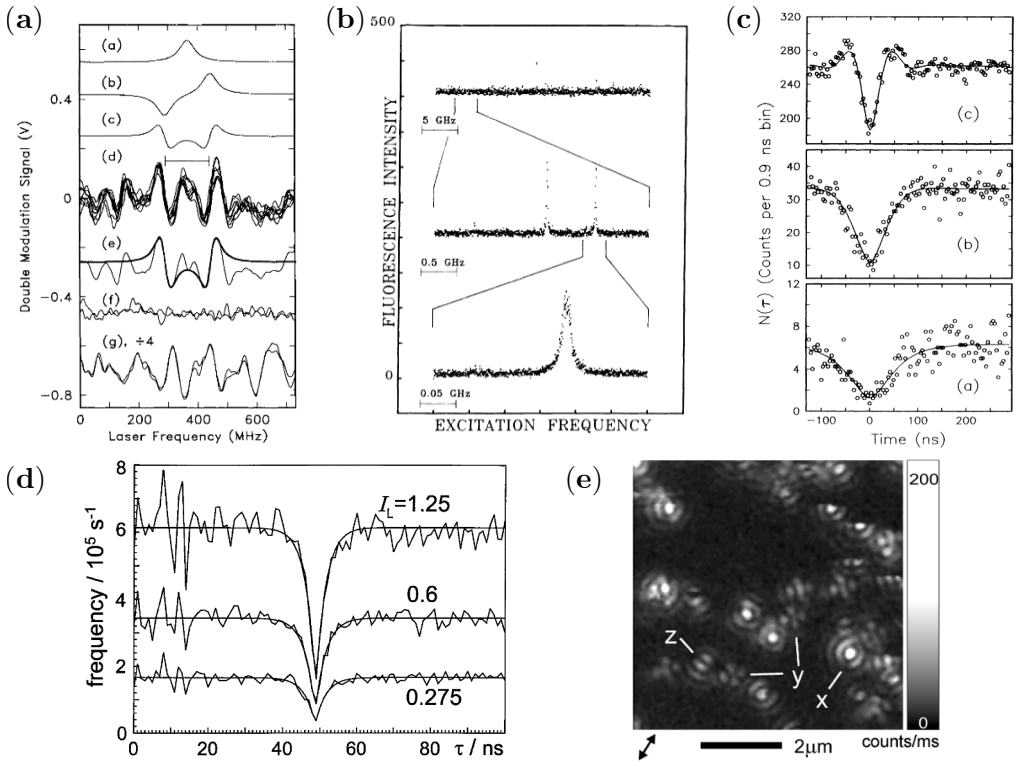

Figure 1.25: (**a**) Single-molecule spectra recorded using frequency modulation Stark double modulation (FMS). a: simulated absorption line, b: simulated frequency modulation spectrum, c: simulated FMS spectrum, d:single molecule spectra, averaged, e: averaged traces fitted to the model (smooth curve), f: signal far off resonance, signal at the O_2 line center. From Ref. [93]. (**b**) Excitation spectra of single molecules from Ref. [94]. (**c**) Second-order correlation measurement at cryogenic temperature from Ref. [95]. (**d**) Second-order correlation measurement at room-temperature on terrylene in *p*-terphenyl from Ref. [96]. (**e**) Confocal single-molecule fluorescence raster scan of 1,1'-dioctadecyl-3,3,3',3'-tetramethylindocarbocyanine embedded in polymethylmethacrylate matrix at room temperature using an annular illumination scheme. From Ref. [97].

ample of how the high sensitivity of those objects enables quantum technology application, such as the emission of indistinguishable photons [111]. The overall impressive achievements of single-molecule studies using PAHs [12] set some goals to achieve with GQDs. Namely, bright and stable emission is required, as well as the ability to prepare single-molecule samples. The interaction of GQDs with potential matrices, or active materials, will be of prime importance for most potential applications of these molecules.

Conclusion

This introductory chapter gives a broad overview of the fields in which the present work is set.

Halide perovskites form a new class of semiconductors that hold great promise due to their outstanding optoelectronic properties, tolerance to defects, and good transport properties. Their processing through standard chemistry techniques enables a whole range of material tunability, from halide substitution to control over the dimensionality of the material to confine charge carriers and the interplay of the organic and inorganic parts of the material. Despite the already competitive technological prowesses achieved in a controlled environment, many fundamental properties of these materials still need to be explored and understood. First, the issue of stability is, of course, of great interest to the industrial field. Then, many excitonic properties are not yet fully understood, as illustrated by the question of the exciton binding energy. I want to mention another topic of interest on perovskites here is the role of interfaces. Those play a significant role in applications [112] because of their roles in charge transport, carriers recombination, and band alignment when forming heterostructures. In Chapter 3, I will present the results of my investigation on the properties of 2D halide perovskites in the context of the developpment of laser sources in the green region of the optical spectrum. Then, I will report on the synthesis and characterization of nanocrystals of perovskites emitting in the same spectral window.

Graphene is another material that holds great promise for applications. Graphene quantum dots can be seen as a graphene derivative, as an attempt to open its gap for optoelectronic applications. Theoretical investigation of these compounds reveals the many possibilities these quantum dots offer in tailoring their shape, size, and functionalization. The practical realization of homogeneous and controlled graphene quantum dots can be achieved through organic chemistry methods. Their high tunability makes them a desirable platform, *e.g.* for single-molecule applications in sensing and quantum technologies. This justifies the need to investigate their spectroscopic properties at the single-molecule level. A study of the properties of a specific family of highly emissive rod-shaped graphene quantum dots, with a focus on the properties at the single-object level will be presented in Chapter 4.

In this context, the high sensitivity of graphene quantum dots to their environment makes them a good candidate for exploring the properties of the surface of halide perovskites at the nanoscopic scale. The investigation of graphene quantum dots on halide perovskite surfaces will be found in Chapter 5.

2 Experimental Methods

Contents

Introduction

The primary tools employed for the characterization of samples throughout this thesis are optical characterization techniques. I classify these techniques into three categories. Ensemble spectroscopy refers to measurements performed using loosely focused optics, and samples are typically solutions or films. Micro-photoluminescence refers to the optical characterization of samples using a microscope objective lens and, as its name suggests, uses the photoluminescence of the sample. It is typically used to characterize films. Finally, single-molecule spectroscopy is very similar to micro-photoluminescence but differs in that a confocal pinhole is used. Other -non-optical- methods were used to characterize the samples presented in this thesis, mainly thanks to our collaborations with other research groups.

In this chapter, I will first present the characterization techniques used to get the results presented in this thesis. I will then highlight some data analysis methods that deserve some attention. Finally, I will present the sample preparation techniques I used. Because of the variety of species and deposition conditions used, I

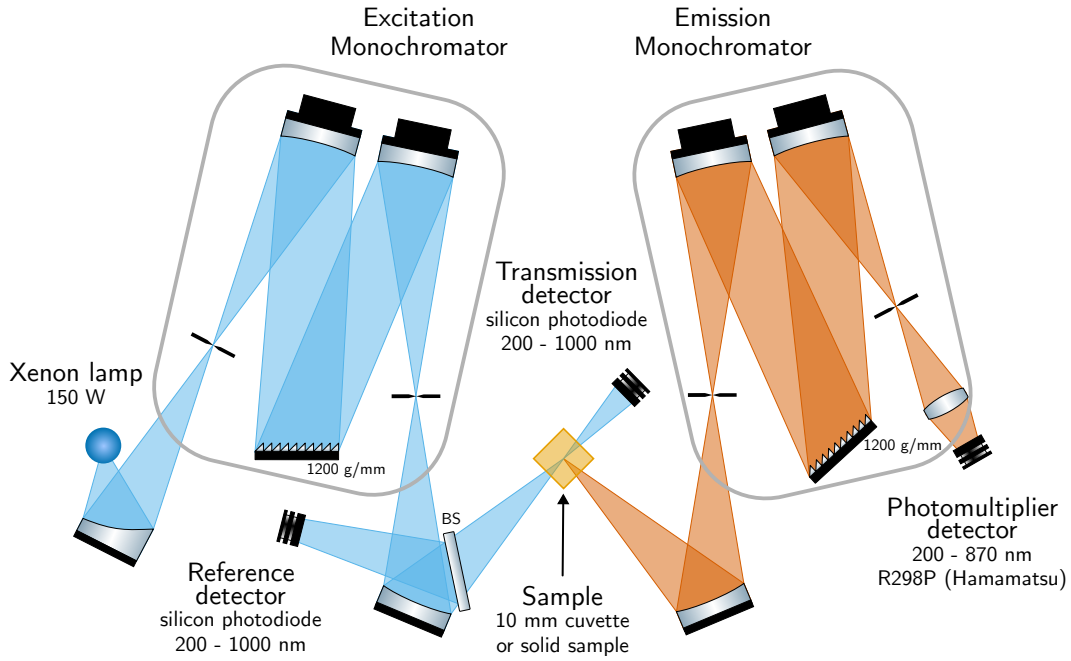

Figure 2.1: Edimburgh Instruments' FS5 ensemble spectroscopy setup. The actual setup is enclosed in a light-tight box. Adapted from Ref. [113].

will only give here a general description of the deposition methods. Furthermore, the synthesis of the species studied (2D perovskite films, perovskite nanocrystals, and graphene quantum dots) are reported in their respective dedicated chapter.

2.1 Experimental apparatus and related techniques

2.1.1 Ensemble spectroscopy

The term ensemble spectroscopy refers to the optical characterization of samples, typically solutions or films, through their properties of absorption and emission using loosely focused optics. This means the properties of many emitters are being investigated at once, which makes for easier sample preparation and, usually, higher signal levels. Various setups and instruments were used to that end in this work, including homemade setups. Still, I chose to present in Figure 2.1 a schematic representation of the FS5 spectrofluorometer from Edinburgh Instruments, as it can perform all the measurements shown in this section. It also produced the large majority of ensemble characterizations presented in this manuscript.

An ensemble spectroscopy setup, or a spectrofluorometer, typically consists of a light source, *e.g.* a xenon lamp or a laser, used to probe a sample. The instrument can then analyze the light reflected (not presented here), transmitted, or emitted

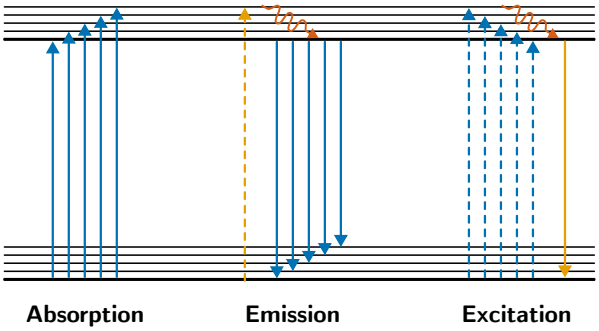

Figure 2.2: Absorption, emission and excitation measurement schemes. The transitions whose intensities are recorded are represented by solid arrows. Dashed vertical arrows symbolize other transitions that are not being recorded, typically the transitions that are used to excite the sample. Wiggly orange arrows correspond to internal conversion and/or vibronic transitions. The transitions that are scanned throughout the measurement are drawn in blue, while those that are fixed are in yellow.

by the sample. When using a xenon lamp, the energy and bandwidth of the excitation can typically be chosen using a first monochromator. Similarly, when performing *e.g.* emission measurements, the energy of the analyzed light can be selected using a second monochromator.

Absorption

As described in the Introduction chapter, the absorption spectrum of a sample gives direct access to its electronic configuration, as only photons whose energy matches an allowed electronic transition will be absorbed.

The absorption spectrum is calculated from the measurement of the transmission of the sample. A typical absorption measurement thus requires two measurements. First, a reference transmission spectrum is recorded, where the sample is replaced by a cuvette filled with solvent or an empty substrate for film samples. The excitation energies are scanned by actioning the excitation monochromator shown in Figure 2.1. The transmission spectrum is calculated by the instrument using the ratio of transmitted power over the power sent to the sample. The latter is measured using the reference detector shown in Figure 2.1. Then, the transmission of the actual sample is recorded using the same procedure. The transitions scanned are schematized in Figure 2.2.

Denoting $T_{\text{ref}}(E)$ and $T_{\text{sample}}(E)$ the transmission spectra of the reference and of the sample respectively, the absorbance can be defined as:

$$\mathcal{A}(E) = -\log_{10}\left(\frac{T_{\text{sample}}(E)}{T_{\text{ref}}(E)}\right) = -\log_{10}\left(\frac{I(E)}{I_0(E)}\right) \tag{2.1}$$

Where $I_0(E)$ and $I(E)$ are the intensity of the light at a given energy that would be sent on and retrieved after the sample respectively if a beam was sent on the sample. Our spectrometer uses the ratio of the transmission spectra instead, which is formally equivalent. Since the amount of transmitted light is expected to be lower than that transmitted by the reference, it is easy to see that Equation 2.1 defines a quantity that spans from 0 (no light absorbed) to arbitrarily high values. However, given the logarithmically scaled definition of absorbance, and because of the signal-to-noise ratio of the detectors, it is unrealistic to expect to be able to interpret spectra with absorbance greater than ~ 3. Some instruments allow recording both the reference and sample transmission measurements simultaneously, using a double light path. Such an instrument (PerkinElmer Lambda 950) has been used early in my thesis and provided some of the measurements reported in Chapter 3.

In addition to showing the allowed electronic transitions for a given sample, the absorption spectrum can be used to measure the concentration of the solution through the Beer-Lambert law [114]. We typically evaluate the concentration of graphene quantum dots solutions using this technique, as the quantities of powder dispersed in the solvent are usually too low to be weighed on a standard chemistry balance. The Beer-Lambert law reads:

$$\mathcal{A}(E) = \ell \cdot \varepsilon(E) \cdot c \tag{2.2}$$

where ℓ is the length of solution traversed by the excitation beam, typically 10 mm, $\varepsilon(E)$ is the molar extinction coefficient at the considered energy, and c is the molar concentration. ε is linked to the absorption cross section σ through $\sigma = \ln(10)\frac{10^3}{\mathcal{N}_\mathrm{A}}\varepsilon$, where $\mathcal{N}_\mathrm{A}$ is the Avogadro constant in mol^{-1}, ε is in $\mathrm{M}^{-1}\mathrm{cm}^{-1}$ and σ in cm^2. The molar extinction coefficient can also be linked to the oscillator strength of a given transition [115].

Emission

When an emitter switches from an electronic excited state to an electronic state of lower energy, we can sometimes observe the emission of a photon whose energy corresponds to the energy difference between those two states. Measuring the energy distribution of those photons is the goal of emission measurement, sometimes also called fluorescence or photoluminescence (PL) measurements.

The principle here is to use a fixed excitation energy and scan a range of positions of the grating within the emission monochromator in Figure 2.1, effectively resulting in scanning the corresponding energy range, as shown in Figure 2.2. An alternative method is to use a CCD array instead of a photomultiplier tube. In that case, the monochromator is fixed during the measurement, which allows for a higher data acquisition rate. Our homemade micro-photoluminescence / confocal fluorescence setups use that kind of detector.

As explained in the first chapter, Kasha's rule [75] states that emission mainly occurs from the lowest excited state. For this reason, emission measurements are

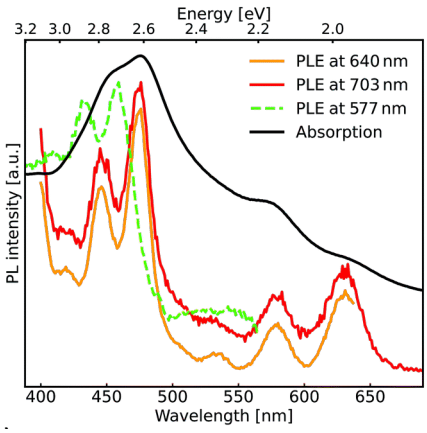

Figure 2.3: Absorption spectrum of a solution of $C_{96}C_{12}$ triangular GQD and PLE spectra collected at the wavelengths of photoluminescence peaks. Reproduced from Ref. [116].

a complement to absorption measurements (see Figure 2.2). The latter tells the experimentalist about the energy levels that can be accessed from the ground state, while the former gives the energy levels that are accessible from the lowest excited state.

Excitation

Another important measurement is the photoluminescence excitation experiment (PLE). This measurement bridges absorption and emission measurements by showing the amount of light emitted at a given transition energy as a function of the energy of the excitation photons. Thus, while absorption spectra measure the existence of allowed optical transitions from the ground state and emission spectra the presence of allowed de-excitation transitions from the lowest excited state, excitation spectra probe a three-step phenomenon. First, the absorption of a photon at the considered excitation energy, then the relaxation of the system towards the lowest excited state, and finally, the de-excitation from the lowest excited state towards the level with the transition corresponding to the observation emission energy. Since the first and third steps are already probed by absorption and emission measurements, excitation measurements provide us with a method to study the relaxation of the system. For systems where the relaxation towards the lowest excited state is efficient, the excitation and absorption spectra should thus superimpose. On the other hand, for example, for systems where the system absorbing the excitation photons differs from the system emitting photons, the two spectra will likely differ. For example, the absorption and excitation spectra of C_{96} triangular GQDs in solution shown in Figure 2.3, because the GQDs form aggregates.

The measurement can be seen as a mirror of the emission measurement. This time, the emission monochromator in Figure 2.1 is set to a fixed position, corresponding to the transition energy for which the measurement is performed, while the excitation monochromator scans a range of excitation energies. As for absorption measurements, the signal measured by the reference detector is used to correct the measurement for the emission spectrum of the excitation lamp.

In complex samples, the excitation spectrum can depend on the emission transition energy considered. This can be accounted for by scanning a range of emission energies for each excitation energy considered, effectively recording an emission spectrum for each excitation energy. This kind of excitation measurement is represented as a two-dimensional map.

Time-resolved photoluminescence

In addition to the steady-state photoluminescence properties of an emitter, one can also measure the transient photoluminescence of a system after a brief excitation, typically $\sim 50\,\mathrm{ps}$ long in our setups. As the emission rate is proportional to the population of emitters in the excited state, this gives a direct measurement of the evolution of the population in the lowest excited state. For example, for a perfect two-level system, the decay will be mono-exponential, and the decay rate corresponds to the sum of the radiative and non-radiative recombination rates.

Figure 2.4 on the facing page shows a typical time-resolved photoluminescence (TRPL) setup, also called a time correlation single photon counting (TCSPC) experiment. A pulsed laser, usually a laser diode with a $\sim 50\,\mathrm{ps}$ pulse width and an adjustable repetition rate, excites the sample repetitively. A synchronization pulse is sent to the computer for each optical pulse. The excitation pulse is typically much shorter than the fluorescence lifetime. Thus, the system is allowed to evolve freely after the excitation. After an amount of time determined by the internal properties of the sample, the system will de-excite through the emission of a photon, which will be collected by the emission monochromator and sent to the detector.

The acquisition card can estimate the distribution of delay times dt between the excitation pulse and the detection of a photon on the photodetector by building a histogram of the measured delay times between INPUT and their preceding SYNC events, as shown in Figure 2.5 on page 46. In practice, some experimental precautions are needed. First, to avoid overloading the acquisition card, it is recommended to adjust the intensity of the excitation laser so that the input count rate remains below 5 % of the synchronization count rate [117] to avoid "pile-up" effect, that is, the detection of multiple photons during one single excitation cycle. Then, it is sometimes necessary to account for the instrument response function (IRF). Figure 2.6 on page 47 shows the instrument response functions of two setups used to acquire the time-resolved photoluminescence data reported in this manuscript. These response functions can be measured by using a highly

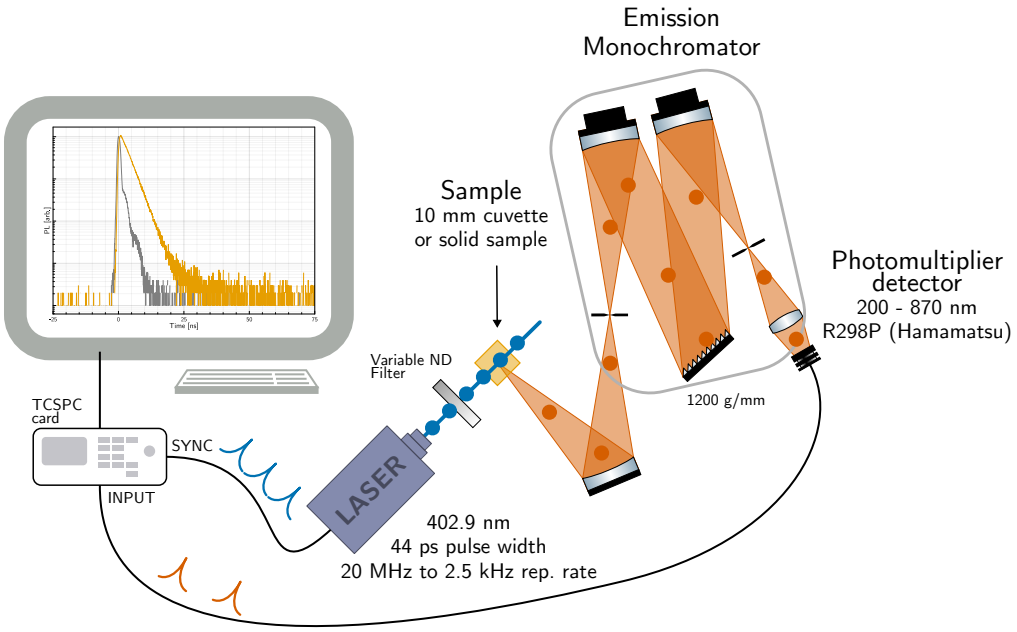

Figure 2.4: Typical time-resolved photoluminescence setup with Edinburgh Instrument's EL-405 laser. In some setups (see Figure 2.9 for example), an avalanche photodiode can be used instead of the photomultiplier.

dispersive solution or reflecting the excitation laser on a glass plate, depending on the nature of the sample being measured. It can be seen that the response function of photomultiplier tubes have widths that are near a nanosecond. Since this is comparable to the photoluminescence lifetime of a molecule, it is necessary to deconvolve the instrument response function from the measurement. This is usually done during data analysis while fitting a model for the population decay. See Subsection 2.2.2 for more detail on the data analysis procedure for time-resolved photoluminescence measurements.

Photoluminescence Quantum Yield

A last ensemble optical characterization technique used in this manuscript is the measurement of photoluminescence quantum yield. This measures the efficiency with which a system emits an absorbed photon and is defined as:

$$\phi = \frac{\text{Number of photons emitted}}{\text{Number of photon absorbed}} \tag{2.3}$$

Two quantities thus need to be measured: the number of absorbed photons and the number of emitted photons. This is measured using an integrating sphere. In our case, this consists of a module (SC-30, Edinburgh Instruments) that replaces

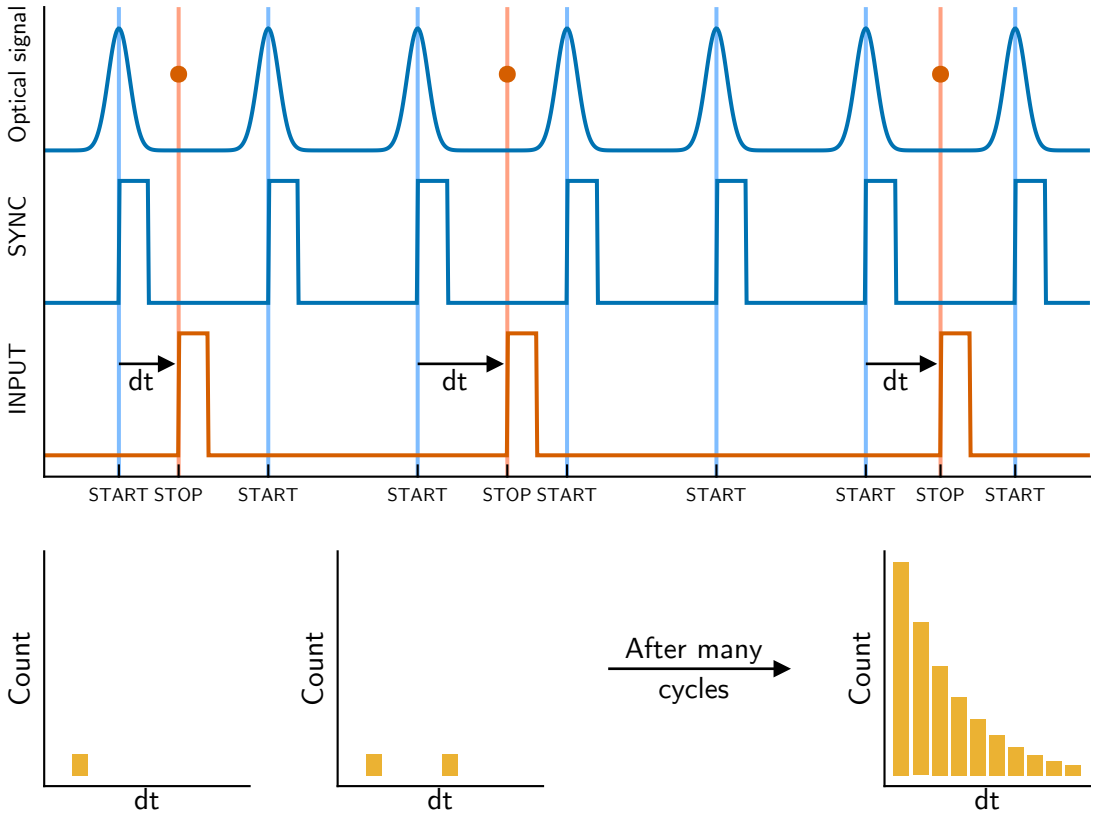

Figure 2.5: Principle of time-correlation single photon counting. The blue optical signal is the intensity of light outputted by the excitation laser. The orange dots correspond to photon counting events on the photomultiplier tube in Figure 2.1. The SYNC and INPUT signals are the signals of the corresponding inputs in Figure 2.4. The successive histograms are calculated from the distribution of delay times *dt* between each INPUT and preceding SYNC events. Adapted from Ref. [14].

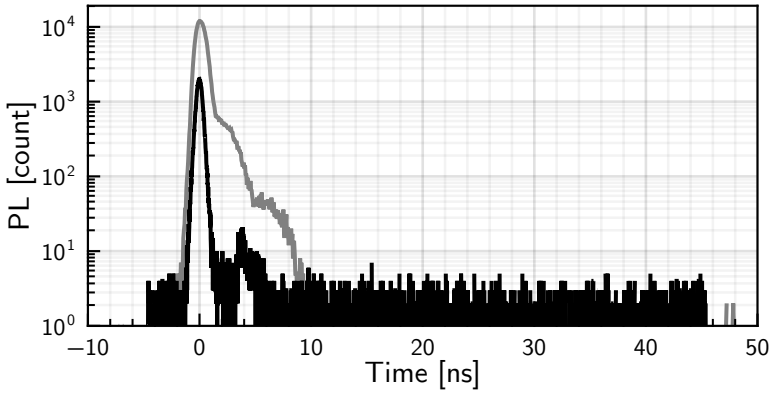

Figure 2.6: IRF of two detectors used to report ensemble time-resolved photoluminescence traces. In gray from a Fluoromax+ (Horiba) spectrometer with a NanoLED solid-state pulsed laser diode (483 nm) and black from the FS5 setup.

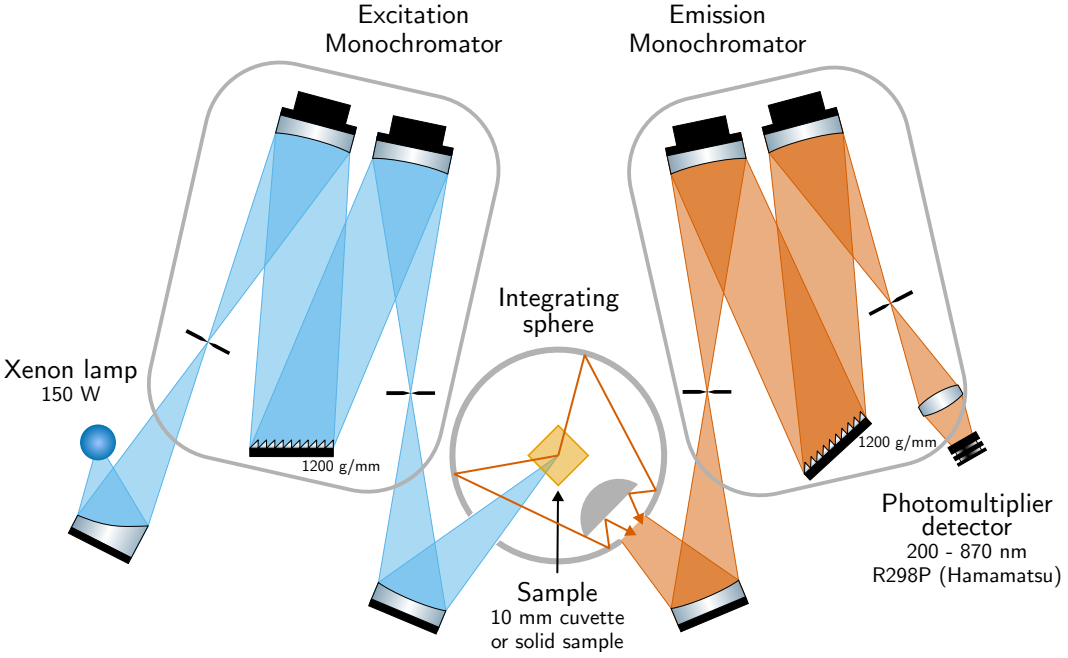

Figure 2.7: Photoluminescence quantum yield measurement setup.

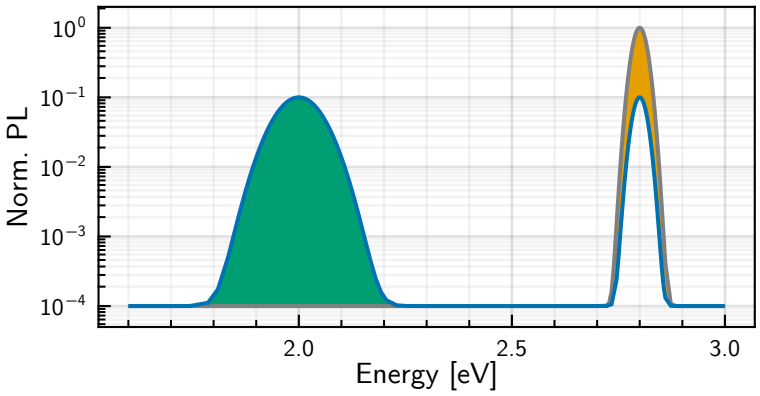

Figure 2.8: Example (simulated) Measurement of photoluminescence quantum yield. The reference spectrum is in gray, while the sample spectrum is in blue. The number of photons absorbed is estimated by the area of the yellow region, while the area of the green region estimates the number of photons emitted. The diffusion is estimated thanks to the background levels.

the standard sample holder of the spectrofluorometer, shown in Figure 2.7. It consists of a spherical hollow box with small apertures for the excitation and emission beams. The sphere's interior is coated with a white diffusive and highly reflective medium, which allows collecting most of the photons emitted by the sample, regardless of the direction of emission. The measurement of photoluminescence quantum yield typically requires two acquisitions: one of a reference (typically a cuvette filled with solvent only) and one of the species of interest. An acquisition on this setup is similar to the acquisition of a photoluminescence spectrum: the excitation monochromator is set to a fixed excitation energy, while the emission monochromator scans a region of interest. We usually excite close to the maximum of absorption to get as much signal as possible. A significant difference between the measurement of a photoluminescence spectrum and an acquisition of photoluminescence quantum yield is that the excitation energy is included in the region scanned by the emission monochromator. This would usually be avoided to prevent damaging the detector but is allowed when using an integrating sphere. In addition, the bandwidth of the excitation monochromator is typically three to ten times smaller than the bandwidth of the emission monochromator. A simulated measurement is shown in Figure 2.8. The number of photons absorbed can be estimated using the area between the reference spectrum and the sample spectrum around the excitation region. The number of photons emitted can be estimated using the area between the curves in the emission region. The photoluminescence quantum yield is then calculated using Equation 2.3.

The technique presented here is named *absolute* quantum yield measurement and is suitable for highly emissive samples such as the ones reported in this manuscript.

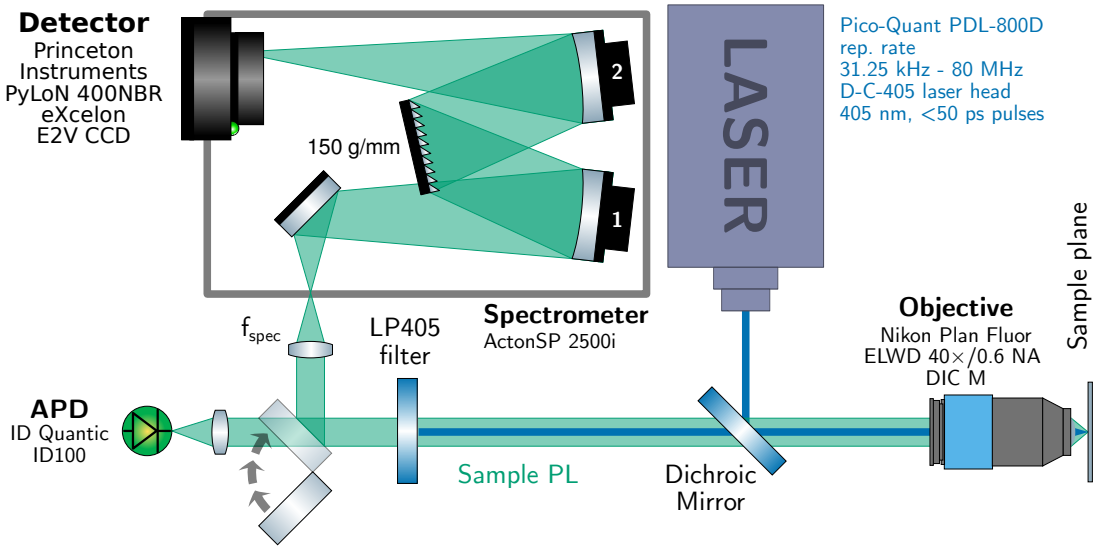

Figure 2.9: Simplified scheme of the micro-photoluminescence setup.

A variant of absolute quantum yield measurement consists of measuring the absorption and emission regions using different bandwidths, typically with a much larger one in the emission region, allowing to measure lowly emissive samples. It is also possible to perform *relative* quantum yield measurement. These do not require an integrating sphere and instead consist of comparing the intensity of the photoluminescence of the sample against that of a reference sample of known quantum yield. This, however, requires careful calibration steps for all emission energies considered.

2.1.2 Micro-photoluminescence and confocal fluorescence microscopy

The micro-photoluminescence (micro-PL) setup used to perform measurements on the films presented in Chapter 3 is shown in Figure 2.9. This can be seen as an intermediary setup between the commercial ensemble characterization setup presented earlier and the confocal fluorescence microscope. The sample is excited by a laser beam focused using a microscope objective lens, and the fluorescence is collected through the same lens. The residual of the laser excitation is filtered out using a long-pass filter. The setup can measure emission spectra as well as time-resolved photoluminescence decay measurements.

Two confocal fluorescence microscopes have been used, shown in Figure 2.10 on the next page. Both are very similar and can often be used interchangeably. The main differences reside in the laser sources available, the single photon detection, and the scanning methods. The first setup uses three piezo axes from Piezosystem.

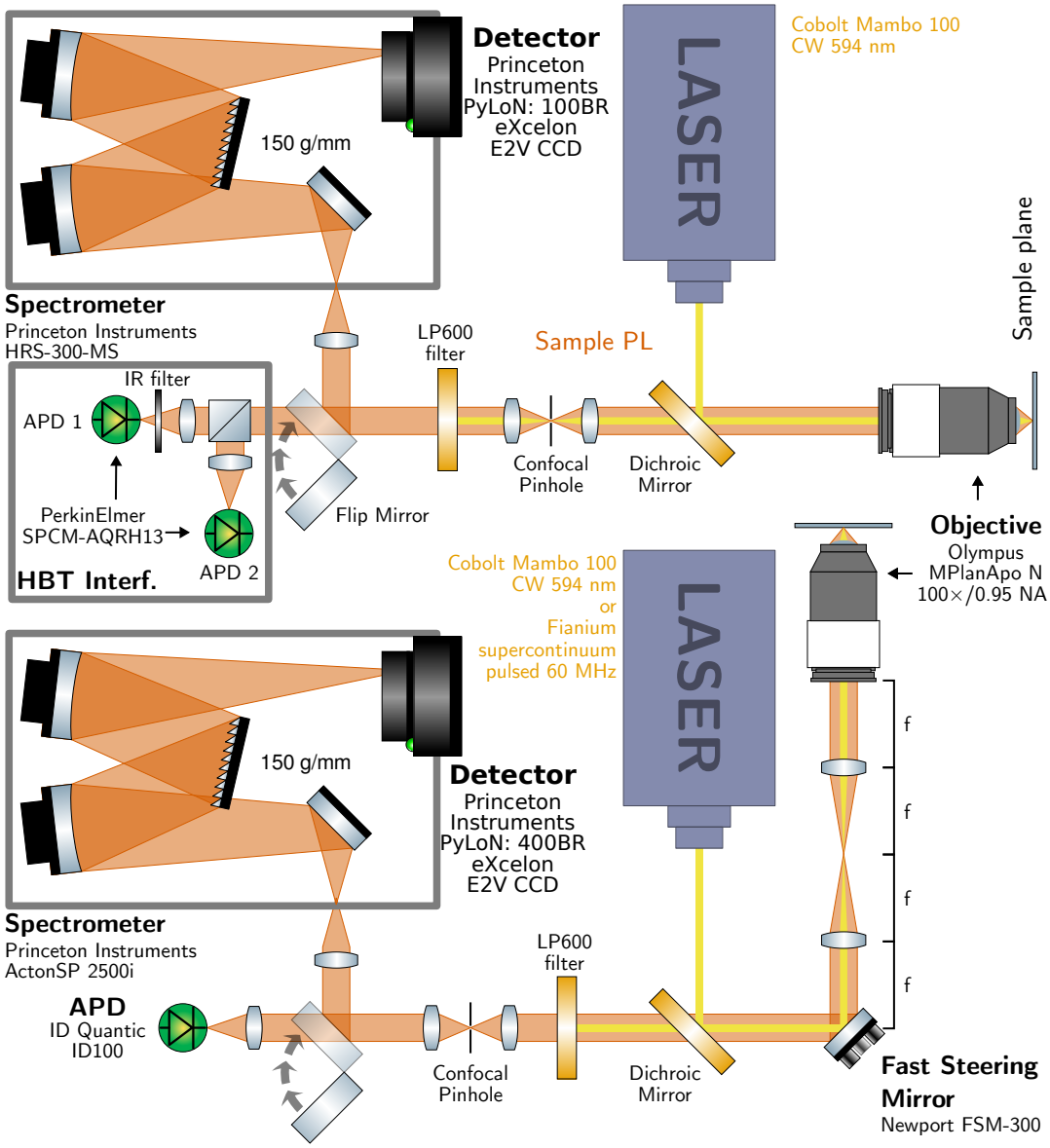

Figure 2.10: The two confocal fluorescence microscopes used to produce the data presented in this manuscript. For simple scans, they can be used interchangeably.

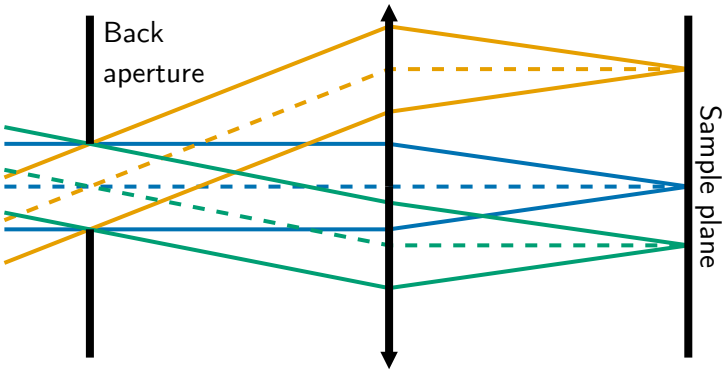

Figure 2.11: Effect of changing the angle of the beam at the back aperture of the objective.

The second one uses a piezo from Piezosystem Jena for the z-axis, and a fast steering mirror optically conjugated to the back aperture plane of the microscope objective through a 4-f system. This is equivalent to controlling the input angle of the collimated laser beam at the back aperture plane while keeping a constant position and thus preventing the beam from missing the back aperture of the microscope objective. The microscope objective effectively can be modeled as a thin lens here, with the back aperture plane and sample planes being respectively at one focal length before and after the lens. This system can be modeled using ray optics in the ABCD matrices formalism:

$$\begin{bmatrix} y_{\text{out}} \\ \theta_{\text{out}} \end{bmatrix} = \begin{bmatrix} 1 & f \\ 0 & 1 \end{bmatrix} \cdot \begin{bmatrix} 1 & 0 \\ -1/f & 1 \end{bmatrix} \cdot \begin{bmatrix} 1 & f \\ 0 & 1 \end{bmatrix} \cdot \begin{bmatrix} y_{\text{in}} \\ \theta_{\text{in}} \end{bmatrix} \tag{2.4}$$

$$= \begin{bmatrix} 0 & f \\ -1/f & 0 \end{bmatrix} \cdot \begin{bmatrix} y_{\text{in}} \\ \theta_{\text{in}} \end{bmatrix} \tag{2.5}$$

Where $y_{\text{in,out}}$ and $\theta_{\text{in,out}}$ are the height and angle of a given ray at the considered end of the system. This equation is illustrated in Figure 2.11. Notably, one can notice that the center ray of the beam always hits the sample plane perpendicularly. Because the light originating from an emitter at the focus of the objective lens would back-propagate following the same path as the laser beam, the photoluminescence beam always presents the same direction of propagation when leaving the fast steering mirror towards the dichroic mirror and the detection setup. The two microscopes are thus functionally equivalent.

Emission spectra

The Princeton Instruments spectrometers we use require a more in-depth understanding of their inner workings than the commercial instrument used for ensemble

characterization. These spectrometers are in a Czerny-Turner configuration. The entrance slit is put on the focal plane of a converging mirror, such that a beam focalized on the entrance slit is collimated and sent towards a reflective grating before being focalized again by a second converging mirror onto a CCD camera.

The resolution of the spectrometer can be evaluated from the characteristics of the optical system. First, considering a monochromatic beam, that we can approximate as a monochromatic plane wave once collimated by the input mirror, we can study the effect of the grating in the situation shown in Figure 2.12a on the next page. The beam reflected by the grating is the result of the interference of N beams, whose intensity can be written:

$$I(\theta_o) \propto \frac{\sin^2 \frac{N}{2}\phi(\theta_o)}{\sin^2 \phi(\theta_o)/2} \tag{2.6}$$

Where N is the number of grooves illuminated by the collimated beam. The phase $\phi(\theta_o)$ comes from the dephasing between two successive groves and reads:

$$\phi(\theta_o) = \frac{2\pi d}{\lambda} (\sin\theta_i + \sin\theta_o) \tag{2.7}$$

Where λ is the wavelength of the light, d is the grating's period, and θ_i and θ_o are the input and output angles of the grating. $I(\theta_o)$ is plotted in Figure 2.12b on the facing page. Since the second converging mirror focalizes the reflected beam on the detector, there is a direct, linear correspondence between θ_o and the position on the detector. This justifies the study of the output intensity of the grating directly as a function of the output angle θ_o. In particular, we can see that the maximum of the reflected intensity is obtained for $\phi = 0$, which corresponds to $\theta_i = \theta_o$, and does not depend on the wavelength. The other successive local maxima are numbered k, and correspond to $\phi = 2k\pi$, or:

$$\sin(\theta_o) = k\frac{\lambda}{d} - \sin(\theta_i) \tag{2.8}$$

Equation 2.8 shows how we can directly map an output angle to a wavelength since the input angle can directly be controlled through the rotation of the grating with respect to the beam collimated by the first converging mirror. And since the output angle is directly mapped to a position in the detector plane, θ_i effectively sets which wavelength gets mapped to the center of the detector. We call that wavelength the central wavelength. A second important factor is the diffraction order k. Spectrometers usually use $k = 1$. However, it is possible to detect higher diffraction orders accidentally. For example, when exciting a sample with a 400 nm laser, a spurious peak may be detected at the position corresponding to $\lambda = 800\,\text{nm}$. This peculiar case is easily dealt with using a long path filter before the spectrometer.

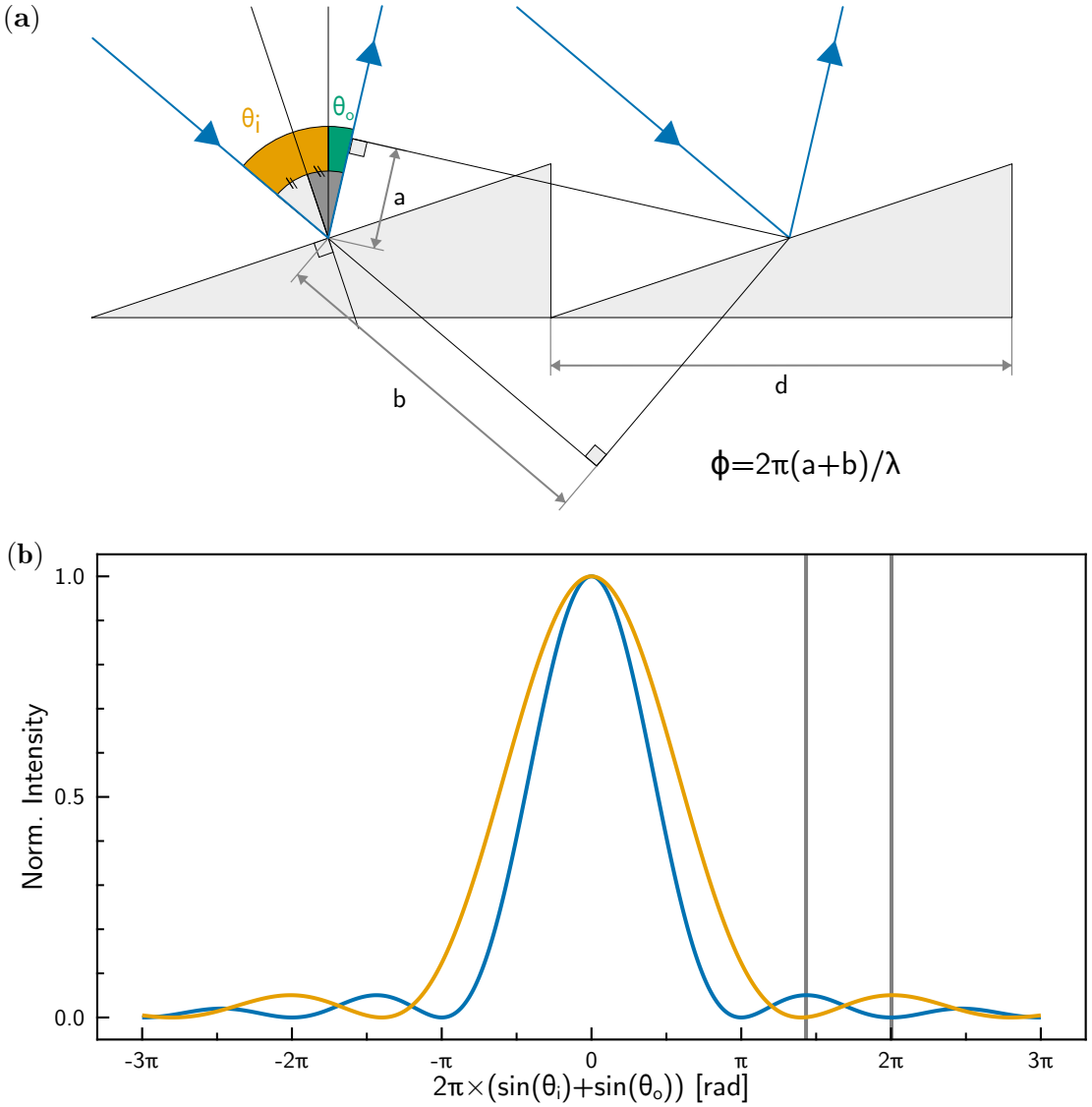

Figure 2.12: (**a**) Study of a blazed grating, and definition of the angles used in this section. (**b**) Intensity diffracted for two wavelengths, verifying the Rayleigh criterion for the first diffraction order.

An intrinsic limit to the ability of a grating to distinguish between two wavelengths can be derived from Rayleigh's criterion. Given a specific wavelength λ, the next resolvable wavelength $\lambda + \mathrm{d}\lambda$ must have its diffraction peak falling at a minimum of the intensity radiated for λ, as shown by the yellow curve in Figure 2.12b. For small steps $\mathrm{d}\lambda$, one can differentiate Equation 2.8 to get the relation of dispersion:

$$\mathrm{d}\lambda = \frac{d}{k} \cos\theta_o \mathrm{d}\theta_o \tag{2.9}$$

From the definition of $I(\theta_o)$, one can see that the angle separating a local maximum to the next local minimum is $\mathrm{d}\phi = 2\pi/N$. And from the definition of $\phi(\theta_o)$ we get (for small $\mathrm{d}\phi$):

$$\mathrm{d}\phi = \frac{2\pi d}{\lambda} \cos\theta_o \mathrm{d}\theta_o \tag{2.10}$$

It follows that $\mathrm{d}\lambda = \lambda/kN$. This expression emphasizes the importance of the number of grooves in the grating that get hit by the collimated beam. For the spectrometer to work at optimal operating conditions, the grating must be used entirely. Since the input slit is at the focal plane of the first converging mirror, the inclusion angle determines the size of the collimated beam. The optimal aperture ratio (sometimes called the *f-number*) is given by the manufacturer. It corresponds to the ratio between the focal length of the lens focusing the beam on the slits (f_{spec} in Figure 2.9) and the diameter of the collimated beam before the lens. For the ActonSP 2500i, the f-number is $f/6.8$. The resolution power of the spectrometer depends on the wavelength considered. Our spectrometer is equipped with gratings with 150, 1200, and 2400 grooves per millimeter, which, supposing we work at the optimal aperture ratio and on the first diffraction order, yields a resolution power at 520 nm of ~ 0.0510 nm, ~ 0.006 nm, and ~ 0.003 nm respectively.

The exact mapping of λ to a given column of pixels on the detector using Equation 2.8 depends on the alignment of the spectrometer. To get as accurate measurements as possible, the software of the instruments corrects the wavelength using a polynomial. The coefficients of the polynomial need to be fitted during a calibration procedure that involves the measurement of a known spectrum, usually a gas lamp. We used the IntelliCal Hg and Ne/Ar dual switchable USB light source from Teledyne Princeton Instruments.

The second parameter that limits the resolution of the spectrometer comes from the finite size of the entrance slit and camera pixels. The relation of dispersion that links the position on the CCD to the wavelength can be found from the angular

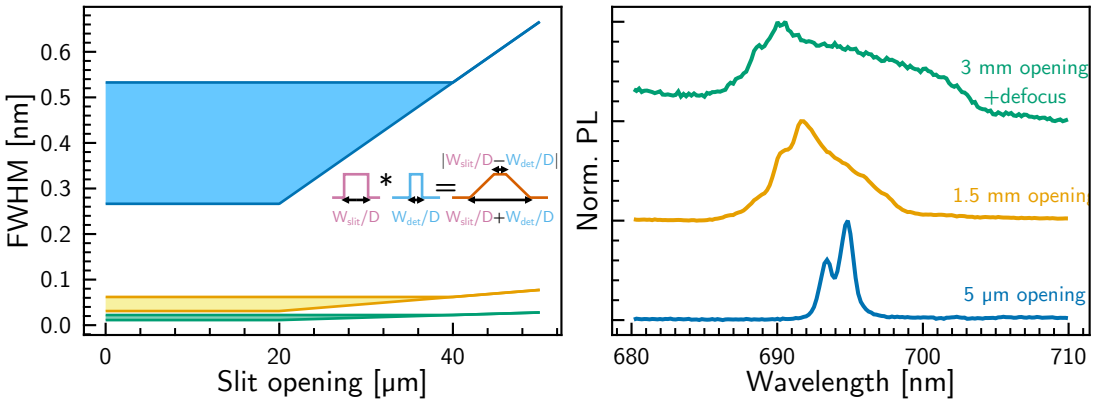

Figure 2.13: (**a**) Theoretical full-width at half maximum (FWHM) of the response function of the spectrometer for three gratings, 150 g/mm (blue), 1200 g/mm (yellow), and 2400 g/mm (green), as a function of the entrance slit width. The detection is taken for one and two-pixel widths. (**b**) Emission spectrum of a nanometric ruby pressed between diamond anvils for various slit widths. The green spectrum has been taken with the object slightly de-focused to fill the whole entrance slit.

dispersion of the grating [118]:

$$D = \frac{\mathrm{d}x}{\mathrm{d}\lambda} = f\frac{\mathrm{d}\theta_o}{\mathrm{d}\lambda} \tag{2.11}$$

$$= f\frac{k}{d}\frac{1}{\sqrt{1-(\frac{k\lambda}{d}-\sin\theta_i)^2}} \tag{2.12}$$

$$\approx f\frac{k}{d}\frac{1}{\sqrt{1-\left(\frac{k\lambda}{2d}\right)^2}} \tag{2.13}$$

Where f is the focal length of the two converging mirrors, 500 mm in the case of the SP-2500i, and 300 mm for the HRS-300-MS spectrometer. The approximation in Equation 2.13 is justified because the grating is usually used with $\theta_i \approx \theta_o$. Considering a rectangular input slit, and rectangular pixels on the CCD, the broadening from these two apertures would be the width of the convolution of two rectangles whose widths depend on the angular dispersion of the grating, W_{slit}/D and W_{pixel}/D.

The CCD detector on the SP-2500i is a 1340 × 400 array of 20 µm × 20 µm pixels. The detector of the HRS-300-MS is similar, but with only 100 pixels on the vertical axis. The dispersion can be calculated directly from Equation 2.13, and is $\sim 75\,\mu\mathrm{m\,nm^{-1}}$, $\sim 632\,\mu\mathrm{m\,nm^{-1}}$, $\sim 1535\,\mu\mathrm{m\,nm^{-1}}$, for the 150, 1200, and 2400 grooves per millimeter grating of the SP-2500i respectively. The two only parameters available to us to improve the resolution of the spectrometer are the

SP2500i

Grating	@520 nm (2.38 eV)	@620 nm (2.00 eV)
150 g/mm	0.41 nm (1.9 meV)	0.36 nm (1.1 meV)
1200 g/mm	0.05 nm (0.2 meV)	0.04 nm (0.1 meV)
2400 g/mm	0.03 nm (0.1 meV)	0.02 nm (0.07 meV)

HRS-300-MS

Grating	@520 nm (2.39 eV)	@620 nm (2.00 eV)
150 g/mm	0.69 nm (3.2 meV)	0.59 nm (1.9 meV)
300 g/mm	0.35 nm (1.6 meV)	0.30 nm (1.0 meV)
900 g/mm	0.16 nm (0.5 meV)	0.10 nm (0.3 meV)

Table 2.1: Line widths of the spectrometers used on the micro-PL and the confocal setup.

slit width and the density of the grating used. Borrowing the visualization idea from Thomas Liu's thesis [14], I show in Figure 2.13a the full-width half maximum of the response of the SP-2500i at 520 nm, accounting for both the width of the slit and of the detection area. For each grating, the top line corresponds to a detection width of two pixels and the bottom one of one pixel. This accounts for the two extreme cases where a peak falls exactly at the center of a pixel and exactly at the junction between two pixels. Notably, two regimes can be observed: one where the slit image on the detector is bigger than the width of a pixel, for which the resolution is proportional to the slit width, and a regime where the slit's width is smaller than the width of a pixel, for which the size of a pixel dominates the resolution. With the SP2500i spectrometer, we use a 100 mm input lens. Assuming a 0.3 cm beam radius before the lens, the spot size in the slit's plane would be approximately 21 µm, which, using the plot in Figure 2.13a, means the response of the instrument is limited by the size of the pixels of the camera. In the worst case scenario, at 520 nm, the line width is thus about 0.5 nm. The resolutions of the two spectrometers used on the micro-PL and confocal setups are reported for the two spectral regions most used in this thesis in Table 2.1 for beam radii at the output of the microscope lens of 0.3 cm and a focusing lens of 100 mm and 50 mm focal length for the SP2500i and HRS-300-MS respectively. Using the diameter of the photoluminescence spot in the slit's plane as the slit's width is reasonable, as opening the slit wider than the spot size in the slit's plane will not widen the instrument's response function[1].

[1]It will, however, allow more stray light to enter the spectrometer and may contribute to deteriorate the quality of the measurement. The response function of the instrument can further be widened because of mis-alignments of the optics, poor focusing of the sample, or even by tilting the camera. Proper alignment procedures are described in the manual of the spectrometers.

The effect of the slit's width can be seen in practice for narrow spectra, such as the emission from a calibration lamp, or as in Figure 2.13b, the emission from a nanometric ruby between two diamond anvils. This measurement was performed using a monochromator (Acton SP-150-i) with a 150 mm focal length and a 600 g/mm grating. The corresponding expected line width is 0.2 nm, which corresponds to a response width of ~ 0.2 nm in the optimal case. The apparent width of the spectrum increases drastically as the slit is expanded.

Excitation spectra

Using the supercontinuum laser, we can use the micro-PL setup to record photoluminescence excitation spectra. In this configuration, we use a piece of glass to reflect part of the excitation beam toward a power meter and the avalanche photodiode to record the number of photons emitted by the sample. By definition, the excitation spectrum at energy E is the ratio of photons emitted by the sample to the number of photons it receives. The rate of photons emitted by the laser can be estimated by the power of the excitation beam through the energy of a photon as $R_{\text{ph}}(E) = \eta P(E)/E$, where η is the product of efficiency of the reflection on the glass and the detection efficiency, and $P(E)$ is the measured power.

For homogeneous samples, such as films, we can use the ratio of the measured emission rate by the rate of photons sent by the excitation laser[2]. For discrete samples, such as single photon emitters, using the power is not adequate. Indeed, the transition rate of the emitter depends on the intensity rather than the power. As the energy of excitation varies, the size of the excitation spot changes, its radius is proportional to the wavelength, and the power is spread on a larger area. This causes the local intensity to decrease. For a film, the fact that intensity diminishes is compensated by the increasing number of emitters being excited. When the emitter is much smaller than the diffraction-limited spot, this is no longer the case, and the excitation rate must be corrected to account for the varying excitation spot area.

Time-Resolved Photoluminescence

The micro-PL setup can perform time-resolved photoluminescence measurements using the method described in Sub-Subsection 2.1.1. The detector here is an avalanche photodiode from ID Quantic (ID100). The acquisition and binning are performed on PicoQuant's TimeHarp 260 card. The instrument response function of the whole setup is shown in Figure 2.14. The response's width is typically ~ 90 ps, which allows considering the response function is a Dirac function when running data analyzes for lifetimes of the order of the nanosecond.

[2]If the transmission of the setup depends on the wavelength, it is also necessary to correct the excitation and emission rates by the adequate transmission efficiency.

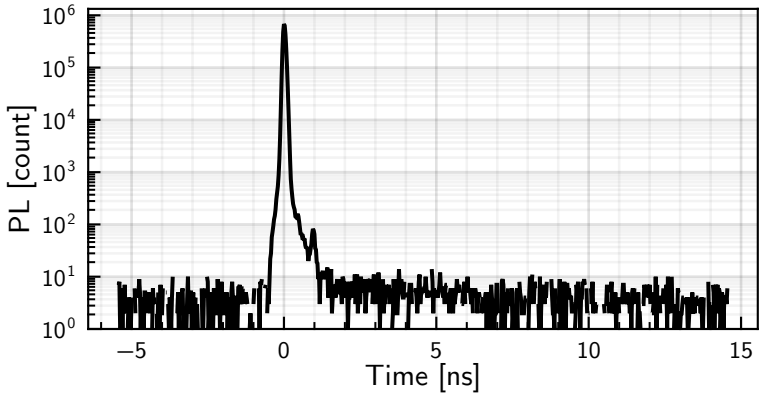

Figure 2.14: Instrument response function for the transient photoluminescence measurements on the micro-PL setup.

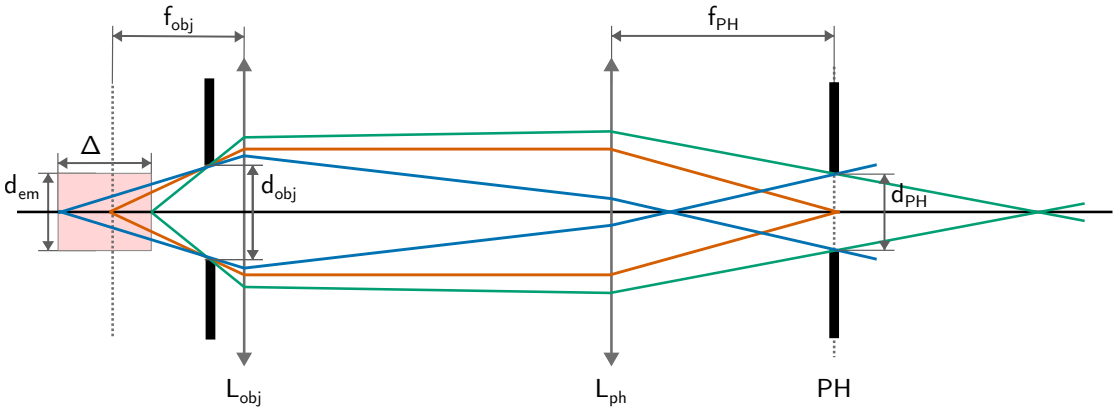

Figure 2.15: Simplified ray-tracing picture of the role of a confocal pinhole.

Confocal pinhole selection

The significant difference between the micro-PL setup and a confocal fluorescence setup is the presence of a pinhole in the detection path, on a plane optically conjugated with the sample plane, as shown in Figure 2.10. Its role is to spatially filter the emission from emitters out of the focus plane that may get excited by the laser beam.

The confocal planes available can be estimated from the numerical aperture and the magnification of the objective. The situation is schematized in Figure 2.15. The diameter of the pinhole must let most of the light from an in-focus emitter pass. The magnification M of an Olympus objective is given for a 180 mm tube lens and reads $M = 180\,\mathrm{mm}/f_{\mathrm{obj}}$, where f_{obj} is the effective focal length of the objective. From there, the size of the image of the emitter in the pinhole plane,

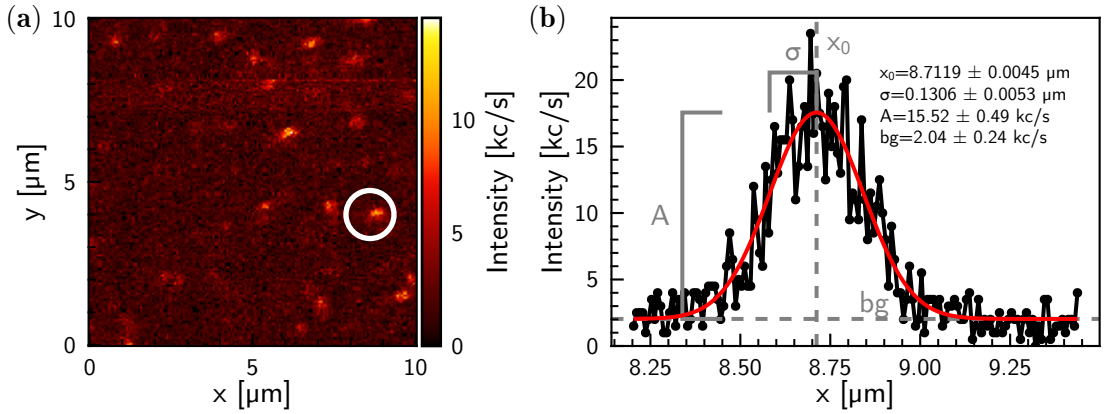

Figure 2.16: (**a**) Confocal raster scan of a sample of graphene quantum dots in a polystyrene matrix. (**b**) Cut along the x-axis of a zoomed-in scan of the area circled in white, corresponding to a single photon emitter. The result of a Gaussian fit is shown in red.

and thus the adequate diameter of the pinhole, is given by $d_{\mathrm{ph}} = f_{\mathrm{ph}}/f_{\mathrm{obj}} \times d_{\mathrm{ex}}$, where f_{ph} is the focal length of the lens used to focus on the pinhole plane, and d_{ex} is the size of the excitation spot in the emitter plane.

The radius of the excitation spot can be calculated using the Rayleigh criterion, which corresponds to the first minimum of an Airy disk.

$$R = 1.22\frac{\lambda}{2\mathrm{NA}} \tag{2.14}$$

Where λ is the excitation wavelength, 594 nm, and NA is the numerical aperture, 0.95. The resulting excitation diameter is ~ 763 nm, which corresponds to a spot size of ~ 42 µm in the pinhole plane. This makes a 50 µm pinhole suitable.

The depth of focus, *i.e.* the ability of the microscope to resolve a system near the focal plane can be assessed using the simplified ray optics scheme in Figure 2.15. The vermilion rays correspond to an emitter exactly in focus. The two other sets of rays, blue and green, correspond to two limiting cases where the rays pass at the edge of the objective pupil and the confocal pinhole. They delimit the depth of field Δ. The volume probed by the microscope can be approximated to a cylinder whose diameter is determined by the diameter of the pinhole d_{ph} as $d_{em} = f_{obj}/f_{ph} \times d_{ph}$, which, given the choice of pinhole matches the diameter of the excitation spot. The depth of field Δ is the height of the cylinder and can be approximated to $\Delta = d_{em}/NA$, which corresponds to a length of ~ 850 nm.

Confocal fluorescence raster scans

The confocal fluorescence microscopes are equipped with scanning capabilities. In associating a level of fluorescence, *i.e.* an event rate on the avalanche photodiodes,

to a set of positions, it is possible to create a fluorescence raster scan. For example, for films of polystyrene embedding graphene quantum dots, this yields photoluminescence maps such as shown in Figure 2.16a on the previous page. Single emitters are much smaller than the diffraction limit. This means they can be approximated as a Dirac function. As a result, we observe in the confocal raster scan the point spread function of the microscope displaced to the position of the emitter. This is shown in Figure 2.16b, where I plotted a cut along the x-axis of a zoomed-in scan around a single emitter. Because the excitation laser can be approximated by a Gaussian beam, the point spread function is well fitted by a Gaussian curve, with a standard deviation of $\sim 130\,\text{nm}$, corresponding to the diffraction limit. Fitting the confocal scans with a Gaussian function allows the software controlling the setup to optimize the position of the microscope objective to get the single emitter exactly in focus and thus extract as much light as possible.

Second order correlation measurements

The second-order correlation function is classically defined as:

$$g^{(2)}(\tau) = \frac{\langle I(t)I(t+\tau)\rangle}{\langle I(t)\rangle^2} \tag{2.15}$$

where $I(t)$ is the intensity of the light coming to the detector. Second-order correlation measurements are performed using two avalanche photodiodes (PerkinElmer SPCM-AQRH13) in a Hanbury Brown - Twiss configuration, as shown in Figure 2.10. An extensive theoretical study of $g^{(2)}(\tau)$ for the graphene quantum dots reported in this thesis is reported in Chapter 4. For now, it suffices to consider $g^{(2)}(\tau)$ as a coincidence function between the two detectors. Because of the discrete nature of the photon counting techniques employed here, the result is often presented as a histogram, un-normalized. To recover $g^{(2)}(\tau)$ from the histogram, one can use the expected value of the histogram if the source under scrutiny was a perfect Poissonian source [119]:

$$g^{(2)}(\tau) = \frac{K(\tau)}{NwR_2} = \frac{K(\tau)}{wR_1R_2T} \tag{2.16}$$

where $K(\tau)$ is the value of the histogram for time τ, N is the total number of points in the histogram, w is the bin width of the histogram, T the duration of the measurement, and R_i the detection rate on detector i.

A typical histogram is shown in Figure 2.17. The dip at 0 delay time is typical for single photon emitters. It is relatively easy to build an intuition on the value of $g^{(2)}(\tau = 0)$ as a function of the number of emitters. Suppose the signal entering the interferometer originates from N sources, with an emission rate Γ. Let T be the duration of the measurement. At infinite delay time, the signal from each emitter is Poissonian, and the value of the histogram corresponds to the sum of

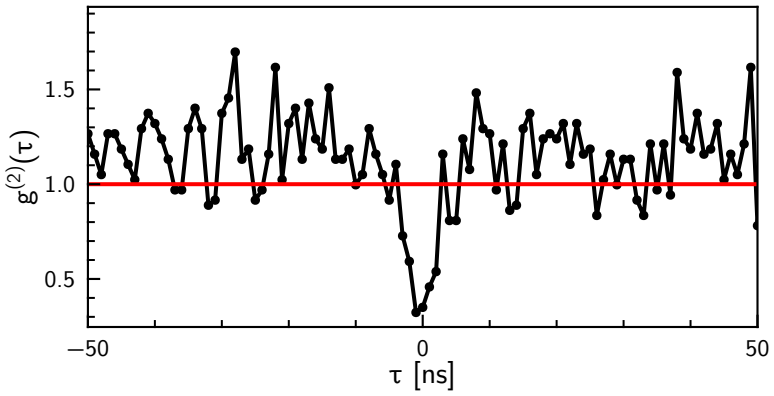

Figure 2.17: Typical normalized second-order correlation histogram obtained for a single photon emitter, here a single $C_{96}tBu_8$ GQD. The horizontal red line shows the expected value of the histogram for a Poissonian source.

these Poissonian sources. This means the value of a bin at infinity is $N \times \Gamma^2 wT$, with w the bin size. For a 0 delay time, assuming the sources are uncorrelated, there is always one source that is not emitting[3]. This means the histogram bin for 0 delay time should have the value $(N-1) \times \Gamma^2 wT$. We can now normalize the histogram by its value at infinite delay time, and we immediately see that its value in zero is directly linked to the number of emitters:

$$g^{(2)}(\tau = 0) = 1 - \frac{1}{N} \tag{2.17}$$

In particular, this makes it easy to identify a single photon emitter using the second-order correlation function: its value at zero delay time must be below 0.5. In presence of a Poisson noise (*e.g.* stray laser light scattered by an optics of the setup), a constant bias can be present in the histogram.

Two acquisition modes can be used to measure second-order correlation functions. The first one is a start-stop method. This works exactly as time-resolved measurements presented in Sub-Subsection 2.1.1, except that instead of having the synchronization input coming from the excitation laser, it now comes from one of the avalanche photodiodes. The other input signal comes from the second detector. To detect events at negative delay times, some hardware requires a delay line to be added between the second input and the acquisition card. As detailed in Chapter 4, this start-stop method is only suitable for measurements at short delay times. For measurements of $g^{(2)}(\tau)$ at long time scales, one needs to resort to time-tagged time-resolved (TTTR) methods. In this configuration, the arrival times of photons on both detectors are recorded independently. The instrument thus provides the experimenter with a list of arrival times for each channel. A

[3]By definition of a single photon source, it only emits one photon at a time.

procedure to obtain the correlation histogram is detailed in Subsection 2.2.3. In addition to calculating the correlation histogram, the TTTR mode enables other analyses, such as creating intensity time traces with arbitrarily thin binning time or calculating the inter-photon waiting time distribution.

During this thesis, three acquisition systems have been used to record correlation histograms. For $g^{(2)}(\tau)$ at short time scales, with the start-stop method, we used a PicoHarp 300 from PicoQuant, a P7887 from FastComtec, and a Time Tagger 20 from Swabian Instruments. The Swabian Instruments card is of peculiar interest here, as it can measure the correlation at negative delay times without the need for a delay line and provide many additional functionalities, such as a built-in normalization of $g^{(2)}$ measurements. The TTTR acquisitions were performed using the PicoQuant card.

The avalanche photodiodes used in the interferometer can sometimes emit a photon after the detection [120], which can then be detected by the second photodetector, a phenomenon called crosstalk and leading to artifacts in the second order correlation histograms. A short-pass filter cutting the infrared radiations above 800 nm inserted in front of one of the photodiodes is enough to remove this artifact.

2.1.3 Other characterization techniques

X-Ray Diffraction (XRD)

X-ray diffraction (XRD) is a method in which a beam of X-rays is diffracted by the sample being analyzed. This technique is particularly suited for the analysis of crystalline samples. The resulting diffractogram maps the angle of the diffracted rays to their intensity and typically consists of a series of sharp peaks. The positions of the peaks are given by Bragg's law and inform the experimenter of the material's structure.

The thin films of perovskite nanocrystals presented in Chapter 3 were characterized by Nicolas Guiblin (Laboratoire Structures, Propriétés et Modélisation des Solides, CentraleSupélec) using a D8 ADVANCE (Bruker, Germany) with a Cu Kα radiation source ($\lambda = 0.154\,18$ nm) at a rate of $2\,^\circ$/min in the scanning angle (2θ) range from 3° to 60°.

Transmission Electron Microscopy (TEM)

Transmission Electron Microscopy (TEM) is a technique in which a beam of electrons is transmitted through a sample and then analyzed to form an image of that sample.

The transmission electron microscopy images presented in Chapter 3 were taken on a JEM 2100 Plus (JEOL) and an accelerating voltage of 200 kV. The high-angle annular dark field scanning TEM (HAADF-STEM) [121] images were taken with

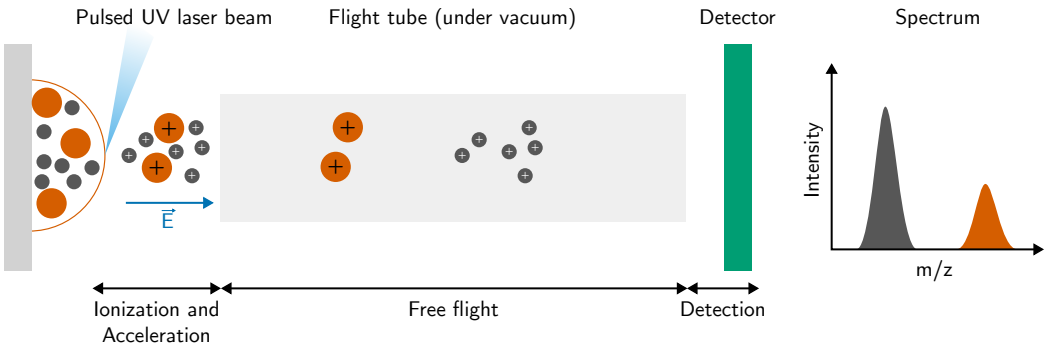

Figure 2.18: Principle of MALDI-TOF. The species to be analyzed are embedded in a matrix that is ablated by a pulsed UV laser, then ionized and accelerated by an electric field. The ions then experience a free flight in a vacuum chamber before detection. Adapted from pedagogie.ac-montpellier.fr

a Titan3 G2 80-300 (FEI ThermoFisher) operating at 200 kV by our collaborators Frédéric Fossard (Laboratoire d'étude des microstructures) and Maxime Vallet (Laboratoire SPMS, Laboratoire de Mécanique Paris-Saclay).

Matrix-assisted laser desorption/ionization, Time of flight (MALDI-TOF)

We assessed the structure and purity of the samples of GQDs studied in Chapter 4 and Chapter 5 using Matrix-assisted laser desorption/ionization, Time of Flight (MALDI-TOF). This is a mass spectrometry technique in which the species to be analyzed is put in a suitable matrix that is ablated by a pulsed UV laser. The species released in the atmosphere are then ionized and accelerated by an electric field. The heaviest species will accelerate to a lesser velocity than their lighter counterparts, which allows the segregation in time of the compounds after a free flight in a vacuum tube. Thanks to the pulsed nature of the ablation laser, it is possible to measure the time of flight and convert a time of flight to a mass, as shown in the schematic. This is a simplified picture since, in practice, various isotopes of the same compound are present in the sample. The abundance of each isotope is known, as well as the efficiency of the ionization process of each compound, which allows the identification of molecules thanks to their specific mass spectrum.

In the context of this study, the spectra were recorded on a Bruker Autoflex speed or a Bruker UltrafleXtreme, and the samples were analyzed in DCTB (trans-2-[3-(4-tert-butylphenyl)-2-methyl-2-propenylidene]malononitrile) matrix.

Atomic Force Microscopy (AFM)

Atomic force microscopy is a technique that allows measuring the topology of a surface using the changes induced to the mechanical properties of a cantilever pro-

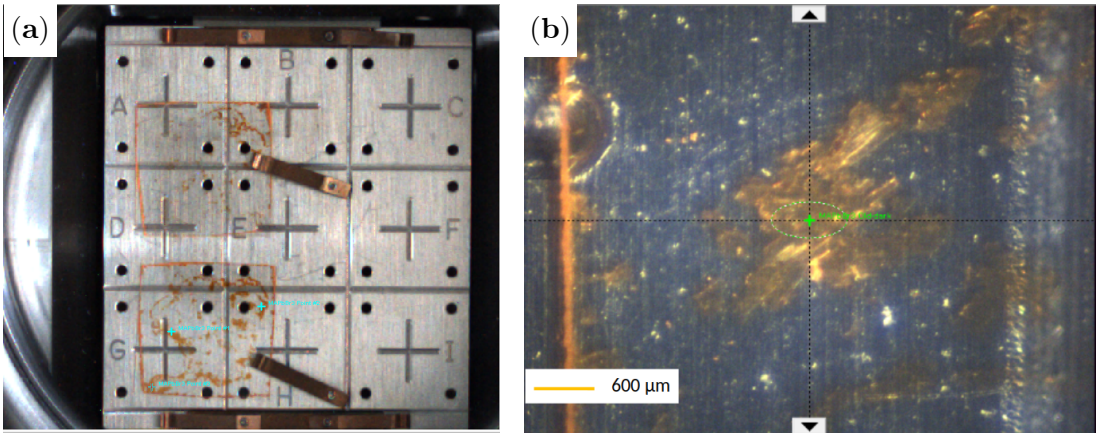

Figure 2.19: (**a**) Mounting of the glass coverslips, once separated, on the XPS spectrometer sample holder. (**b**) Camera visual of the positioning of the analysis spot on the perovskite crystal

longed by a tip when that tip is in close proximity to the atoms of the surface. The cantilever is typically set to oscillate at a few hundreds of kilo-Hertz. The actual oscillation frequency is measured using a laser focused on the cantilever, which allows the detection of changes in the mechanical properties of the system and effectively measures the distance between the cantilever and the surface. Various acquisition modes exist for atomic force microscopes, such as tapping, where the cantilever oscillates far from the surface and only comes in contact with it at the extremity of its course, and contact, where the cantilever is kept in contact with the surface. We typically use the contact mode. By scanning the area of interest, it is then possible to record a height map of that area.

The surfaces of the perovskite crystals used in Chapter 5 have been characterized using an atomic force microscope (MFP3D standalone, Asylum Research) with silicon tips (AC160TS, Olympus).

X-Ray photoelectron spectroscopy (XPS)

X-ray photoelectron spectroscopy (XPS) was used to characterize the surface chemistry of the perovskite substrates presented in Chapter 5. This technique allows probing around 10 nm depth from the surface of materials and informs about the chemical composition as well as the chemical environment of the species.

The process consists of irradiating a sample with an X-ray source causing the emission of photoelectrons, whose energy is measured by the device (under ultra-high vacuum), effectively producing a spectrum. The energy of these photoelectrons is representative of the various electronic orbitals of atomic species excited and their modification by their environment. Wide scans browsing the whole energy range (also called survey spectrum) are measured and can be completed to

get a further insight on the atomic bindings by high energy resolution spectra acquisition by focusing on the spectral region of the main elements of interest. After careful calibration of the spectrometer, the area under the peaks is measured, and corrective factors sensitivity factors are applied (sensitivity factors, transmission function, inelastic mean free path...) to obtain atomic percentages. Additionally, fitting the high energy resolution spectra can be done to precisely determine the species nature, based on the chemical shifts, and determine their proportion.

In the case of perovskites, specific care has to be taken to ensure the reliability of measurements in UHV and under X-rays irradiation. Even if we expect that the bromine-based perovskite substrates developed are more stable than iodine-based perovskites, a similar analytical methodology, thoroughly described in Ref. [122] has been employed.

The measurements were performed by Muriel Bouttemy at the CEFS2 (Centre d'Etude et de Formation en Spectroscopies électroniques de Surface) in "Institut Lavoisier de Versailles" (ILV). The samples, consisting in millimeter-sized crystals are enclosed between glass coverslips, were transferred to ILV. After separating the glass coverslips, one of them was mounted on the sample holder, as shown in Figure 2.19a, leading to a brief exposure to ambient air before the introduction inside the spectrometer, NEXSA XPS system from Thermo Fischer Scientific, using an Al kα source (1486.6 eV). The source power selected for the measurements was 72 W (12 kV, 60 mA). Charge compensation was necessary. The chamber pressure was approximately 3×10^{-7} mbar. The beam size was set at 300×600 µm to best match the size of the crystals, and positioning was realized thanks to an infra-red camera, as shown in Figure 2.19b.

2.2 Data analysis methods

2.2.1 Data coordinate changes

As explained previously, the instruments usually report spectra as a function of wavelengths. However, it is generally easier to interpret absorption, emission, and excitation spectra as a function of the corresponding energy. The wavelength λ can be translated to its corresponding energy using $E = \frac{hc}{\lambda}$. For an emission spectrum, this is, however, not sufficient. Indeed, in that case, the actual unit of the spectrum is in signal (number of counts) per unit wavelength. When translating it to energy representation, it is also necessary to translate the spectrum to signal per unit energy [123]. If the spectrum is denoted f, we have by conservation of energy $f(E)\mathrm{d}E = f(\lambda)\mathrm{d}\lambda$. Combining both equations yields:

$$f(E) = f(\lambda)\frac{\mathrm{d}\lambda}{\mathrm{d}E} = -f(\lambda)\frac{hc}{E^2} = -f(\lambda)\frac{\lambda^2}{hc} \tag{2.18}$$

This correction is minimal for sharp photoluminescence peaks. For example, for a peak centered at 510 nm, which extends 10 nm on each side, there is a 10 %

variation of the correction coefficient on the whole peak. The correction becomes more relevant for broader spectra.

It is also important to note that this correction factor is only relevant for emission spectra, as absorption and excitation spectra are each the result of the ratio of two other measurements, whose correction factors cancel-out [124].

2.2.2 Time-resolved photoluminescence models

As explained in Sub-Subsection 2.1.1, time-resolved photoluminescence experiments allow the measurement of excited population decay within the sample. In the general case of a linear regime, the system is described by an n levels system, which means the evolution of the system is governed by Equation 2.19.

$$\frac{\mathrm{d}}{\mathrm{d}t}\begin{bmatrix} p_1(t) \\ \vdots \\ p_n(t) \end{bmatrix} = \mathbf{A}\begin{bmatrix} p_1(t) \\ \vdots \\ p_n(t) \end{bmatrix} \tag{2.19}$$

Where $p_i(t)$ is the population of state i and $\mathbf{A}$ is a matrix of transition rates. This kind of modelization is, for example, adequate for systems where the emitters can be temporarily trapped in a dark state before being released back to the emissive state. The general solution of this system reads:

$$\begin{bmatrix} p_1(t) \\ \vdots \\ p_n(t) \end{bmatrix} = \exp(\mathbf{A})\begin{bmatrix} p_1(0) \\ \vdots \\ p_n(0) \end{bmatrix} \tag{2.20}$$

Without loss of generality, one can assume that photoluminescence occurs from state 1. Since absorption happens quickly because of the intense and short laser excitation, we further assume that the system starts in this excited state, *i.e.* $p_i(0) = \delta_{1,i}$. It results that the excited population is described by equation Equation 2.21.

$$p_1(t) = c_1 e^{\lambda_1 t} + \cdots + c_k e^{\lambda_k t} \tag{2.21}$$

Where the λ_i are the eigenvalues of $\mathbf{A}$ and the c_i are coefficients to be determined. When performing ensemble measurements, we can also observe multi-exponential decay when several species emit within the sample.

Thus, the general procedure for fitting a time-resolved photoluminescence dataset consists in choosing a suitable dimension of $\mathbf{A}$, that is, choosing a number of exponential terms k, and fitting the convolution of the instrument response function and Equation 2.21 to the histogram. Several methods are suitable for fitting exponential decays [125, 126]. Throughout my PhD, I mainly used non-linear least-squares and Bayesian methods [127] for fitting decays. While Bayesian methods are very intuitive, they do not significantly improve the fitting procedure for

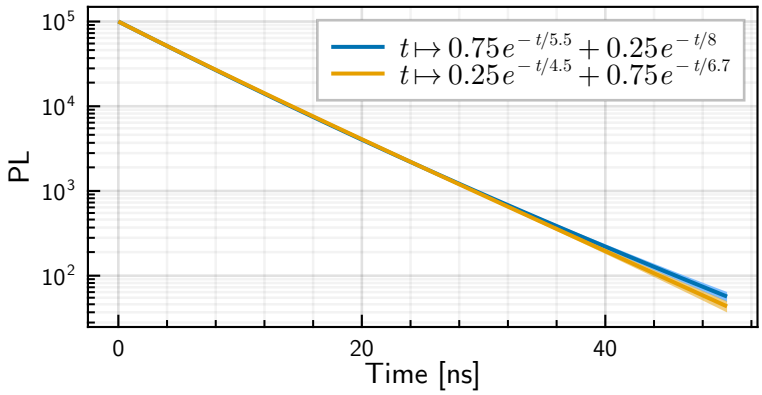

Figure 2.20: Simulation of two intensity decay curves with the expected variance from shot noise in the detector. Adapted from Ref. [128].

the kind of low-dimensional and relatively small datasets that concern us. Thus, the population decays presented in this manuscript have all been fitted using the least-square method, minimizing Pearson's χ^2 deviation between the model and data.

Fitting population decay histograms is necessary to extract characteristic decay times. However, the procedure can be complicated when the decay is not strictly mono-exponential, and it is tempting to keep adding exponential terms to the model until it fits the data. Caution must be advised, as multi-exponential models are notoriously difficult to fit correctly [128]. For example, Figure 2.20 shows the expected fluorescence decay from two different systems that are nonetheless close to indiscernible. There are methods to discriminate between models. For example, looking at the residual of the fitting procedure, that should be white noise. Grinvald and Izchak, Steinberg [129] propose to use the autocorrelation of the residual. Discussing in greater detail optimal fitting procedures for multi-exponential decays is beyond the scope of this chapter. For our purposes, it is sufficient to keep a conservative approach, keeping the number of exponential terms in models as low as possible, justifying the addition of new exponential terms by a physical model, and having a critical approach to a dataset fitted with multi-exponential decays with several decay rates close to one another.

2.2.3 Efficient algorithm for the calculation of $g^{(2)}(\tau)$ from TTTR data

A naive implementation for the computation of $g^{(2)}(\tau)$ from a series of photon arrival times, for example, as measured from a TTTR data acquisition, can be achieved directly using Equation 2.15. Given a list of photon arrival times, one can build a histogram corresponding to the intensity over time, I_t, denoted using

discrete time index t. One can then calculate the photon-correlation histogram using:

$$J(\tau) = \sum_t I_t I_{t-\tau} \tag{2.22}$$

where τ is discretized for simplicity of notations. For a histogram step time of 100 ns, and a measurement time of 120 s, I_t would contain 1.2×10^9 elements. Even if all of them were not stored at once in memory, using Equation 2.22 would quickly become intractable and require long treatment times.

A more efficient algorithm has been proposed by Wahl *et al.* [130]. It can be further accelerated using memoization techniques. For $g^{(2)}(\tau)$ histograms calculated from TTTR measurements used in Sub-Subsection 4.2.4, I use a slightly modified version of their algorithm that allows using arbitrary lag times. The algorithm is fully reported in Algorithm 2. The inner-most `for` loop can be trivially parallelized, further accelerating the calculation. Briefly, the algorithm works directly on the arrival times rather than generating a time-binned histogram. For each lag time τ, it iterates on the two vectors being correlated, f and g, one of which is "lagged" by τ. It increments the histogram bin corresponding to τ each time two arrival times are separated by τ. To avoid missing strong correlations whose corresponding lag time is not comprised in the vector of lag times, the algorithm is complemented by a time coarsening step, reported in 1. This effectively acts as a triangular averaging window.

A complete comparison of the complexity of both algorithms is reported by Wahl *et al.* [130], which does not account for the parallelization of the inner-most `for` loop we use. Briefly, for the range of photon count rates we use, the optimized algorithm is expected to be at least one order of magnitude quicker than the naive implementation. As an example for a typical trace, with 238 logarithmically-spaced lags ranging from 500 ns to 106 s, our Julia implementation runs in ~ 2.5 s. At the same time, the standard Julia implementation[4] needs ~ 15 s[5]. Furthermore, for actual computations, we would like to calculate correlations with lower correlation times, which we could not perform using the naive binning method as the operating system will kill the computing process before the binned vector can be computed completely. This further highlights the relevance of the efficient algorithm, as it does not suffer this limitation.

2.2.4 Software packages and libraries

The work presented in this manuscript has been largely facilitated by the use of many free software programs. I list here the most instrumental ones.

[4] `autocorr` from StatsBase.jl (https://juliastats.org/StatsBase.jl/stable/).

[5] The comparison was run using Julia `v1.9.3` on a laptop with a 12th Gen Intel(R) Core(TM) i7-1265U CPU, with 16 GB RAM.

Data: t_i, a vector of T arrival times, and τ, a lag time.
Result: coarsed and weights two vectors of coarsed times and weights.
Initialize each $t\_div\_\tau_i$ to $t_i \div \tau$;
coarsed $\leftarrow$ empty list;
weights $\leftarrow$ empty list;
for $i = 1$ **to** T **do**
  if coarsed *is not empty and* last(coarsed) $= t\_div\_\tau_i$ **then**
    last(weights) $\leftarrow$ last(weights + 1);
  else
    Append 1 to weights;
    Append $t\_div\_\tau_i$ to weights;
  end
end
weights $\leftarrow$ weights $\times \tau$
Algorithm 1: Time coarsening routine. $\div$ denotes the Euclidean division.

First, our experiments are controlled and automated using the Qudi framework [131], which provides an easy and versatile platform for connecting Python with many instruments used in confocal microscopy experiments.

Then, the data analysis presented here has been mostly treated using the Julia programming language [132]. It combines a high-level syntax with performances comparable to those expected from low-level languages such as C or C++. Albeit relatively new, the Julia ecosystem provides many tools that have proven useful, such as DrWatson.jl [133], a library enabling a systematic data analysis environment, or DataFrames.jl [134], a package that facilitates handling tabular data. The most instrumental of the Julia packages used here is perhaps Makie.jl [135], which was used to generate most of the figures of this manuscript.

All other original illustrations in this manuscript have been generated with Inkscape [136], sometimes using Alvise Vianello's optical components library [137].

Although the software used to drive our instrument has, most of the time, closed sources, some manufacturers release publicly the specifications of the file formats they use, allowing more in-depth analysis of the measurements than what a simple text file would or even enable analyzes that would otherwise have been impossible. This is the case of Princeton Instruments with their spectroscopy file format and PicoQuant with their time-tagged file format. This allowed me to write simple libraries in Julia to handle the corresponding spectroscopy[6] and time-tagged[7] files.

[6] https://github.com/klafyvel/SPEFiles.jl
[7] https://github.com/Klafyvel/PicoQuantTTTR.jl

Data: f_i, and g_i two ordered vectors of respectively F and G arrival times, τ_k, a vector of K lag times, and δt, the time resolution of the detector.
Result: $J_k = g^{(2)}(\tau_k) \times \langle I(t) \rangle^2$
for $k = 1$ **to** K **do**
  (coarsed_f, weight_f) ← coarsetime(f, τ_k);
  (coarsed_g, weight_g) ← coarsetime(g, τ_k);
  if *i = 1* **then**
    scaler ← $\tau_k / \delta t$;
  else
    scaler ← $(\tau_k - \tau_{k-1}) / \delta t$;
  end
  $J_k \leftarrow 0$;
  $i \leftarrow 1$;
  $j \leftarrow 1$;
  start_from_lagged ← False;
  while $i \leq F$ *and* $j \leq G$ **do**
    if start_from_lagged **then**
      if coarsed_g$_j$ + $\tau_k \geq$ coarsed_f$_i$ **then**
        if coarsed_g$_j$ = coarsed_f$_i$ **then**
          $J_k \leftarrow J_k$ + weight_f$_i$ × weight_g$_j$;
          $j \leftarrow j + 1$;
        end
        start_from_lagged ← False
      else
        $j \leftarrow j + 1$;
      end
    else
      if coarsed_f$_i \geq$ coarsed_g$_j$ + τ_k **then**
        if coarsed_g$_j$ = coarsed_f$_i$ **then**
          $J_k \leftarrow J_k$ + weight_f$_i$ × weight_g$_j$;
          $i \leftarrow i + 1$;
        end
        start_from_lagged ← True
      else
        $i \leftarrow i + 1$;
      end
    end
  end
  $J_k \leftarrow J_k$/scaler
end

Algorithm 2: Efficient algorithm for calculation of $g^{(2)}(\tau)$.

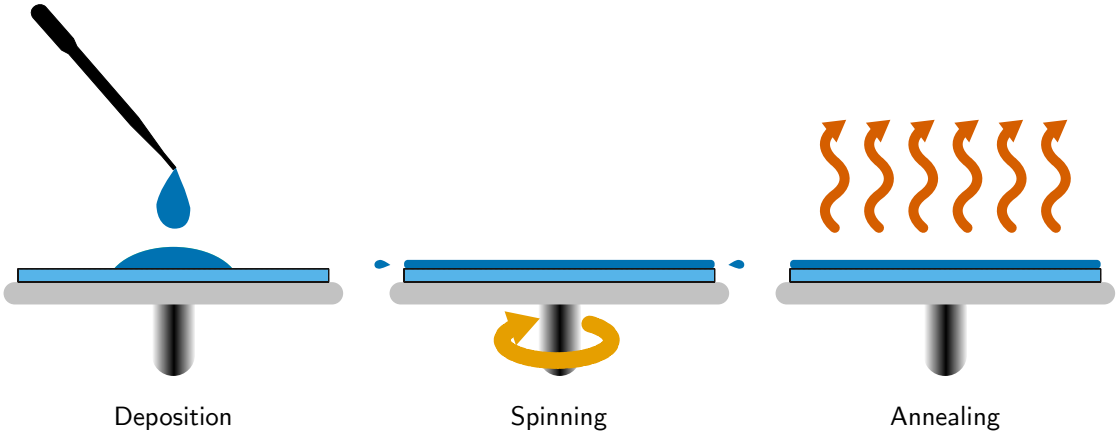

Figure 2.21: Three steps of the spin-coating process. The solution is first deposited on the substrate, which is then set to spin. The solution forms a film because of the rotation, which then dries to form the final film. The third optional step is annealing to evaporate the solvent remaining in the film.

2.3 Samples preparation

Because of the variety of samples reported in this manuscript, I chose to present here mainly the principle of the methods rather than the precise numerical details.

2.3.1 Drop-casting

Drop-casting is, perhaps, the simplest way one can think of to form a film. It consists of letting a drop of solution dry on a substrate. This process can be improved using an oven. The low pressure and increased temperature help evaporate the solvent. This was particularly useful to produce films of perovskite nanocrystals in Chapter 3 and of graphene quantum dots in Chapter 4.

2.3.2 Spin-coating

Spin-coating is a well-known technique for the deposition of homogeneously-thick thin films [138]. It consists of depositing a drop of solution on the substrate before making it spin at a controlled rate. The process is illustrated in Figure 2.21. Briefly, the solution will then follow two different regimes. First, part of the fluid is spun off the substrate. Then, as the film is sufficiently thin, thinning is dominated by the evaporation of the solvent. The process has been extensively studied [139, 140], and various model exists to describe it accurately. A simple model can be used to determine the thickness h of a polymer film from the deposition conditions [141]:

$$h \propto \frac{c^{\alpha}}{\sqrt{\omega}} \tag{2.23}$$

Where c is the concentration in the polymer of the solution, α depends on the solvent, polymer, and substrate, and ω is the rotation speed.

Spin-coating can sometimes be followed by an annealing step to fully evaporate the remaining solvent. In particular, we found that it is a necessary step to obtain clear polystyrene films for embedding graphene quantum dots.

2.3.3 Synthesis of $MAPbBr_3$ single crystals

The last chapter of this manuscript reports results about graphene quantum dots deposited on $CH_3NH_3PbBr_3$ ($MAPbBr_3$) substrates. Here, I described their synthesis and method of crystallization.

The first step of the synthesis consists of dissolving the constituents of the crystals in a solution of N,N-Dimethylformamide (DMF). We prepare a solution at 0.9 M of $MAPbBr_3$ with 1.1 excess of MABr by dissolving 111 mg of MABr and 331 mg of $PbBr_2$ in 1 mL of DMF. The solution is agitated in an ultrasound bath at 50 °C until it is clear and transparent.

The first trials we ran used bulky crystals. These crystals are easily obtained by letting the $MAPbBr_3$ solution crystallize while maintaining a temperature of 50 °C. However, these proved unpractical to work with as they are complicated to use on the confocal microscope, their surface is not very smooth, and cleaving them is messy and unpredictable.

Drawing inspiration from methods previously developed in our group for the synthesis of two-dimensional perovskites [65], we then developed a method to grow the crystals under constraints. For this, we start by cleaning two thin glass substrates (Schott Nexterion Coverslip, 0.170 ± 0.005 mm thick) using a plasma cleaner. We then deposit a drop of solution between the two coverslips (typically 7 µL). In the early stages of developing the method, we used to keep the sample at 50 °C during the crystallization process. We have since then moved to room temperature as it produces wider crystals, although it takes longer (typically 2 to 3 days). XPS studies reported in Chapter 5 have also shown that it is best to keep the sample in the dark. Hence, we keep the samples covered by an aluminum sheet during the crystallization process and for storage. Before using the substrate, the top coverslip can easily be peeled off (the glass coverslips are thin enough to bend slightly without breaking) to expose the perovskite crystals. The resulting crystals are millimeter-sized, with a thickness of a few tens of micrometers. An in-depth characterization is available in Subsection 5.1.1.

Conclusion

The experimental methods used throughout my thesis have been reviewed. A large panel of methods, from ensemble characterization to in-depth single-object measurements were presented. This chapter is necessarily limited. For readers wishing to deepen their understanding of the methods provided here, Lakowicz [142] is a good starting point. For new PhD students starting in the group, the theses of Thomas Liu [14], Shen Zhao [13] present in depth the spectroscopy methods used for single-molecule experiments, and the thesis of Thomas Campos [56] has a more extended presentation of the non-optical characterization techniques used for perovskites.

Halide perovskites: hybrid semiconductors for light emission

3

Contents

Introduction

Solid-state-based sources are key to the efficient production of light, not only for conventional lighting, but also for telecommunication and sensing applications. In this context the availability of materials with an emission in desired regions of the visible, near-infrared and near-UV spectrum is a first requirement. For example, the development of the first blue-emitting LEDs in the early 1990s [143] led to a breakthrough that impacted the world well beyond the field of solid-state physics. Interestingly, the development of efficient LEDs with emission in the green region has stalled behind that of blue LEDs. The unavailability of efficient green-emitting LEDs is referred to as the *green gap* and present major difficulties, which are not yet fully explained, nor overcome [144–148]. Development of white-emitting LEDs would also benefit from the availability of efficient green-emitting LEDs. Indeed, a common strategy to produce white light involves using green, yellow, and red phosphors to convert blue light emitted by an LED into white

light, which limits the overall efficiency of the device [149]. Availability of efficient green emitters would allow replacing this down-conversion by direct color mixing. Similarly to LEDs, the unavailability of efficient green-emitting semiconductors fuels the research on materials and laser architectures that could bridge the *green gap* [150]. Such sources are desirable, for example for visible light communication, sensing through fiber-coupled microlasers, or microlaser arrays.

In this context, halide perovskites have emerged over last ten years as a promising family of semiconductor materials. They consist in corner-sharing octahedra with a metallic ion at the center, often lead, halide cations -Cl, Br, or I- forming the corners, as shown in Figure 1.10 on page 15. The structure is complemented by organic, usually methylammonium or formamidium, or inorganic, usually cesium, cations in the space between the octahedra. They have seen a surge in interest, in particular thanks to their remarkable performances in photovoltaic applications [39]. Halide perovskites are particularly relevant for light-emitting devices. Their synthesis through soft chemistry techniques allows tuning their band gap easily over the whole visible spectrum, just by changing the halogen part. Br-based perovskites are particularly relevant in the context of the *green gap*, because they exhibit emission in that region of the electromagnetic spectrum. $MAPbBr_3$ is perhaps the best known Br-based perovskites. However, it has proven to be difficult to work with in devices, notably because of the presence of pinholes in the perovskite layer [151] and the influence of grain size in thin films [152]. In that context, fully-inorganic perovskites, such as $CsPbBr_3$, are promising. Firstly, they offer greater stability than the hybrid $MAPbBr_3$ containing the volatile MA organic part. Secondly, they can easily be used as nano-crystals with an excellent photoluminescence quantum yield, and they also appear to be well-suited for quantum optics to produce single-photon sources [153]. And thirdly, they present increased facility of integration within devices such as photonic structures.

The optical properties of perovskites can further be tuned by controlling the dimensionality of the semiconductor. Quasi-2D perovskites consisting of controlled number of octahedra layers separated by big organic cations give a new degree of freedom for adjusting the band gap of the medium. Those materials present a strong excitonic character, with a binding energy of $\sim 100\,\mathrm{meV}$ because of the quantum and dielectric 2D-confinement of the exciton within the inorganic layer. One of the most famous 2D perovskite is PEA_2PbI_4 (PEPI), a "pure" 2D phase consisting in single layers of octahera separated by phenylethylamonium cations. Although I-based perovskites typically have a bandgap in the red, or infra-red, PEPI exhibits an emission in the green region because of the confinement of the excitons. 2D perovskites tend to be much more stable than their 3D counterpart thanks to the organic part protecting the inorganic compounds from ambient atmosphere. This organic part of the perovskite forms a third parameter for the tuning of halide perovskites properties, as they allow importing many methods and properties from organic electronics, *e.g.* for tuning energy transfers within the medium [69].

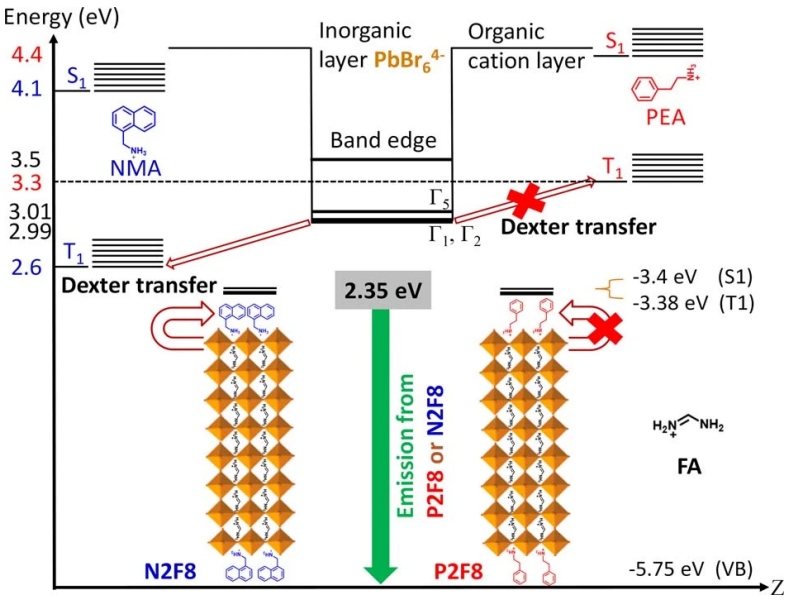

Figure 3.1: Triplet excitons quenching mechanism proposed by Qin *et al.* [70]. The triplet state in NMA lies at lower energy than the triplet exciton state in the inorganic part of the perovskite, allowing Dexter transfer because of the proximity with the spacer cation. On the other hand, that transfer is not possible when PEA is used, because its first triplet state lies higher than the triplet exciton state. Reproduced from Ref. [70].

In this chapter, I describe a study of Br-based quasi-2D perovskite thin films for laser emission in the green region of the spectrum. Then, I describe how, in collaboration with Cédric Mayer, we developed a synthesis method for highly calibrated $CsPbBr_3$ nanocrystals and present a study of the resulting nanocrystals.

3.1 Quasi-2D Perovskite thin films

The use of 2D halide perovskites for laser applications is enticing because of the advantages promised by this class of material. First, the dimensionality adds a new degree of freedom to fine tune the emission wavelength of the device. Then, using 2D perovskites has been shown to increase the stability of perovskites solar cells [56]. The strong exciton binding energy should also favor lasing. Finally, the organic cation spacer allows the use of triplet management techniques imported from organic electronics. However, the literature offers little reports of lasing from a "pure" 2D perovskite, and none from thin-films of "pure" 2D perovskites. To overcome the difficulty of displaying laser emission from 2D perovskites, studies often resort to using quasi-2D perovskites, that is layered perovskites with layers that are several octahedra-thick.

In this context, Qin *et al.* [69] have shown how choosing the appropriate organic spacer in formamidium (FA)-based lead-bromide quasi-2D perovskites allows harvesting both triplet and singlet excitons in electrically pumped LEDs based on quasi-2D perovskites with an average number of layers equals to 8 (see Figure 1.15a on page 21 for the definition of the number of layers in a 2D perovskite). They were able to prevent non-radiative recombination of triplet excitons by the replacement of the organic spacer 1-naphthylmethylamine bromide (NMA) with phenylethylammonium (PEA), which has a triplet energy level higher than the energy level of triplet excitons in the inorganic phase. Later, the same group used this knowledge of triplet exciton management to explore the phenomenon known as "lasing death" in continuously-pumped lasers [70]. Using the reverse strategy as for their LEDs, they showed that using NMA-based quasi-2D perovskites allowed them to quench the long-lived triplet excitons, thus preventing singlet-triplet annihilation, as shown in Figure 3.1.

In this section I present our attempt at reproducing their result, by synthesizing $PEA_2FA_{n-1}Pb_nBr_{3n+1}$ and $NMA_2FA_{n-1}Pb_nBr_{3n+1}$, $\langle n \rangle = 8$, quasi-2D perovskites thin-films. We also extended our test to replacing FA with methylammonium (MA), a well-known organic cation widely used in the perovskite community.

3.1.1 Synthesis of the films

I followed the synthesis proposed by Qin *et al.* [69]. Briefly, the samples are prepared using one-step spin-coating method. The precursor (typically 50 µL) is spin-coated at 4000 rpm for 30 s with an acceleration of 2000 rpm/s^2. An antisolvent (Toluene) is sprayed (typically 30 µL) on the sample after a few seconds of rotation. The samples are then baked for 15 min at 100 °C on a hotplate.

The precursors were prepared by adding a 25 % molar ratio of 1-naphthylmethylamine bromide (NMABr) or phenylethylammonium bromide (PEABr) to a solution with 1:1 ratio of formamidium bromide (FABr) or methylammonium bromide (MABr) in dimethylformamide (DFM) at 0.4 M. The four solutions are then stirred in an ultrasonic bath at 50 °C, until all powders are dissolved (typically $\sim$ 3 hr).

3.1.2 Optical characterization

I characterized the synthesized samples through their steady-state absorption and photoluminescence spectra. The absorption spectra shown in Figure 3.2 on the facing page feature sharp peaks ranging from $\sim$ 2.60 eV to $\sim$ 3.23 eV, which we attribute to the presence of various quasi-2D phases in the film. This is strikingly different from the samples reported by Qin *et al.* [69], which do not feature the sharp absorption peaks characteristic of low n quasi-2D perovskite phases (reproduced in Figure 3.3 on page 80). Because of the absence of the characteristic

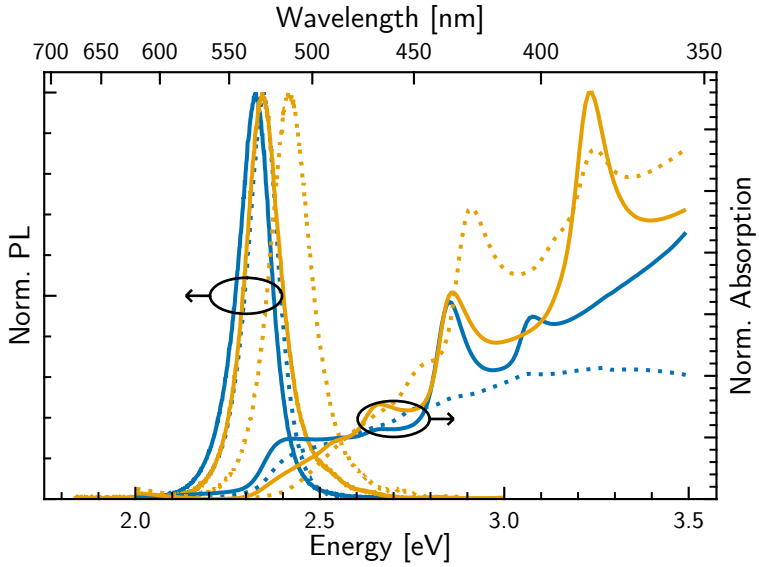

Figure 3.2: Photoluminescence and absorption spectra of $PEA_2MA_{n-1}Pb_nBr_{3n+1}$ (dotted blue), $PEA_2FA_{n-1}Pb_nBr_{3n+1}$ (solid blue), $NMA_2MA_{n-1}Pb_nBr_{3n+1}$ (dotted yellow), and $NMA_2FA_{n-1}Pb_nBr_{3n+1}$ (solid yellow). The photoluminescence peaks are at 2.35 eV, 2.33 eV, 2.41 eV, and 2.34 eV. The photoluminescence spectra were excited at 405 nm with a picosecond pulsed laser at 80 MHz repetition rate.

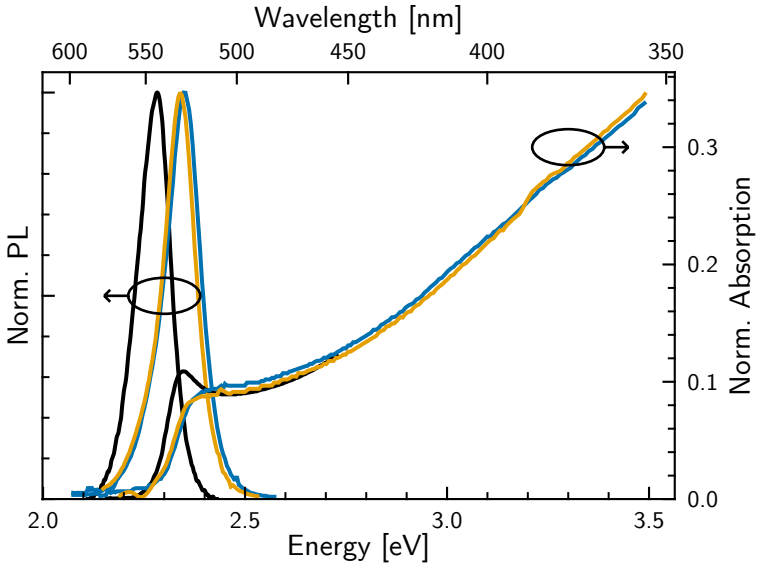

Figure 3.3: Photoluminescence and absorption spectra reported by Qin *et al.* [69] on their samples of $PEA_2FA_{n-1}Pb_nBr_{3n+1}$ (blue) and $NMA_2FA_{n-1}Pb_nBr_{3n+1}$ (yellow), $\langle n \rangle = 8$. In black are the absorption and photoluminescence spectra of bulk $FAPbBr_3$ thin films reported in Ref. [154].

excitonic peak of $FAPbBr_3$ at the band-edge of their absorption spectra, the authors claim that no 3D phase is present in their film. It should be noted, however, that for large $\langle n \rangle$, it can be difficult to differentiate the 2D phase from a 3D phase solely from the absorption spectrum. The authors thus complement their study with X-ray diffraction and grazing-incidence wide-angle X-ray scattering, and claim the main phase of their films is the $\langle n \rangle = 8$ phase, forming pellets of ~ 20 or more cubic cells. We believe our films feature a larger proportion of $n < 8$ phases. Moreover, no edge is visible in the absorption spectra, except for $PEA_2FA_{n-1}Pb_nBr_{3n+1}$, which could thus present the $n = 8$ phase.

The emission spectra of $PEA_2MA_{n-1}Pb_nBr_{3n+1}$, $PEA_2FA_{n-1}Pb_nBr_{3n+1}$, $NMA_2MA_{n-1}Pb_nBr_{3n+1}$, and $NMA_2FA_{n-1}Pb_nBr_{3n+1}$ shown in Figure 3.2 are narrow, and centered at 2.25 eV, 2.33 eV, 2.41 eV, and 2.34 eV respectively. The emission peaks reported by Qin *et al.* [69] lie at 2.34 eV and 2.35 eV for their NMA- and PEA-based perovskites, which matches well our measurement. For FA-based perovskites, this is a higher photoluminescence energy than the 2.27 eV reported for $FAPbBr_3$ monocrystals [155]. This is less the case for MA-based perovskite, as the photoluminescence peak we measured on $MAPbBr_3$ monocrystals lies at 2.31 eV (see Chapter 5). These energies of emission are compatible with emission from high-order quasi-2D perovskites.

Despite the presence of low-n phases in our samples, we decided to increase the

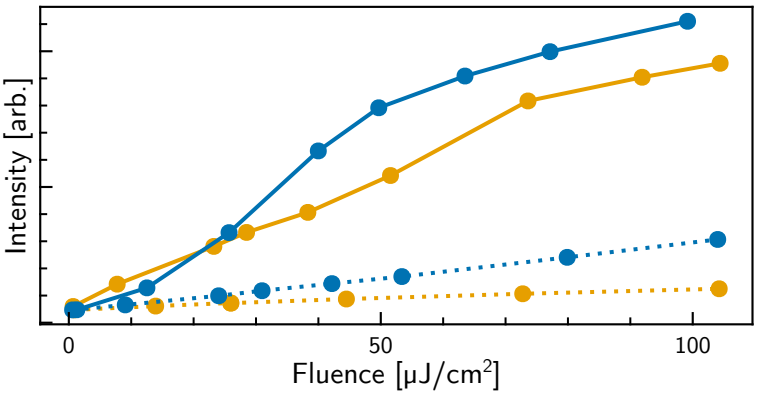

Figure 3.4: Intensity of photoluminescence of $PEA_2MA_{n-1}Pb_nBr_{3n+1}$ (dotted blue), $PEA_2FA_{n-1}Pb_nBr_{3n+1}$ (solid blue), $NMA_2MA_{n-1}Pb_nBr_{3n+1}$ (dotted yellow), and $NMA_2FA_{n-1}Pb_nBr_{3n+1}$ (solid yellow) against fluence of excitation at 400 nm, 125 kHz, picosecond pulses.

excitation fluence. Figure 3.4 shows the integrated fluorescence spectrum against the excitation fluence. First, the FA-based samples (solid line) appear more bright than their MA-base counterparts (dotted lines). Then, the NMA-based perovskites are almost systematically less bright than their PEA counterparts. This is compatible with the mechanism proposed by Qin *et al.* [69] where NMA quenches the triplet excitons and thus prevents harvesting the carriers involved for light emission. Despite our best efforts, and reaching pump fluences higher than the 16 $\mu J/cm^2$ fluence reported by Qin *et al.* [69], we were not able to observe any hint of amplified spontaneous emission: no sudden increase in the photoluminescence intensity nor sharpening of the photoluminescence spectrum. This is probably due to the quality of our samples and the limited power range available on our laser at the time.

3.2 Synthesis and characterization of highly calibrated $CsPbBr_3$ nanocrystals

Because we faced experimental challenges that limited our ability to explore the laser effect in perovskites, we focused on the characterization and synthesis of the material. $CsPbBr_3$ is a 3D perovskite that is fully inorganic, and thus holds promises to overcome some of the stability issues that limit the applications of hybrid organic-inorganic perovskites such as $MAPbBr_3$. This perovskite can be synthesized as single-crystals [156, 157], which is useful for photodetection and the detection of ionizing radiations. It is perhaps more famously known for its ability to form nanocrystals. The synthesis of $CsPbBr_3$ nanocrystals by the hot injection

method has been pioneered by Protesescu *et al.* [7] and quickly enabled them to demonstrate multiple applications of these nanocrystals, among which the formation of superlattices for superfluorescence [158], emission of single-photons [153], or low-threshold spontaneous emission and lasing [159]. The hot injection method produces highly calibrated nanocrystals, but requires high temperatures and an inert atmosphere, which would limit the mass production of nanocrystals. An alternative synthesis route has been proposed for $CsPbBr_3$ nanocrystals, ligand assisted re-precipitation [57, 58]. In brief, it consists in dissolving the ionic species in a solvent until an equilibrium is reached, and then pushing the solution to a non-equilibrium state of supersaturation. This prompts the spontaneous formation of crystals until a new equilibrium is reached. The re-precipitation method was first adapted to $CsPbBr_3$ nanocrystals by Li *et al.* [160]. These methods scale much better than the hot injection method, but is harder to control to form highly calibrated nanocrystals. Here I describe a new synthesis method based on a re-precipitation method proposed by Wei *et al.* [161] that produces highly calibrated $CsPbBr_3$ nanocrystals and present a characterization of their optical properties. This work was led in collaboration with Cédric Mayer, who designed and optimized the synthesis [162], while I synthesized samples and conducted their optical characterization.

3.2.1 Synthesis

The synthesis, shown in Figures 3.5a and 3.5b on the next page is a re-precipitation method. It draws inspiration from the work of Wei *et al.* [161]. Following their synthesis, we first solubilize Cs_2CO_3 powder in oleic acid (2.5×10^{-5} mol in 1 mL) and TOABr (0.1 mmol) and $PbBr_2$ (0.1 mmol) in toluene (10 mL). Both solutions are stirred while heating slightly (45 °C) until all powder has dissolved. Both solutions are then mixed and stirred for 5 min . Finally, the solution is centrifugated at 10 000 rpm for 10 min and the nanocrystals are recovered and redispersed in toluene, forming the species in solution hereafter denoted PVK-TOA. The solution of PVK-TOA is yellow and turbid and consists in polydisperse $\sim$ 100 nm-large crystals.

The nanocrystals are then obtained by pouring a precursor in the PVK-TOA solution. The precursor solution is prepared by mixing two solutions. The first one consist in 0.1 mmol of $PbBr_2$ and 0.122 mL in 1 mL of dimethylformamide (DMF), the second one is 2.5×10^{-5} mol of Cs_2CO_3 and 0.122 mL of oleic acid in 1 mL of DMF. The two solutions are then mixed together. Finally, 12.5 µL of phenethylamine (PEA) is added to the precursor right before the solution is poured to the solution of PVK-TOA. The solution turns to transparent yellow in a matter of seconds, as shown in Figure 3.5c.

It should be noted here that in this chapter I refer to the first species as PVK-TOA and to the second as nanocrystals. This is because the latter consist in well calibrated 10 nm-wide nanocrystals, while the former is typically much larger, and

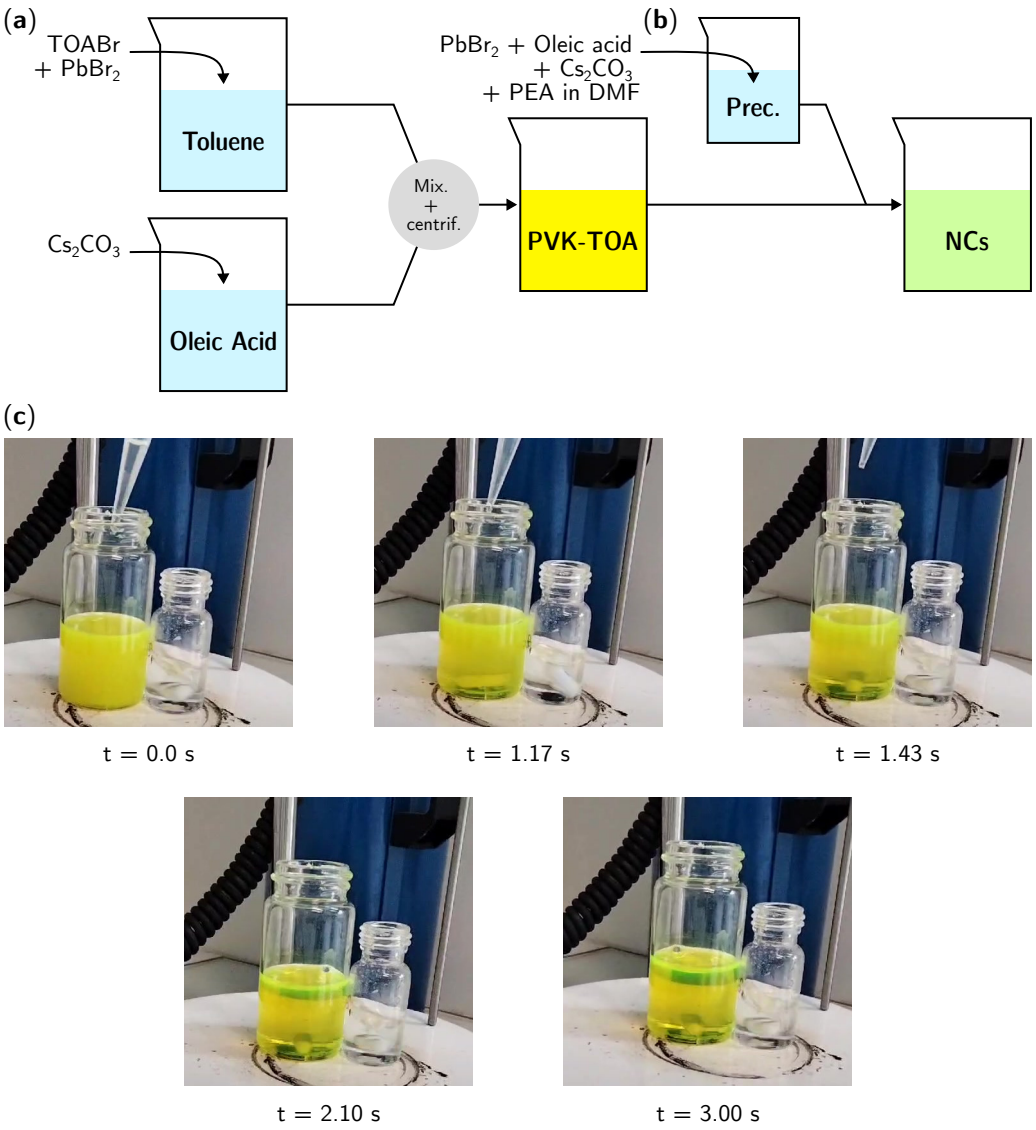

Figure 3.5: Schematic representation of the synthesis of (**a**) PVK-TOA, and then (**b**) $CsPbBr_3$ nanocrystals. (**c**) Excerpt of a video showing the PVK-TOA in solution being cut into $CsPbBr_3$ nanocrystals. The full video is available at https://media.hal.science/hal-04310797.

I thus choose not to refer to it as a "nano" object.

3.2.2 Structure of the nanocrystals

The synthesized species were analyzed using transmission electron microscopy (TEM). As stated earlier, Figure 3.6a shows PVK-TOA is polydisperse, and presents $\sim 100\,\text{nm}$-sized crystals. The polydispersity and size of the species may explain the turbid aspect of the solution through scattering of light.

The $CsPbBr_3$ nanocrystals on the other hand, are remarkably mono-disperse on large scales, as shown in Figure 3.6b and Figure 3.6c. The cubes tend to self-organize on the TEM grid into large arrays of nanocrystals. Using high-resolution TEM, it is possible to get highly detailed image of a single $CsPbBr_3$ nanocrystal, as shown in Figure 3.6d, displaying the arrangement of atoms at the surface of the crystals.

The high calibration of the nanocrystals can be quantified by analyzing the TEM images. To that end, we use a watershed algorithm to segment the TEM images and identify the crystals [163]. This yields a list of pixels belonging to each nanocrystals, from which we can estimate the size of a nanocrystal by taking the square root of the area[1]. Figures 3.7a and 3.7b on page 86 show the labelling of the PVK-TOA crystals, while Figures 3.7d and 3.7e show the labelling process for nanocrystals. Figure 3.7c shows the resulting dispersion in size of 52 PVK-TOA crystals. The average length is $\sim 20\,\text{nm}$ with a standard deviation of $\sim 30\,\text{nm}$. This is strikingly different from the dispersion in sizes of the nanocrystals. Indeed, Figure 3.7g shows the distribution of sizes of 921 nanocrystals. The distribution is almost Gaussian and exhibits a mean of $\sim 10\,\text{nm}$ with a standard deviation of $\sim 1.2\,\text{nm}$. This confirms the intuitions built from the synthesis on one part, as we expect less dispersion from small, well calibrated, objects, and from the electronic microscopy images. It is interesting here to use the TEM images to evaluate the size of the gap between nanocrystals. To that end, I measured systematically the distances between the centers of neighboring nanocrystals. Since we know the average size of a nanocrystal, the average gap between two neighboring nanocrystals is simply given by the difference between the distance of the centers and the size of the objects. The measurement of the distances between the nanocrystals' centers can be calculated using the Delaunay triangulation [164] of the network constituted by the nanocrystals, shown in Figure 3.7f. The histogram of the corresponding distances is given in Figure 3.7h. The histogram features two peaks. This can be understood by looking at the triangulation that a perfect square grid would yield as shown in the inset. In that model case, one third of all edges of the graph would be diagonals, in yellow in Figure 3.7h, while two third of them would be vertical or horizontal edges, in blue in Figure 3.7h. The corresponding

[1] For cubic nanocrystals this yields the size of the nanocrystal. For rectangular crystals, such as PVK-TOA, this yields the geometric average of the two sides' widths.

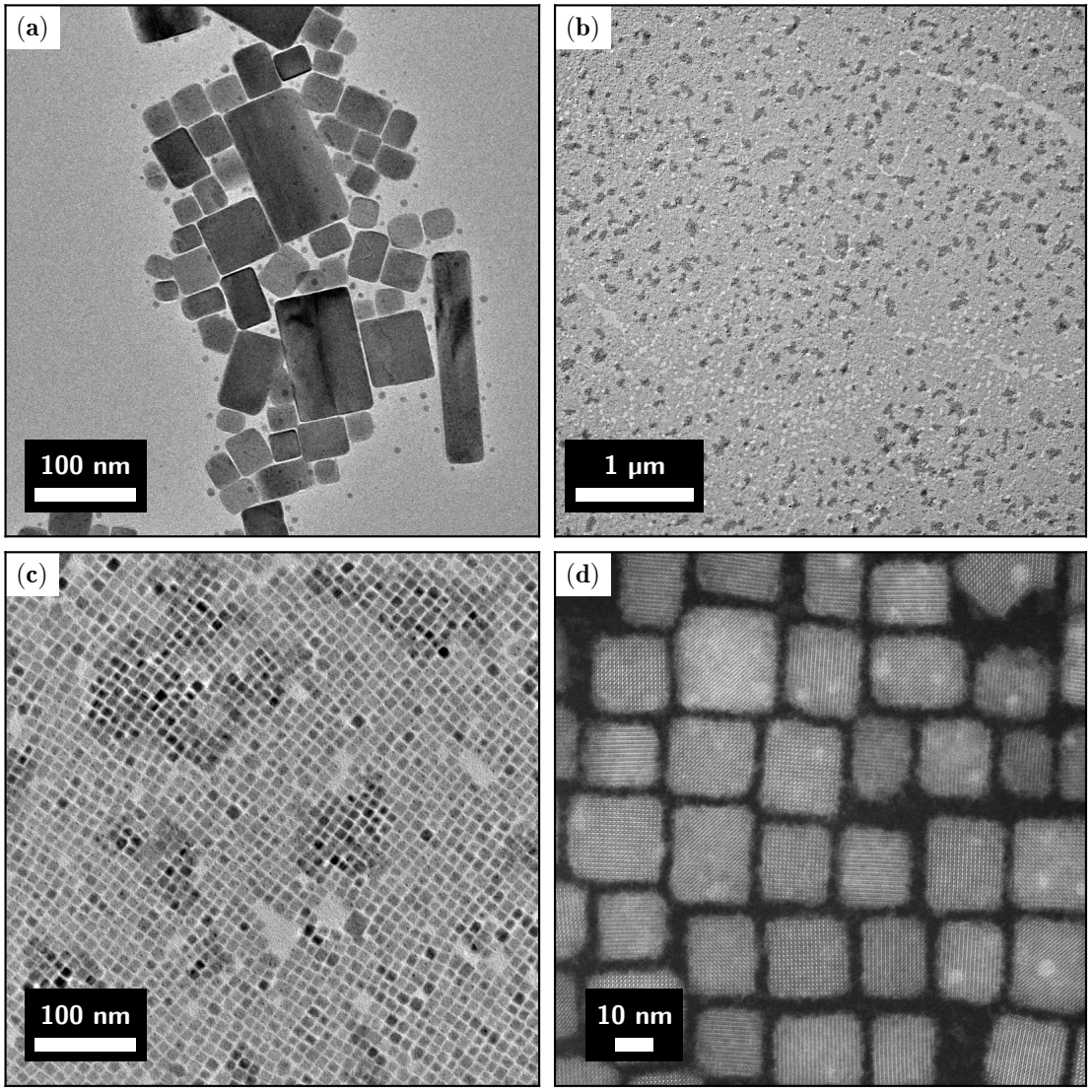

Figure 3.6: Transmission electron microscopy (TEM) and high-angle annular dark field scanning TEM image of (**a**) PVK-TOA, (**b**), (**c**) $CsPbBr_3$ nanocrystals at various scale lengths, showing the self-organization of the material. (**d**) High-resolution transmission electron microscopy image of $CsPbBr_3$ nanocrystals, showing the disposition of the lattice.

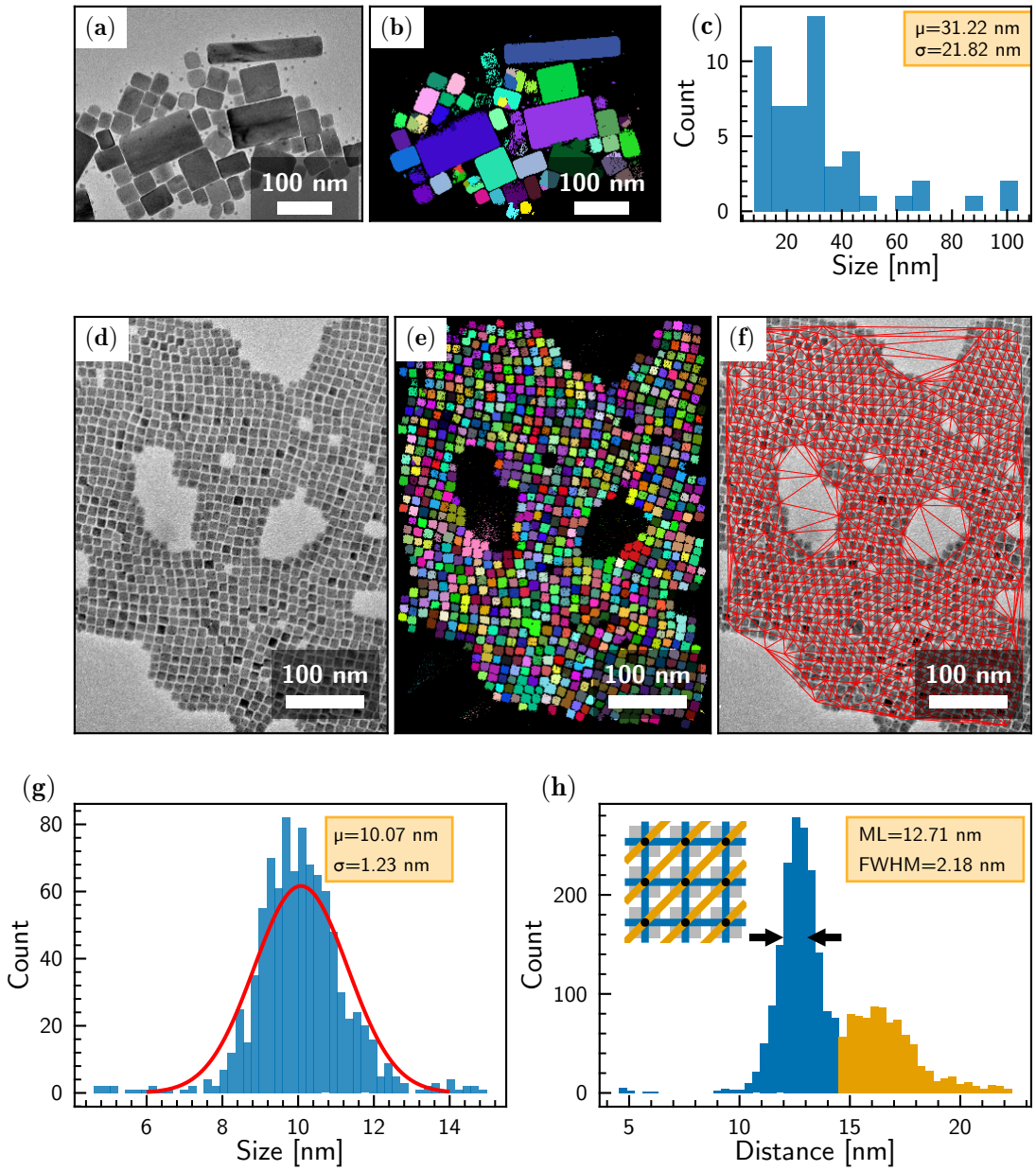

Figure 3.7: (**a**) TEM image of PVK-TOA. (**b**) TEM image of PVK-TOA labelled by the watershed algorithm. (**c**) Histogram of sizes calculated from the TEM image of PVK-TOA. (**d**) TEM image of nanocrystals. (**e**) TEM image of nanocrystals labelled by the watershed algorithm. (**f**) Delaunay triangulation graph of the labelled nanocrystals crystals. (**g**) Histogram of sizes calculated from the TEM image of nanocrystals. The mislabelled crystals that actually correspond to several nanocrystals visible in (**e**) have been removed from the dataset. (**h**) Histogram of distance between nodes in the triangulation graph of nanocrystals, *i.e.* distance between the centers of the nanocrystals. The inset shows the triangulation on an idealized infinite square grid, and the color code of the edges corresponds to the color code on the histogram. FWHM, Full Width at Half Maximum, ML, Maximum of Likelihood.

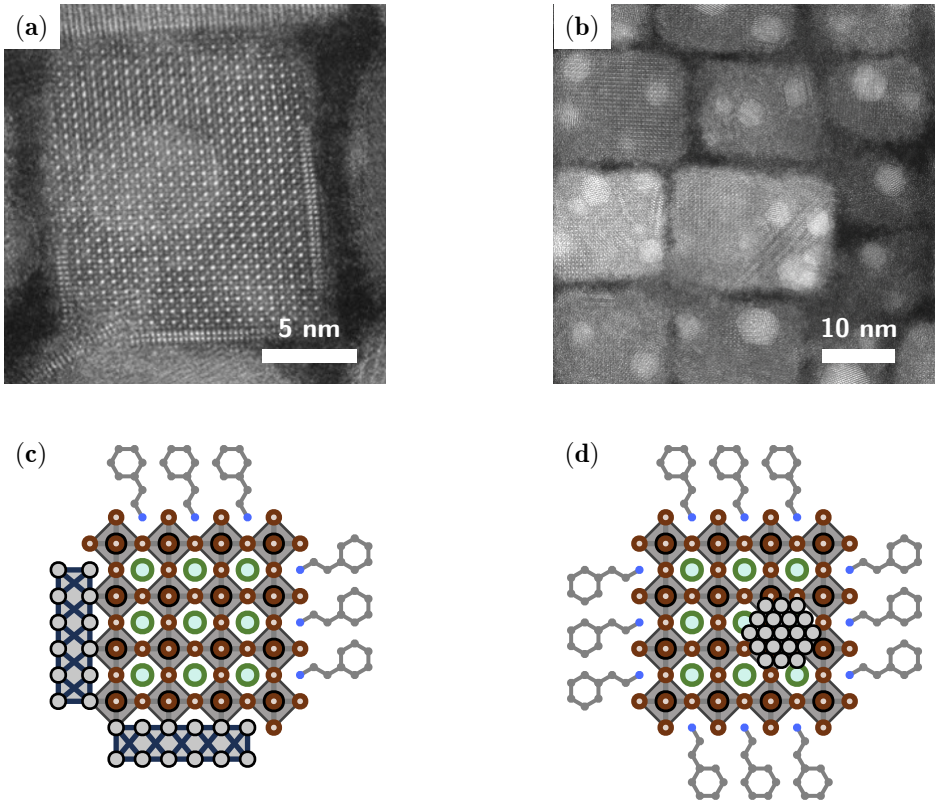

Figure 3.8: (**a**) TEM images of $CsPbBr_3$ nanocrystal featuring PbO_2 nanostructures. (**b**) White Pb^0 nanodots at the surface of $CsPbBr_3$ nanocrystals. (**c**) Schematic of nanocrystals with PbO_2 nanostructure. (**d**) Schematic of nanocrystals with Pb^0 nanodots.

parts of the histogram are highlighted using the same color code. For our purpose, it is thus sensible to take the maximum of the distribution, at $\sim 12.7\,\text{nm}$, for the average distance between nanocrystals' centers and the full width at half maximum, $\sim 2.18\,\text{nm}$ as the deviation. This yields a gap between two neighboring nanocrystals of approximately 2 nm, which is comparable to the interlayer distance in 2D halide perovskites [165].

Some higher resolution images, for example Figure 3.6d or Figure 3.8b, present white spots on the surface of the nanocrystals. These correspond to metallic Pb^0 nanodots. We attribute their presence to the release of Pb^{2+} cations during the slicing process. In addition to the nanodots shown in Figure 3.8b, we can also observe PbO ribbons [166] on the grid, as shown in Figure 3.8a. Lee *et al.* [167] propose a mechanism explaining the formation of these structures, where distortions induced by defects carrying positive (respectively, negative) charges at the

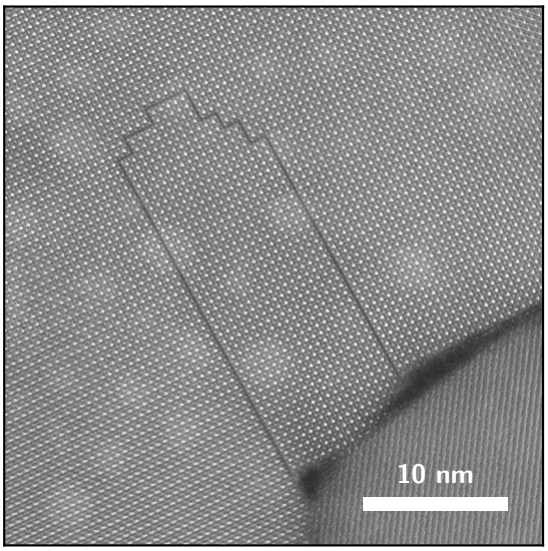

Figure 3.9: TEM images of PVK-TOA partially cut by the addition of PEA to the solution.

surface (respectively, core) of the nanocrystals cause the reduction (respectively, oxidation) of atoms with opposite charges, leading to the formation of Pb^0 (respectively, PbO_2). The presence of metallic lead is often interpreted as a marker for the presence of surface defects [168, 169], and might be used as markers to develop new syntheses producing less of them.

TEM and HR-TEM investigations also allowed us to investigate in detail the process leading to the transformation of bulky poly-disperse PVK-TOA crystals to organized mono-disperse $CsPbBr_3$ nanocrystals. To identify the species in the precursor solution responsible for the slicing of the bulky PVK-TOA crystals, we added each component of the precursor individually to solutions of PVK-TOA. The only resulting sample presenting small nanocrystals was prepared with PEA, although the resulting nanocrystals were more polydisperse than the nanocrystals obtained with the full precursor. This indicates the amine is responsible for slicing PVK-TOA into small nanocrystals, while the other components of the precursor help with the calibration. We were able to further confirm the role of PEA by stopping the reaction early[2] ($\sim 1\,\text{min}$) when using a PEA-only precursor. The resulting TEM picture shown in Figure 3.9 presents partially cut crystals. We thus propose a reaction mechanism where PEA attacks the surface of bulky PVK-TOA crystals and replaces Cs^+ cations along crystallographic planes, while the other constituents of the precursor constraint the size and monodispersity of the nanocrystals. A similar action of PEA has been reported by Huang, Wang,

[2]Depositing a droplet of solution on the TEM grid stops the reaction, as the solvent evaporates quickly.

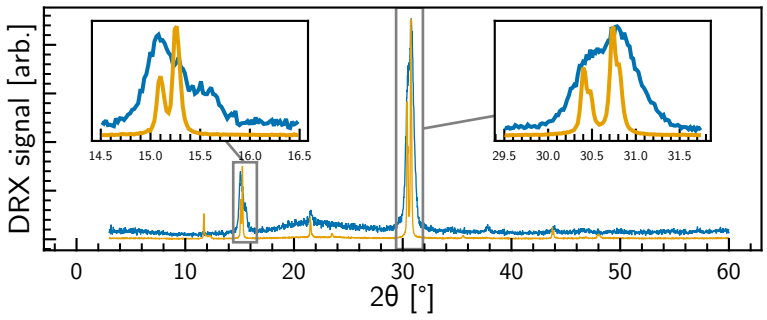

(h,k,l)	d [Å]	2θ [°]
(0, 1, 0)	5.8862	15.0393
(1, 0, 0)	5.8221	15.2057
(1, 1, 0)	4.1393	21.4498
(1, 0, 1)	4.1295	21.5015
(1, 0, -1)	4.1043	21.6348
(1, 1, 1)	3.3805	26.3427
(1, 1, -1)	3.3667	26.4529
(0, 2, 0)	2.9431	30.3458
(2, 0, 0)	2.9111	30.6878
(1, -2, 0)	2.6266	34.108

Figure 3.10: XRD pattern of PVK-TOA crystals (yellow) and $CsPbBr_3$ nanocrystals (blue), and reference (ICSD 18-364) data for monoclinic structure ($5.827 \times 5.891 \times 5.827$, $\beta = 89.65$).

and Balakrishnan [170], who were able to reversibly switch between 2D and 3D phases of $MAPbBr_3$ nanocrystals by adding either PEA or methylammonium (MA) cations. This kind of cation swap has also been reported by Garcia-Arellano *et al.* [171].

We carried X-Ray Diffraction (XRD) studies on the synthesized nanocrystals. Figure 3.10 shows X-Ray diffraction pattern of both PVK-TOA and the nanocrystals. First, the peaks of PVK-TOA appear much better resolved than the peaks of the nanocrystals, which may be explained by the comparatively small size of the latter species. Then, the diffraction pattern can be identified to a monoclinic structure with a ~ 5.82 Å lattice parameter. This result can be further confirmed thanks to high-resolution imaging of the nanocrystal showing directly the lattice formed by the atoms at the surface of the nanocrystals, as shown in Figure 3.8a. Reports from the literature on $CsPbBr_3$ nanocrystals mainly consist in orthorhombic [172] and cubic [7] structures, although some groups observe monoclinic structures [160]. Caution must be advised, as diffraction patterns of monoclinic and orthorhombic structures are similar, especially when the peaks are not well resolved.

3.2.3 Optical characterization in solution

I first characterized the optical properties of $CsPbBr_3$ nanocrystals in solution. As shown in Figure 3.11a, the absorption and emission spectra of PVK-TOA and of the nanocrystals are very similar. The absorption spectra feature an excitonic peak at 2.44 eV for PVK-TOA and 2.45 eV for the nanocrystals. The photoluminescence peak is at 2.42 eV for the former which gives a Stokes shift of $\sim$ 20 meV, while it is at 2.41 eV for the latter, with a Stokes shift of $\sim$ 40 meV. This value is typically close to the bandgap of bulk $CsPbBr_3$ crystals ($\sim$ 2.25 eV) [156, 157,

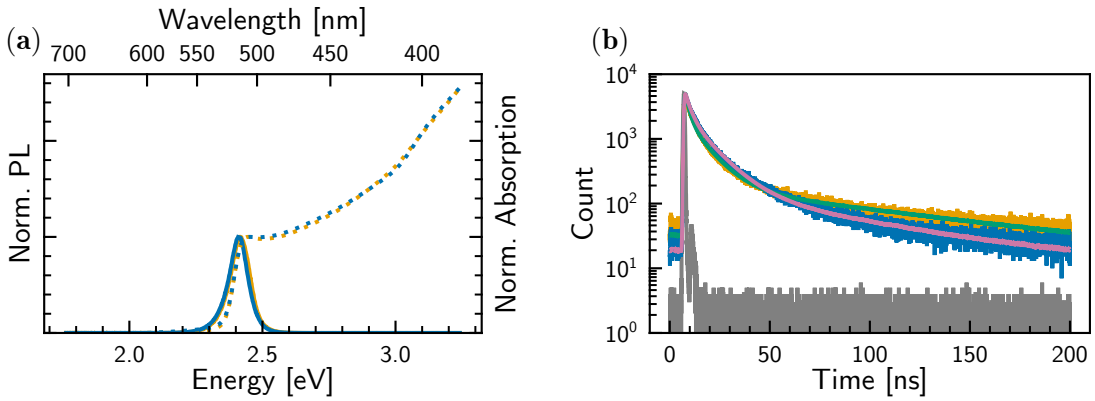

(c)

Species	f_1	τ_1 [ns]	f_2	τ_2 [ns]
PVK-TOA	0.2024 ± 0.0016	1.894 ± 0.013	0.4321 ± 0.0026	9.802 ± 0.048
Nanocrystals	0.2124 ± 0.0002	2.566 ± 0.021	0.5561 ± 0.0029	11.345 ± 0.057
Species	f_3	τ_3 [ns]	χ^2	$\bar{\tau}$ [ns]
PVK-TOA	0.3655 ± 0.0025	99.03 ± 0.05	2.01	40.80 ± 0.35
Nanocrystals	0.2315 ± 0.0027	64.55 ± 0.41	1.57	21.80 ± 0.21

Figure 3.11: (**a**) Absorption (dotted lines) and emission (solid lines) of PVK-TOA (yellow) and $CsPbBr_3$ nanocrystals (blue). (**b**) Time-resolved photoluminescence traces of PVK-TOA (yellow) and $CsPbBr_3$ nanocrystals (blue). The decay curves were successfully fitted with a tri-exponentials model (green and magenta respectively). (**c**) Estimates of the parameters of the tri-exponentials fit, reduced χ^2 test and average lifetime.

173], and matches the bandgap of nanocrystals with the same size synthesized by the hot-injection method [7] or the ligand-assisted re-precipitation method [160]. This is consistent with the expected low confinement in $CsPbBr_3$ nanocrystals of $\sim 10\,\mathrm{nm}$, where the exciton Bohr radius is about 7 nm [7]. The proximity to the absorption spectrum of bulk $CsPbBr_3$ allows the estimation of the effective cross-section of a single nanocrystal. Using the linear absorption coefficient of bulk $CsPbBr_3$ [174] at high energy (3 eV) to avoid variations in the excitonic peak intensity, one can scale the absorption spectrum of the nanocrystal solution to obtain their linear absorption coefficient. Then, using the estimate of the size of the nanocrystals ($\sim 10\,\mathrm{nm}$), the absorption cross-section is retrieved by multiplying the linear absorption coefficient by the volume:

$$\sigma(E) = \frac{\alpha_{\mathrm{bulk}}(3\,\mathrm{eV})}{\mathcal{A}(3\,\mathrm{eV})} \times V \times \mathcal{A}(E) \tag{3.1}$$

Where $\alpha_{\mathrm{bulk}}(E)$ is the linear absorption coefficient of the bulk material, $\mathcal{A}(E)$ the absorption spectrum of the solution of nanocrystals, and V the volume of a nanocrystal. This yields an absorption cross-section of $\sim 700\,\mathrm{Å}^2$ at 2.5 eV. Dividing the volume of a nanocrystal by the cell volume ($\sim 210\,\mathrm{Å}^3$), this corresponds to an absorption cross-section of $\sim 0.15\,\mathrm{Å}^2$ per cell. The corresponding molar extinction coefficient is $\sim 1.84 \times 10^7\,\mathrm{M}^{-1}\mathrm{cm}^{-1}$. This absorption cross-section is one order of magnitude higher than *e.g.* the absorption cross-section of the graphene quantum dots studied in the following chapters. The high absorption cross-section of $CsPbBr_3$ nanocrystals makes them bright, and thus a suitable platform for single-object investigation in the weak confinement regime [46, 175, 176].

Figure 3.11b shows the transient photoluminescence curve of PVK-TOA and the nanocrystals. Both curves can be fitted using three exponential decays. The resulting parameters are shown in Figure 3.11c. Both species feature a fast decay of about 2 ns that accounts for $\sim 20\,\%$ of the intensity, followed by a second decay of $\sim 30\,\mathrm{ns}$ accounting for approximately 40 % of the intensity of PVK-TOA's photoluminescence and 55 % of the nanocrystals. Finally, a long decay rate of 100 ns in PVK-TOA and 65 ns in the nanocrystals accounting for 36 % and 20 % of the intensity respectively. The corresponding average lifetimes are $\sim 40\,\mathrm{ns}$ and $\sim 20\,\mathrm{ns}$, which is consistent with the literature reports for $CsPbBr_3$ nanocrystals [7] but is higher than the reports ($\sim 10\,\mathrm{ns}$) for PVK-TOA [161]. The tri-exponential model is associated with surface trap states in the literature [177], with the intermediary time corresponding to recombination of excitons, while the short and long times are associated with trap states. Overall, the behavior of emitters in both materials is quite similar at short times, which is in line with the low confinement picture brought by transmission electron microscopy and steady-state optical characterization. At longer time however, the charge carriers recombine more quickly in the small nanocrystals, which may hint at the presence of more defects in PVK-TOA.

I assessed the photoluminescence quantum yield of the nanocrystals using an in-

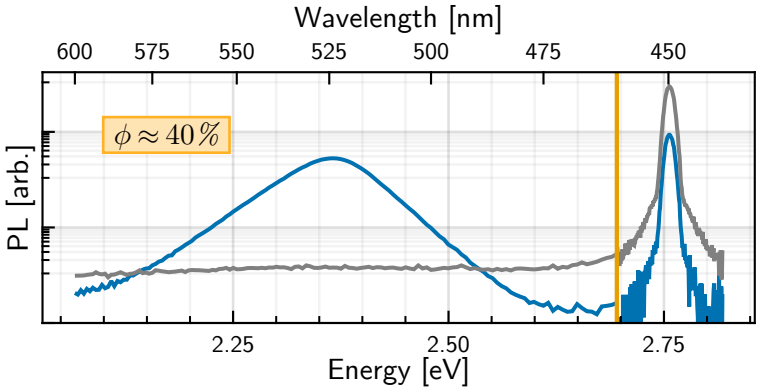

Figure 3.12: Photoluminescence quantum yield measurement on a solution of $CsPbBr_3$ nanocrystals. The emission and scattering regions were measured with two different slit widths. The emission region has been re-scaled to match the scattering region. The spectrum of the nanocrystals is in blue, and the reference in gray. The delimitation between regions is marked by the vertical yellow line. The difference in background level is due to diffusion, and only alter the quantum yield calculation marginally.

tegrating sphere. Briefly, the quantum yield is determined by the ratio of the number of photons emitted by the number of photons absorbed (see Sub-Subsection 2.1.1 for details on the method). The former is determined by integrating the emission spectrum while the latter can be measured by integrating the difference between the excitation of the solution and the excitation of the solvent alone. Figure 3.12 shows the spectra corresponding to those two measurements. The calculated photoluminescence quantum yield is $\sim 40\,\%$, which is on-par with the quantum yield reported by Protesescu *et al.* [7] for their first report of $CsPbBr_3$ nanocrystals synthesis, although the literature is rich in reports of near-unity quantum yield $CsPbBr_3$ nanocrystals obtained through ligand engineering[178–182]. During the writing of this manuscript, Cédric Mayer continued his work on developing this synthesis. In particular, he worked on replacing the PEA cation with other amines, allowing the nanocrystals to approach a quantum yield of unity. As a point of comparison, the quantum yield of PVK-TOA is typically $\sim 11\,\%$.

The solution resulting from the synthesis of the nanocrystals presents a high optical density, which is impractical for optical characterization, and thus prompted us to work with diluted solutions. Figure 3.13a on the facing page show the photoluminescence and absorption spectra of solutions of nanocrystals for various concentrations. These solutions range from the synthesis product (dilution 1:1) to a dilution ratio of 1000, and can be mapped to the concentration in single nanocrystals using the estimated absorption cross-section. The corresponding concentrations range from $\sim 4 \times 10^{-7}\,\text{M}$ (synthesized solution) to $\sim 2 \times 10^{-10}\,\text{M}$

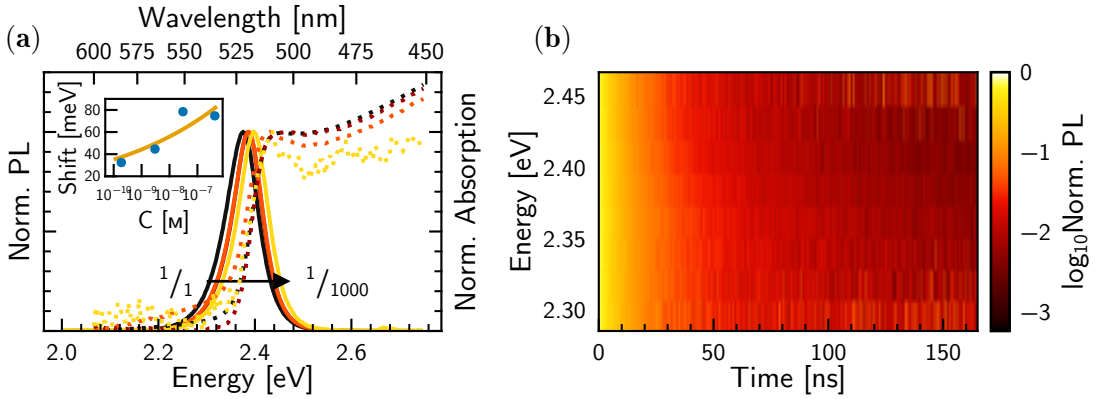

Figure 3.13: (**a**) Photoluminesence (solid) and absorption (dotted) spectra of solutions of $CsPbBr_3$ nanocrystals for relative dilution ratios of 1:1 (black), 1:10 (red), 1:100 (orange), and 1:1000 (yellow). The inset shows the corresponding Stokes shift against concentration on nanocrystals. The yellow line shows the result of a power law fit with exponent 0.102 ± 0.041. (**b**) Time-resolved photoluminescence traces normalized at time 0 showing the uniform decay rate over the whole spectral range.

(1:1000 dilution ratio). The figure shows the position of the bandgap varies little across the concentrations, while the photoluminescence consistently shifts towards higher energies as the concentration decreases. As a result, the Stokes shift is seen increasing with the concentration in nanocrystals, from $\sim 32\,\text{meV}$ to $\sim 75\,\text{meV}$, as shown by the inset. This is consistent with literature reports of the variation of observed Stokes shifts with increasing concentration in solutions of nanocrystals due to reabsorption [183].

Finally, by recording the time-resolved photoluminescence for limited spectral ranges across the emission spectrum, one can compare the decay curves as a function of the emission energy. This is shown in Figure 3.13b. The decays have been normalized at time 0 and show the uniformity of the decay rate across emission energies. This is consistent with the high calibration of the nanocrystals observed in transmission electron microscopy.

3.2.4 Films of nanocrystals

Preparation of films

The study of $CsPbBr_3$ can also be carried on in the solid state, which is particularly relevant to determine its properties for device applications. Typically, those require a controlled thickness, low roughness, and the absence of pinholes. To make the films, we drop-casted solutions containing either PVK-TOA or the

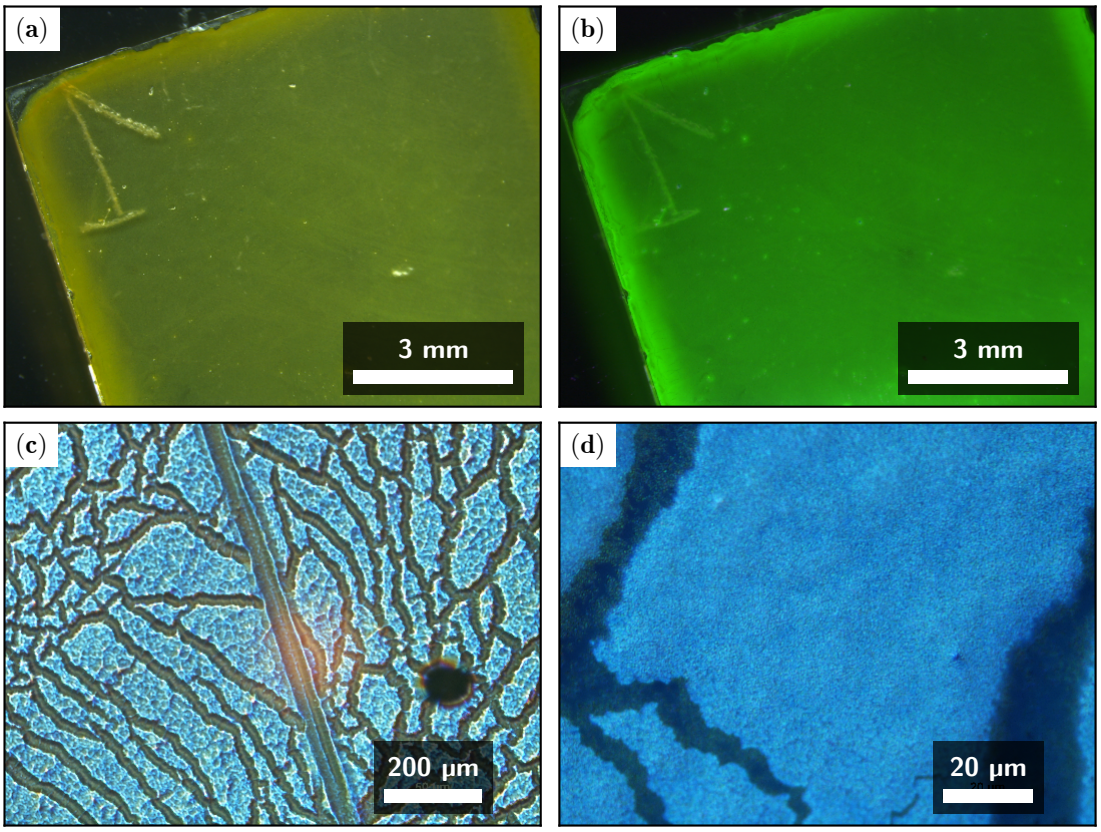

Figure 3.14: (**a**) Film of drop-casted nanocrystals. (**b**) Film of drop-casted nanocrystals under UV illumination. (**c**) Optical microscopy image of a drop-casted nanocrystal film. The oblique straight line has been manually carved for profilometry measurements. (**d**) Close-up picture of the film, showing the "cracks" surrounding more uniform areas.

nanocrystals on quartz substrates. The substrates were first cleaned by successive ultrasonic bath at 50 °C in an RBS solution (15 min), then water (15 min) and finally ethanol (25 min). They were then plasma-cleaned for 10 min and finally stored in a Toluene bath before use. I found that this later step improves greatly the quality of the films. This is likely due to the surface of the substrate being chemically prepared with -OH terminations by the cleaning process. The toluene solvent in which the nanocrystals are dispersed being apolar, it may have trouble forming a homogeneous film on that surface. The toluene bath thus unprepare the substrate, making it possible to form more homogeneous films of nanocrystals afterwards. The same preparation procedure allowed us to conduct preliminary tests in depositing nanocrystal films on glass substrates via spin-coating.

The drop-casting procedure yields films with good coverage of the substrate, as

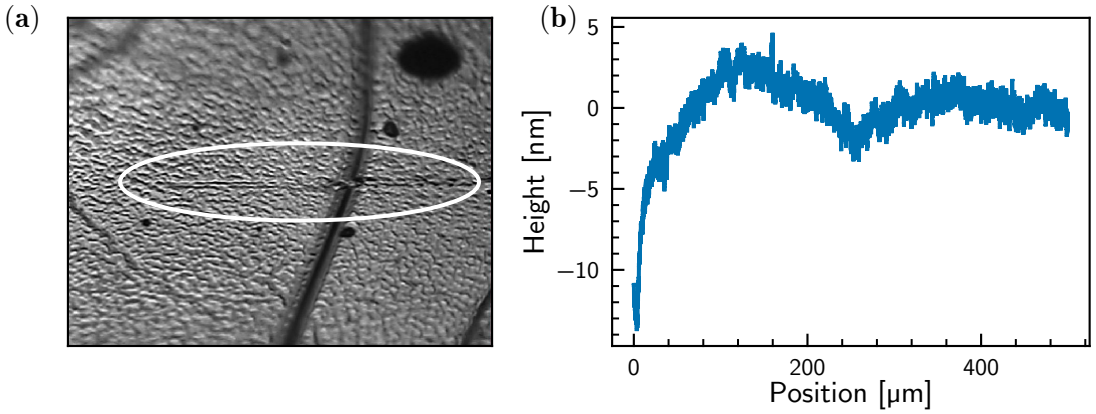

Figure 3.15: (**a**) Close-up photograph of the area probed by the profilometer. The horizontal line highlighted by the ellipse is the scratch caused by the tip of the instrument to the nanocrystal film. (**b**) Resulting profile of the film.

shown in Figure 3.14a, that keep their bright green fluorescence (Figure 3.14b). Closer inspection of the films, such as shown in Figures 3.14c and 3.14d, reveals the presence of "cracks" in the film of nanocrystals, which may result from the drying process.

I tried to assess the thickness of the film using profilometry. This proved ineffective, as even with the lowest force setting (0.03 mg), the tip would leave a scratch on the film, as shown in Figure 3.15a. The resulting profiles are hard to interpret at best (Figure 3.15b), but hint at a film that is thinner than 100 nm.

Stability of films

I compared the ability of $CsPbBr_3$ nanocrystals to sustain ambient atmosphere conditions. To do so we prepared two films, one with $CsPbBr_3$ nanocrystals, the other with PVK-TOA. I then let both films age for a week[3]. Figure 3.16a on the next page shows the absorption spectra of both films just after their synthesis, after one day, and after a week of exposure to ambient atmosphere. The absorption of the nanocrystals film remains stable over the period of time considered, whereas the absorption of the PVK-TOA film considerably red-shifts over the course of one day, and features a prominent peak at 2.38 eV. This strikingly different behavior is retrieved in the photoluminescence spectra. Figure 3.16b shows the emission spectra from both films right after synthesis, and after a week. The spectra for each species are normalized on the spectrum of the first day. While it is hard to be completely quantitative with these measurements, as they were taken on a micro-photoluminescence setup, which is sensitive to the quality of the focus and

[3]The two films were stored in a plastic box in an office, exposed to sunlight, ambient atmosphere, and hard-working PhD students.

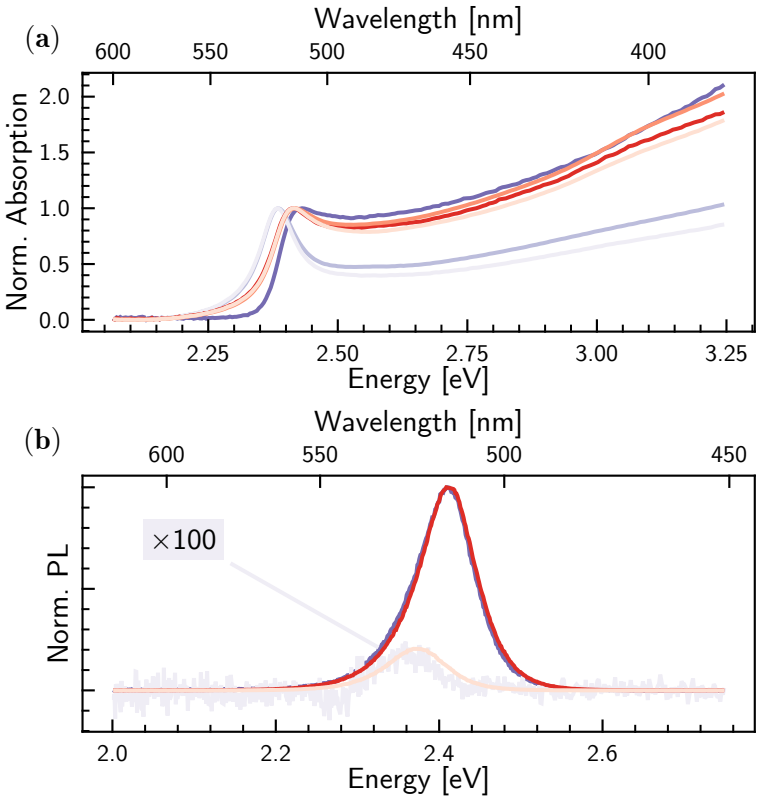

Figure 3.16: (**a**) Absorption spectra of PVK-TOA (purple) and $CsPbBr_3$ nanocrystal (red) films at time of synthesis (dark colors), after a day in ambient atmosphere (medium dark colors) and after a week of exposure to ambient atmosphere (lighter colors). (**b**) Photoluminescence spectra of PVK-TOA (purple) and $CsPbBr_3$ nanocrystal (red) films at time of synthesis (dark) and after a week of exposure to ambient atmosphere (light), excited at 405 nm.

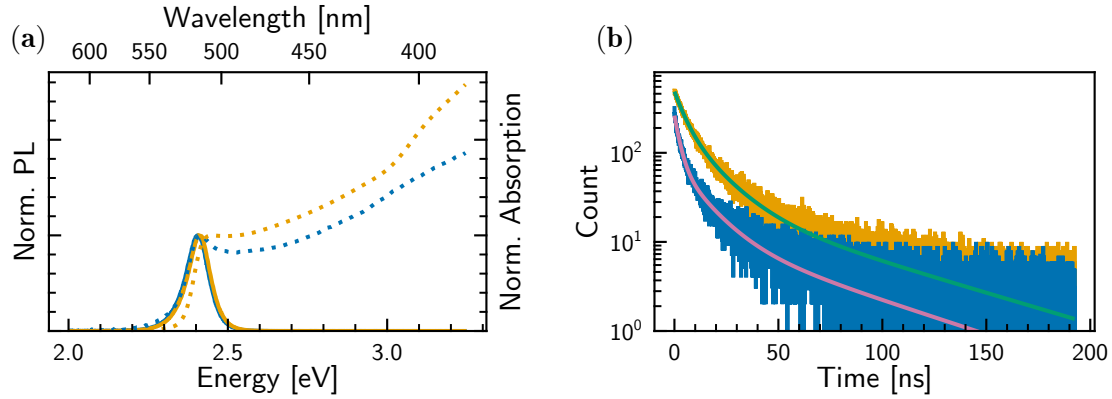

(c)

Sample	f_1	τ_1 [ns]	f_2	τ_2 [ns]
Solution	0.224 ± 0.011	4.76 ± 0.18	0.460 ± 0.017	14.33 ± 0.46
Film	0.2377 ± 0.0092	2.550 ± 0.077	0.399 ± 0.015	12.58 ± 0.45
Sample	f_3	τ_3 [ns]	χ^2	$\bar{\tau}$ [ns]
Solution	0.316 ± 0.014	62.9 ± 1.2	1.92	27.53 ± 0.84
Nanocrystals	0.363 ± 0.014	56.9 ± 1.3	3.69	26.31 ± 0.93

Figure 3.17: (**a**) Absorption (dotted line) and photoluminescence (solid line) spectra of solution (yellow) and resulting film (blue) of $CsPbBr_3$ nanocrystals. The photoluminescence spectra were excited at 405 nm. (**b**) Time-resolved photoluminescence traces of solution (yellow) and resulting film (blue) of $CsPbBr_3$ nanocrystals. The decay curves were successfully fitted with a tri-exponentials model (green and magenta respectively). (**c**) Estimates of the parameters of the tri-exponential fit, reduced χ^2 test and average lifetime.

to small variation in the alignment, we can say for sure that the photoluminescence of the PVK-TOA film is almost completely quenched after a week. In contrast, the film of $CsPbBr_3$ nanocrystals remains bright. This is an important property of the nanocrystals, and highlights the role of an increased ligand coverage of the object in protecting the perovskite from deterioration.

Optical characterization

We were first interested in the effect on the photophysics of the nanocrystals of going from the solution to a thin film. Figure 3.17a shows the absorption and photoluminescence spectra of a solution of nanocrystals and the resulting film. The absorption spectrum of the film features an excitonic peak at 2.42 eV and is red-shifted by 33 meV compared to the absorption spectrum of the solution. Similarly, the maximum of the photoluminescence spectrum of the film lies at 2.41 eV and is red-shifted by $\sim$ 5 meV compared to the photoluminescence spectrum of the solution. Interestingly, the Stokes shift of the film, $\sim$ 10 meV, is much smaller

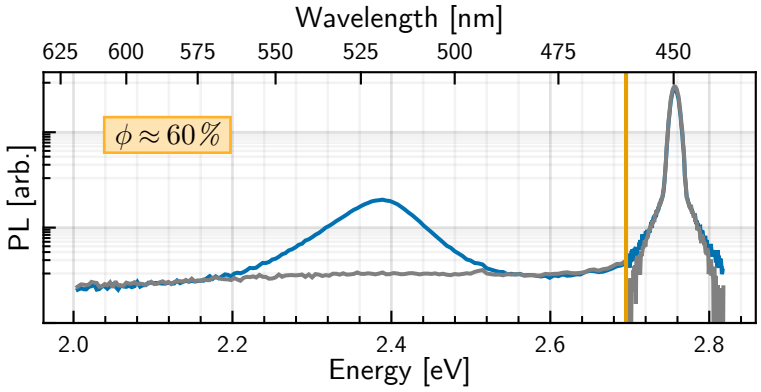

Figure 3.18: Photoluminescence quantum yield measurement on a film of $CsPbBr_3$ nanocrystals. The emission and scattering regions were measured with two different slit widths, and the emission region was re-scaled to produce the plot. The reference is in gray and the emission spectrum of the nanocrystals is in blue. The two regions are delimited by the vertical yellow line.

than the Stokes shift of the solution, $\sim 38\,\text{meV}$. The spectroscopy of the solution is performed on a diluted sample, which means the actual Stokes shift is likely higher. We attribute the difference in energies of the solution and the solid state to solvatochromism effects. The difference in Stokes shift may be explained by reabsorption in the solution.

Figure 3.17b shows the transient photoluminescence traces of the same solution and film. The decays are fitted using a tri-exponential model, and feature similar decay rates and associated fractional contributions, as shown in Table 3.17c. The average photoluminescence lifetimes of both samples are approximately 27 ns.

Figure 3.18 shows a photoluminescence quantum yield measurement on a film of nanocrystals, amounting to $\sim 60\,\%$. Since the absorption of a thin film is low compared to *e.g.* a solution of nanocrystals, this measurement should only be interpreted as an order of magnitude. Similarly to the transient photoluminescence traces, the photoluminescence quantum yield of the nanocrystals thus remains similar between both samples.

Investigating the solid state introduces new challenges compared to the investigation of solutions. For example the drying process can create the conditions for the re-precipitation of unwanted species. Figure 3.19 on the facing page shows the absorption spectra of solutions and their resulting films. The three solutions were synthesized from the same initial PVK-TOA solution, but the slicing process involved increasing ratios of PEA in the precursor solution. The three solution absorption spectra superimpose nearly perfectly. However, the absorption spectra of the films are distinct. First, we can see an increasing absorption peak at high energy ($\sim 3\,\text{eV}$), which we attribute to the formation of 2D $(PEA)_2PbBr_4$

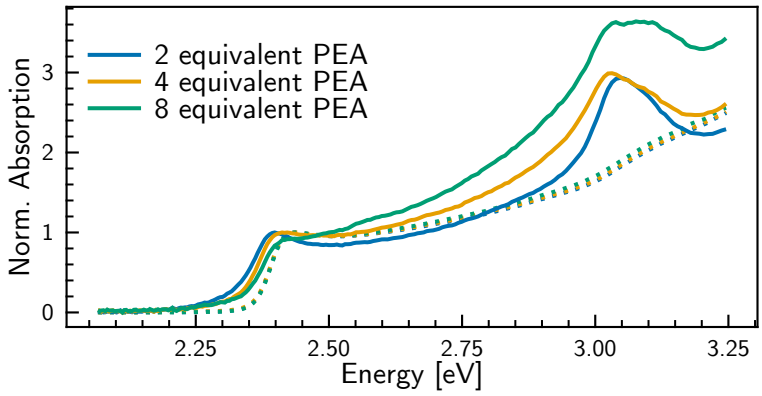

Figure 3.19: Absorption of solutions of $CsPbBr_3$ nanocrystals (dotted lines) and their resulting films (solid lines) with PEA in excess at three different ratios.

species [184, 185]. Second, the band-edge shifts towards higher energies as the ratio of PEA increases, which could indicate a higher quantum confinement of the emitters. We can then postulate that, as the solution dries on the substrate, the concentration in PEA increases, prompting it to attack the nanocrystals to form 2D nanoplatelets. This mechanism highlights the sensitivity of perovskite nanocrystal films to preparation conditions, and may contribute as a guideline when working towards nanocrystal-based devices.

Similarly to our study on quasi-2D films, we tried to increase the excitation fluence on a film of $CsPbBr_3$ nanocrystals. The resulting photoluminescence spectra are shown in Figure 3.20a. A small red-shift is observed as the excitation fluence is increased, with a position of the maximum of photoluminescence varying from 2.41 eV to 2.38 eV. We attribute this to reabsorption within the sample. The corresponding photoluminescence intensity is plotted in Figure 3.20b. The photoluminescence intensity is clearly seen stalling at higher excitation fluence. This may be explained by some non-linear effects, such as exciton-exciton annihilation, that would cause the photoluminescence quantum yield to decrease at high excitation fluence.

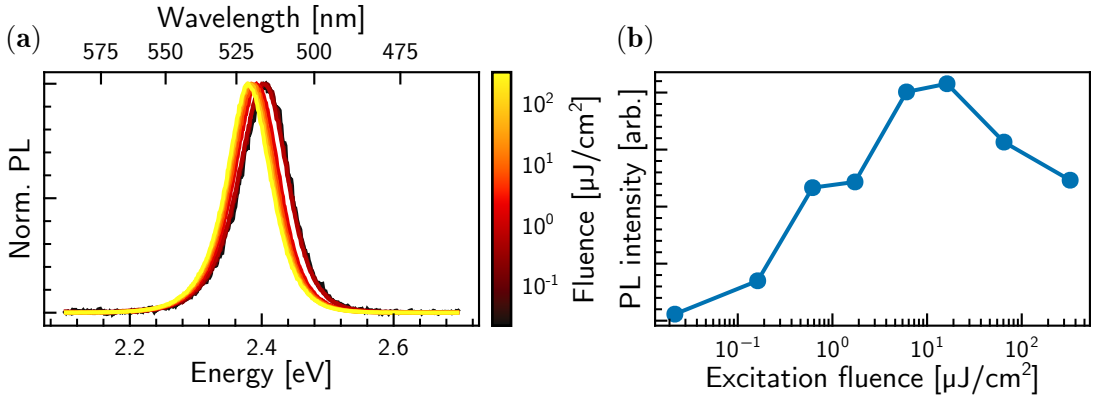

Figure 3.20: (**a**) Photoluminescence spectra of a film of $CsPbBr_3$ nanocrystals with increasing fluence. The excitation wavelength was 405 nm, repetition rate 2.5 MHz with tens of picosecond long pulses. (**b**) Evolution of the integrated photoluminescence intensity of the spectra reported in (**a**).

Conclusion

We were first interested in low-dimensional halide perovskites because of their high tunability and direct bandgap in the visible range, making them good candidate for building laser device. Our study highlighted the role of the organic cations in the optical properties of spin-coated films. Replacing formamidium with methylammonium in the quasi-2D films reported by Qin *et al.* [69] appears to have drastically reduced their fluorescence quantum yield. Similarly, we found results compatible with the mechanisms they propose for the quenching of triplet excitons by the big organic spacers.

We then turned our efforts towards the synthesis and characterization of $CsPbBr_3$ nanocrystals at room temperature. We developed a simple new synthesis method based on previously reported ligand-assisted re-precipitation methods. Our method yields highly calibrated 10 nm-wide $CsPbBr_3$ nanocrystals with an optical bandgap in the green region of the spectrum, and photoluminescence lifetime and quantum yield similar to those reported in the literature for similarly sized $CsPbBr_3$ nanocrystals. I showed that the deposition of nanocrystals on a substrate does not alter their properties significantly, as they keep similar photoluminescence and absorption spectra, photoluminescence lifetime and photoluminescence quantum yield. I also showed that the nanocrystals displayed remarkable stability under ambient atmosphere. The work on the synthesis and characterization of $CsPbBr_3$ nanocrystals was published in collaboration with Cédric Mayer [162].

Our initial goal of studying the laser effect in perovskite has been severely impeded by the premature death of our main femtosecond pump laser, forcing us to

	Material	Architecture	Pump	Threshold	Ref.
QD	$CsPbBr_3$	Film†	400 nm, 100 fs, 1 kHz	20 µJ/cm^2	[186]
	$CsPbBr_3$	Film†	800 nm, 35 fs, 1 kHz	192 µJ/cm^2	[187]
	$CsPbBr_3$	Film†	400 nm, 100 fs 335 nm, 10 ns	5 µJ/cm^2 450 µJ/cm^2	[159]
	$CsPbBr_3$	DBR	400 nm, 100 fs 400 nm, 5 ns	11 µJ/cm^2 900 µJ/cm^2	[188]
	$CsPbBr_3$	DBR	400 nm, 50 fs, 1 kHz 355 nm, 5 ns, 10 Hz	0.39 µJ/cm^2 98 µJ/cm^2	[189]
	$CsPbBr_3$	Film†	355 nm, 7 ns, 40 Hz	17 µJ/cm^2	[190]
	$MAPbBr_3$	DFB	405 nm, CW	15 W/cm^2	[191]
2D	$NMA_2FA_{n-1}Pb_nBr_{3n+1}$, $\langle n\rangle = 8$	S.c. film†	337 nm, 3 ns	16.7 µJ/cm^2	[70]
		DFB	337 nm, 3 ns 488 nm, CW	4.7 µJ/cm^2 45 W/cm^2	
	$PEA_2FA_{n-1}Pb_nBr_{3n+1}$, $\langle n\rangle = 8$	S.c. film†	337 nm, 3 ns	33.1 µJ/cm^2	
		DFB	337 nm, 3 ns 488 nm, CW	32.8 µJ/cm^2 59 W/cm^2	
	$PEA_2A_{n-1}Pn_nBr_{3n+1}$, (A:MA, Cs)	*	400 nm, 35 fs, 1 kHz	143 µJ/cm^2	[192]
	$PEA_2FA_{n-1}Pn_nXr_{3n+1}$, (X:Br, I), $n = 1...5$	S.c. film†	400 nm/550 nm, 150 fs	8.5 µJ/cm^2	[193]
	PEA_2PbI_4	DBR (exfoli.)	488 nm, CW	5.7 W/cm^2	[194]

Table 3.1: Literature reports of lasers and amplified spontaneous emission (ASE, marked with a †) in 2D halide perovskites and quantum dots at room temperature. A film architecture only allows ASE. DBR: Distributed Bragg Reflector. DFB: Distributed FeedBack. S.c.: spin-coated. CW: Continuous Wave. * Subwavelength cavity formed by glass substrate and UV glue cap, the perovskite film was spin-coated.

carry the optical studies against excitation power using a laser diode and strongly focused. This is less than ideal as the literature reports of laser effect in perovskites mostly use femtosecond excitation. Table 3.1 on the previous page shows some literature reports of amplified spontaneous emission and laser effect in films and monocrystals of 2D and 0D perovskites similar to those studied in this chapter. It is clear that the laser threshold varies widely. In particular some materials studied in this chapter, such as $NMA_2FA_{n-1}Pb_nBr_{3n+1}$, should have been observed lasing under excitation fluences accessible to our setup, which we could not confirm. This highlight the importance of the optimization of the material when working with perovskites.

Our work on $CsPbBr_3$ nanocrystals has led to a fruitful collaboration with the group of Johann Bouclé in XLim. In the framework of the thesis of Quanq-Huy Do, they were able to develop an LED by embedding the nanocrystals within a polymer matrix [195]. The study of the synthesis of perovskite nanocrystals is still an ongoing project. As shown in the study of 2D perovskite films, the role of the organic part is instrumental in the properties of halide perovskites. With this in mind, Cédric Mayer is currently working on the optimization of the synthesis, using other organic cations to replace PEA in the synthesis and optimize the quantum yield, calibration, and tunability of the nanocrystals.

$C_{96}tBu_8$ Graphene Quantum Dots, from Solution to Single-Molecule Experiments.

4

Contents

Introduction

Ever since its discovery, graphene has been studied extensively because of its intriguing physical properties as a semimetal. Reducing the dimensionality of graphene is an enticing goal, as it can make the material optically active. This has lead to many developments in the field of graphene nanotubes, graphene nanoribbons and graphene quantum dots (GQDs). These low-dimensional graphene-based objects pave the way to many applications in the domain of quantum technologies, for example Terahertz controlled single-electron gates [196]. Graphene quantum dots are members of the polycyclic aromatic hydrocarbons family, and are promising for applications where single molecules shine, such as localized probe in molecular crystals [103, 197, 198], fine-tuning of their zero-phonon line through laser-induced change to their local environment [110], or room-temperature single-photon sources for quantum technologies [105, 199, 200]. Nano-graphene can also be used as contact materials to control other quantum emitters [201, 202].

This chapter and Chapter 5 mainly focus on the study of $C_{96}tBu_8$, a rod-shaped GQD consisting in 96 sp^2 carbon atoms surrounded by eight bulky *tert*-butyl groups, in various environments. These GQDs are synthesized through a bottom-up method, as opposed to other synthesis methods such as top-down methods [203], and in solution, as opposed to *i.e.* on-surface synthesis [204]. Our collaborators

Daniel Medina-Lopez and Stéphane Campidelli [205] developed a method allowing the synthesis of a whole family of GQDs with similar geometrical features and physical properties. The study of the photophysics of the GQDs in solution has been done in the framework of the thesis of Thomas Liu [14]. I joined the research effort on these objects towards the end of his PhD, starting with the measurement of the photoluminescence quantum yield in solution. I then studied the GQDs at the single-molecule level.

I will first present the system, with a quick review of the synthesis method and a first assessment of the purity of the samples through mass spectrometry. I will then present the properties in solution of the four GQDs synthesized and discuss the role of the bulky *tert*-butyl groups in preventing the aggregation of GQDs in solution. In a second part, I will present our investigation of the properties of $C_{96}tBu_8$ at the single-molecule level in a polystyrene matrix at room temperature, ranging from steady-state optical properties to deepened characterization of the system through transient analysis. A statistical study of the purity of the samples will also be presented.

4.1 Presentation of the system

4.1.1 Synthesis of the GQDs and preparation of the solutions

The synthesis of the GQDs was developed by our collaborators in CEA-Nimbe, Daniel Medina-Lopez and Stéphane Campidelli, and can yield rod-shaped GQDs of controlled size, ranging from 78 to 132 sp^2 carbon atoms, as shown in Figure 4.1 on the facing page. Briefly, they synthesize dendrimers of suitable size, forming the "skeleton" of the GQD, before oxidizing them in a presence of $FeCl_3$ in a mixture of dichloromethane and nitromethane under argon flux, as shown in Figure 4.2 for the synthesis of $C_{96}tBu_8$. Figure 4.3 on page 106 shows how, using Matrix-Assisted Laser Desorption/Ionization-Time of Flight (MALDI-ToF) mass spectrometry, the mass spectrum is consistent with the predicted mass of the molecule. It also shows the purity of the sample. The presence of the GQDs is attested by the peak corresponding to the completely cyclodhydrogenated product, denoted M^+. Before any purification step (Figure 4.3a), the mass spectrum features peaks corresponding to by-products such as partially-fused, chlorinated or hydroxylated GQDs. To improve the purity of the samples, classical purification techniques, such as size exclusion chromatography with tetrahydrofuran (THF) as eluent preceded by an ultra-centrifugation step are employed. As a result the mass spectrum is much more pure, as shown in Figure 4.3b.

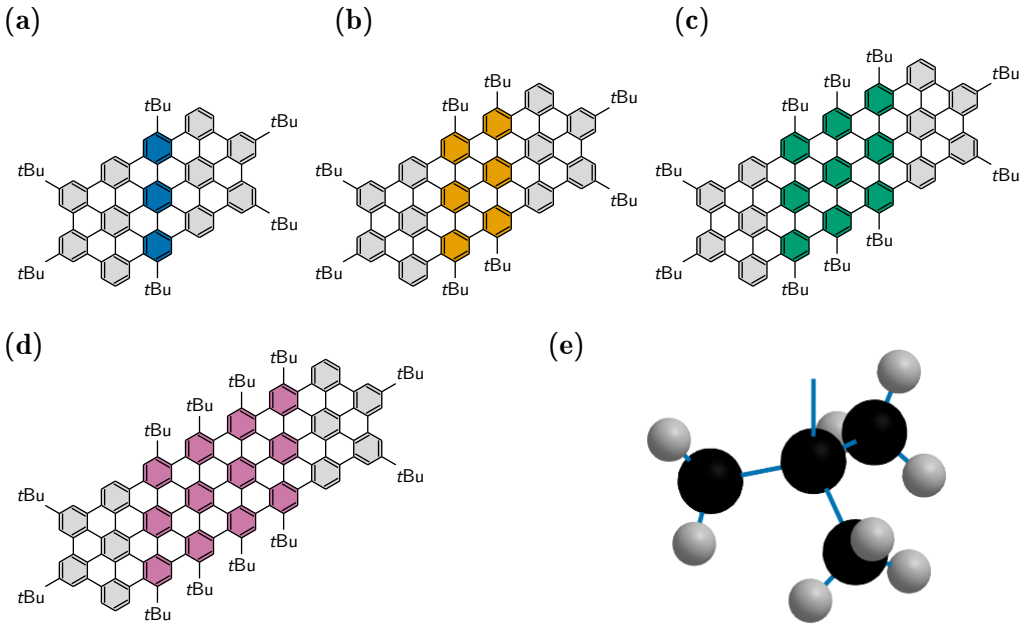

Figure 4.1: Chemical structure of (**a**) $C_{78}tBu_6$, (**b**) $C_{96}tBu_8$, (**c**) $C_{114}tBu_{10}$, (**d**) $C_{132}tBu_{12}$, and of a (**e**) *Tert*-butyl (tBu) group.

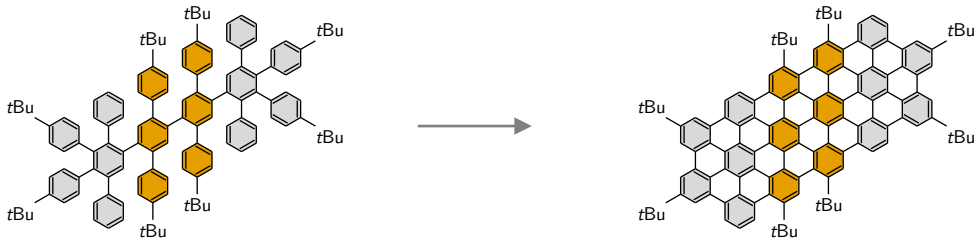

Figure 4.2: Synthesis of $C_{96}tBu_8$ by oxidation of a dendrimer.

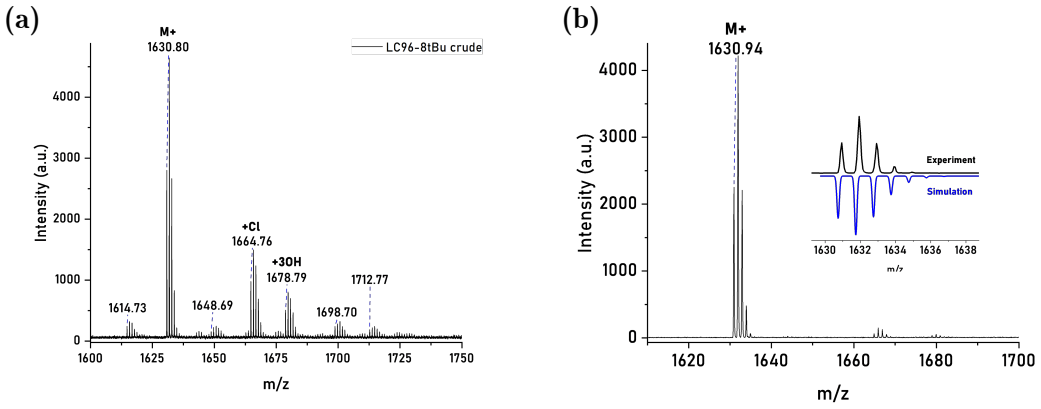

Figure 4.3: Matrix-Assisted Laser Desorption/Ionization-Time of Flight (MALDI-ToF) mass spectrometry of $C_{96}tBu_8$ (**a**) after oxidation of the dendrimer, and before any purification step, and (**b**) after ultracentrifugation for 30 minutes and size exclusion chromatography using THF as eluent.

GQD	in TCB	in THF
$C_{78}tBu_6$	$\sim 87\,000\,\text{M}^{-1}\text{cm}^{-1}$ at 443 nm	N.A.
$C_{96}tBu_8$	$\sim 458\,000\,\text{M}^{-1}\text{cm}^{-1}$ at 469 nm	$\sim 489\,000\,\text{M}^{-1}\text{cm}^{-1}$ at 462 nm
$C_{114}tBu_{10}$	$\sim 196\,000\,\text{M}^{-1}\text{cm}^{-1}$ at 443 nm	N.A.
$C_{132}tBu_{12}$	N.A.	N.A.

Table 4.1: Available molar extinction coefficient of the GQDs at their peak of absorption in trichlorobenzene (TCB) and tetrahydrofuran (THF). N.A.: Not Available.

4.1.2 Optical properties of solutions of GQDs

Steady-state optical properties

The samples were delivered to us as powders, that we dissolved in either tetrahydrofuran (THF) or trichlorobenzene (TCB). Figure 4.4a on the facing page shows the absorption and excitation spectra of all four GQDs. The excitation and absorption spectra superimpose well, and feature distinctive sharp peaks corresponding to optical transitions and their vibronic replica. Furthermore, the position of the spectra appear red-shifted as one moves towards bigger GQDs, which reproduces well the intuition that a larger GQD means a lower quantum confinement of electrons and thus exhibit optical transitions at lower energies. Moreover, the ratio between the heights of the main and the lowest-energy absorption peaks diminishes with longer GQD and nears unity in the case of $C_{132}tBu_{12}$. This is due to the polarization of the first transition being oriented along the long axis of the GQD, as will be shown in anisotropy measurements.

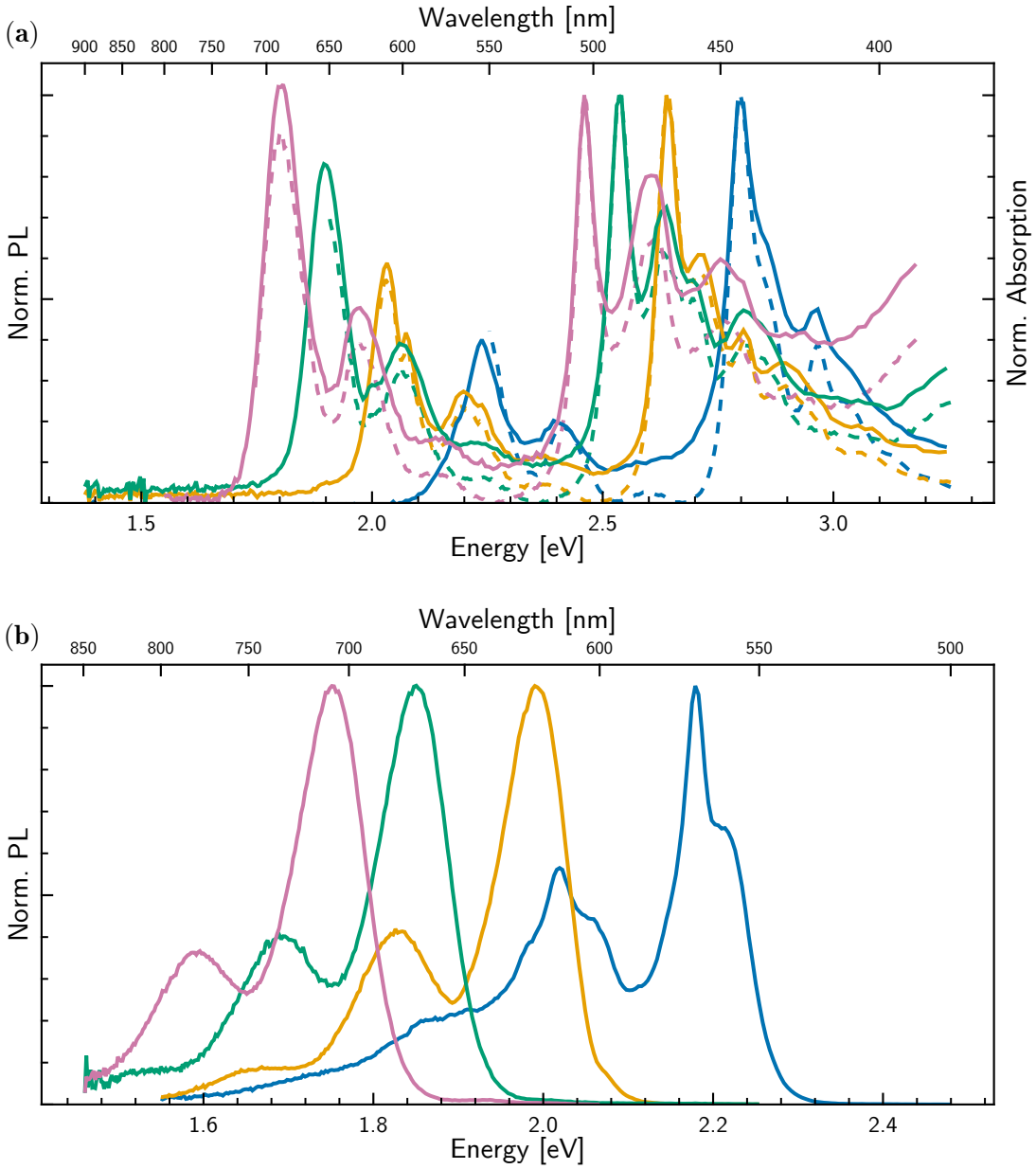

Figure 4.4: (**a**) Absorption (solid lines) and excitation (dashed lines) spectra and (**b**) emission spectra of $C_{78}t\text{Bu}_6$ (blue), $C_{96}t\text{Bu}_8$ (yellow), $C_{114}t\text{Bu}_{10}$ (green), and $C_{132}t\text{Bu}_{12}$ (magenta) in TCB.

GQD	Transition	Calc.	Meas.	Transition	Calc.	Meas.
$C_{78}tBu_6$	S_1 (H→L)	2.24 eV	2.23 eV	S_4 (H→L+1)	2.76 eV	2.79 eV
$C_{96}tBu_8$	S_1 (H→L)	2.02 eV	2.03 eV	S_4 (H→L+1)	2.57 eV	2.64 eV
$C_{114}tBu_{10}$	S_1 (H→L)	1.86 eV	1.90 eV	S_5 (H→L+1)	2.44 eV	2.54 eV
$C_{132}tBu_{12}$	S_1 (H→L)	1.74 eV	1.81 eV	S_6 (H→L+2)	2.34 eV	2.46 eV

Table 4.2: Calculated and measured (in TCB) lowest-energy and main absorption peaks of all GQDs.

GQD	ZPL	Stokes shift	ΔE
$C_{78}tBu_6$	2.18 eV	59.0 meV	159.7 meV
$C_{96}tBu_8$	1.99 eV	42.4 meV	164.1 meV
$C_{114}tBu_{10}$	1.85 eV	45.3 meV	161.4 meV
$C_{132}tBu_{12}$	1.75 eV	53.7 meV	160.0 meV

Table 4.3: Main features of the emission spectra of all four GQDs. ZPL: Zero-Phonon Line, ΔE: splitting between ZPL and first vibronic replica.

The molar extinction coefficient of the GQDs, shown in Table 4.1, has been measured by Daniel Medina-Lopez in various solvents by dissolving a known mass of GQD powder in solvent and measuring the optical density of the resulting solution. The coefficient is then retrieved using Beer-Lembert's law. Table 4.1 allows us to estimate the concentration of our solutions by simply measuring the absorption spectrum. This is particularly relevant as the masses of GQD needed to prepare the solutions we use are usually too small (typically less than a milligram) to be reliably measured on our balance, and because solvent evaporation, particularly THF, causes concentration to increase in a matter of days.

Figure 4.4b shows the photoluminescence spectra for the four GQDs. They all exhibit sharp vibronic features. The emission of $C_{78}tBu_6$ is noticeably different from the three others, as it features additional sharp peaks around the zero phonon line and its vibronic replica. We attribute that to the formation of dimers in the solution and I will discuss the reasons why later. The emission spectra reproduce the red-shifting of the zero-phonon line observed in the absorption spectra as the GQDs get bigger. The GQDs in solution exhibit a zero-phonon line comprised between 2.18 eV and 1.75 eV with a Stokes shift comprised between 42 meV and 59 meV. This falls in the expected range of Stokes shifts measured on other polycyclic aromatic hydrocarbons such as dibenzopyrene ($\sim$ 60 meV), hexabenzocoronene ($\sim$ 83 meV), or supernaphthalene ($\sim$ 30 meV) [206]. For all the GQDs considered, the splitting between the 0-0 and the 0-1 line is about 160 meV, which we attribute to the vibrational energy of C=C bonds. The details of the positions of the zero-phonon lines, Stokes shifts, and splittings are reported in Table 4.3.

Density Functional Theory (DFT) calculation performed by our collaborators

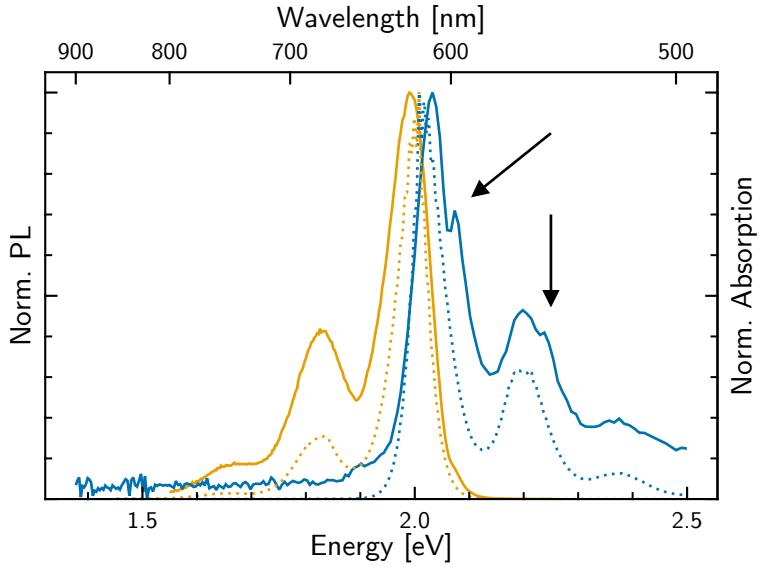

Figure 4.5: Theoretical (dotted lines) and experimental (solid lines) absorption (blue) and emission (yellow) spectra of $C_{96}tBu_8$.

Silvio Osella, Nicolas Rolland, and David Beljonne (University of Warsaw, University of Mons) allows us to attribute the absorption peaks to electronic transitions within the GQD [205]. Table 4.2 reports the theoretical transition energies of the lowest singlet transition and of the main absorption peak for all four GQDs, as well as the corresponding energy measured in Figure 4.4a. The calculated transition energies are remarkably well in accordance with the energies measured in TCB. Using Time-Driven DFT (TDFT), our collaborators were able to simulate the absorption and emission spectra of the GQDs, as shown in Figure 4.5. The main features of the experimental spectra are well accounted for by the theoretical spectra. We retrieve the sharp features and the vibronic replica of the transitions. The shoulders around 2.07 eV and 2.23 eV marked by the arrows in the experimental absorption spectrum are not present in the theoretical absorption spectum and were attributed to the presence of conformers in the solution [205].

The theoretical investigation of the properties of the GQDs, and of $C_{96}tBu_8$ specifically, gives a deepened understanding of the physics of GQD. In particular, the polarization of the optical transitions is well predicted by TDDFT. Figure 4.6a, Figure 4.6b, and Figure 4.6c on the next page show the transition densities for S_1, S_4, and S_9 of $C_{96}tBu_8$, also reported in Table 4.2. The two transitions are predicted to present perpendicular polarized dipoles. This has been verified by Thomas Liu [14] through anisotropy measurements in solution. The comparison between the theoretical polarized absorption spectra and the anisotropy measurement is presented in Figure 4.6d and Figure 4.6e. The theory matches well the

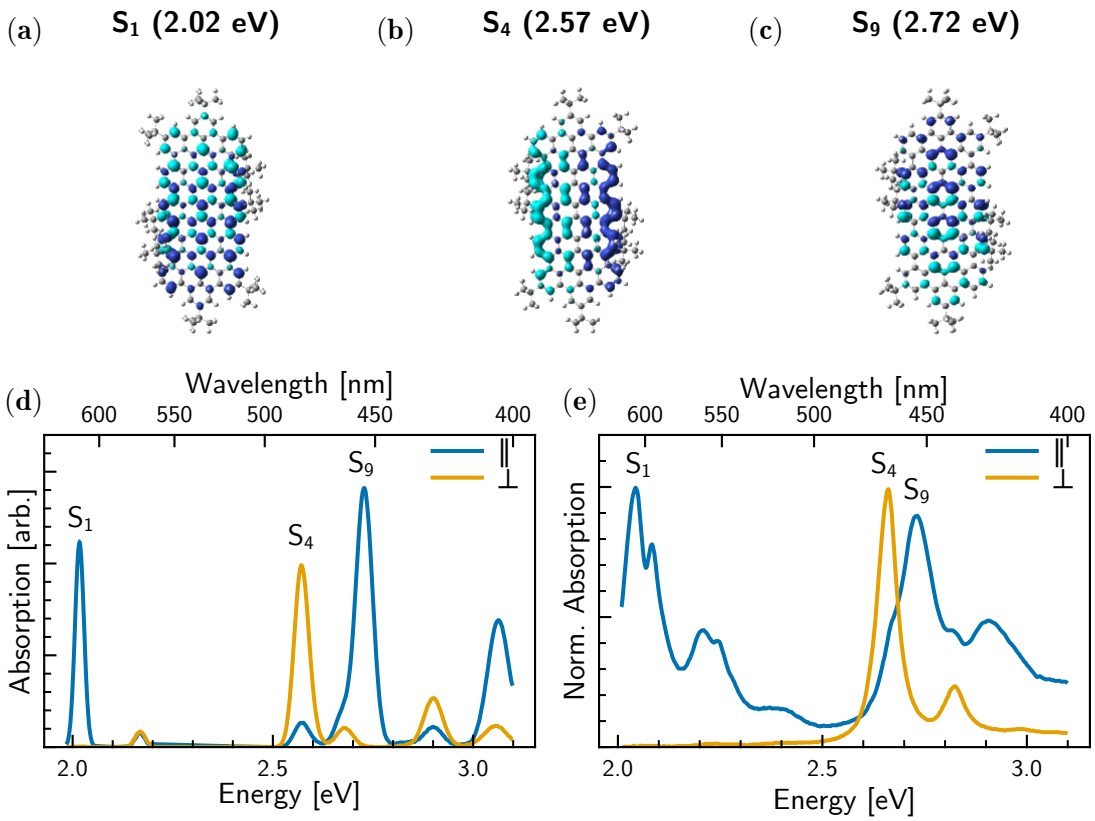

Figure 4.6: Calculated transition densities for (**a**) S_1, (**b**) S_4, and (**c**) S_9. (**d**) TDDFT calculations of absorption along parallel (blue) and perpendicular (yellow) axes of the GQD. (**e**) Polarization resolved excitation spectra extracted from anisotropy experiments corresponding to absorption polarized parallel (blue) and perpendicular (yellow) to the emission dipole. Adapted from Ref. [205].

experimental data.

Overall, this family of GQDs distinguish themselves by the clearly resolved sharp features in both the absorption and emission spectra, which sets them apart from previously reported large polycyclic aromatic hydrocarbons [79, 116, 207].

Transient optical characterization and photoluminescence quantum yield

The lifetime of the excited state of all four GQDs in solution was determined through time-resolved photoluminescence measurements. Figure 4.7 on the following page shows the resulting traces. Those from the two smaller GQDs require two exponentials in the model to be fitted correctly, although the fractional contribution [128] of the second exponential in the case of $C_{96}tBu_8$ accounts for about 5 %, versus 50 % for $C_{78}tBu_6$. The traces from the two longer GQDs can be fitted by a single exponential. Overall, the lifetime in solution decreases as the size of the GQD is increased, ranging from ~ 5 ns for the short component of $C_{78}tBu_6$ to ~ 2.3 ns for $C_{132}tBu_{12}$. The quasi mono-exponential decay of the three largest GQDs is a good indication of the purity of the corresponding solutions. Indeed, as we expect the de-excitation from the first excited singlet to the ground state to be akin to a two-levels system, the presence of multiple exponential components in the decay could be interpreted as a marker of the presence of multiple species within the solution. This is not the case for the three biggest molecules. For $C_{78}tBu_6$ we know dimers are present within the solution, as will be discussed in the following Sub-Subsection.

My main contribution to the ensemble characterization of this familly of GQDs consisted in the determination of their photoluminescence quantum yield in solution. Briefly, the photoluminescence quantum yield is the ratio of the number of photons emitted per photon absorbed, and is measured using an integrating sphere on our spectrofluorometer (Edinburgh instruments SC-30 sphere, FS-5 spectrometer, see Chapter 2). The procedure yields the spectra shown in Figure 4.8 on page 113. We first measure a spectrum resulting from the scattering of the excitation light in the solvent alone, with the slit opening on the measurement side typically ten times smaller than the opening on the excitation side, yielding the curves in gray. We then replace the cuvette with a similar one containing the molecule, with an optical density comprised between 0.1 and 0.3 in 1 cm, and perform the same measurement as previously. The photoluminescence quantum yield is then determined by integrating the difference between the two curves. If we denote R and S the integrated reference and sample spectra, and index scat. and em. the restrictions of these integrals to the excitation and emission areas respectively, the photoluminescence quantum yield is calculated as:

$$\phi = \frac{S_{\text{em.}} - R_{\text{em.}}}{R_{\text{scat.}} - S_{\text{scat.}}} \tag{4.1}$$

To first assess the reliability of our setup, we measured the photoluminescence

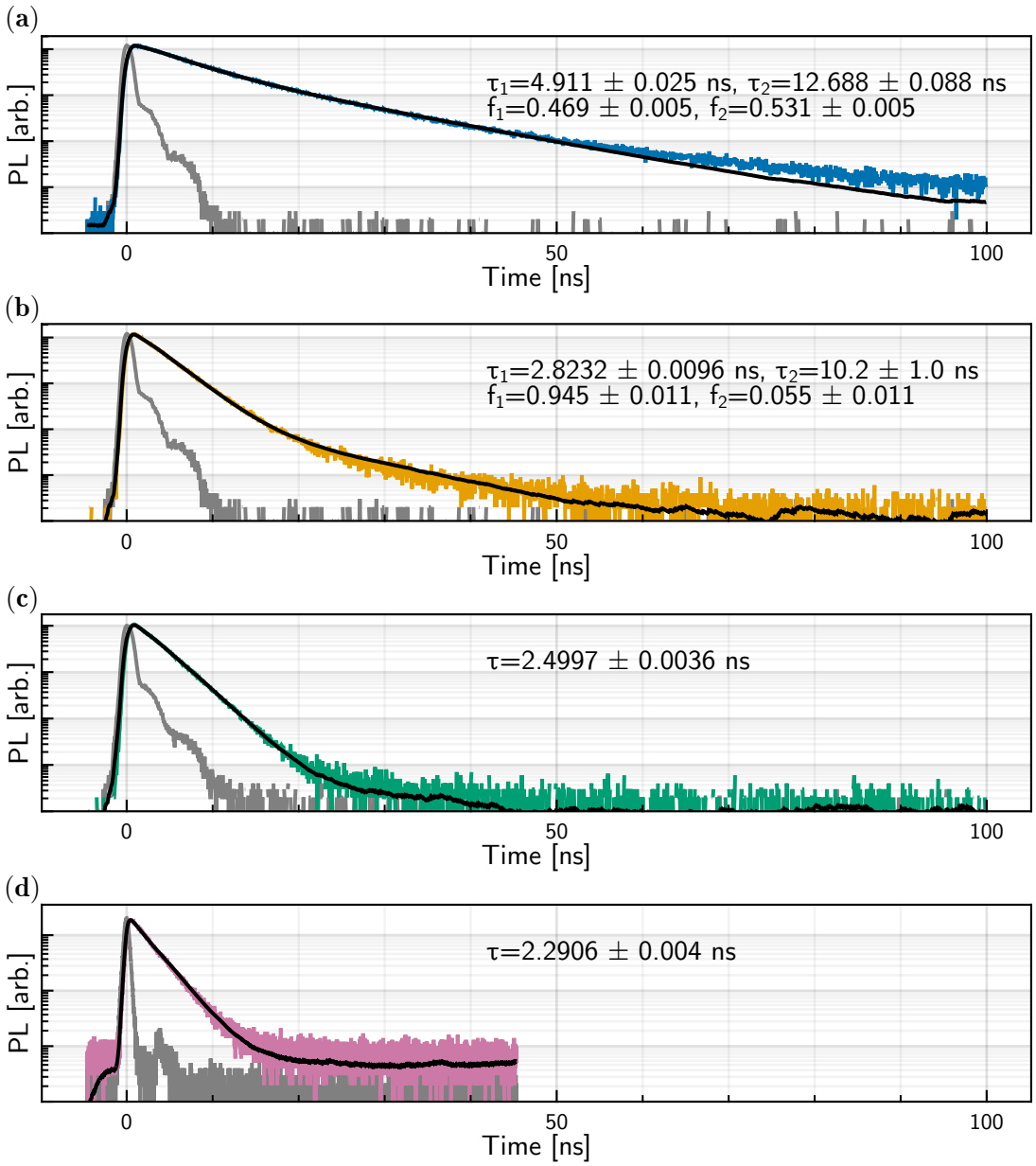

Figure 4.7: Time-resolved photoluminescence traces of (**a**) $C_{78}tBu_6$, (**b**) $C_{96}tBu_8$, (**c**) $C_{114}tBu_{10}$, and (**d**) $C_{132}tBu_{12}$. The instrument response functions are plotted in light gray, and the result of simple- or bi-exponential fit procedures (convoluted with the IRF) are plotted in black. $C_{78}tBu_6$, $C_{96}tBu_8$, and $C_{114}tBu_{10}$ were excited using a pico-second laser diode at 483 nm, with collection at 570 nm, 623 nm, and 673 nm respectively. $C_{132}tBu_{12}$ was measured on a different spectrometer than the three others, and was excited using a pico-second laser diode at 403.5 nm with collection at 705 nm.

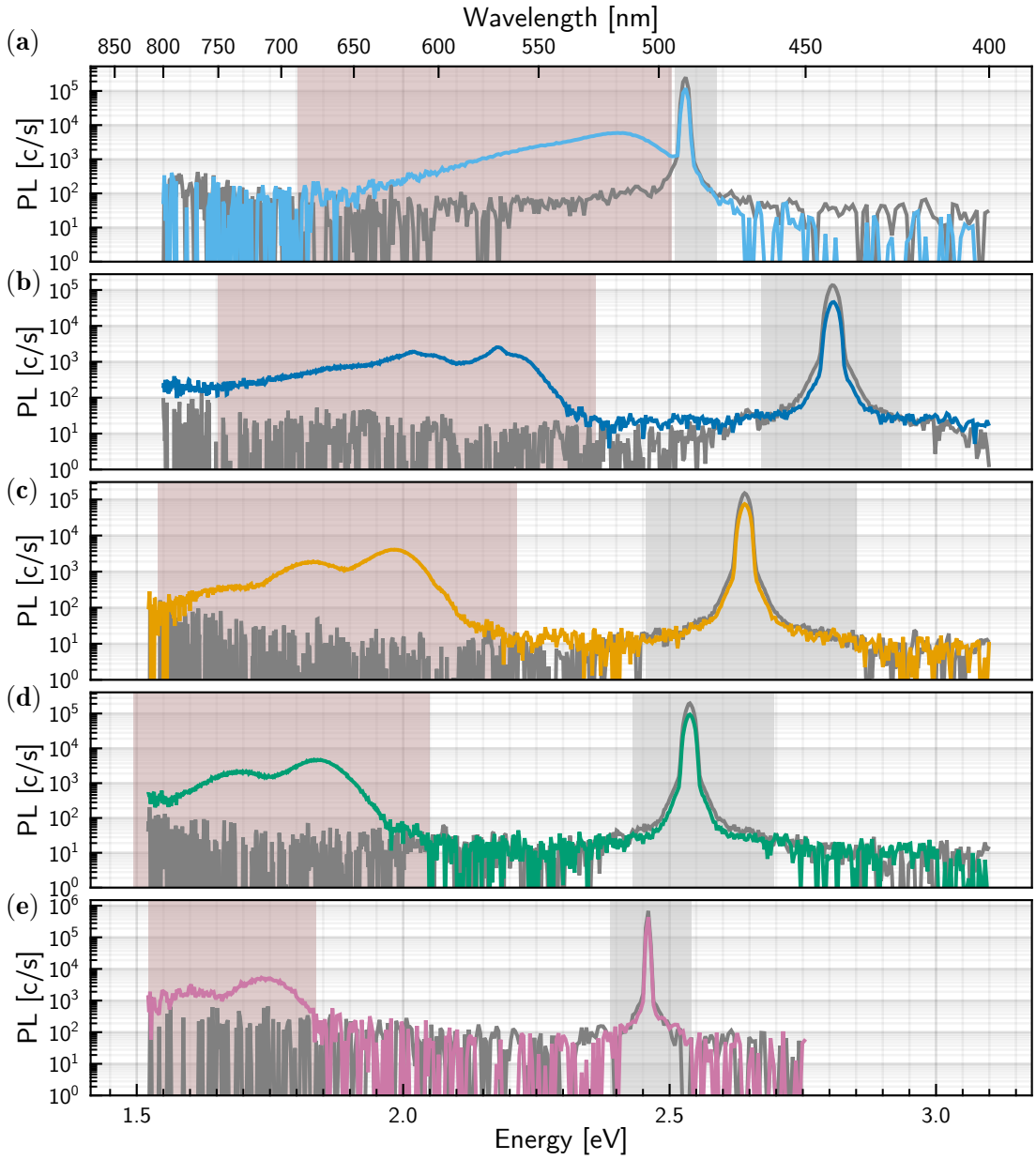

Figure 4.8: Determination of photoluminescence Quantum Yield in solution of (**a**) Fluorescein, (**b**) $C_{78}tBu_6$, (**c**) $C_{96}tBu_8$, (**d**) $C_{114}tBu_{10}$, and (**e**) $C_{132}tBu_{12}$. The scattering spectrum is in gray, and the areas integrated for the measurement of the scattering and the emission are marked in light gray and light red respectively. The quantum yield was estimated to 91 %, 56 %, 94 %, 91 %, and 88 % respectively.

quantum yield of a reference chromophore: fluorescein. Its quantum yield is known to be 0.925±0.015 [208] for an excitation energy of 2.53 eV. We measured 0.9118 on a sample in a 0.1 M NaOH solution with an optical density of 0.24 and excitation energy of 2.53 eV, which provides confidence in the good quality of the other measurements. We chose to excite the GQDs at the maximum of absorption, *i.e.* 2.79 eV, 2.64 eV, 2.54 eV, and 2.46 eV for $C_{78}tBu_6$, $C_{96}tBu_8$, $C_{114}tBu_{10}$, and $C_{132}tBu_{12}$ respectively. The measured quantum yield of the three largest GQDs is approximately 90 %, with a maximum of 94 % for $C_{96}tBu_8$, although the quantum yield of $C_{114}tBu_{10}$ and $C_{132}tBu_{12}$ may have been underestimated due to the lack of sensitivity of our detector at low energies. The quantum yield of $C_{78}tBu_6$ is noticeably lower, 56 %, which we attribute to aggregation of the GQD in solution (see next Sub-Subsection for an in-depth explanation). Overall, the high quantum yield of these GQDs makes them promising for optoelectronics applications.

About the non-aggregation of $C_{96}tBu_8$ in solution

As shown in Figure 4.4, the shape of the absorption and emission spectra of $C_{78}tBu_6$ differ from the spectra of the other members of the family. This is attributed to the formation of $C_{78}tBu_6$ dimers in the solution, as evidenced by the comparatively longer photoluminescence lifetime of $C_{78}tBu_6$, as well as its smaller photoluminescence quantum yield compared to other GQDs of the family. This has been highlighted by our theoretician collaborators through the calculation of the Potential of Mean Force curves corresponding to the formation of dimers [205].

The simulation consists in putting two GQDs in their most stable conformation in a cubic box filled with TCB molecules. First, the two GQDs are left evolving freely for 80 ns to let the system reach equilibrium. Then, a harmonic potential is progressively switched-on around each GQD's center of mass to keep them 20 Å apart before being pushed against each-other until the separation between the centers of mass was 2 Å and then being pulled back to a 20 Å separation distance.

The simulation was run on two GQDs, $C_{78}tBu_6$ and $C_{96}tBu_8$, and the resulting free-energy push and pull curves are shown in Figure 4.9a and Figure 4.9b on the facing page, respectively. Both push curves feature three minima, labelled min.1, min.2, and min.3 in the figure. The first one at around 7 Å corresponds to a situation where a single layer of solvent molecules is present between the two GQDs and needs to be evacuated before the molecules can be brought any closer to each other, resulting in a potential barrier in the push curve. The removal of the solvent between the GQDs leads to brutal changes in the conformation of the molecules, which in turns creates artifacts in the push curves that need to be corrected, as shown by the dashed black curves in Figure 4.9a and Figure 4.9b. The two other minima correspond to the formation of dimers in the solution. For $C_{78}tBu_6$, minimum 2 corresponds to a situation where one of the GQDs has its *tert*-butyl groups pointing outwards while the *tert*-butyls of the second GQD point inwards, as shown in Figure 4.9c. This conformer exists in solution, which means

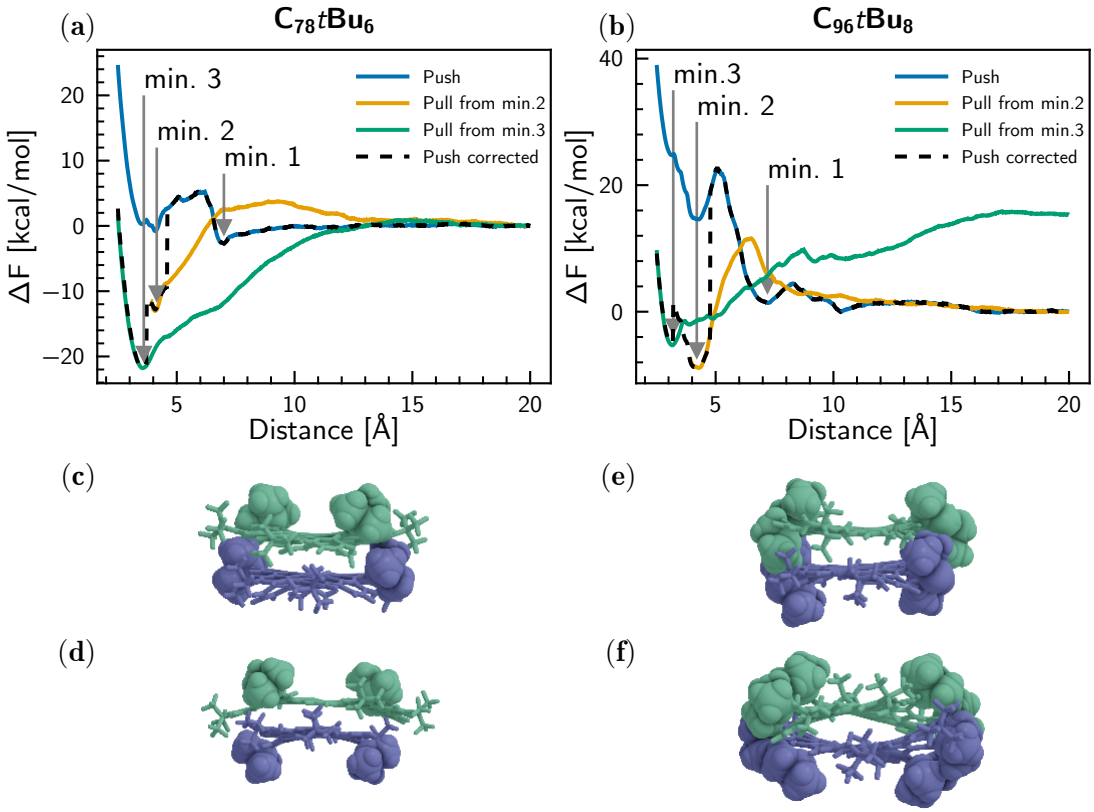

Figure 4.9: (**a**) Push and pull curves computed for $C_{78}tBu_6$. (**b**) Push and pull curves computed for $C_{96}tBu_8$. (**c**), (**d**) Configurations of $C_{78}tBu_6$ for minima 2 and 3. (**e**), (**f**) Configurations of $C_{96}tBu_8$ corresponding to minima 2 and 3.

the dimer is expected to be present in the solution and explains the shape of the emission spectrum of $C_{78}tBu_6$ and the multi-exponential decay of time-resolved photoluminescence. The situation at minimum 2 is similar for $C_{96}tBu_8$, where half the *tert*-butyl groups point outwards. However, minimum 2 is much harder to reach for $C_{96}tBu_8$, due to the conformational change needed which translates in an important potential barrier around 5 Å in the push curve in Figure 4.9b. Finally, for both GQDs, minimum 3 corresponds to a situation where all *tert*-butyls groups point outwards. For $C_{96}tBu_8$, the pulling curve from minimum 3 does not exhibit any potential barrier that could impede the formation of such dimer in solution. Schematically speaking, this corresponds to a situation where both GQDs can slide on top of each other to form the dimer. The formation of such a dimer in solution, however, is not possible because the conformer with all the *tert*-butyl groups pointing outwards cannot exist in solution due to the large intermolecular strain involved.

4.2 Single-molecule study of $C_{96}tBu_8$

The non-aggregation of $C_{96}tBu_8$ in solution, as well as its high photoluminescence quantum yield and well-defined spectroscopic properties prompted us to study the GQD at the single-molecule level. In this section, I will detail our findings on $C_{96}tBu_8$ dispersed in polystyrene thin films at high dilution ratio.

4.2.1 Description of samples

We started with GQDs dispersed in spectroscopic-grade THF. The exact concentration was first assessed through its optical density, then diluted until a suitable dilution ratio was obtained. A solution with 10 % w.r.t. of polystyrene in THF was then prepared. The solution was heated at 75 °C for 30 minutes to dissolve the polystyrene beads completely. Both solutions were then mixed in equal volumetric quantities. Reported concentrations in this section correspond to the calculated concentration of GQDs in the resulting solution, typically 60 pM.

The films were then prepared by spin-coating the mixture on glass substrates. The substrates were plasma-cleaned for 20 minutes beforehand. The rotation speed was 1000 rpm, acceleration 500 rpm/s, and rotation time 180 s. The samples were dried on a hot plate (90 °C) for 1 h. The resulting films were 1 to 2 µm thick, measured with a profilometer.

4.2.2 Steady-state properties of single $C_{96}tBu_8$ in polystyrene matrix

Figure 4.10a on the next page shows a typical raster confocal fluorescence scan of a sample excited by a 594 nm (2.087 eV) continuous wave laser. It features

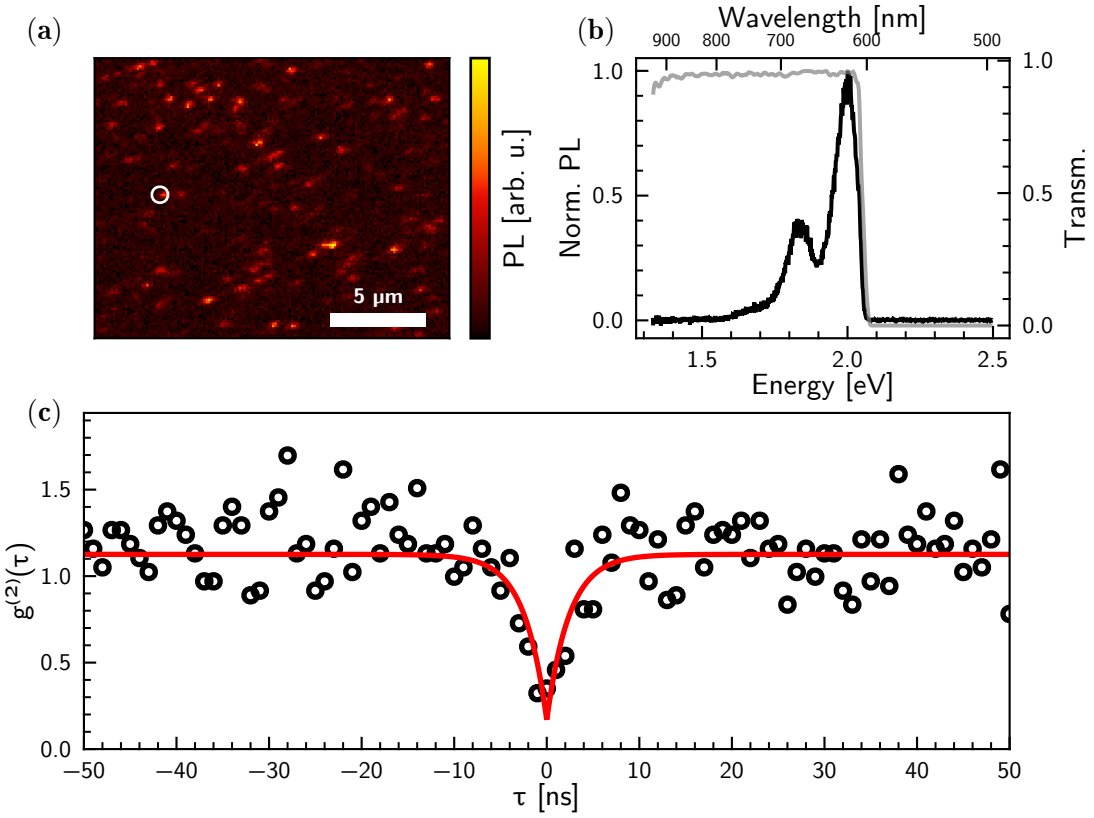

Figure 4.10: (**a**) Confocal raster scans of sample with $C_{96}tBu_8$ in polystyrene matrix displaying diffraction-limited emission spots. Concentration in the solution was $\sim$ 50 pM. (**b**) Typical PL spectrum of a single $C_{96}tBu_8$, measured on the diffraction-limited spot circled in white in the raster scan. The transmission of the setup is plotted in light gray. (**c**) Typical second-order correlation measurement, excited at 0.15 kW/cm^2. The histogram (black circles) is fitted using a single exponential with a constant added to account for bunching (solid red line). $g^{(2)}(\tau)$ at origin is fitted at 0.17, and the characteristic time of the exponential is 2.43 ns.

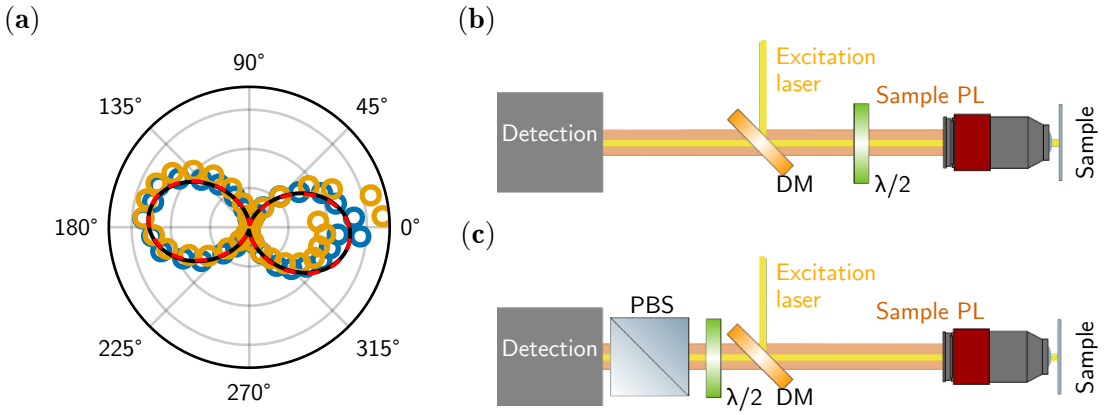

Figure 4.11: (**a**) Emission polarization diagram (blue circles) fitted with Malus' law (solid black line) and excitation polarization diagram (yellow circles) fitted with Malus' law (dashed red line). The two fit superimpose nearly perfectly. Both signals are integrated photoluminescence over the whole emission spectrum. (**b**) Principle of the measurement of the excitation polarization diagram. (**c**) Principle of the measurement of the emission polarization diagram. DM: Dichroic mirror, $\lambda/2$: Half-wave plate, PBS: Polarizing beam splitter. The half-wave plate is mounted on a computer-controlled rotating mount.

diffraction-limited spots, that we selected for spectroscopic studies. A typical emission spectrum is shown in Figure 4.10b. It features a zero-phonon line centered at 2.00 eV and two vibronic replica at 1.83 eV and 1.66 eV respectively. Some variations in the positions of the peaks were observed, and a more thorough investigation will be presented in Subsection 4.2.3. To ensure that we studied a single GQD at a time, we recorded second-order correlation measurements, $g^{(2)}(\tau)$, on diffraction-limited spots. A typical measurement is shown in Figure 4.10c. For now, $g^{(2)}(\tau)$ measurements can be seen as a comparison between the coincidence rate of a given source with that of a Poissonian source. This means that the dip below 0.5 at 0 time-delay indicates a clear deviation from a pure Poissonian source. It shows that it is highly unlikely to detect two photons at the same time, which in turns indicates the emitter under scrutiny is a single-photon emitter, *i.e.* a single $C_{96}tBu_8$. The characteristic time needed for the curve to approach one is 2.43 ns, and is typically close to the photoluminescence lifetime for low excitation intensities. This $g^{(2)}(\tau)$ measurement will be discussed later in Subsection 4.2.4.

The theoretical investigation of $C_{96}tBu_8$ lead by our collaborators has highlighted the dipole-like nature of optically active transitions of the molecule. This has been further confirmed by anisotropy measurements in solution. In particular, the S_1 transition is polarized along the longest dimension of the GQD. This means that when $C_{96}tBu_8$ is excited in close resonance to S_1, then the light emitted by

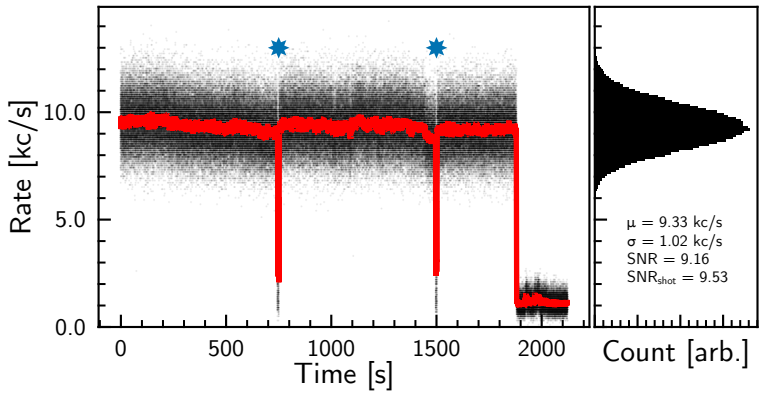

Figure 4.12: Time trace of the measured emission of a single emitter excited at $0.15\,\mathrm{kW/cm^2}$. Binning rate is 100 Hz. The moving average over 2 s is plotted in solid red. Manual adjustments of the setup are marked with a blue star, and the final drop in intensity corresponds to the death of the molecule. Other variations are attributed to experimental instabilities. The histogram on the right is obtained from all the points that are not included in the manual adjustments and after the death of the emitter. The signal to noise ratio (SNR) shows the signal is shot-noise limited.

the system must be polarized in the same direction as the polarization of excitation for which the emission is the brightest. Once a single GQD has been selected, this is easily verified using the two simple setups shown in Figure 4.11b and Figure 4.11c, for excitation and emission scans respectively. Briefly, for excitation scans, a computer-controlled half-wave plate placed in the excitation path allows controlling the excitation polarization. For emission scans, the half-wave plate is placed on the detection path before a polarizing beam splitter. For both experiments, the background is recorded at each polarization angle and subtracted from the measurement. Typical excitation and emission diagrams resulting from these experiments are shown in Figure 4.11a. Both diagrams were fitted using Malus' law ($I(\theta) = I_0 \cos^2\theta$), and the resulting polarization curves superimpose perfectly, as expected from theoretical models and anisotropy measurements in solution.

A typical time trace at low excitation intensity ($0.15\,\mathrm{kW/cm^2}$) is shown in Figure 4.12. A signal-to-noise ratio (SNR), the ratio between the mean value of the signal and the amplitude of the random variations around that mean, of 9.16 is measured. The excellent agreement with the expected theoretical SNR (~ 9.53) demonstrates that our measurement is shot noise limited. Indeed, because the photon events distribution at the considered time scales follows a Poisson distribution with a large number of events, we can assume the fluctuations to be Gaussian noise. Because the standard deviation of such shot noise process is the square root of the average number of events N, the theoretical SNR is $\frac{N}{\sqrt{N}}$. We also stress

that no blinking was recorded for binning rate used (100 Hz) and that the photon count rate remains constant under continuous illumination for up to thirty minutes, demonstrating that $C_{96}tBu_8$ GQDs in the polystyrene matrix are remarkably stable, despite that no particular precaution has been taken to reach this result. Thus, we foresee that GQDs stability can even be increased by a careful choice of matrix and preparation steps.

4.2.3 Assessment of the purity $C_{96}tBu_8$ samples

When working at single-molecule levels of dilution, the limited quantity of emitters in the sample can make it challenging to ensure that a peculiar emitter is not an impurity. Considering the emission spectrum is not always sufficient, as some impurities have emission spectra similar to that of a GQD. This problem has been raised in several studies, and different hypotheses have been proposed for the origin of those impurities, ranging from solvent impurities [209] to organic impurities from the caps of glass vials [210], impurities in polymer matrices [207], or defects in silica [211]. A thorough investigation of fluorescent impurities in single-molecule experiments can be found in references [14, 116, 212]. In this subsection I highlight the high purity of the single-molecule samples studied in this chapter through the statistical study of the emission spectra of diffraction-limited spots in polystyrene films against the concentration in $C_{96}tBu_8$ of the solution used to prepare the sample.

To study the purity of our samples, we decided to record the emission spectra orginating from diffraction-limited spots for various concentrations of GQDs. Spectra were classified using a simple three-emission-peaks model. The model comprises three Lorentzian peaks and the transmission of the setup based on manufacturer data for the dichroic mirror and clean-up filter and was fitted on each normalized spectrum using the Levenberg–Marquardt algorithm with the input parameters given in Table 4.13b on the facing page. Data points outside the transmission region of the filter were given a null weight. Spectra were post-selected to remove fit results that would be difficult to interpret, for example spectrum whose shape does not correspond to the three lines expected. An example of a fit result is shown in Figure 4.13a. The samples were prepared with various concentrations of $C_{96}tBu_8$, ranging from ~ 6 pM to ~ 153 pM, and a control sample without GQDs. As expected, the density of emitters available on a confocal scan decreases with lower concentrations of $C_{96}tBu_8$ in the solution, as shown in Figure 4.14 on page 122.

Some diffraction-limited spots are observable in the control sample made only of polystyrene, with no GQDs. Figure 4.15 on page 122 compares the emission spectrum of a single impurity with the emission spectrum of a solution of GQDs. It features a zero-phonon line around 2 eV, with vibronic replica that could be expected on a GQD. This highlights the need for the identification of a concentration of GQDs in the solution used to make the film that is sufficiently high that a diffraction-limited spot in the film almost certainly corresponds to a GQD. Fig-

(**a**)

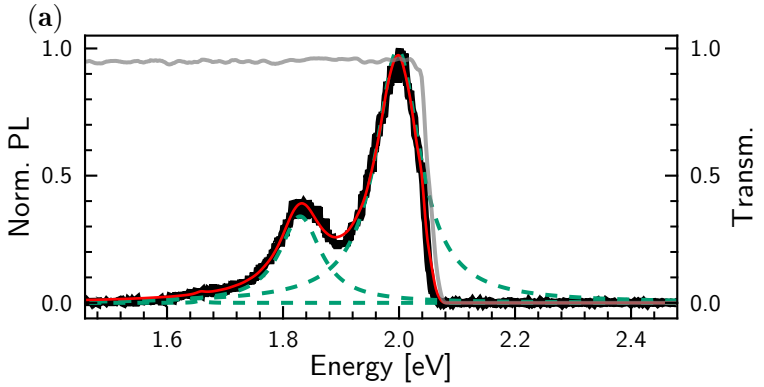

(**b**)

Peak	Amplitude [norm.]			Center [eV]			HWHM [meV]		
	Init.	Min.	Max.	Init.	Min.	Max.	Init.	Min.	Max.
1	1	0	$+\infty$	2.0	1.90	2.10	100	6	162
2	1/3	0	$+\infty$	1.83	1.75	1.9	100	6	138
3	0.1	0	$+\infty$	1.67	1.55	1.75	50	10	250

Figure 4.13: (**a**) Spectrum of a single $C_{96}tBu_8$ (black line) fitted with three Lorentzian peaks (red line). Individual peaks are shown in dashed green. We take the transmission of the optics of the setup (shown in light gray from manufacturer data) into account in the fitting procedure. (**b**) Input parameters for Levenberg-Marquardt algorithm. HWHM, Half Width Half Maximum.

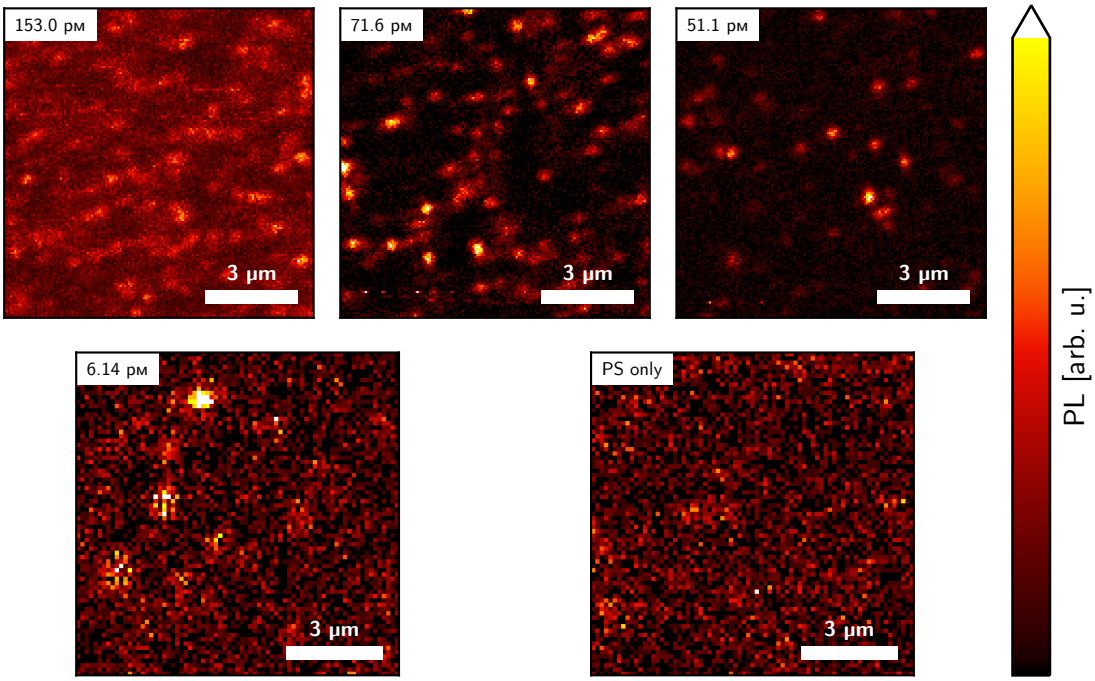

Figure 4.14: Confocal raster scans of four films with decreasing GQD concentration in the solution and reference sample with polystyrene matrix only.

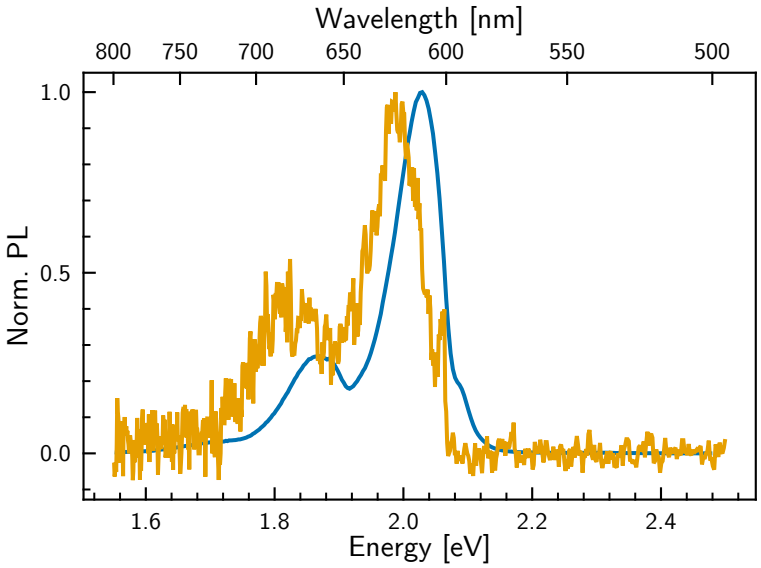

Figure 4.15: Emission spectra of $C_{96}tBu_8$ in solution (blue) and of a single impurity in the polystyrene matrix (yellow).

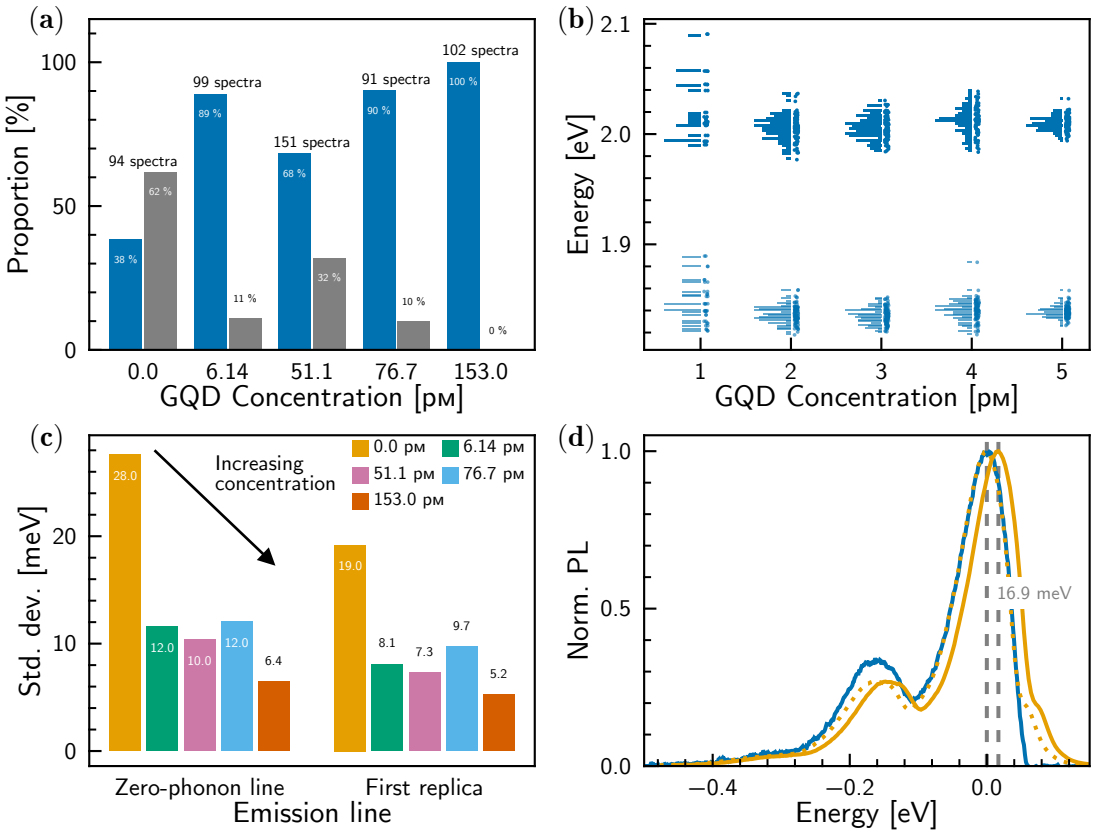

Figure 4.16: (**a**) Proportion of successfully (dark blue) and unsuccessfully (gray) fitted spectra observed in films against the concentration of $C_{96}tBu_8$ in the solution. (**b**) Distribution of position of the zero-phonon line (dark blue) and first vibronic replica (light blue) emission peaks of successfully fitted spectra. (**c**) Evolution of the standard deviation of the peaks' distribution for the concentrations of solution studied. (**d**) Comparison of the PL spectrum from a solution of $C_{96}tBu_8$ (solid yellow line) and the sum of all PL spectra from our most concentrated polystyrene sample, 164 pM (102 spectra, solid blue line). Energies are centered around the zero-phonon line of the averaged spectrum (2.016 eV). The dotted yellow line is the spectrum in solution shifted by 9.4 meV, so zero-phonon line is at 0 eV to compare its line width with that of the averaged spectrum.

ure 4.16a compares the proportion of spectra successfully and unsuccessfully fitted by the model. As expected from the observation of the spectrum of an impurity, a significant proportion of spectra (38 %) can be fitted by the model. We can also see that the proportion of spectra successfully fitted by the procedure tends to increase when the concentration of $C_{96}tBu_8$ in the solution increases. When looking at the distribution of zero-phonon lines and first vibronic replica of the spectra successfully fitted by the model, shown in Figure 4.16b, one can see that the control sample is distinctively set apart from the other samples. Indeed, its distribution is much more widely spread out, almost uniformly between 1.98 eV and 2.1 eV. On the other hand, the distributions of the samples with GQDs are more tightly packed, and resemble more and more to a normal distribution centered on 2 eV as the concentration is increased. We then calculated the standard deviation for each set of zero-phonon line associated with a concentration. Figure 4.16c shows the evolution of the standard deviation of histograms for both emission peaks. The standard deviation decreases as $C_{96}tBu_8$ concentration increases, hinting that all emitters added in the polystyrene matrix, when increasing concentration, have approximately the same emission energy.

From the evolution of the ratio of successfully fitted spectra and the decreasing standard deviations shown in Figure 4.16c, we see that increasing the concentration in the solution before spin-coating mainly increases the concentration of $C_{96}tBu_8$ in the film. Another phrasing of this last affirmation is that fluorescent impurities in our samples do not arise from residual compounds from the synthesis of GQDs. The remaining possible impurities sources are thus substrate degradation, polymer matrix, and impurities from the solvent.

As most of the emitters in the most concentrated sample appear to be $C_{96}tBu_8$, it makes sense to link the emission spectrum of those emitters to the emission spectrum in solution. Figure 4.16d shows the emission spectrum in solution as well as the mean of all 102 emission spectra recorded on our most concentrated sample (164 pM). Both spectra have the same general features and, despite a ~ 10 meV red-shift of the averaged spectrum, the same line widths. We attribute this red shift to solvatochromism. As emission in the solution originates from individualized emitters, and because the distribution of zero-phonon line is very narrow, the similar line widths of the averaged spectrum and the spectrum in solution show that the broadening in the emission spectrum of the solution is mostly homogeneous.

4.2.4 Time-domain characterization of single $C_{96}tBu_8$ in polystyrene matrix

Three-levels model of a GQD

As shown in Subsection 4.2.2, the emission and the lowest absorption energy of single $C_{96}tBu_8$ are strongly polarized. As such, an exhaustive description of the

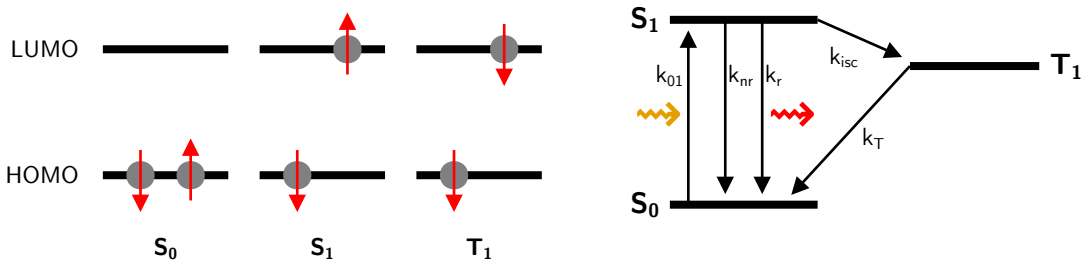

Figure 4.17: (**a**) Model electronic states used in this section. (**b**) Corresponding three-level system for the fluorescence of $C_{96}tBu_8$.

GQD in the framework of the first quantization would be based on the electric dipole Hamiltonian and make use of the density operator [19, 24, 31] which, in the basis of states from Figure 4.17b can be written:

$$\rho = |\psi(t)\rangle \langle\psi(t)| = \begin{bmatrix} \rho_{00} & \rho_{01} & 0 \\ \rho_{10} & \rho_{11} & 0 \\ 0 & 0 & \rho_{TT} \end{bmatrix} \tag{4.2}$$

Where S_0, S_1, and T_1 have been labeled 0, 1, and T respectively. This results in the Bloch system described by Equations 4.3, 4.4, 4.5, and 4.6.

$$\frac{\mathrm{d}}{\mathrm{d}t}\rho_{00} = k_{10}\rho_{11} + k_T\rho_{TT} - i\Omega/2\ \rho_{01} + i\Omega/2\ \rho_{10} \tag{4.3}$$

$$\frac{\mathrm{d}}{\mathrm{d}t}\rho_{11} = -(k_{10} + k_{\mathrm{isc}})\rho_{11} + i\Omega/2\ \rho_{01} - i\Omega/2\ \rho_{10} \tag{4.4}$$

$$\frac{\mathrm{d}}{\mathrm{d}t}\rho_{TT} = k_{\mathrm{isc}}\rho_{11} - k_T\rho_{TT} \tag{4.5}$$

$$\frac{\mathrm{d}}{\mathrm{d}t}\rho_{01} = -i\Omega/2\ \rho_{00} + i\Omega/2\ \rho_{11} + (i\delta_L - \Gamma_2)\rho_{01} \tag{4.6}$$

Where Ω is the Rabi frequency, with $\hbar\Omega = |\vec{\mu}_{01} \cdot \vec{E}|$, $\vec{\mu}_{01}$ is the transition dipole moment, Γ_2 is the rate of de-phasing of the S_0-S_1 coherence, δ_L is the de-tuning between the excitation and the molecule's transition and k_{10}, k_{isc}, and k_T are the rates of incoherent transitions between S_1 and S_0, S_1 and T_1, and T_1 and S_0 respectively. This system can be solved through a Laplace transformation [198]. Under certain conditions, such system can display Rabi oscillations between state S_0 and S_1 at short times. However, in the case of our study, the coherence time between S_0 and S_1 is very small because we work at room temperature in a solid matrix, and because of the vibronic states of the molecule. This makes the $S_0 \rightarrow S_1$ transition irreversible, and allows further simplifications of the modelization to only account for the probabilities of occupancy of each state.

The three-levels system can thus be studied analytically by investigating the probabilities p_0, p_1, and p_T of occupancy of states S_0, S_1, and T_1, as shown in Figure 4.17b. The transition rates give a straightforward differential equation for this system.

$$\frac{\mathrm{d}}{\mathrm{d}t}\begin{bmatrix} p_0 \\ p_1 \\ p_T \end{bmatrix} = \begin{bmatrix} -k_{01} & k_{10} & k_T \\ k_{01} & -k_{10}-k_T & 0 \\ 0 & k_{\mathrm{isc}} & -k_T \end{bmatrix}\begin{bmatrix} p_0 \\ p_1 \\ p_T \end{bmatrix} \tag{4.7}$$

Where $k_{10} = k_{\mathrm{r}} + k_{\mathrm{nr}}$ is the effective transition rate from S_1 to S_0, accounting for both radiative and non-radiative pathways. As we know that the sum of the three probabilities equals one, we can simplify the system and reduce the dimension of the matrix to be 2×2. This yields Equation 4.8.

$$\frac{\mathrm{d}}{\mathrm{d}t}\mathbf{p}(t) = \begin{bmatrix} -(k_{01}+k_T) & (k_{10}-k_T) \\ k_{01} & -(k_{10}+k_{\mathrm{isc}}) \end{bmatrix}\mathbf{p}(t) + \begin{bmatrix} k_T \\ 0 \end{bmatrix} \tag{4.8}$$

where $\mathbf{p}(t) = (p_0(t), p_1(t))^\intercal$. This system is more easily solved through a Laplace transformation, which gives

$$s\mathbf{p}(s) - \mathbf{p}(0) = \begin{bmatrix} -(k_{01}+k_T) & (k_{10}-k_T) \\ k_{01} & -(k_{10}+k_{\mathrm{isc}}) \end{bmatrix}\mathbf{p}(s) + \frac{1}{s}\begin{bmatrix} k_T \\ 0 \end{bmatrix} \tag{4.9}$$

$$\mathbf{p}(s) = \begin{bmatrix} s+(k_{01}+k_T) & (k_T-k_{10}) \\ -k_{01} & s+(k_{10}+k_{\mathrm{isc}}) \end{bmatrix}^{-1}\begin{bmatrix} k_T/s+1 \\ 0 \end{bmatrix} \tag{4.10}$$

where s is the complex Laplace variable, and it is assumed that the system is initially prepared in state S_0, which is the case when a photon has just been emitted. The vector on the right-hand side of Equation 4.10 can then be rewritten as

$$\mathbf{p}(s) = \frac{k_T+s}{s(s-\lambda_+)(s-\lambda_-)}\begin{bmatrix} k_{10}+k_{\mathrm{isc}}+s \\ k_{01} \end{bmatrix} \tag{4.11}$$

where the following intermediary variables have been introduced:

$$\lambda_\pm = \frac{1}{2}(-b \pm \sqrt{\Delta}) \tag{4.12}$$

$$\Delta = b^2 - 4c \tag{4.13}$$

$$= ((k_{01}+k_T) - (k_{10}+k_{\mathrm{isc}}))^2 + 4k_{01}(k_{10}-k_T) \tag{4.14}$$

$$b = k_{01} + k_{10} + k_{\mathrm{isc}} + k_T \tag{4.15}$$

$$c = k_{01}(k_T + k_{\mathrm{isc}}) + k_T(k_{10}+k_{\mathrm{isc}}) \tag{4.16}$$

Then, partial fraction decomposition yields

$$\mathbf{p}(s) = \underbrace{\begin{bmatrix} \frac{k_T(k_{10}+k_{\mathrm{isc}})}{\lambda_+\lambda_-} & \frac{(k_T+\lambda_+)(k_{10}+k_{\mathrm{isc}}+\lambda_+)}{\lambda_+(\lambda_+-\lambda_-)} & \frac{(k_T+\lambda_-)(k_{10}+k_{\mathrm{isc}}+\lambda_-)}{\lambda_-(\lambda_--\lambda_+)} \\ \frac{k_{01}k_T}{\lambda_+\lambda_-} & \frac{k_{01}(k_T+\lambda_+)}{\lambda_+(\lambda_+-\lambda_-)} & \frac{k_{01}(k_T+\lambda_-)}{\lambda_-(\lambda_--\lambda_+)} \end{bmatrix}}_{=\mathbf{A}}\begin{bmatrix} \frac{1}{s} \\ \frac{1}{s-\lambda_+} \\ \frac{1}{s-\lambda_-} \end{bmatrix} \tag{4.17}$$

Finally, well-known Laplace transforms allow converting the expression in Equation 4.17 back to temporal space, which reads

$$\mathbf{p}(t) = \mathbf{A} \begin{bmatrix} 1 \\ e^{\lambda_+ t} \\ e^{\lambda_- t} \end{bmatrix} \tag{4.18}$$

The expression for $p_T(t)$ can be retrieved using $p_T(t) = 1 - (p_0(t) + p_1(t))$.

It is interesting here to highlight the behavior of the system as a function of excitation power. Typical solutions for the probabilities of occupancy are shown in Figure 4.18a on the next page for varying excitation power, *i.e.* varying k_{01} coefficients. In these plots we assume $k_{\text{isc}} = k_T = k_{10}/1000$, which is consistent for our system, where the inter-system crossing rate and the triplet de-excitation rate are expected to be low compared to the de-excitation rate of S_1 [13]. Three situations arise from this picture, characterized by two transitions. First, for $t \leq \frac{1}{|\lambda_-|}$ state S_1 starts getting populated. Then, for $\frac{1}{|\lambda_-|} \leq t \leq \frac{1}{|\lambda_+|}$, state S_1 reaches a steady state, during which state T_1 is not yet stabilized. Finally, after $t = \frac{1}{|\lambda_+|}$, the three levels have reached their steady states where $p_1 = p_T$, because we chose $k_{\text{isc}} = k_T$. Similarly, when the pumping rate k_{01} is below k_{10}, the characteristic de-excitation time of level S_1, the steady-state value of p_1 for long times is below that of p_0. As k_{01} gets above k_{10}, so does p_1 compared to p_0.

From the expression of p_1, it is possible to get an analytical expression of the second-order correlation function, $g^{(2)}(\tau)$. This is of peculiar interest since $g^{(2)}(\tau)$ is directly measurable, as shown in Chapter 2 (Experimental Methods). This correlation is defined classically as

$$g^{(2)}(\tau) = \frac{\langle I(t)I(t+\tau)\rangle}{\langle I(t)\rangle^2} \tag{4.19}$$

where $\langle\cdot\rangle$ denotes the ensemble average. We can set $t = 0$ because the process is ergodic. From a photon-counting experiment point-of view, this is similar to correlating the photon-rates on the detector. In particular, the detected photon rate is $\eta k_r p_1(\tau)$, where η is the detection efficiency of our setup. To obtain the expression for $g^{(2)}(\tau)$, one needs to normalize this by the steady-state emission rate. Combining this with Equation 4.18 yields

$$g^{(2)}(\tau) = 1 + \frac{\mathbf{A}_{22}}{\mathbf{A}_{21}} e^{\lambda_+ t} + \frac{\mathbf{A}_{23}}{\mathbf{A}_{21}} e^{\lambda_- t} \tag{4.20}$$

$$= 1 - \left(1 - \frac{\mathbf{A}_{22}}{\mathbf{A}_{21}}\right) e^{\lambda_- t} + \frac{\mathbf{A}_{22}}{\mathbf{A}_{21}} e^{\lambda_+ t} \tag{4.21}$$

where $\mathbf{A}_{ij}$ denotes the element at position ij in matrix $\mathbf{A}$ in Equation 4.18. Conveniently, this means the $g^{(2)}(\tau)$ measurement is independent from the detection

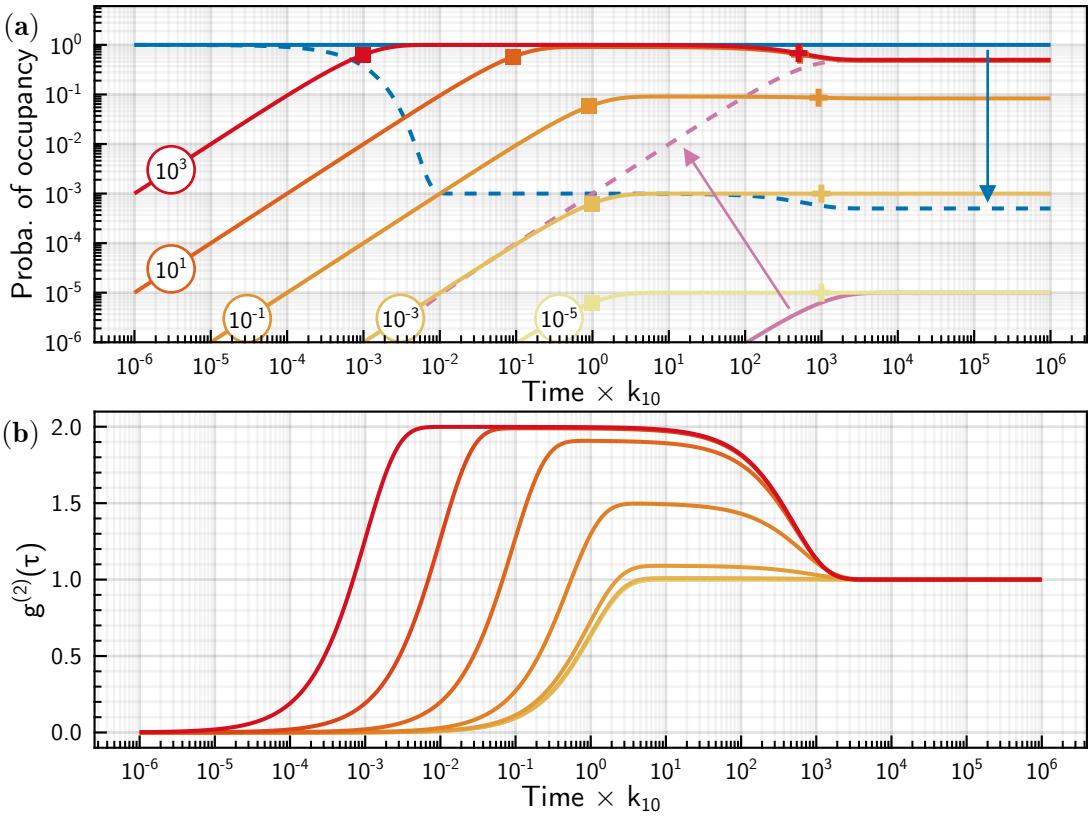

Figure 4.18: (**a**) Probability of occupation of each state after time delay τ, for various excitation intensities corresponding to increasing values of k_{01} from $10^{-5}k_{10}$ to $10^{3}k_{10}$. The probability of occupancy of S_1 is plotted from yellow to red. The probabilities of occupancy of S_0 and T_1 are plotted in blue and purple respectively. For those two states, only the lowest and highest pump rates in solid and dashed lines. The squares mark the position of $1/|\lambda_-|$ and the crosses of $1/|\lambda_+|$, the two characteristic times of the system. The other rates were fixed at $k_{\text{isc}} = k_T = k_{10}/1000$. (**b**) Corresponding $g^{(2)}(\tau)$ plots.

efficiency of the setup. The theoretical $g^{(2)}(\tau)$ measurements calculated using Equation 4.21 are shown in Figure 4.18b, for an increasing pumping rate. It can be seen that the bunching behavior ($g^{(2)}(\tau) > 1$) before reaching the steady state is more and more visible as the pump power is increased. In the following paragraphs, I will show how the variations of the $g^{(2)}(\tau)$ curve can be used quantitatively to access some characteristic relaxation rates of the system.

The expressions in matrix $\mathbf{A}$ are rather impractical, and can be simplified in the case of our system. In particular, due to the low spin-orbit coupling, the rate of inter-system crossing is low, which can be translated in terms of transition rates:

$$k_{01}, k_{10} \gg k_{\text{isc}}, k_T \tag{4.22}$$

Developing $\lambda_\pm$ to the smallest non-zero order then yields

$$\lambda_- \approx -(k_{01} + k_{10}) \tag{4.23}$$

$$\lambda_+ \approx -\left(k_T + \frac{k_{01}k_{\text{isc}}}{k_{01} + k_{10}}\right) \tag{4.24}$$

Then, $\mathbf{A}_{22}/\mathbf{A}_{21}$ can be simplified to the smallest non-zero order.

$$\frac{\mathbf{A}_{22}}{\mathbf{A}_{21}} \approx \frac{k_{01}k_{\text{isc}}}{k_T(k_{01} + k_{10})} \tag{4.25}$$

Equation 4.23 is of peculiar interest in the determination of k_{10}. Indeed, as k_{01} linearly depends on the excitation intensity, Equation 4.23 reads

$$-\lambda_- = k_{10} + \frac{\sigma(E_{ex})}{E_{ex}} I_{ex} \tag{4.26}$$

where E_{ex} is the energy of excitation, $\sigma(E_{ex})$ is the absorption cross-section at E_{ex}, and I_{ex} is the intensity of the pump. As shown in Figure 4.18a and Figure 4.18b, the dynamics at short time-scales (up until $1/|\lambda_-|$) is dominated by the process of populating level S_1. This means it is possible to estimate k_{10} and $\sigma(E_{ex})$ from Equation 4.26 by recording $g^{(2)}(\tau)$ measurements at short time-scales as a function of the pump intensity. Conversely, measuring $g^{(2)}(\tau)$ for longer timescales allows estimating λ_+. In particular, Equation 4.24 can be rewritten

$$-\lambda_+ = k_T \left(1 + \frac{\mathbf{A}_{22}}{\mathbf{A}_{21}}\right) \tag{4.27}$$

$$= k_T + k_{\text{isc}} \frac{1}{1 + k_{10}/k_{01}} \tag{4.28}$$

Another important tool at our disposal for the study of the time-dependent behavior of single-photon emitter is the waiting time distribution [213–216]. This

is the time one has to wait before a photon is detected when a photon has just been detected. This can be expressed from the expression of $p_1(t)$ [217]. Suppose a photon has just been detected, let $J(\tau)$ be the probability of detecting a photon after time τ, $K(\tau)$ the waiting time distribution, and $L_n(\tau)$ the probability of detecting the n^{th} photon at time τ. $J(\tau)$ is proportional to the second-order correlation function $g^{(2)}(\tau)$. We know that

$$J(\tau) = L_1(\tau) + L_2(\tau) + ... \tag{4.29}$$

i.e. the probability of detecting a photon after time τ is the probability of detecting any photon after time τ. It is also possible to relate the probability of detecting photon number $n+1$ to the probability of detecting photon number n.

$$L_{n+1}(\tau) = \int_0^\tau K(\tau - t) L_n(t)\, \mathrm{d}t \tag{4.30}$$

Which states that the probability of detecting the next photon is the probability of detecting the current photon and that a new photon is detected. This can be inputted in Equation 4.29.

$$J(\tau) = \underbrace{L_1(\tau)}_{K(\tau)} + \int_0^\tau K(\tau - t) L_1(t)\, \mathrm{d}t + \int_0^\tau K(\tau - t) L_2(t)\, \mathrm{d}t + ... \tag{4.31}$$

Which, after a Laplace transform, reads

$$J(s) = K(s) + K(s)J(s) \tag{4.32}$$

$$K(s) = \frac{J(s)}{1 + J(s)} \tag{4.33}$$

For example, a Poissonian source outputs a constant photon rate, which reads $J(\tau) = \eta\alpha$ with η the detection efficiency of the setup and α a constant rate. Equation 4.33 reads $K(s) = \eta\alpha/(s + \eta\alpha)$, which yields $K(\tau) = \eta\alpha e^{\eta\alpha\tau}$. We thus retrieve the classical result that the waiting time distribution of a Poissonian source is a decaying exponential. We now come back to the three-levels model of a GQD. At long delay time, the short-time anti-bunching characterized by rate λ_- in Equation 4.18 has vanished, and $p_1(t)$ corresponds to an exponential approach, *i.e.*

$$p_1(\tau) = \mathbf{A}_{21} + \mathbf{A}_{22} e^{\lambda_+ \tau} \tag{4.34}$$

With $J(\tau) = \eta k_r p_1(\tau)$, we now have

$$K(\tau) = A e^{k_a \tau} + B e^{k_b \tau} \tag{4.35}$$

where

$$A/B = -\frac{(\mathbf{A}_{21}+\mathbf{A}_{22})k_a - \mathbf{A}_{21}\lambda_+}{(\mathbf{A}_{21}+\mathbf{A}_{22})k_b - \mathbf{A}_{21}\lambda_+} \tag{4.36}$$

$$k_{a,b} = \frac{-(\eta k_r(\mathbf{A}_{21}+\mathbf{A}_{22}) - \lambda_+) \pm \sqrt{(\eta k_r(\mathbf{A}_{21}+\mathbf{A}_{22}) - \lambda_+)^2 + 4\lambda_+\eta k_r \mathbf{A}_{21}}}{2} \tag{4.37}$$

The expressions for k_a and k_b depend on the efficiency of the setup, which is difficult to determine reliably. However, the ratio of the amplitude of each exponential can easily be rewritten by factoring-out $\mathbf{A}_{21}$ and using Equation 4.27,

$$A/B = -\frac{k_a + k_T}{k_b + k_T} \tag{4.38}$$

$$k_T = -\frac{Ak_b + Bk_a}{A+B} \tag{4.39}$$

which yields a convenient procedure for the determination of the triplet lifetime[1]. We know from Figure 4.18b that when the excitation intensity is increased, the bunching behavior is more visible in the $g^{(2)}(\tau)$ curve. Thus, the waiting-time distribution should be bi-exponential at long time-scales. Fitting the model in Equation 4.35 to the distribution then yields k_T through Equation 4.39.

Short timescales characterization of $C_{96}tBu_8$

At short timescales, $g^{(2)}(\tau)$ measurements are usually performed using two avalanche photo-diodes on a Hanbury Brown Twiss (HBT) interferometer in a start-stop configuration. This means the histogram that is actually measured is the one originating from the waiting time distribution. However, at short timescales Equation 4.33 shows that $K(\tau)$ and $J(\tau)$ are equivalent[2]. See Chapter 2 (Experimental Methods) for further explanations on technical aspects of the method.

A typical $g^{(2)}(\tau)$ curve is shown in Figure 4.19a on the following page. There is a clear antibunching at short times that indicates emission from a single molecule. The model in Equation 4.21 has been fitted on the data and was used to normalize the curve. The value of $|\lambda_+|$ is not reliable here, because of the limitations of the start-stop method at long timescales. $|\lambda_-|$ however is well interpretable using Equation 4.23. Since the curve in Figure 4.19a was taken for low excitation intensity, we can approximate $|\lambda_-|$ to k_{10}, that is, the de-excitation rate from S_1 to S_0. The estimated value for k_{10} is $0.210 \pm 0.034\,\mathrm{ns}^{-1}$, which corresponds to a

[1] The minus sign in front of Equation 4.39 is not an issue, as k_a and k_b are taken negative is their definition.

[2] One can convince themselves by looking at the expression of $K(\tau)$ for well-known distributions $J(\tau)$. For example, if $J(\tau)$ is a delayed Dirac, $J(\tau) = \delta(t - t_0)$, then $K(\tau)$ is a Dirac comb delayed by t_0. So for timescales shorter or equal to t_0, $J(\tau) \sim K(\tau)$.

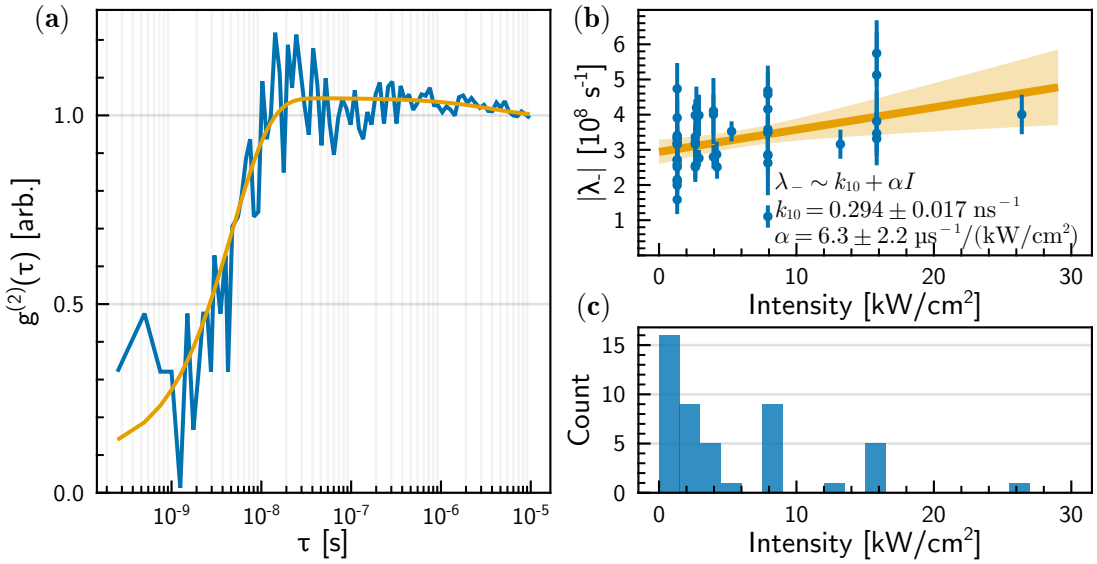

Figure 4.19: (**a**) Example $g^{(2)}(\tau)$ curve (blue) fitted using a three-levels model (yellow). The excitation energy was 2.64 eV. (**b**) $|\lambda_-|$ fitted on 47 $g^{(2)}(\tau)$ curves obtained for various GQDs at various intensities of excitation (black crosses). The dependence of $|\lambda_-|$ on intensity was fitted by a linear model (yellow line). The interval of confidence of the fit is given by the light yellow area. (**c**) Histogram of number of measurements against intensity in (**b**).

lifetime of 4.75 ± 0.77 ns. For comparison, the lifetime measured in solution was 2.8231 ± 0.0096 ns, which corresponds to a radiative lifetime of ~ 2.65 ns given the photoluminescence quantum yield of 94 %[3]. The measured photoluminescence lifetime in the polystyrene matrix is thus noticeably higher than the lifetime in solution.

To confirm that first impression, we conducted a statistical study and recorded 47 $g^{(2)}(\tau)$ traces on various GQDs for various excitation intensities and fitted the model of Equation 4.21 on the data. The fitted values of $|\lambda_-|$ are reported as a function of the excitation intensity in Figure 4.19b. Equation 4.23 shows that we should expect a linear relation between the intensity and $|\lambda_-|$. The intercept gives $k_{10} = 0.294 \pm 0.017\,\mathrm{ns}^{-1}$, or $\tau_{10} = 3.4 \pm 0.2$ ns, which is again higher than the lifetime measured in solution, and would hint towards a reduced photoluminescence quantum yield in the polystyrene matrix. The slope of the linear fit gives access to a rough estimate of the absorption cross-section through Equation 4.26, and yields $\sigma(2.087\,\mathrm{eV}) = 21.2 \pm 7.4\,\mathrm{Å}^2$, which is slightly lower than the cross-section reported for triangle-shaped GQDs with 96 sp^2 carbon atoms, where the absorption cross-section was estimated to $\sim 100\,\mathrm{Å}^2$ [13]. The absorption cross-section can be compared to the molar extinction coefficient measured in solution reported in Table 4.1. Scaling the molar absorption coefficient using the absorption spectrum to account for the difference in excitation energy yields an absorption cross-section cross-section in solution of $11\,\mathrm{Å}^2$, which is the same order of magnitude as the one estimated in the polystyrene matrix.

The short lifetime of the excited state of our GQD makes it promising for telecommunication applications, where the fluorescence lifetime limits the transmission rate. The literature often compares the absorption of carbonated emitters in terms of absorption cross-section per carbon atoms. In the case of $C_{96}tBu_8$ this is approximately $0.22\,\mathrm{Å}^2$/C. This value is similar to the reported value for triangular 96 sp^2 GQDs [13] ($1\,\mathrm{Å}^2$/C), single terrylene diimide [218] ($0.6\,\mathrm{Å}^2$/C), or $(6, 5)$ single wall carbon nanotubes [219] ($0.4\,\mathrm{Å}^2$/C). In that aspect, the absorption of $C_{96}tBu_8$ seems well in line with the absorption of other carbonated emitters.

Long timescales characterization of $C_{96}tBu_8$

To overcome the limitations of the start-stop method and access the photon statistics at long timescales, one can resort to time-tagging methods. In brief, the experimental setup remains the same, with two avalanche photodiodes in a HBT configuration, but instead of histogramming the time delay between the detection of a photon on each diode, the hardware records the time of arrival on each detector independently. We are thus provided with a list of photon arrival times. Those

[3]The photoluminescence quantum yield ϕ is related to the radiative and non-radiative decay rates as $\phi = \frac{k_r}{k_r + k_{nr}}$ when the decay is mono-exponential.

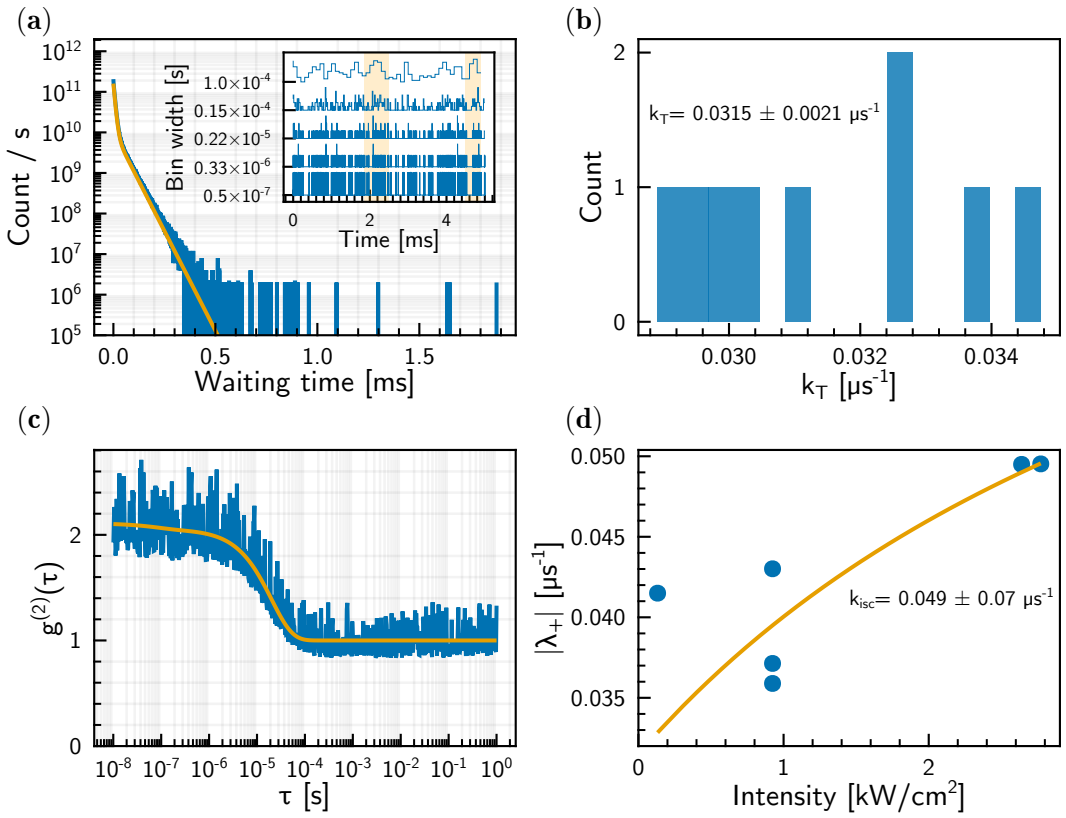

Figure 4.20: (**a**) Waiting time distribution showing a clear bi-exponential behavior, fitted in yellow. The inset shows a selected time trace with coarsening bin width to illustrate the bunching of photons. (**b**) Distribution of k_T estimated from waiting time distributions through Equation 4.39. (**c**) $g^{(2)}(\tau)$ calculated from the same time-tagged measurement as (**a**). The theoretical model from Equation 4.21 is fitted in yellow. (**d**) Evolution of $|\lambda_+|$ as a function of excitation intensity, with $|\lambda_+|$ estimated from $g^{(2)}(\tau)$ measurements. The result of fitting the model of Equation 4.27 to the data with the saturation intensity and k_{isc} as free parameters (k_T is taken from (**b**)) is shown in yellow.

arrival times can be interpreted either directly, by calculating the inter-photon arrival times and estimating the waiting-time distribution, or by calculating the second order correlation using the algorithm described in Subsection 2.2.3. Here, I use the waiting time distribution to estimate k_T through Equation 4.39, as it is much easier to get a waiting time histogram with a good signal-to-noise ratio (a few seconds of exposures is often enough), allowing the use of most of the measurements performed. $g^{(2)}(\tau)$ calculations on the other hand are more demanding, and it is thus more difficult to get a satisfactory signal-to-noise ratio. They will be used to estimate k_{isc}.

A typical photon waiting-time distribution is shown in Figure 4.20a[4]. The bi-exponential distribution due to photon-bunching is clearly visible. The inset shows a binning of the photon arrival time with coarsening bin widths, illustrating the phenomenon of bunching: for coarser bin widths (1×10^{-4} s), there are local maxima ~ 1 ms broad corresponding to bunches of photons at finer bin widths. k_T can then be estimated from the bi-exponential fit using Equation 4.39. Some waiting-time distributions, especially at low excitation intensity, are quasi-mono-exponential. Using them would lead to errors in the estimate of k_T, so we chose to remove the distributions where one of the two fractional contributions was lower than 5 %. This yields Figure 4.20b, which shows a histogram of the estimates of the triplet de-excitation rate, k_T. The estimates are rather narrowly distributed, despite the small number of measurements, and give $k_T = 0.0315 \pm 0.0021\,\mu\text{s}^{-1}$, which is well in accordance with the value of $0.053 \pm 0.001\,\mu\text{s}^{-1}$ previously reported for triangular GQDs with 96 sp^2 carbons [13].

If the time-tagged measurement can be run long enough without the emitter bleaching, one can calculate the second-order correlation histogram and fit Equation 4.21 to long timescale $g^{(2)}(\tau)$, as shown in Figure 4.20c. A clear photon bunching is measured at delay times comprised between 1×10^{-8} s and 1×10^{-5} s, which matches the bi-exponential waiting-time distribution obtained from the same time-tagged measurement in Figure 4.20a. Repeating the experiment on several emitters and plotting the parameter $|\lambda_+|$ as a function of excitation intensity yields Figure 4.20d. Despite the small amount of data points, one can fit Equation 4.27 to the data, with parameter k_T fixed to the value estimated using the waiting time distributions and get a rough estimate for the inter-system crossing rate, $k_{\text{isc}} \approx 0.049\,\mu\text{s}^{-1}$, which is again compatible with the rate of $0.025 \pm 0.005\,\mu\text{s}^{-1}$ previously reported on triangular GQDs [13].

The inter-system crossing rate and the triplet lifetime are of prime importance for single molecule experiments and applications. As will be discussed later in Section 5.2, photo-bleaching most likely occur from the triplet state on glass substrates. It is also from the triplet state that the molecule is more likely to react

[4]Note that the time scales considered here are way longer than the dead-time of a single APD (typically ~ 50 ns), which is the limiting factor for detection. Thus, we do not need to concern ourselves with things like instrument response functions here.

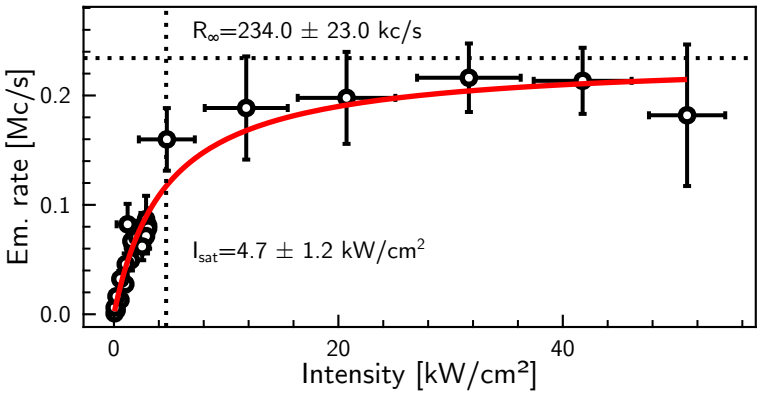

Figure 4.21: Saturation curve of a single $C_{96}tBu_8$ (black circles). The curve is fitted to the model in equation 4.41, yielding a saturation intensity of $4.7 \pm 1.2\,\mathrm{kW/cm^2}$ and an asymptotic rate of $234 \pm 23\,\mathrm{kc/s}$.

with ambient oxygen, as the ground state of O_2 is a triplet state [220] that is more likely to react with the excited triplet state of the GQD. Well-known polycyclic aromatic hydrocarbons such as terrylene in molecular crystals [221] exhibit much longer triplet lifetime, 0.4 ms, compared to the lifetime we measure on our GQD, 30 µs. The probability of entering the triplet state is also small, as shown by the ratio of $k_{10}/k_{\mathrm{isc}} \approx 6000$, which means that on average $C_{96}tBu_8$ enters the triplet state once every 6000 cycles, which explains the good stability measurements that was discussed in the steady-state analysis. This value is particularly high compared to others poly-cyclic aromatic hydrocarbons at room temperature such as pentacene (~ 20) [198, 222], terrylene (~ 200) [96], or dibenzo[hi,st]ovalene functionalized aryl (~ 700) [223], which highlights the suitability of our molecule for single-molecule experiments.

Saturation measurements: quantum yield in the polystyrene matrix

The high stability of single $C_{96}tBu_8$ allows for intensity saturation measurements. Figure 4.21 shows the emission rate of a single $C_{96}tBu_8$ for various excitation intensities. We can see that the measured count rate reaches a saturation of $\sim 200\,\mathrm{kc/s}$. The measured photon rate can be retrieved for a three-levels system such as the one used to model the GQD [224]. The count rate on the detector reads $R = \eta_{\mathrm{det}} k_r p_1(\infty)$, where η_{det} is the detection efficiency of the setup, k_r the radiative de-excitation rate of S_1, and $p_1(\infty)$ is the asymptotic probability of occupancy of S_1. Expanding the definition of R with the expression of $p_1(\infty)$, and using the

simplified expressions of λ_+ and λ_- yields:

$$R = \eta_{\text{det}} \frac{k_r}{1 + \frac{k_{10}}{k_{01}} + \frac{k_{\text{isc}}}{k_T}} \tag{4.40}$$

$$= R_\infty \frac{1}{1 + I_{\text{sat}}/I} \tag{4.41}$$

where $I = k_{01} \frac{E_{ex}}{\sigma(E_{ex})}$ is the intensity of excitation, $I_{\text{sat}} = \frac{E_{ex}}{\sigma(E_{ex})} \frac{k_{10} k_T}{k_T + k_{\text{isc}}}$ is the saturation intensity, and $R_\infty = \eta_{\text{det}} k_r \frac{k_T}{k_T + k_{\text{isc}}}$ is the saturated count rate. Inputing the previously estimated parameters of the system yields $I_{\text{sat}} \approx 18.2\,\text{kW/cm}^2$, but the big uncertainty on k_{isc} gives a relative uncertainty of almost 100 % on that estimation. Fitting this model to the data in Figure 4.21 yields a saturated emission rate R_∞ of 234 ± 23 kc/s and a saturation intensity I_{sat} of 4.7 ± 1.2 kW/cm^2, which is consistant with the rough estimate of I_{sat} given previously. We can interpret the saturated emission rate by linking it to the quantum yield of the system. By definition, the quantum yield ϕ reads

$$\phi = \frac{\text{Number of photons emitted}}{\text{Number of photon absorbed}} \tag{4.42}$$

which can be re-written, considering that relaxation mainly occurs from S_1 to S_0 since the inter-system crossing rate is much smaller than the rate of de-excitation,

$$\phi = \frac{k_r}{k_r + k_{nr}} \tag{4.43}$$

or $k_r = \phi k_{10}$. We can then re-write the saturated emission rate

$$R_\infty = \eta_{\text{det}} \phi k_{10} \frac{k_T}{k_T + k_{\text{isc}}} \tag{4.44}$$

As all the other parameters have been determined in the previous subsections, we can thus estimate $\eta_{\text{det}}\phi \approx 0.002 \pm 0.0018$. η_{det} can reasonnably be estimated to 5 %. This means the estimated quantum yield in the polystyrene matrix is 4 %, which is surprisingly low compared to the quantum yield in solution (94 %), the quantum yield of the triangular GQDs (35 %) [13], or the quantum yield reported for other polycyclic aromatic hydrocarbons [200, 225]. This may be due to an overestimated collection efficiency of the setup, which could be controlled using well-known single emitters such as nano-diamonds with a single nitrogen-vacancy, where the radiative rate should be ~ 5 MHz with a saturation intensity of about 70 kW/cm^2. If the reason for the low measured quantum yield is not the setup, then we should investigate the causes of non-radiative decays. For example, studying the GQD at cryogenic temperatures may reduce decay resulting from the coupling to phonons in the polymer matrix and the GQD may display a higher quantum yield as a result.

Conclusion

The synthesis method developed by our collaborators yields highly pure samples, as shown by the mass-spectrometry and single-molecule studies. It gives access to a whole family of GQDs with a tunable zero-phonon line.

Optical studies in solution revealed the brightness of the GQDs thanks to their near-unity quantum yield. This is most likely due to their good individualization in the solution thanks to the bulky *tert*-butyl groups. DFT and TDDFT theoretical models of the GQDs match remarkably well the experimental measurements. It is also possible to explain the individualization of the largest GQDs in solution thanks to theoretical simulation showing that the conformers involved in the formation of dimers are not stable in solution. The work on the family of rod-shaped GQDs and their synthesis was published in August 2023 [205].

Single-molecule studies of $C_{96}tBu_8$ have shown that single-molecule in a polystyrene matrix are straightforwardly obtained. We showed that the steady-state optical properties of single GQDs in the polystyrene matrix remain similar to the ones in the solution, and highlighted the high purity of the samples. This work has been published in October 2023 [226]. Transient analysis of the emission allowed the characterization of the emitter, which we identify to a three-level system. The estimates of the transition rates match well the rates reported in the literature for similar systems. The photoluminescence quantum yield in the polystyrene matrix estimated from the saturated emission rate, however, is surprisingly low[5]. This may be due to a poor calibration of our setup.

Despite this uncertainty on the quantum yield in the polystyrene matrix, $C_{96}tBu_8$ appears to be a good candidate for deepened single-molecule studies. In particular, it may be particularly interesting to study this molecule in various environments. In the following chapter, I will present a study of $C_{96}tBu_8$ on a perovskite crystal. At the time of writing this chapter, our group is also trying to embed another GQD, $C_{114}tBu_{10}$, in molecular crystals based on the dendrimer used to synthesize $C_{78}tBu_6$. Other groups have also started trying to embed $C_{96}tBu_8$ in antracene crystals. Overall, these studies in molecular crystals may open new areas of studies of the GQDs, such as the study of Stark effects due to the induction of local fields in the crystal.

Other studies of the GQDs in solution using femto-second transient analysis are also being carried on in our group. Eventually, this should lead to a deeper

[5] After the writing of this manuscript, and before the defense, we could run some time-resolved photoluminescence measurements on 15 single GQDs. We found a perfectly mono-exponential decay, with a lifetime of $\tau = 2.40 \pm 0.33\,\mathrm{ns}$. Assuming the polystyrene matrix only adds non-radiative decay paths, and because polystyrene has approximately the same refractive index as the TCB used to measure the quantum yield in solution, we can estimate the radiative decay rate as $k_\mathrm{R} = \phi_\mathrm{solution} \times \tau_\mathrm{solution} \approx 0.33\,\mathrm{ns}^{-1}$. This then allows to estimate a quantum yield in polystyrene of $\phi_\mathrm{PS} = k_\mathrm{R} \times \tau = 80 \pm 10\,\%$. The hypothesis of a low transmission of our setup is thus priviledged to explain the low count rates measured in saturation experiments.

understanding of the electronic dynamics of the GQDs. In particular, early results suggest the characteristic time of the $S_2 \rightarrow S_1$ transition is of the order of 100 fs.

5 $C_{96}tBu_8$ on $MAPbBr_3$ Substrate

Contents

Introduction

The photophysics of single $C_{96}tBu_8$ has been well characterized in Chapter 4. In particular, we have shown that their high photoluminescence quantum yield in solution and the high purity of our samples makes them particularly suitable for single-molecule experiments. At the single-molecule level, $C_{96}tBu_8$ exhibits a stable, strongly polarized emission with spectra similar to the ones measured in the solution. As shown in Chapter 3, halide perovskites present interesting optical properties along with ease of synthesis at room temperature using soft chemistry procedures. Building upon the attractive photo-physical properties of these GQDs, we decided to investigate the possibilities of coupling $C_{96}tBu_8$ to active surfaces, such as $MAPbBr_3$ crystals. In particular, 3D perovskites are interesting because their surface is expected to be free from ligands, allowing to bring the GQDs as close as possible to the crystal. Investigating properties arising from coupled systems is enticing, as it could hint at new clues beneficial to the study of both lead-halide perovskites and nano-graphenes, especially effects originating from the interface.

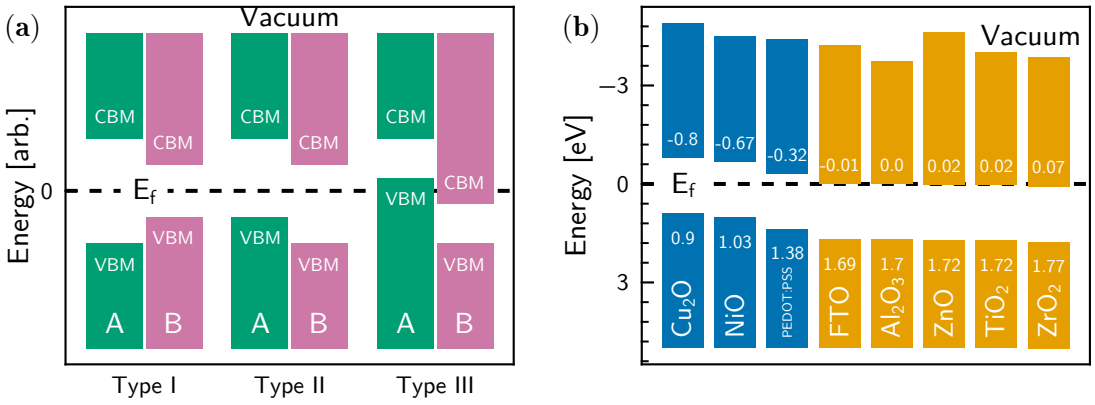

Figure 5.1: (**a**) Band alignments of two materials A and B for the three types of heterostructures. (**b**) Band offset of $MAPbI_3$ films on various substrates. Valence band maxima are derived from linear fits on band onset, and vacuum levels are determined from XPS. Conduction band minima are derived from the calculated band gap of 1.7 eV. *p*-doped substrates are pictured in blue, *n*-doped substrates in yellow. Adapted from Ref. [227].

First, band alignment is a key factor in the determination of the physics at the interface of a heterostructure. Figure 5.1a shows three band alignments corresponding to three types of heterostructures. Among them, types I and II are of peculiar interest. A type I band alignment in a heterostructure typically results in charge or energy transfers from the highest bandgap medium towards the lowest bandgap one [228]. Type II heterostructures, on the other hand, can result in original spectroscopic properties such as the existence of interlayer excitons, which are bound electron-hole pairs where each charge lives in a separate layer. Typical evidence of the existence of an interlayer exciton includes the appearance of a broad low-energy photoluminescence peak, modification of the photoluminescence decay time, and a photoluminescence excitation spectrum which features the absorption of the exciton of both bare materials. The interlayer exciton physics is thus highly dependent on band alignment and on materials forming the heterostructure [229]. This gives rise to a whole range of studies demonstrating interlayer excitons from heterostructures formed by various materials, such as transition metal dichalcogenide (TMD) on TMD [230, 231], or 2D-perovskite on TMD [232, 233].

Predicting the exact band alignment for our system is not trivial. First, crystals are usually described in the Fourier domain and present bands of allowed energy states for the electrons. In contrast, molecules are best described using configuration diagram coordinates, *i.e.* in real space, and present discrete energy levels. Textbook predictions of the behavior of an interface between two semiconductors would require a comparison of band alignments against vacuum level. Some works

use a hybrid approach to compare molecular energy levels to band alignment in the semiconductor [71] but even then singlet-singlet energy transfer should be handled with care, as excitons in halide perovskite experiment strong spin-orbit coupling due to Pb orbitals [43] and thus do not present a pure-spin character. Even assuming that discrete, real-space, molecular levels and wave vector spaces energy configurations can theoretically be compared, the comparison of the experimental position of the conduction band minimum (CBM) and valence band maximum (VBM) to the lowest unoccupied and highest occupied molecular orbitals (LUMO and HOMO) is challenging. The position of the VBM in perovskites is usually determined by examining photoemission processes, and the position of the CBM inferred either through theoretical calculations or spectroscopic measurement of the bandgap energy [234]. In contrast, positions of the highest occupied and lowest unoccupied molecular orbitals are determined for molecules using cyclic voltammetry. Thus, comparing the experimental values of band positions for both materials is perilous. Moreover, perovskite films' gaps are known to be sensitive to the nature of their substrates. Figure 5.1b shows the positions of valence band maxima, conduction band minima, and ionization potentials of $MAPbI_3$ films for various substrates. The position of the CBM and VBM is seen to vary by up to 50 % of the gap's value depending on the substrate, and the variability of the position of the bands is greater for p-doped substrates. Thus, knowing the bulk energy-level alignment may not be enough to determine the band alignment of the heterostructure reliably.

In this context, a trial-and-error-based approach with an actual realization of the heterostructure and characterization of its properties appears to be suitable. Due to its stable and bright photoluminescence, and because its geometrical features make it possible to bring it close to a surface, $C_{96}tBu_8$ is a good candidate to such realizations. For the same reasons, choosing a monocrystaline 3D perovskite means we have an easy way to synthesize crystalline semiconductor compound that is free from surface ligands and thus should allow atomic proximity between the GQD and the crystal.

Second, halide perovskites are also an attractive substrate to play with graphene quantum dots properties. Indeed, thanks to their excellent electronic properties [235], they could be a good candidate to electrically pump single nano-graphenes in the context of single-photon emitters devices. Moreover, graphene is an excellent conductor for spin [236], notably thanks to a very low spin-orbit coupling [237, 238]. Halide perovskites, on the other hand, possess strong spin-orbit coupling due to Pb orbitals [43]. Perovskites could thus be used locally in graphene spin circuits to alter spin-orbit interactions, effectively building graphene spin valves [239]. Graphene quantum dots inherit many properties of graphene, low spin-orbit coupling being one of them. They are also members of the family of polycyclic aromatic hydrocarbons. Molecules in this family are known to possess a triplet state T_1 lying between the ground state S_0 and the first

singlet state S_1 [240, 241]. Transfers from S_1 to T_1 and from T_1 to S_0 require a spin flip, and are thus highly unlikely, making T_1 a meta-stable state. As a result, when the molecule enters this meta-stable state, it remains in that state for an extended period, typically up to tens of micro-seconds or more. Because the triplet state is not coupled to light, the molecule appears dark during the time it remains in that state. This behavior is named *blinking*. For our GQDs, we anticipated that a transfer of spin-orbit coupling from the substrate would result in T_1 being more easily accessed by the molecule, resulting in a higher blinking rate. This blinking rate can be directly assessed in single-molecule experiments through photon counting or *via* $g^{(2)}(\tau)$ measurements. See Chapter 2 (Experimental Methods) for more technical details and Chapter 4 for an example of characterization of the triplet state of the GQDs.

Building heterostructures with graphene quantum dots and perovskites is thus appealing because of the rich photophysics we can expect to investigate, from charge or energy transfer to spin-orbit interactions.

At the time we started our study, $MAPbBr_3$ monocrystals were an appealing candidate to use as a substrate because they are easily synthesized, and the band-gap lies at higher energies (2.31 eV) than the zero-phonon line of $C_{96}tBu_8$ (2.00 eV in polystyrene matrix), allowing spectroscopic studies of single GQDs without having their fluorescence masked by the emission from the perovskite.

The deposition of quantum dots at the surface of a substrate requires a specific study. First, the formation of films is not guaranteed, as molecules could diffuse on the substrate and get ejected. Second, diluting the solutions down to single-molecule experiments concentrations may not be enough to perform single-object experiments, as molecules may be attracted to specific sites of the substrate. For example, porphyrin molecules have been shown to form self-assembled islands on nitrogen-doped graphene substrates [242]. As such, I will start this chapter by describing my investigation of the formation of films of GQDs on the perovskite substrate. Then, the spectroscopic properties of the films will be investigated, from routine photoluminescence spectra to excitation spectra, time-resolved photoluminescence decays, and investigation of the effects of concentration.

Second, I will assess the stability of $C_{96}tBu_8$ on $MAPbBr_3$ and compare the result to the stability on a glass substrate. A statistical study of the stability will show the relevance of the perovskite substrate compared to the glass substrate.

Finally, I will present the results obtained using an extremely low concentration of $C_{96}tBu_8$, aiming at single-molecule experiments. A specific focus will be given to the dynamics of the photoluminescence.

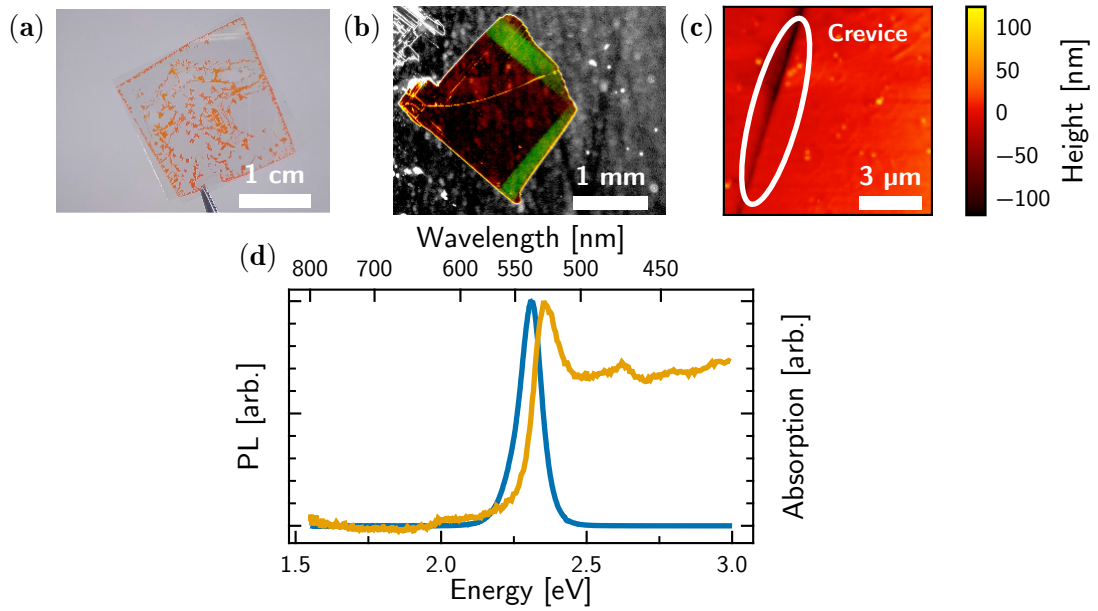

Figure 5.2: (**a**) Photograph of $MAPbBr_3$ crystals between glass coverslips. (**b**) Close-in view of a millimeter-sized crystal. The green bands are due to photoluminescence of the perovskite excited by the blue LEDs of the microscope. The surroundings of the crystal have been grayed-out to make it more visible. (**c**) AFM scan of the surface of a crystal. The surface roughness of the whole area is 17.81 nm. When the highlighted crevice is removed the roughness is $\sim$ 10 nm. (**d**) Spectroscopy of $MAPbBr_3$ crystals. The emission spectrum (blue) was obtained by exciting the medium at 405 nm, and the absorption spectrum (yellow) was measured on a thin film.

5.1 Films of $C_{96}tBu_8$ on $MAPbBr_3$ substrate

We first investigated the formation of films of $C_{96}tBu_8$ at the surface of $MAPbBr_3$. This section aims to present these samples and give a descriptive picture of their spectroscopy.

5.1.1 Description of samples

$MAPbBr_3$ crystals on glass substrates were prepared following the method described in Subsection 2.3.3. The synthesis yields millimeter-sized crystals that are enclosed between glass coverslips, as shown in Figure 5.2a. Figure 5.2b shows a zoomed-in view of a single crystal after removal of one of the glass coverslips, the green bands visible on the top and right edges of the crystal are due to pho-

toluminescence caused by the excitation of the crystal by the grazing blue light of the microscope LEDs. The synthesized crystals are relatively smooth, Atomic Force Microscopy (AFM) scans showed that the roughness of the surface is about 17.81 nm while the crystal is several microns thick[1]. The AFM scans show the presence of crevices at the surface of the perovskite. In Figure 5.2c, the roughness of the right side of the scan, that is where there is no crevice, is only $\sim$ 10 nm. The size of the crystals, as well as their smoothness, means we can easily target them on the confocal fluorescence microscope and avoid unexpected reflections of the excitation laser from surface asperities on the crystals.

Emission and absorption spectra of the synthesized material are shown in Figure 5.2d. The direct measurement of absorption spectra is not possible because of the thickness of the sample, the presented spectrum was measured on a thin-film sample obtained by spin-coating of the $MAPbBr_3$ solution. While spin-coating yields thin-films with absorption low-enough to be measured on a spectrometer, the small size of the crystals creates Rayleigh scattering, which must be corrected from the absorption spectrum. The absorption spectrum features a clear excitonic peak at 2.35 eV. The Stokes shift is approximately 40 meV, with a photoluminescence peak at 2.31 eV. The photoluminescence vanishes for energies lower than 2 eV, this means the material is suitable for using GQDs with a zero-phonon line in the 2.0 eV region.

X-ray photo-emission spectroscopy (XPS) investigation of the crystals was conducted by our collaborator Muriel Bouttemy at "Institut Lavoisier de Versailles". The method has been briefly described in Sub-Subsection 2.1.3. A typical survey spectrum acquired on the perovskite is shown in Figure 5.3a on the next page, evidencing the presence of the expected elements, C, N, O, Pb, and Br. Note that two survey spectra were acquired, one at the beginning of the analysis sequence and the other at the end, showing a slight atomic reorganization under X-rays. The reproducibility of the measurement and homogeneity of the composition was verified on three different crystals. In addition, to assess the stability of the surface chemistry of the perovskite, we compared four samples corresponding to perovskite crystals that had been either kept sealed between two glass coverslips or separated to expose them to ambient air and had been kept in the dark or exposed to day dark/light cycles in the laboratory. The samples are labeled "Air Dark", "Air Light", "Sealed Dark", and "Sealed Light", and the corresponding high resolution scans of specific orbitals are shown in Figures 5.3b, 5.3c, 5.3d, 5.3e, and 5.3f.

First, the atomic percentages obtained for these four samples are shown in Table 5.1 on page 148. The peaks positions of C at 285.8$\pm$0.2 eV, N at 401.5$\pm$0.2 eV, Pb at 137.9 $\pm$ 0.2 eV, and Br at 67.8 $\pm$ 0.2 eV are consistent with the one expected [243] but 1 eV lower for all the spectra, which we attribute to surface

[1] Our AFM cannot measure thicknesses bigger than 4 µm, but manual adjustment of the height of the sample after the maximum reach of the AFM has been attained let us think that the crystal is 10 µm thick.

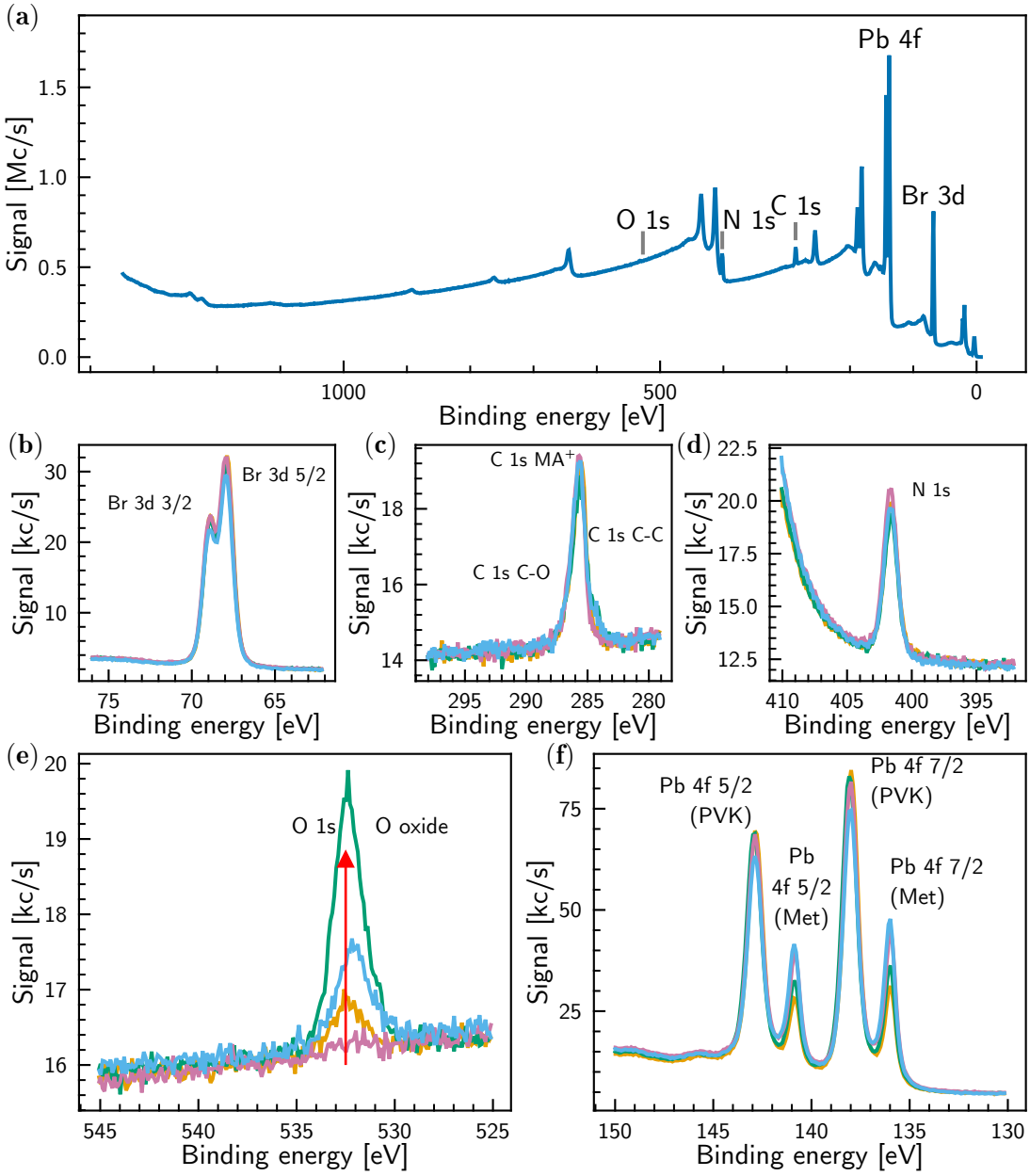

Figure 5.3: (**a**) XPS survey spectrum measured on the perovskite's surface with identification of the main transitions of the constitutive elements. The specific orbitals tracked are shown in high resolution in (**b**) for Br 3d, (**c**) for C 1s, (**d**) for N 1s, (**e**) for O 1s, and (**f**) for Pb 4f. In the high resolution scans, the green lines corresponds to the sample exposed to air and light ("Air Light"), light blue to the sample protected from air and exposed to light ("Sealed Light"), yellow to the sample exposed to air and protected from light ("Air Dark"), and purple to the sample protected from air and light ("Sealed Dark").

	Air Dark	Air Light	Sealed Dark	Sealed Light
C 1s	14.8	14.9	14.4	15.6
Br 3d	62.4	59.0	62.3	59.3
N 1s	12.2	11.0	13.1	15.6
O 1s	1.3	5.5	0.0	2.5
Pb 4f	9.2	9.6	10.2	10.2

Table 5.1: XPS atomic percentages measured on the samples.

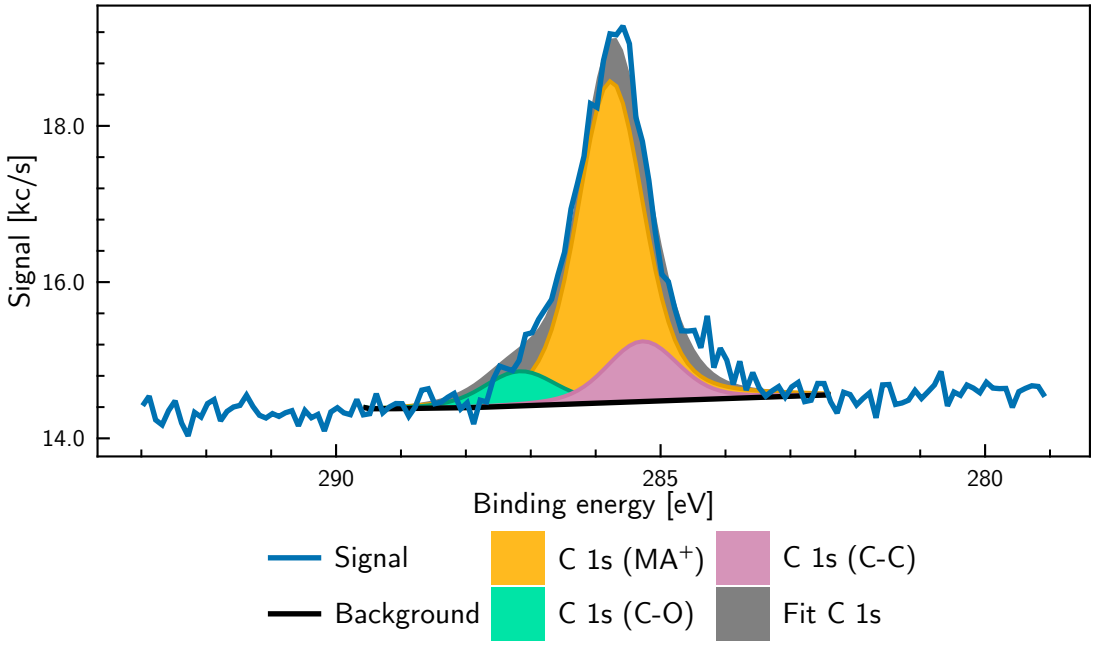

Figure 5.4: Result of the fitting procedure on the signal from the C 1s orbital. The various peaks account for the environment of the carbon atom.

Ratio	Air Dark	Air Light	Sealed Dark	Sealed Light	Expect.
C*/Pb	1.31	1.20	1.19	1.17	1.1
N/Pb	1.32	1.14	1.29	1.23	1.1
O/Pb	0.14	0.57	0.00	0.24	0
C*/N	0.99	1.05	0.93	0.95	1
C*/Br	0.19	0.20	0.19	0.20	0.35
N/Br	0.20	0.19	0.21	0.21	0.35
Pb/Br	0.15	0.16	0.16	0.17	0.32
C/Pb	1.60	1.54	1.41	1.53	1.1
C/N	1.21	1.35	1.10	1.25	1
C/Br	0.24	0.25	0.23	0.26	0.35
Pb^{2+}/Pb^0	3.16	2.71	2.04	1.70	

Table 5.2: Atomic ratios deduced from atomic proportions given in Table 5.1. C* denotes the atomic percentage originating only from MA^+ cations (*i.e.* after substraction of the C contamination). The second part of the table accounts for all carbon species (including contamination). The third part compares the peaks of ionic and metallic lead. The expected ratios account for a 10 % excess of MABr in the synthesis.

potential effects. Interestingly, one should note that whatever the sample, a very low amount of oxygen is detected, at the detection limit for the sealed dark sample and reaching only 5.5 at % for the air light sample. The C content is also low and practically entirely attributed to MA^+ after fitting of the peaks. To model C 1*s*, three contributions are required: one for MA^+, two for the adventitious carbon contamination (C-C and C-O bonds), as shown for Figure 5.4. Details on the fitting procedure to obtain the atomic percentages are available in Ref. [244]. The difference between the amount of O 1s and O 1s (C-O) gives the amount of O oxyde: 0 %, 4.4 %, 0 %, and 1.1 % for Air Dark, Air Light, Sealed Dark, and Sealed Light respectively. The only possible attribution of this oxide is lead oxidation, hardly visible as the amount is very low as well as the chemical shift of Pbox with respect to Pb in the perovskite structure. On the other hand, the presence of elemental lead is clearly depicted in Figure 5.3f for all the samples, but with different proportions. Noticeably, we can see the sample that was protected both from light and ambient air do not exhibit any trace of oxygen. The presence of oxygen seems to be caused by the exposition to light, which advocates for storing the perovskite samples in the dark. Concerning surface contamination, a very low carbon sticking is shown, with at maximun 4 at %, which is remarkable.

To assess the composition of the surface probed, one can look at the relative atomic ratios and compare them with the ratios expected from the synthesis condition (MABr is put with 10 % excess). This comparison is made in Table 5.2. This table shows the amount of methylammonium is close to the expected ratio, and

validate the fitting procedure. On the other hand, the ratio of each species against bromide is systematically low, which advocates for a higher amount of that species on the surface of the perovskite. Finally, the atomic percentages used to produce Table 5.1 allow comparing the amounts of metallic (positionned $\sim 2\,\text{eV}$ lower than Pb^{2+}) and ionic lead (lead in the perovskite matrix and Pbox). It is known that $CsPbBr_3$ nanocrystals tend to form metallic lead on their surface [167], which would be consistent with our observations here. The higher amount of elemental lead is measured for the sealed dark sample, the most preserved from ageing, and can be explained by its oxidation in the presence of air and during light exposition, as already observed for triple cation halide perovskite [122].

Overall, the XPS study shows that our method of synthesis and storage of $MAPbBr_3$ crystals produces samples with a relatively pure surface which presents some metallic lead and a low carbon contamination, making it suitable for single-molecule experiments. Profiling measurements were not tested, as Ar^+ bombardment is renowned for causing lead reduction [245].

$C_{96}tBu_8$ films were prepared by drop-casting concentrated solutions of GQDs in TCB on the surface of $MAPbBr_3$ crystals. The solvent was then evaporated in a stove under vacuum at 60 °C.

5.1.2 Characterization of $C_{96}tBu_8$ films

We investigated the morphology of the films through confocal fluorescence raster scans. Figure 5.5a on the next page shows the result of such a scan, excited at 2.06 eV. The map features sharp bright lines at 17.5 kc/s surrounded by mostly dark areas. As the perovskite, even soaked in TCB, does not display any fluorescence when excited at energies this low, and given the purity of our GQD samples (as seen in Chapter 4), these lines can be attributed to the fluorescence of $C_{96}tBu_8$.

As a point of comparison, Figure 5.5b shows a film formed in the same conditions on a glass substrate. The film is much more homogeneous than the one presented in Figure 5.5a, the various dark spots observed being due to "holes" burned in the film using the excitation laser.

To understand this striking difference between the films of GQDs formed on glass and on perovskite substrates, one can look at the morphology of the perovskite surface. To do so, we compared the photoluminescence maps of the same region when exciting either only the GQDs, or both the GQDs and the perovskite. In the former case we excite below the perovskite's gap, while in the latter we excite above the gap, and the photoluminescence is largely dominated by the perovskite's one, making it possible to see the details of the surface. Figure 5.5c features a fluorescence raster scan of the perovskite substrate excited at high energy (3.06 eV) of the same area as in Figure 5.5a. The spatial distribution of the emission in Figure 5.5c gives an overview of the shape of the substrate's surface. As such, the positions of the bright lines of $C_{96}tBu_8$ in Figure 5.5a appear to match very well

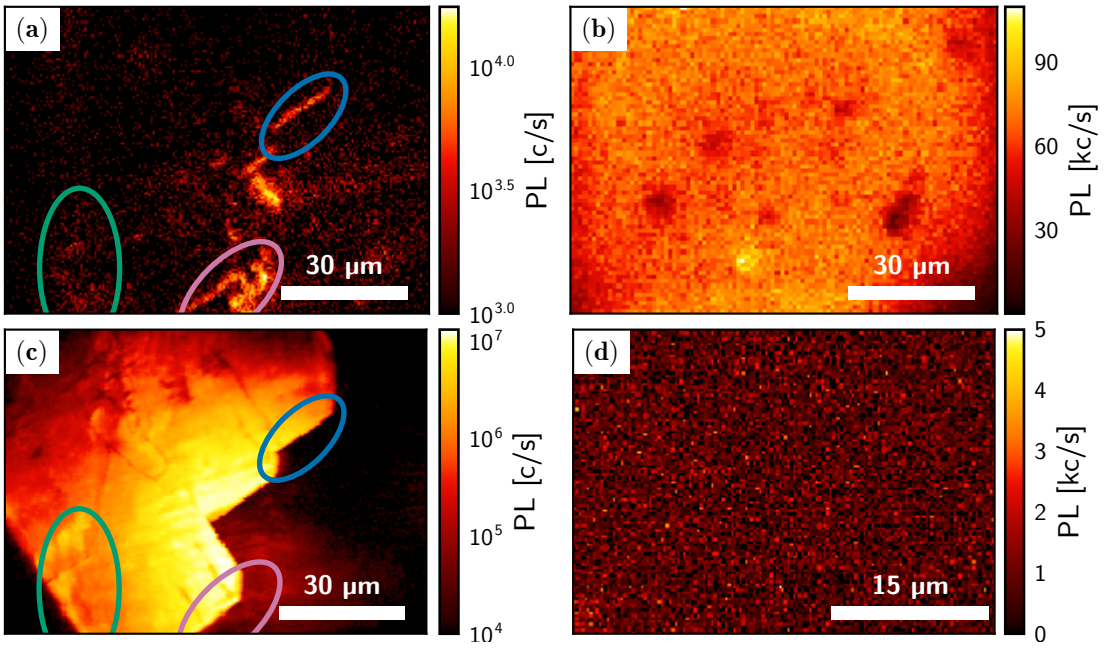

Figure 5.5: (**a**) PL raster scan of $C_{96}tBu_8$ film drop-casted on $MAPbBr_3$ substrate excited at 2.17 eV. (**b**) PL raster scan of a film of $C_{96}tBu_8$ in TCB drop-casted on glass substrate. The excitation energy was 2.17 eV. (**c**) PL raster scan of the same area as in (**a**), excited at 3.06 eV, integrated for energies lower than 2.07 eV. (**d**) Photoluminescence raster scan of a $MAPbBr_3$ crystal soaked in TCB, then dried for 2h30 at 60 °C. Excitation energy was 2.06 eV. Scans (**c**) and (**a**) were excited using the supercontinuum laser (60 MHz repetition rate) whereas scan (**b**) was excited using our continuous wave Cobolt laser.

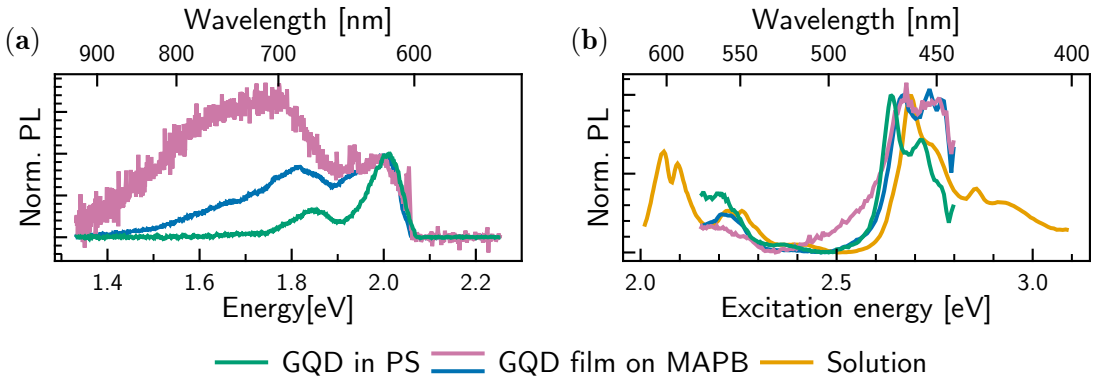

Figure 5.6: (**a**) Photoluminescence spectrum recorded on $C_{96}tBu_8$ film on $MAPbBr_3$ substrate (blue line) and of typical single $C_{96}tBu_8$ in polystyrene matrix (green line). Also represented is a deformed photoluminescence spectrum sometimes observed on $MAPbBr_3$ substrate (pink line). (**b**) Excitation spectrum of $C_{96}tBu_8$ in THF solution (yellow line), $C_{96}tBu_8$ film in polystyrene matrix (green line), $C_{96}tBu_8$ film on $MAPbBr_3$ substrate (blue line), and deformed photoluminescence spectrum on $MAPbBr_3$ (pink line), normalized at $S_0 \rightarrow S_2$ absorption peak.

the sharp features in the raster scan of the perovskite (highlighted by the ellipses). These sharp features were attributed to the presence of crevices at the surface of the crystal, as shown in the AFM scan in Figure 5.2c. We thus conclude that the formation of films on the surface of $MAPbBr_3$ mainly occurs on sharp geometric features, such as crevices or holes. This may be explained by the deposition process; the solution could dry more slowly in those areas since it is less exposed to the atmosphere. This yields a picture of the samples towards the end of the drying process where flat surfaces have already dried, but small pockets of highly concentrated solutions still exist in holes and crevices. In the following subsection, I will describe further the spectroscopy of the GQD films, and in particular report on our investigation of the spatial distribution of GQDs on the surface of the perovskite to check on their presence away from the sharp geometric features of the crystal.

5.1.3 Spectroscopy of $C_{96}tBu_8$ films

Measurements on $C_{96}tBu_8$ films

To further confirm the correct deposition of $C_{96}tBu_8$ at the surface of $MAPbBr_3$, emission and excitation spectra were recorded. Those are shown in Figure 5.6b.

The spectrum on perovskite substrate features the expected zero-phonon line and phonon replica. A large variety of spectra shapes were observed, with varying aspect-ratio between the main emission peak and first replica. Some are very close to the spectrum of a single GQD in a polystyrene matrix, as shown by the blue curve in Figure 5.6a, while others differ much more from the single-molecule case, as shown by the pink curve. Those emission spectra originate from $C_{96}tBu_8$ and the reason for the modifications will be detailed in the following Sub-Subsection.

We also performed control experiments where we deposited TCB on top of $MAPbBr_3$ crystals. Figure 5.5d shows a typical photoluminescence raster scan of such a perovskite crystal soaked in TCB. The crystal remained dark for excitations at 2.07 eV. This means we can be confident in the attribution of photoluminescent spots on actual samples to the presence of $C_{96}tBu_8$, and not to some degradation of the perovskite by the solvent.

For the brightest films, it is possible to record excitation spectra such as displayed in Figure 5.6b. This figure also features the excitation spectra of $C_{96}tBu_8$ in THF solution and in a polystyrene matrix. Both excitation spectra on $MAPbBr_3$ and in polystyrene appear red-shifted compared to the spectrum in solution by 17 meV and 52 meV, respectively. Save for this redshift, the excitation spectrum of $C_{96}tBu_8$ film on $MAPbBr_3$ substrate matches very well its solution counterpart. Because of their similarities with spectra in the polystyrene matrix and in solution, both the emission and excitation spectra are clear indications that the photophysics of the GQD film on a perovskite substrate is not dominated by interactions with the semiconductor and that the chemistry of the molecule is not modified by the deposition process.

The characterization of the crystals reported previously allows us to assume that they are homogeneous and flat at the scale of a few microns. Thus, we attribute the local variations of photoluminescence intensity on these scales on the raster scans to local variations in emitters' density. This allows the recording of emission spectra for various local densities of GQDs. Figure 5.7a on the following page shows a photoluminescence raster scan where emission spectra were taken at positions of various intensities. Figure 5.7b shows the corresponding emission spectra, as well as a typical emission spectrum from a single $C_{96}tBu_8$ in a polystyrene matrix for comparison. These spectra clearly show the evolution of the aspect ratio between the zero-phonon line and the first phonon replica. At high intensities, emission from the lower energy part of the spectrum dominates. As intensity decreases, the aspect ratio also decreases, and emission from higher energies, close to the zero-phonon line, dominates. Figure 5.7 also shows red-shifting of both the high energy peak, from 1.99 eV for the lowest concentrations to 1.95 eV for the highest, and the low energy peak, from 1.73 eV to 1.82 eV. Spectra similar to the ones presented in Figure 5.7 were also observed on glass substrates, further confirming that these do not originate from a chemical modification of the emitter by the perovskite.

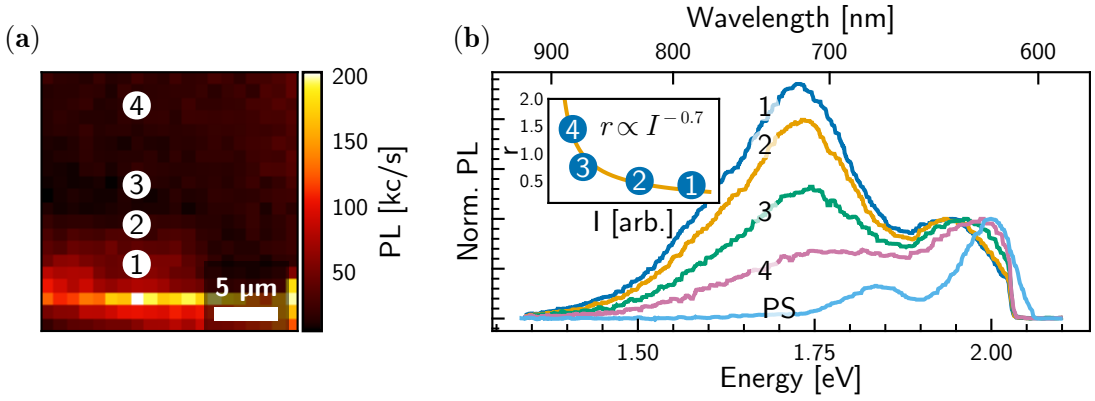

Figure 5.7: Comparison of PL spectra of $C_{96}tBu_8$ on $MAPbBr_3$ crystal. Excitation at 2.13 eV with our pulsed supercontinuum laser. (**a**) PL raster scan of $C_{96}tBu_8$, the brighter points indicate higher integrated PL and thus higher concentration of emitters. (**b**) PL spectra taken on points indicated in (**a**). A typical spectrum in a polystyrene matrix is plotted in light cyan for reference. The inset shows the ratio r between the peak at high energy and the peak at lower energy. The yellow line is a guide to the eye and corresponds to a power law fit of the ratio against intensity, with characteristic power -0.62.

The deposition of GQD films on perovskite substrates highlighted two effects. First, variations in local density of emitters correlates with a red-shift and broadening of the emission spectrum. This effect increases with the local density of emitters. Second, the excitation spectra unveiled that these emitters are still GQDs, because these spectra match the excitation spectrum in solution. This means absorption in these films occurs from the same system as in solution, namely the monomer $C_{96}tBu_8$, while emission undergoes a more complex process. The fact that this process seems accentuated at higher local surface concentrations hints at multi-chromophoric effects. In the following, I will review the basic properties reported in the literature on such systems.

A brief introduction to the physics of molecular aggregates

A first tentative explanation of the physics at play in our GQD film may be the formation of aggregates. The next paragraphs will focus on building an intuition of the physics of aggregates.

Following the introduction to Kasha theory [246] proposed by Hestand and Spano [247], I present Kasha theory, in its simplest form. It allows the classification of aggregates of molecules in two categories, H- and J-aggregates, using only dipole-dipole interaction and ignoring vibronic coupling or wave function overlaps.

Employing the point-dipole approximation, the interaction term between two molecules **1** and **2** can be written as in Equation 5.1.

$$J_C^{pd} = \frac{\vec{\mu}_\mathbf{1} \cdot \vec{\mu}_\mathbf{2} - 3(\vec{\mu}_\mathbf{1} \cdot \hat{R})(\vec{\mu}_\mathbf{2} \cdot \hat{R})}{4\pi\varepsilon R^3} \tag{5.1}$$

Where $\vec{\mu}_{\mathbf{1},\mathbf{2}}$ is the dipole moment of the indexed molecule, $\vec{R} = R\hat{R}$ the vector connecting both molecules, and ε is the dielectric constant of the surrounding medium. It can be seen from Equation 5.1 that in the case when both dipoles are co-planar, J_C^{pd} can be rewritten as:

$$J_C^{pd} = \frac{\mu^2(1 - 3\cos^2\theta)}{4\pi\varepsilon R^3} \tag{5.2}$$

From there emerges a limit angle, named "magic angle" in the literature, $\theta_M \approx 54.7°$. For angles below θ_M, J_c^{pd} is negative and we classify the structure as a J-aggregate, whereas for angles above θ_M they are classified as H-aggregates. The sign of J_c^{pd} has a direct influence on the photophysics of the aggregate. For example, in a molecular dimer, Coulombic interaction leads to the formation of two delocalized states : in- and out-of-phase, shown in Figure 5.8a on the next page. In each case, only the in-phase component is optically active, thus, the two types of aggregates are optically distinguished. In J-aggregates, absorption is red-shifted while in H-aggregates absorption is blue-shifted.

When the model is extended to N molecules, then the Frenkel exciton Hamiltonian reads (in units where $\hbar = 1$) [247]:

$$H_{ex} = E_M + D + \sum_{m,n} J_{m,n} \left|m\right\rangle \left\langle n\right| \tag{5.3}$$

where E_M is the energy of transition $S_0 \rightarrow S_1$ for the gas-phase monomer, D the gas-to-crystal frequency-shift, $J_{m,n}$ the coulombic coupling constant between molecules m and n, and $|n\rangle = |g_1, g_2, ..., e_n, ..., g_n\rangle$ is the locally excited state for the n^{th} monomer. Applying periodic boundaries conditions (this is equivalent to considering large aggregates), the eigenvectors of this Hamiltonian read:

$$\left|k\right\rangle = \frac{1}{\sqrt{N}} \sum_n e^{ikn} \left|n\right\rangle, \quad k = \pm 2j\pi/N,\ j \in 1...N \tag{5.4}$$

For our purpose, we can suppose that the coupling constant only depends on the distance between chromophores, *i.e.* $J_{m,n} = J_{|m-n|}$. Applying the Hamiltonian in

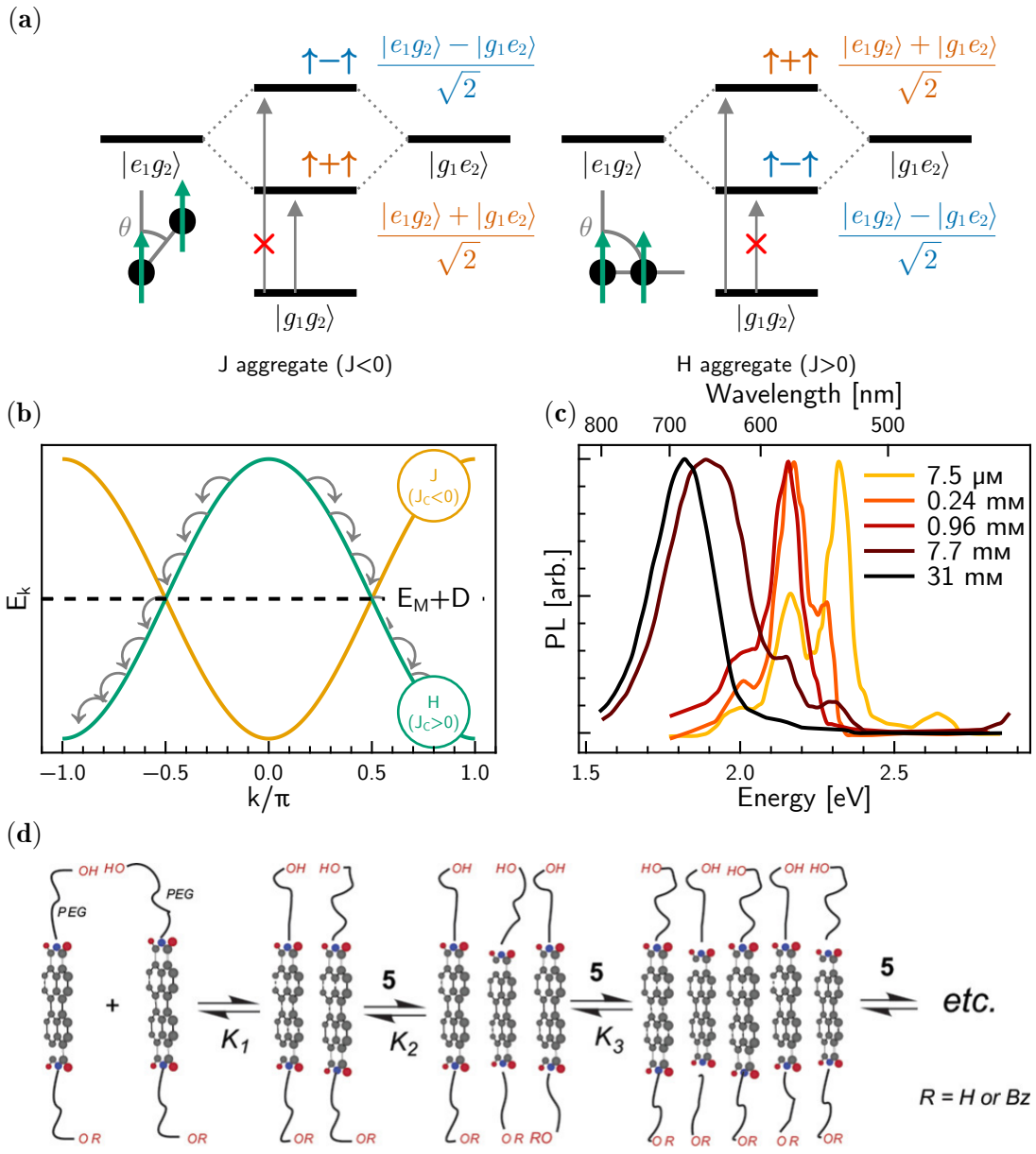

Figure 5.8: (**a**) Energy diagrams in J- and H-aggregates. The black dots with green arrows picture the orientation of the dipoles. Adapted from Ref. [247]. (**b**) Dispersion in J- and H-aggregates. Adapted from Ref. [247]. (**c**) Photoluminescence of bis-N,N-(2-(2-(2-(2-hydroxyethoxy)ethoxy)ethoxy)ethyl) perylene tetracarboxylic diimide in $CHCl_3$ at various initial concentrations excited at either 369 or 429 nm. Adapted from Ref. [248]. (**d**) Schematic of the aggregates studied in Ref. [248].

Equation 5.3 to the eigenvector $|k\rangle$ then yields:

$$H_{ex}|k\rangle = (E_M + D)|k\rangle + \sum_{m,n} J_{|m-n|}|m\rangle\langle n|k\rangle \tag{5.5}$$

$$= (E_M + D)|k\rangle + \sum_{m,n} J_{|m-n|}|m\rangle \sum_j e^{ikj}\langle n|j\rangle \tag{5.6}$$

$$= (E_M + D)|k\rangle + \sum_m |m\rangle e^{ikm} \sum_n J_{|m-n|}e^{ik(n-m)} \tag{5.7}$$

$$= \left(E_M + D + \sum_n J_{|m-n|}e^{ik(n-m)}\right)|k\rangle \tag{5.8}$$

When only the nearest neighbors are taken into account, that is taking only the two terms of the sum in Equation 5.8 for which $|m-n| = 1$, the energy reads:

$$E_k = E_M + D + 2J_C \cos k \tag{5.9}$$

The resulting dispersion curve is shown in Figure 5.8b. State $k = 0$ is a local minimum in the dispersion diagram for J-aggregates, because of the sign of J_C in that case, so emission is expected to occur there, with an expected red-shift. For H-aggregates, fast intraband relaxations transform the $k = 0$ exciton to a $k = \pi$ exciton before any photoluminescence can occur. However, the transition dipole moment operator reads $\hat{\mathbf{M}} = \vec{\mu}\sum_n (|g\rangle\langle n| + |n\rangle\langle g|)$, where $|g\rangle$ is the ground state of the system, where all molecules are in their ground state. It follows that $\hat{\mathbf{M}}$ is non-vanishing for $k = 0$ exciton only. This means that, in this simplistic model, H-aggregates should be optically dark. For H-aggregates to become bright, some symmetry-breaking effects are required, such as vibronic effects or charge transfers.

More advanced models are available in the literature. First, the point-dipole approximation breaks down when molecules become closer than approximately the effective size of the dipole and new expressions for J_C are required to take into account the extension of the dipole [249]. Then, additional effects can be added to the Hamiltonian, such as vibronic coupling [250–252] or charge transfer effects [253].

Wang *et al.* [248] have investigated experimentally the formation of aggregates of perylene-based molecules in solution of $CHCl_3$. The geometry of the aggregates is shown in Figure 5.8d. Figure 5.8c shows the evolution of emission spectra as the concentration in chromophores increases. From a standard emission spectrum for a polycyclic aromatic hydrocarbon at low concentration, with resolved vibronic replica, to a broad unstructured, red-shifted emission spectrum as the concentration increases. This reproduces well the intuition built above : for big H-aggregates, the zero-phonon line becomes unfavored for emission, and emission is made possible through various relaxation channels, creating a broad, unstructured emission spectrum at lower energies.

Nature of the coupling in excimers

The formation of excimers is another way in which molecule interaction can happen, and is sometimes difficult to distinguish from aggregation. In particular, in aggregates where the distance between two molecules is sufficiently small so that a significant wave function overlap between neighboring molecules is observed, emission tends to happen from excimer states [247]. This is particularly true for cofacial aggregates, *i.e.* H-like aggregates [254]. The formation of excimers involves the interaction between an excited molecule and its neighbor in the ground state. In fact, Bialas and Spano [255] showed that describing excimer states requires taking into account the role of Frenkel exciton, charge transfer states, *intra*molecular vibrations, and *inter*molecular vibrations. It has been shown in the literature that excimer states rapidly localize to a dimer on a femtosecond timescale [256, 257], making it possible for Bialas and Spano to reproduce with great accuracy the experimental spectra of perylene diimides excimers using the Holstein-Peierls Hamiltonian

$$H_{\mathrm{HP}} = H_{\mathrm{F}} + H_{\mathrm{CT}} + H^{\mathrm{f}}_{\mathrm{vib}} + H^{\mathrm{s}}_{\mathrm{vib}} \tag{5.10}$$

where H_{F} is the electronic Frenkel Hamiltonian, similar to the one developped in Section 5.1.3, H_{CT} is the charge transfer part of the Hamiltonian, $H^{\mathrm{f}}_{\mathrm{vib}}$ accounts for fast *intra*molecular vibronic coupling, and $H^{\mathrm{s}}_{\mathrm{vib}}$ incorporates the slow *inter*molecular vibronic coupling. In particular, they showed that excimer signature can be induced either through local coupling of the dimer charge transfer states to *inter*molecular vibrational mode, or non-local coupling, which involves the modulation of the coupling between Frenkel and charge-transfer states by an *inter*molecular vibrational mode.

Experimentally, signatures of an excimer state is usually shown by a broad, unstructured red-shifted emission spectrum [258], while the absorption remains very similar to the monomer [259], albeit structured emission is sometimes still observed in excimers [260, 261] . Bialas and Spano [255] showed that, at room temperature, structured emission can be observed in excimer systems because of thermally activated states forming from the coupling between low-energy Frenkel-like states and low-energy charge transfer states. Another consequence of the formation of excimers is the appearance of longer photoluminescence lifetimes [258, 262–264], due to the charge transfer character of excimers.

Excimers in $C_{96}tBu_8$ films on $MAPbBr_3$ substrate

The theoretical elements from the literature on excimers were reported in the previous paragraphs. In our samples, we observe a red-shift of the emission spectra and an evolution in shape (Figure 5.7b), which corresponds well to the spectra reported by Wang *et al.* [248] and reproduced in Figure 5.8c: the photoluminescence spectra are red-shifted and evolve towards broader, red-shifted spectra as the concentration increases. This is compatible both with the formation of excimers

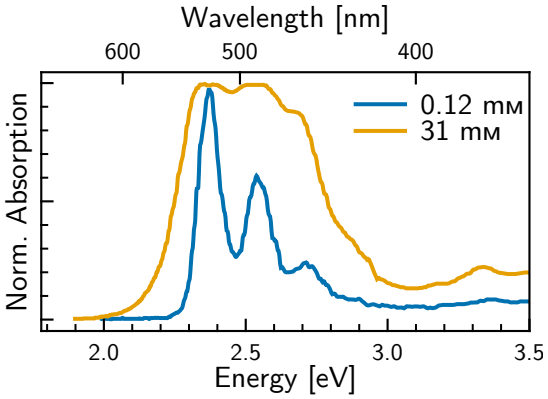

Figure 5.9: Absorption spectra of perylene diimides for two concentrations. Adapted from Ref. [248].

or the presence of aggregates. However, the excitation spectrum of our GQDs is almost unchanged compared to the excitation (and absorption) spectrum of the monomer in solution or polystyrene matrix. This is in contrast to the aggregation of the perylene-based molecules reported by Wang *et al.* [248], reproduced in Figure 5.9. In that latter figure, the absorption spectrum is seen to broaden at higher concentration, even though it remains at the same energy. This broadening is incompatible with excimers, as it means absorption does not happen from the monomer anymore. These two experimental facts lead us to conclude that emission occurs from excimer states in $C_{96}tBu_8$ films on $MAPbBr_3$ substrates. This also means the excited levels in those films have a lower energy than the monomer state, which may impede or change the efficiency of energy transfers between the perovskite and the GQDs. In this context, a single-molecule level study may be necessary to unveil the physics at the interface of $MAPbBr_3$.

5.2 Stability of $C_{96}tBu_8$ on perovskite substrates

The study of films of $C_{96}tBu_8$ allowed us to perform a study of the stability of the GQDs' photoluminescence on $MAPbBr_3$ and compare it with the stability on a glass substrate.

The comparison of typical fluorescence rate time traces on both substrates are shown in Figure 5.10a on the following page. The film on glass is seen quickly deteriorating and reaches the background level in approximately one second. On the other hand, the film on perovskite substrate demonstrates superior stability and requires hundreds of seconds to halve the initial signal level.

To confirm this first intuition, we performed a statistical study of half-life time on both substrates. Figure 5.10b features a histogram of the recorded half-life

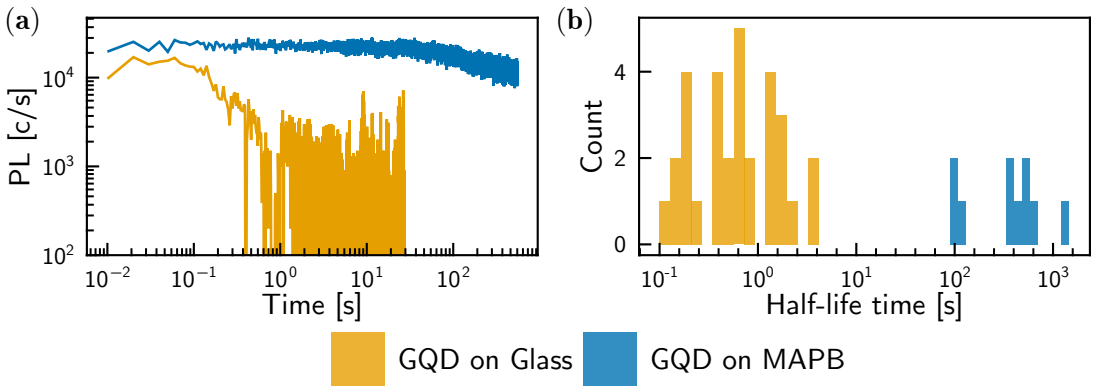

Figure 5.10: (**a**) Example time-traces of integrated PL for $C_{96}tBu_8$ films on glass (yellow line) and on $MAPbBr_3$ (blue line). (**b**) Distribution of time required to halve the initial photoluminescence intensity upon continuous wave illumination at 2.09 eV, 0.396 kW/cm^2 for glass substrate (yellow) and $MAPbBr_3$ substrate (blue).

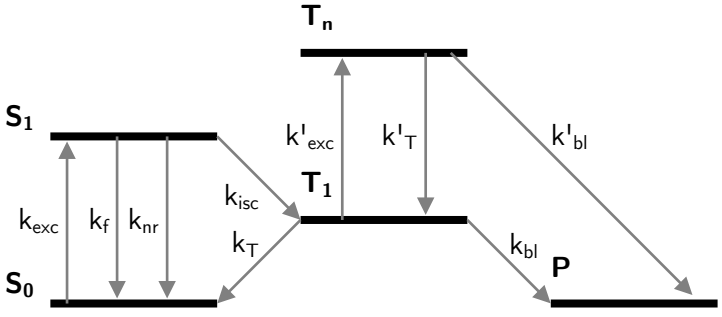

Figure 5.11: Five-levels system explaining the photobleaching mechanism through transition from triplet state T_1, and the excited triplet T_n, to photobleached state P. Adapted from Ref. [265].

time. $C_{96}tBu_8$ on glass substrate appear short-lived, with emission dropping in a matter of 0.9 s on average with a standard deviation of 0.98 s, while the half-life time on perovskite is, on average, 472 s with a standard deviation of 405 s. The shorter lifespan of $C_{96}tBu_8$ films on glass is best explained by the presence of charge states on the substrate that can induce photobleaching [266]. This mechanism is often described using a five-levels, such as shown in Figure 5.11 system where photoexcitation of the triplet state leads to photobleaching [265, 267]. In Figure 5.11, the molecule is described by the three-levels system that was extensively discussed in Chapter 4, to which an excited triplet state ($\mathsf{T_n}$) and a photobleached state (P) have been added. The two triplet states are able to interact with charge states on the substrate, leading to photobleaching of the molecule. Other mechanisms have also been proposed, involving singlet-triplet anihilation under continuous-wave excitation [268]. In most cases, the photobleaching involves a triplet state and a transfer from that state towards the substrate. Thus, the difference in survival time of the GQDs on glass and perovskite may be explained by either a lesser rate of transition towards triplet states on the perovskite, or a lesser coupling of the GQD to that substrate. The former seems unlikely, given the reason why we chose to study GQDs on perovskite substrates in the first place was because we thought we could increase the inter-system crossing in the GQD. On the other hand, a lesser coupling to the substrate may be explained by a lack of charge states on the perovskite substrate, or a difference in band alignment.

The increased stability on the perovskite is an important factor opening the way to the study of $C_{96}tBu_8$ at the single-molecule level.

5.3 Lowering density of emitters – towards single-molecule experiments

As shown in Section 5.1, the photophysics of $C_{96}tBu_8$ films does not appear to be altered by the perovskite substrate and is instead dominated by group effects. The good stability on $MAPbBr_3$ reported in Section 5.2 made it reasonable to try to lower the density of emitters and aim for single-molecule experiments. The goal was to isolate single molecules and reduce the effects of inter-molecule interactions, and perhaps unveil interactions between a single molecule and the $MAPbBr_3$ substrate.

5.3.1 Description of the samples

$MAPbBr_3$ crystals were prepared as described previously, and then spin-coated with a solution containing $C_{96}tBu_8$. The typical concentration of the solution was 0.15 µM, which is about ten times smaller than the typical concentration used in the drop-casting experiments described previously. The solution was spin-coated at 1000 rpm, with acceleration at 100 rpm/s and rotation duration of 180 s.

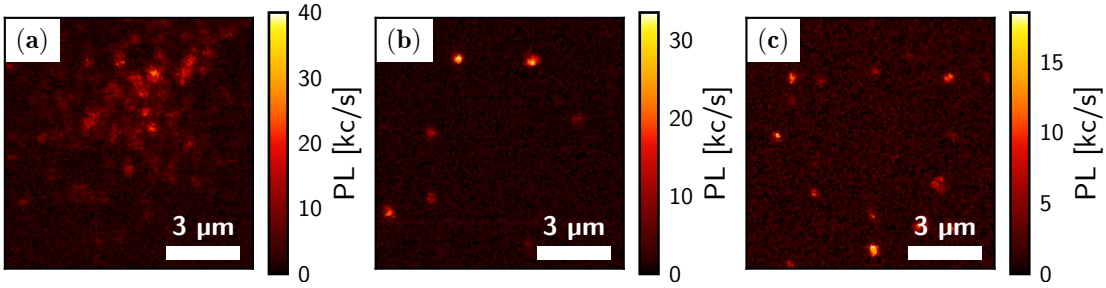

Figure 5.12: (**a**) Typical photoluminescence raster scan of $C_{96}tBu_8$ on $MAPbBr_3$, spin-coated from TCB solution. Excitation intensity was $0.54\,kW/cm^2$.(**b**) Photoluminescence raster scan of $C_{96}tBu_8$ on $MAPbBr_3$, spin-coated from TCB solution, featuring diffraction-limited emission spots. Excitation intensity was $0.26\,kW/cm^2$. (**c**) Typical photoluminescence raster scan of $C_{96}tBu_8$ on $MAPbBr_3$, spin-coated from THF solution. Excitation intensity was $0.26\,kW/cm^2$.

A typical photoluminescence raster scan is shown in Figure 5.12a. This scan features large photoluminescence spots, which is not the result we aimed for, as our goal was to perform single-molecule experiments. We tried to control the density of emitters on the substrate through careful adjustments to the concentration of the deposited solution. Although we were sometimes able to obtain raster scans featuring diffraction-limited spots, such as in Figure 5.12b, the procedure was unreliable and reproducibility was low. This prompted us to switch solvent and use THF instead. THF evaporates at a higher rate than TCB and is generally considered a better solvent to use for spin-coating operations. This greatly improved our samples and the reproducibility of our experiments. A typical raster scan is shown in Figure 5.12c, where diffraction-limited spots are clearly identifiable.

As with films from TCB solution, we performed control experiments with pure THF spin-coated on $MAPbBr_3$ and confirmed that no emission spots were observable after the addition of the solvent. This means we can safely attribute emission spots to the presence of $C_{96}tBu_8$.

5.3.2 Expected signal levels

Figure 5.12c shows a typical photoluminescence raster scan of $C_{96}tBu_8$ on $MAPbBr_3$ substrate. Several diffraction-limited emission spots are observable, with various signal levels. As shown previously, $C_{96}tBu_8$ can aggregate at the surface of the perovskite. As such, it is worth knowing a range of possible emission rates for single $C_{96}tBu_8$ on this surface. In this sub-section, I propose a simple geometric-optics model to compare the emission rate of a GQD in a polystyrene matrix and in air. The model of a GQD in air is a good upper limit to the amount of light extracted from a single GQD at the surface of a perovskite. Indeed, in

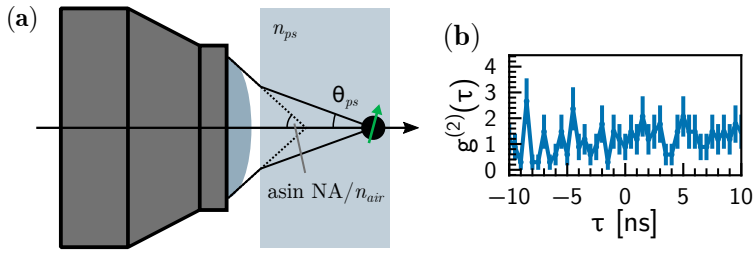

Figure 5.13: (**a**) Schematic of angles used to calculate the collection efficiency in polystyrene films. (**b**) Second order correlation measurement on a diffraction-limited bright (100 kc/s) spot.

the case of a dipole radiating in the vicinity of a dielectric[2], the amount of power extracted would actually be lower than in the case of a dipole in free space [269].

First, it is essential to realize that GQDs in air and in polystyrene are excited at the same rate, as Snell-Descartes' law of refraction implies that numerical aperture is conserved throughout the interface. Under the approximation that our microscope uses Gaussian beams, that means a GQD in polystyrene or in air receives the same amount of light, and we are thus only concerned with the amount of emitted light collected by the microscope objective.

Since the polystyrene films discussed in Chapter 4 are typically 2 µm-thick, we can assume a simplistic model for the emission where a single GQD emits in all directions, without taking into account the glass substrate beneath. In this model, the light collected from the emitter is limited by the solid angle that is collected by the objective. Figure 5.13a shows a schematic of the situation. Snell-Descartes law of refraction links the numerical aperture of the microscope, NA, the refractive index of polystyrene, n_{ps}, and θ_{ps}, the highest angle that gets transmitted at the interface.

$$\theta_{ps} = \arcsin \frac{\mathrm{NA}}{n_{ps}} \tag{5.11}$$

The collection efficiency η_{ps} is then given by the ratio between the solid angle of collection and 4π sr, and reads

$$\eta_{ps} = \frac{1}{4\pi} \int_0^{\theta_{ps}} 2\pi \sin\alpha \mathrm{d}\alpha = \frac{1 - \cos\theta_{ps}}{2} \tag{5.12}$$

As our setup uses a 0.95 NA objective, and assuming the refractive index of polystyrene is 1.58 [270], Equation 5.12 yields $\eta_{ps} \approx 0.1$. This is likely overestimated, as the refractive index is not constant whe considering wide angles as is the case here.

[2]Which is a valid approximation for the perovskite here, since it does not absorb at the energy levels where the GQD emits.

The same procedure can be applied to a hypothetic $C_{96}tBu_8$ in air. The collection angle is then only limited by the numerical aperture of the objective, and Equation 5.12 then yields $\eta_{air} \approx 0.3$. This upper limit for the GQDs on perovskite is thus three times higher than the extraction efficiency for single GQDs in a polystyrene matrix.

In these conditions when looking for single GQDs, and given the emission rate measured on single $C_{96}tBu_8$ in polystyrene is about 8 kc/s, we chose to set aside the brightest spots at 100 kc/s and concentrate on spots with a fluorescence rate lower than 30 kc/s. This is further confirmed when looking at the second-order correlation function for a bright spot at 100 kc/s, such as shown in Figure 5.13b where no anti-bunching is observed, ruling out the possibility of single-molecule emission. These brighter spots could nonetheless be the subject of an independent study, for example to determine the exact reasons leading to their appearance.

5.3.3 Spectroscopy of diffraction-limited $C_{96}tBu_8$ spots on $MAPbBr_3$

Figure 5.14a on the next page shows a typical photoluminescence raster scan of a diluted solution of $C_{96}tBu_8$ in THF spin-coated on a $MAPbBr_3$ crystal. As discussed above, the brightest point at 100 kc/s should be ignored. The raster scan features several diffraction-limited spots at $\sim$ 30 kc/s that are good single-emitters candidates.

We can see from Figure 5.14b that, the photoluminescence spectra of diffraction-limited spots on $MAPbBr_3$ come in a whole variety of shapes, and some differ quite strikingly from the typical spectrum of single-molecules in a polystyrene matrix. In particular, the zero-phonon line appears dimmed while the first and second phonon replicas appear enhanced. It is also unclear whether these diffraction-limited emission spots originate from single molecules. Indeed, Figure 5.14c shows that there is no clear $g^{(2)}(\tau = 0) < 0.5$ that would prove we are in the presence of single-molecule emitters. Moreover, time-resolved photoluminescence spectra on diffraction-limited spots such as in Figure 5.14d revealed an increase in fluorescence lifetime ($\sim$ 3.65 ns) compared to the lifetime in solution ($\sim$ 2.85 ns for the main component) or of single GQDs in polystyrene matrix ($\sim$ 3.4 ns from fitting the power dependence of the $g^{(2)}$ short-time component).

The excellent stability of $C_{96}tBu_8$ on perovskite substrates under continuous illumination prompted us to perform photoluminescence excitation (PLE) measurements using a supercontinuum laser. See Sub-Subsection 2.1.2 for more details on PLE experiments and how normalization should be performed with our confocal microscope. Even with normalization out of the way, PLE spectra can be a challenge on these emissive perovskite substrates when the emitter that is being probed is not bright enough to overcome emission from the volume of the perovskite substrate. For example, Figure 5.15a on page 166 shows the emission spectra mea-

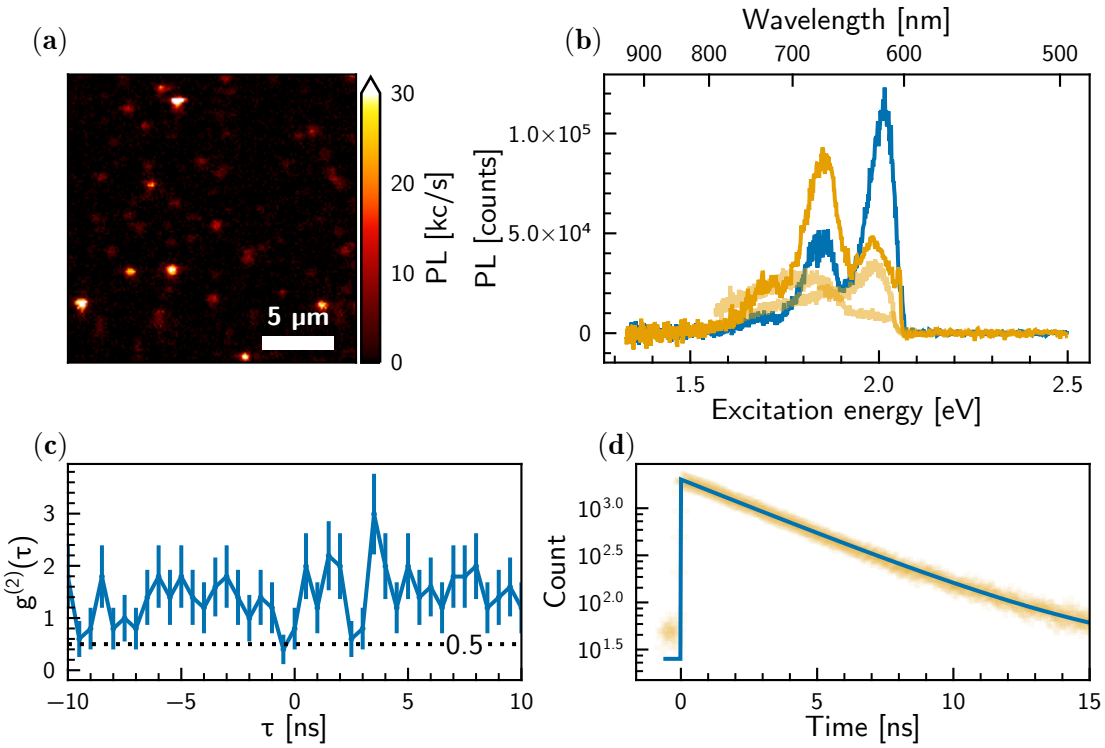

Figure 5.14: (**a**) Confocal fluorescence raster scan of spin-coated low density solution of $C_{96}tBu_8$ on $MAPbBr_3$. Excitation energy 2.09 eV, excitation intensity 0.370 kW/cm^2. (**b**) Emission spectrum of diffraction-limited spot on $MAPbBr_3$ (yellow line). The corresponding signal rate on the raster scan was $\sim$ 30 kc/s. A typical emission spectrum from $C_{96}tBu_8$ in polystyrene is plotted in solid blue. The spectrum in polystyrene is scaled to account for different exposure times and excitation intensities. (**c**) Second-order correlation ($g^{(2)}$) measurement on diffraction-limited spot (solid blue). The confidence interval is plotted with solid black lines. (**d**) Time-resolved photoluminescence trace of a diffraction-limited spot (light yellow cross), with the corresponding mono-exponential fit (solid blue) of characteristic time 3.65 ns.

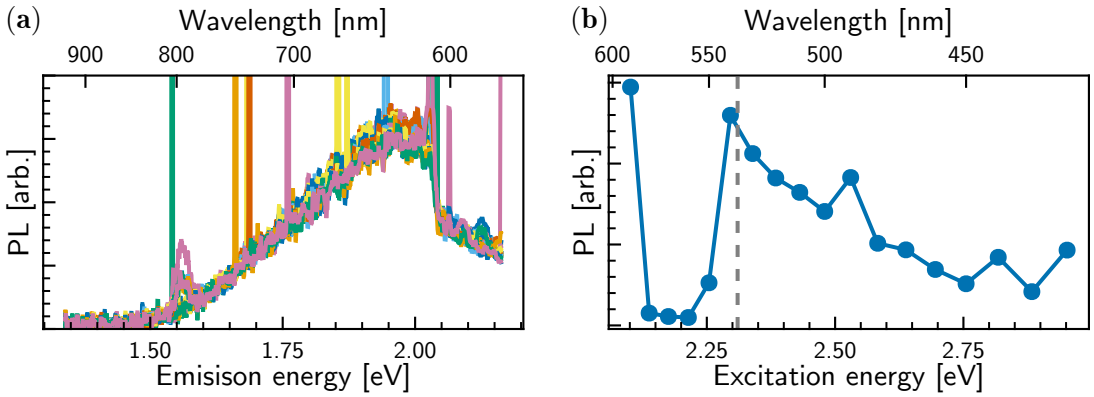

Figure 5.15: (**a**) Spectra over the region of interest for probing $C_{96}tBu_8$ emission spectrum at various excitation energies, uncorrected from excitation power. The vertical lines are due to cosmic rays hitting the detector during the exposure time (typically one minute). The emission is dominated by the photoluminescence of $MAPbBr_3$. (**b**) Resulting excitation spectrum for this system, obtained by integrating the spectra in (**a**). The vertical light gray dashed line represents the band gap of $MAPbBr_3$.

sured on a low density film of $C_{96}tBu_8$ on $MAPbBr_3$ for various excitation energies, including above the perovskite band-gap. The tail from the perovskite emission overlaps the emission originating from the GQD, making it impossible to record proper excitation spectra of the GQD. This is well illustrated by Figure 5.15b, which shows an excitation spectrum taken from photoluminescence integrated for energies under 2.07 eV. This corresponds to the excitation spectrum of the perovskite. The overlap of the photoluminescence of the perovskite over the region were photoluminescence of the GQD is expected makes it impossible to interpret the resulting excitation spectrum. This effect may be mitigated by using more local excitation routes, such as two photons absorption, or shifting the zero-phonon line of the GQD to lower energies by using bigger molecules. Another solution is to use thinner crystals, for example using pressed spin-coated perovskite thin films, or exfoliated crystals.

In conclusion, the decreasing zero-phonon line, accompanied by a $g^{(2)}(\tau = 0)$ greater than 0.5 despite diffraction-limited spots being visible, and an increased lifetime let us think of a possible formation of excimers, as we know from our study of $C_{96}tBu_8$ films that the GQDs can aggregate on the surface of the perovskite. Furthermore, it is possible to have excimers displaying structured emission, as shown in the case of covalently-bound molecular dimers in perylene-based systems [256] in Figure 5.16a on the next page. We know from the spectroscopy of $C_{96}tBu_8$ in

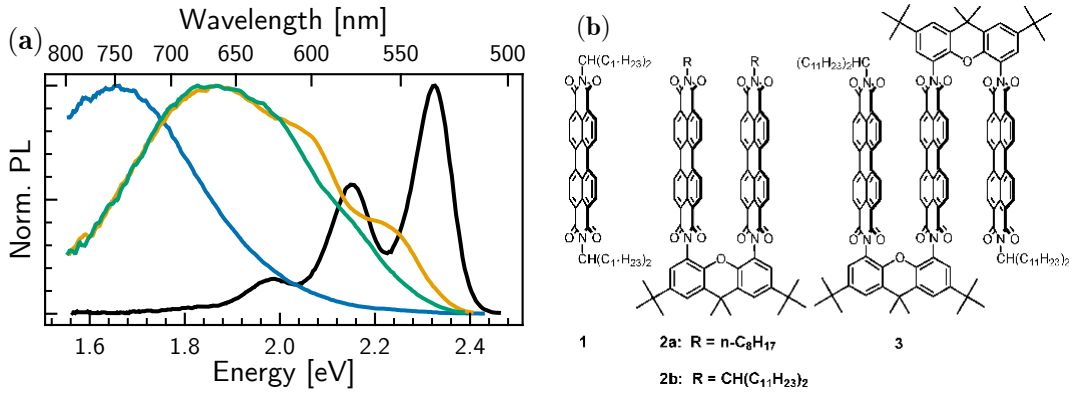

Figure 5.16: (**a**) Emission spectra of PDI monomer **1** (in black), of covalently bound molecular dimers **2a** (in blue) and **2b** (in green), and of covalently bound molecular trimer **3** (in yellow). (**b**) Structures of the molecules. Adapted from Ref. [256]

solution presented in Chapter 4 that those GQDs do not form stable dimers in solution. However, theoretical simulations made by our collaborators [205] showed that GQDs from the family of $C_{96}t\text{Bu}_8$ can form dimers, as long as there is a conformation where most *tert*-butyl groups point outwards, allowing the two GQDs to slide on each other. For $C_{96}t\text{Bu}_8$, the two most stable conformers in solution, UD-DU and UD-UD shown in Figure 5.17a and Figure 5.17b respectively, do not allow the formation of aggregates. Figure 5.17c shows a conformer of $C_{96}t\text{Bu}_8$ where all tBu groups point outwards, and that would allow the formation of dimers if the resulting structure was not unstable in solution due to molecular strain and thermal agitation.

Since the conformers that would allow for the formation of aggregates are not stable in solution, they must form during the drying of the film or through the excitation process. Interestingly, no trace of true single $C_{96}t\text{Bu}_8$ on the surface of $MAPbBr_3$ was found during our investigations. While that does not mean they do not exist, we can propose three paths explaining this observation.

The first explanation would be that the aggregated form is more stable in the solid state. As the film dries during spin-coating, the number of solvent molecules each GQD "sees" decreases. This means conformer states that used to be forbidden because they involved larger intramolecular strains would become accessible. In this scenario, single molecules encountering other single molecules during the drying process would be able to aggregate in stable dimer states.

A second explanation would be that single $C_{96}t\text{Bu}_8$ cannot fix easily at the surface of $MAPbBr_3$. As such, they would slide on the surface and get ejected from the substrate. A possible explanation would be that only some conformations, namely ones where the *tert*-butyl groups point outwards, can adhere to the per-

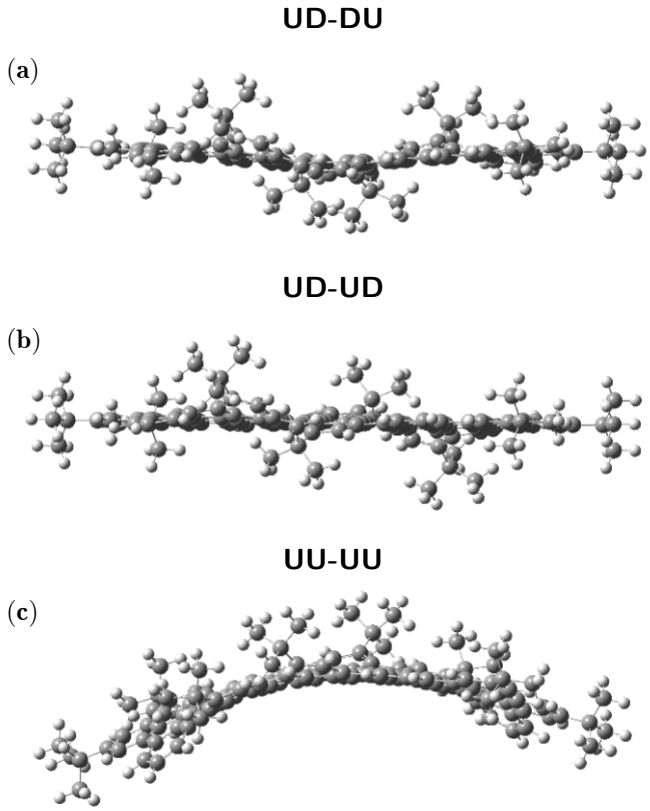

Figure 5.17: (**a**), (**b**) Stable conformers of $C_{96}tBu_8$ in solution. (**c**) $C_{96}tBu_8$ conformer allowing the formation of dimers in solution, although thermal agitation prevents it to be stable. **U** and **D** denote the relative positions of the tBu groups. Reproduced from Ref. [205].

ovskite surface. An alternate version of this scenario is that molecules adherence to the substrate is favored on specific, punctual, points such as surface defects. Thus, the molecules would end up at the same position on the substrate not because they form stable dimers towards the end of the drying process, but because of the few spots available to them on the crystal. This process would be similar to the self-assembly of porphyrin molecules on graphene substrate reported by Pham *et al.* [242].

A third and final scenario is that single $C_{96}tBu_8$ exist at the surface of $MAPbBr_3$ but are not visible on the confocal fluorescence microscope. That could be caused by transfers from single $C_{96}tBu_8$ to the substrate. That would mean that transfer is favored in the case of single molecules but is not in the case of aggregates, possibly because they have a lower zero-phonon line energy. In particular, in 2D perovskites, energy transfers between the organic cation and inorganic lattice are known to play a major role in the photophysics of the medium. For example Qin *et al.* [69] have shown that the choice of 2D spacer in $(NMA/PEA)_2FA_{n-1}Pb_nBr_{3n+1}$ (n=1 to 8) has a major impact on the external quantum efficiency of perovskite LEDs, because of the difference in triplet energy levels between NMA and PEA leading to triplet quenching when NMA is used. Conversely, use of tetrazine molecules in 2D perovskites is known to quench the emission of the perovskite [71], through a process that may involve energy transfers between both singlet and triplet states of the inorganic layer and the tetrazine. These studies focusing on 2D perovskites are of prime interest for the study of our system, even though our perovskite is 3D, because they involve organic molecules in close proximity to the inorganic lattice, much like the case of a GQD on a perovskite crystal. In this scenario, transfer may happen when $C_{96}tBu_8$ enters the triplet state, similarly to how photobleaching happens on glass substrates. Potential transfers between an organic molecule and a perovskite must however be examined with great caution, as spin properties of excitons in the inorganic part of the perovskite endure strong spin-orbit coupling because of the lead atoms.

The first scenario involves the formation of stable dimers, which matches poorly with the single-molecule-like emission spectrum that is often observed during emission spectrum dynamics recording, such as in Figure 5.19a. Conversely, in the third scenario, the fact that we do not observe single molecules on our perovskite crystals would mean that the transfer from the GQD to the perovskite is highly efficient. This conflicts with our study of the dynamics of the emission spectra, which shows stable monomer-like emission, sometimes for tens of seconds, as will be detailed in the next Subsection. We note, however, that this third scenario would benefit from a theoretical study of the GQD-perovskite system. At the time of writing this chapter, the second scenario thus appears the more likely. Perovskites crystals are known to possess many defects, that play a major role in their photophysical properties [61]. The presence of these defect at the surface would not be too surprising, and could form local traps for the molecule. This hypothesis may be tested

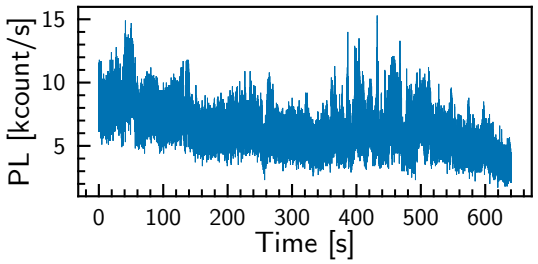

Figure 5.18: Integrated photoluminescence trace from a diffraction-limited spot. The trace was taken at the same time as the $g^{(2)}(\tau)$ curve in Figure 5.14c.

using very clean perovskites crystal, grown using techniques similar to atomic layer deposition.

5.3.4 Photoluminescence dynamics of diffraction-limited spots

Since the transient and nanosecond behaviors of $C_{96}tBu_8$ on $MAPbBr_3$ substrate showed a behavior unlike the ones observed in solution or at the single-molecule level, we decided to investigate the dynamics of the photoluminescence at the scale of the second.

Figure 5.18 shows the integrated photoluminescence trace recorded at the same time as the second-order correlation in Figure 5.14c. This plot features clear discrete dynamics during the first seconds of recording, similar to what is expected in single-molecule experiments. To deepen our understanding of these discrete behaviors, we investigated the spectra associated with these variations in photoluminescence intensity.

Photoluminescence spectra with short exposure time (typically 250 ms) were recorded on diffraction-limited spots. Figure 5.19a on the facing page shows a typical measurement result, where the photoluminescence spectra are plotted vertically and concatenated to show their evolution as time passes. Note that these spectra were taken with a higher excitation intensity ($\sim 2\,\mathrm{kW/cm^2}$) than those in *e.g.* Figure 5.14 ($\sim 0.37\,\mathrm{kW/cm^2}$). At this higher intensity of excitation, the count rate of the detector was $\sim 100\,\mathrm{kc/s}$.

First, even though binning time is much higher than in Figure 5.18, some blinking is still observable, as well as some spectral jitter. This is best seen in Figure 5.19b, which shows the evolution of the area under the spectrum curve over time. It also features the contributions of the spectra high- and low-energy parts. Noticeably, most of the higher frequency variations in the overall integrated photoluminescence seem to be explained by variations in the high-energy part of the spectrum. This is consistent with the observations made in Figure 5.19a: when the spectrum jitters, the main emission peaks suddenly appear at low energies, which makes the high-energy part of the spectrum appear dark. This is an indi-

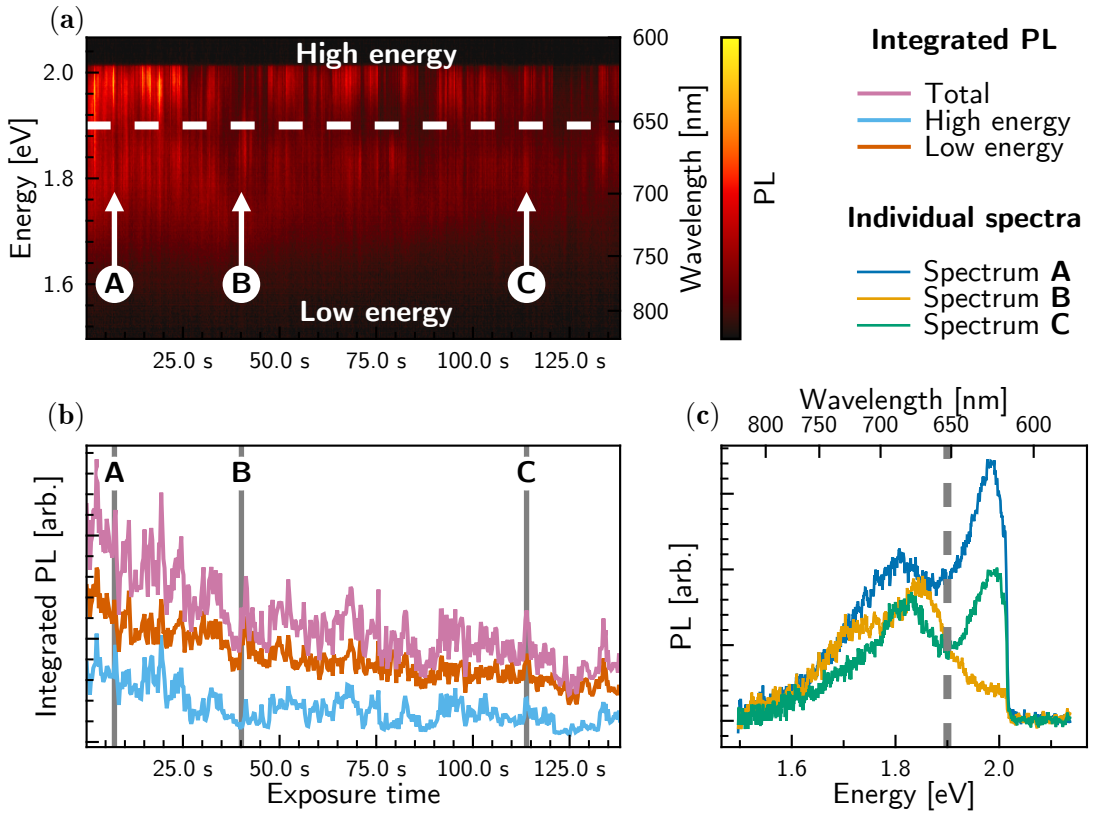

Figure 5.19: (**a**) Photoluminescence dynamics of a diffraction-limited spot under continuous excitation at 2.09 eV, 2.01 kW/cm^2. Each column of the heatmap corresponds to a spectrum taken with a 250 ms exposure time. The dashed white line materializes the limit between low and high energies at 1.88 eV. (**b**) Integrated photoluminescence traces for the entirety (reddish purple), high-energies part(sky blue), and low-energies part (vermilion) of the spectra in (**a**). (**c**) Chosen spectra taken at various timestamps in (**a**). The arbitrary limit between high and low energies is marked by the dashed gray line.

cation that the process at the origin of the spectral jittering may be affecting the zero-phonon line more than the other emission channels.

Then, to highlight the discrete jumps between states, the shape variations of the spectra can be investigated. Figure 5.19c features three spectra taken at timestamps (in progressing order) A, B and C, also highlighted in Figure 5.19a. The spectra at timestamps A and C show that the standard emission spectrum of a GQD is retrieved after the jump. The spectrum at timestamp B, corresponding to the jump, exhibits a different behavior than the other two spectra. Its main peak is located at $\sim 1.85\,\mathrm{eV}$ instead of $\sim 1.95\,\mathrm{eV}$ at the other timestamps. This is not attributable to some photobleaching of the molecule, since spectrum C highlights the recovery of the original emission spectrum. This hints at a temporary local environment or conformational change in the system.

5.3.5 Tools for the characterization of the dynamics

To have a more systematic view of the evolution of the photoluminescence signal, the dynamics are analyzed using two statistical signal analysis tools: the power spectral density and the Allan deviation, which I will briefly introduce. The methodology developed here is adapted from the methodology widely used in the domain of frequency stability analysis, and a more complete introduction can be found in Ref. [271]. In this framework, we try to classify the signal being analyzed using analogies with known noise classes.

Power Spectral density

Power spectral density is a well-known tool for statistical analysis of signals [272]. For a wide-sense-stationary random process $x(t)$, the Wiener-Khintchine theorem [273, 274] introduces its power spectral density $S(f)$ as

$$S(f) = \int_{-\infty}^{\infty} e^{2i\pi f\tau}\Gamma(\tau)\mathrm{d}\tau \tag{5.13}$$

Or equivalently

$$\Gamma(\tau) = \int_{-\infty}^{\infty} e^{-2i\pi f\tau}S(f)\mathrm{d}f \tag{5.14}$$

Where $\Gamma(\tau)$ is the signal's autocorrelation, defined as

$$\Gamma(\tau) = \langle x(t)x(t-\tau)^*\rangle \tag{5.15}$$

Where $\langle\cdot\rangle$ denotes the statistical average[3] and $\cdot^*$ is the complex conjugation operation.

[3]Note that for ergodic signals, this can be estimated by integrating $x(t)x(t-\tau)^*$ over sufficiently long times.

When the signal is also ergodic, the power spectral density can be written

$$S(f) = \lim_{T\to\infty} \frac{1}{T}|\hat{x}_T(f)|^2 \tag{5.16}$$

Where $\hat{x}_T$ is the Fourier transform of x calculated over an integrating time T.

Plotting $S(f)$ in log-log format allows us to quickly identify well-known distributions and infer statistical properties of signals.

The power spectral density can be estimated using the Welch method [275]. Briefly, this allows using overlapping samples of the input signal to reduce the variance of the periodogram estimator and, thus, of the power spectral density estimator.

Note that strictly speaking, the power-spectral density only applies to wide-sense stationary signals, that is, signals whose mean and autocovariance[4] do not vary with respect to time and whose second moment is finite for all time. However, we use it to analyze non-stationary processes, for example in the case of $1/f$ noise (which I will introduce later). This is possible because we window the signal before analysis. In its simplest form, the window used is a simple rectangular window, which means that we only record the signal for a finite amount of time. This means we can expect windowing effects in the power spectrum observed. Other analysis methods, such as Allan deviation, do not have this limitation.

Allan deviation

The Allan deviation, denoted $\sigma_y(\tau)$, is a less common analysis method. It was first introduced to assess the frequency stability of clocks[276, 277]. The idea is to calculate a two-samples variance. Given $y(t) = \frac{\nu(t)-\nu_n}{\nu_n}$ the fractional frequency of a clock, where $\nu(t)$ is the frequency function of the clock and ν_n the nominal frequency, the Allan variance is defined as

$$\sigma_y^2(\tau) = \frac{1}{2}\left\langle(\bar{y}_{n+1} - \bar{y}_n)^2\right\rangle \tag{5.17}$$

Where $\bar{y}_n = \frac{1}{\tau}\int_{t_n}^{t_n+\tau} y(t)\mathrm{d}t$ is the average over time τ of the fractional frequency, $\langle\cdot\rangle$ denotes the ensemble average, and t_n is the time step considered. From there, the Allan deviation is simply the square root of the variance.

Much like the Welch method improves the power spectral density measurement, there is a better estimator for the Allan deviation [278]. Indeed, as Equation 5.17 stands, for a time-series of averaged fractional frequencies acquired with time-step τ, the explicit calculation of σ_y^2 reads

$$\sigma^2(n\tau_0, M) = \frac{1}{2\frac{M-1}{n}} \sum_{i=0}^{\frac{M-1}{n}-1} (\bar{y}_{n(i+1)} - \bar{y}_{ni})^2 \tag{5.18}$$

[4]The covariance of the process with itself, *i.e.* $E[X_{t_1}X_{t_2}] - E[X_{t_1}]E[X_{t_3}]$ where X_t is the random process and $t_{1,2}$ are two times.

where M is the number of frequency samples in one fractional-frequency average, and $n \leq M - 1$. M is the discretized counterpart of integration time T. This estimator is inefficient in that, for large values of n, it only uses $1/n$ of the available data points. An alternative, unbiased estimator is

$$\sigma_y^2(n\tau, M) = \frac{1}{2n^2(M-2n+1)} \sum_{j=0}^{M-2n} \underbrace{\left(\sum_{i=j}^{j+n-1} y_{i+n} - y_i \right)^2}_{=[n\times(\bar{y}_{j+n}-\bar{y}_j)]^2} \tag{5.19}$$

This estimator behaves much better for large values of n, as it uses all available samples.

As mentioned before, the Allan deviation was first introduced to characterize the stability of clocks. For our purposes, however, we need to bend the use-case of this metric[279, 280]. Instead of calculating the fractional-frequency average, we will replace y_n in the above expressions with the measurement of our signal, *e.g.* the position of the zero-phonon line or the count rate on the photodetector.

A short typology of noises

The analysis of the following photoluminescence dynamics will proceed by treating signal variations as noises. In particular, we will be interested in three kinds of noises, shown in Figure 5.20.

White noise This kind of noise is shown in blue in Figure 5.20a. It is characterized by a constant power spectral density, as shown in Figure 5.20b, and an Allan deviation proportional to the reciprocal of the square root of τ, as shown in Figure 5.20c. The origins of this noise are multiple, one of them being shot noise resulting from the fluctuation of the number of photons detected on a photodetector.

Random telegraph noise Also called "burst" noise. It consists of instantaneous transitions between two or more levels. It can be modeled by a telegraph process, where the probability of transitioning from one state to the other after some time is governed by an exponential law. Note that the characteristic time of transition from state a to state b needs not to be the same as the one for the transition from state b to state a. An example of such noise is shown in Figure 5.20a. The power spectral density of random telegraph noise is Lorentzian and is characterized in log-log plots such as in Figure 5.20b by a -2 slope at higher frequencies. It can be shown [281] that the power spectral density of a random telegraph process reads:

$$S_{RTN}(f) = \frac{4w_a w_b (x_a - x_b)^2 \tau}{1 + (2\pi f)^2 \tau^2} \tag{5.20}$$

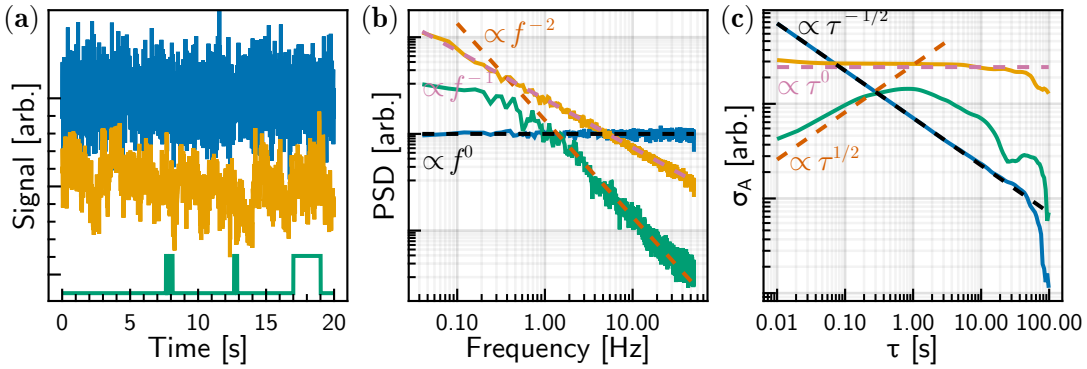

Figure 5.20: Examples of computer-generated noises. (**a**) Examples of white noise (blue line), $1/f$ (or "flicker") noise (yellow line), and telegraphic noise (green line). The latter has a characteristic transition time from level zero to level one of 4 s and from level one to level zero of 0.4 s. (**b**) Power spectral densities of the signals in subfigures (**a**), using the same color code. Characteristic power laws are given in dashed black for white noise, dashed pink for $1/f$ noise, and orange for telegraph noise. (**c**) Allan deviations of the signals in (**a**) using the same color code. Characteristic power laws for white, $1/f$, and telegraph noises are given using the same color code as in (**b**).

where $\tau^{-1} = \lambda_{ab} + \lambda_{ba}$ is the total rate of transition, $w_{a,b} = \lambda_{b,a} \times \tau^{-1}$ are the probabilies of occupancy of states a and b, $\lambda_{a,b}$ are the transition rates from a to b and from b to a, and $x_{a,b}$ are the values of the signal in states a and b. Conversely, random telegraph noise is best detected in Allan deviation plots thanks to its proportionality to the square root of τ on shorter time scales, as shown in Figure 5.20c. This kind of noise can be observed in many physical systems, *e.g.* two-level resistance fluctuations in clean metallic constrictions [282], or in metal-oxide-semiconductor field-effect transistors [283].

Flicker noise This is also referred to as "pink noise" or "$1/f$" noise. A sample realization is in yellow in Figure 5.20a. Note that this signal is not stationary. The power spectral density of this noise is shown in Figure 5.20b and is proportional to $\frac{1}{f}$. Its Allan deviation is shown in Figure 5.20c and is constant. This kind of noise arises in many physical systems, and determining the exact behavior at very low frequencies is an active research area [284, 285]. It may be displayed in systems involving many random telegraph process sources with various relaxation times [286]. $1/f$ noise may also arise from the interaction between a two-state fluctuator with local defects [287], causing the two-state system's properties to change with time.

5.3.6 Interpretation of the PL dynamics of diffraction-limited emitters

Dynamics of the integrated photoluminescence

Figure 5.21 shows a typical integrated photoluminescence trace of a single $C_{96}tBu_8$ in polystyrene matrix and from a diffraction-limited spot at the surface of $MAPbBr_3$ crystals where the GQDs have been deposited. The integrated photoluminescence of a single $C_{96}tBu_8$ in polystyrene shown in Figure 5.21a is very stable and is shot-noise-limited, which is expected for single molecule emitters [279]. On the other hand, the integrated photoluminescence trace of a diffraction-limited spot on $MAPbBr_3$ shown in Figure 5.21b presents a richer behavior, with discrete jumps and variations in intensity. The difference between the two traces is better understood in the frequency domain, shown in Figure 5.21c. The emission from a single molecule of $C_{96}tBu_8$ displays a nearly constant power spectral density, which is well in accordance with a white noise-dominated signal due to shot noise. On the contrary, the shortest frequencies of the signal in Figure 5.21b are dominated by $1/f$ noise, up until $\sim 5\,\mathrm{Hz}$, where white noise takes over the primary dynamics, at the same level as for single molecule emission. The behavior at low frequencies illustrates the wandering behavior of the integrated photoluminescence signal, while the fact that highest frequencies are dominated by white noise at the same level as for a single molecule in a polystyrene matrix means the photoluminescence

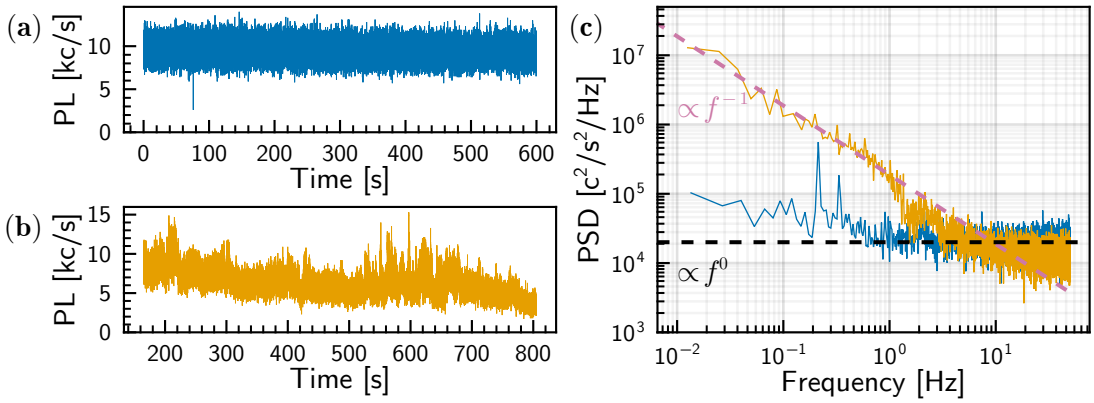

Figure 5.21: (**a**) Typical photoluminescence trace of a single $C_{96}tBu_8$ in polystyrene matrix. (**b**) Photoluminescence trace from a diffraction-limited spot on $MAPbBr_3$. (**c**) Power spectral density of signal (**a**) (blue line) and signal (**b**) (yellow line). Characteristic power laws are given as a guide to the eye using the same color codes as in Figure 5.20b.

signal levels are comparable, *i.e.* the number of emitters producing the time trace in Figure 5.21b is close to unity.

Figure 5.22 on the next page features several integrated photoluminescence traces collected on diffraction-limited emitters on various samples. The figure also shows the power spectral densities and Allan deviations of the traces. The relevance of frequency and time domain analysis is striking here. Indeed, the $1/f$ feature in the frequency domain is clearly apparent in the plots, with some traces also displaying hints of shot-noise-induced white noise at the highest frequencies. Conversely, the Allan deviation is almost flat, which is expected for signals dominated by $1/f$ noise. For longer time scales, the Allan deviation sometimes features an increase proportional to $\sqrt{\tau}$, which corresponds to the discrete jumps shown in the time traces. Finally, the presence of white noise at higher frequencies can also be found at the shortest time scales of the Allan deviations.

It is known that $1/f$ noise can originate from the combination of multiple sources of random telegraph noises. For example trapping and de-trapping of charge carriers in a doped semiconductor can lead to the observation of 1/f noise [285]. In that context, it is tempting to attribute the presence of $1/f$ noise in the time traces of our samples to the combination of random telegraph noises originating from the coupling and de-coupling of excimers on the perovskite surface. The variability in the random telegraph noise sources may originate from the presence of multiple excimers, or from variability in the strength of the excimer coupling, or a combination of both. We are currently preparing a study of the dynamics against the PL intensity of the emitter under scrutiny to try to verify this hypothesis.

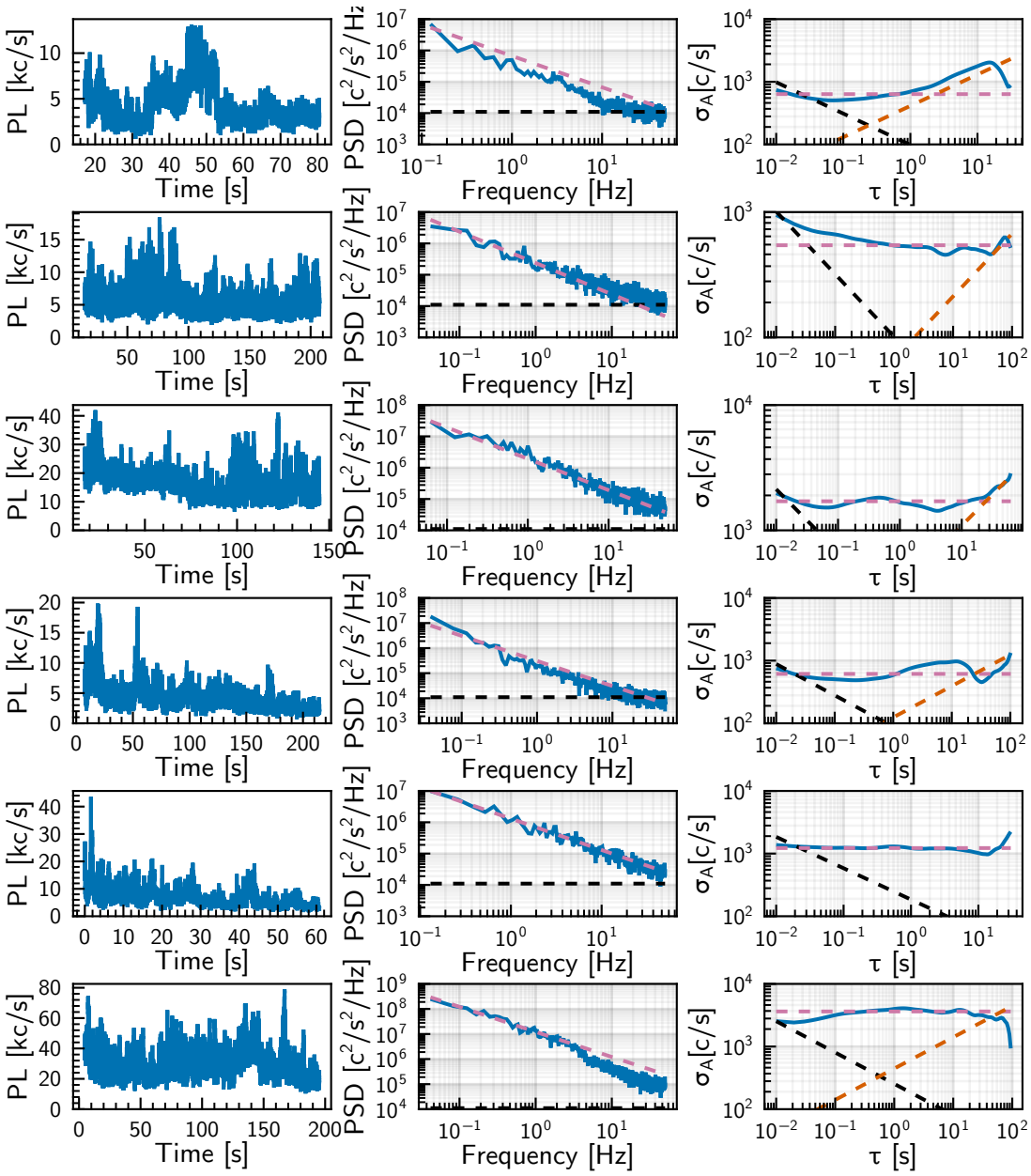

Figure 5.22: Time traces taken on multiple diffraction-limited emitters from various samples. The excitation intensity was approximately 0.5 kW/cm^2. On each row is the time trace, its power spectral density and Allan deviation. Power law tendencies are plotted using the same color code as in Figure 5.20: black is white noise, pink is $1/f$ noise and orange is random telegraphic noise.

Dynamics of the zero-phonon line

Similarly to analyzing the integrated photoluminescence time traces, we tried to interpret the evolutions of the photoluminescence spectra over time under continuous excitation using the abovementioned tools.

Figure 5.23 on the following page presents the evolution of photoluminescence spectra of diffraction-limited emitters over time under continuous excitation. The spectra in Figures 5.23a, 5.23d, and 5.23g are taken on different spots but with increasing illumination intensity. Each individual spectrum was fitted using a two-Lorentzian model similar to the one used in Chapter 4, yielding a curve of the position of the zero-phonon line over time. Those signals can then be analyzed through their power spectral densities, shown in Figures 5.23b, 5.23e, and 5.23h, and Allan deviation, shown in Figures 5.23c, 5.23f, and 5.23i.

The spectral trace taken at lower excitation intensity ($\sim 0.26\,\mathrm{kW/cm^2}$) suffers from a high exposure time, resulting in low sampling frequency. It seems, however, that the power spectral density and Allan deviation are dominated respectively by f^0 and $\tau^{-1/2}$ components, meaning that the positions of the zero-phonon lines are mostly dominated by white noise. The situation becomes more interesting in Figures 5.23d and 5.23g. The power spectral density of the zero-phonon line in Figure 5.23d, shown in Figure 5.23e, presents a slight dip at $\sim 0.2\,\mathrm{Hz}$ that could be interpreted as a $1/f$ behavior. This is further highlighted by the Allan deviation in Figure 5.23f, where a clear τ^0 component takes over the $\tau^{-1/2}$ component that dominates at shorter times. This τ^0 component is typical for $1/f$ noise. An even richer dynamics is displayed by the zero-phonon line in Figure 5.23g, excited at $\sim 2.09\,\mathrm{kW/cm^2}$. Its power spectral density in Figure 5.23h features slopes between -1 and -2 that could be consistent with some components of the Allan deviation in Figure 5.23i, and could highlight the flickering position of the zero-phonon line in this measurement.

As for the dynamics of the integrated photoluminescence, we want to characterize better the correlation of the dynamics to the intensity of the photoluminescence. The experimental limiting factor here is the integration time of the spectrometer. We plan to overcome this limitation by using single photon counters preceded by a spectral filter, which will allow us to measure the dynamics of specific parts of the spectrum with high resolution in time.

Single excimer-like states of $C_{96}tBu_8$ on $MAPbBr_3$ crystals

Integrated photoluminescence traces where the signal features additional behaviors besides the pure white shot-noise is observed throughout the literature. Hofkens *et al.* [288] report the coupling of chromophores that functionalize a single dendrimer, shown in Figure 5.24a on page 181. They observe photoluminescence traces that feature various discrete levels of count rate and attribute them to couplings and de-couplings of chromophores. Furthermore, they report changes in emission spec-

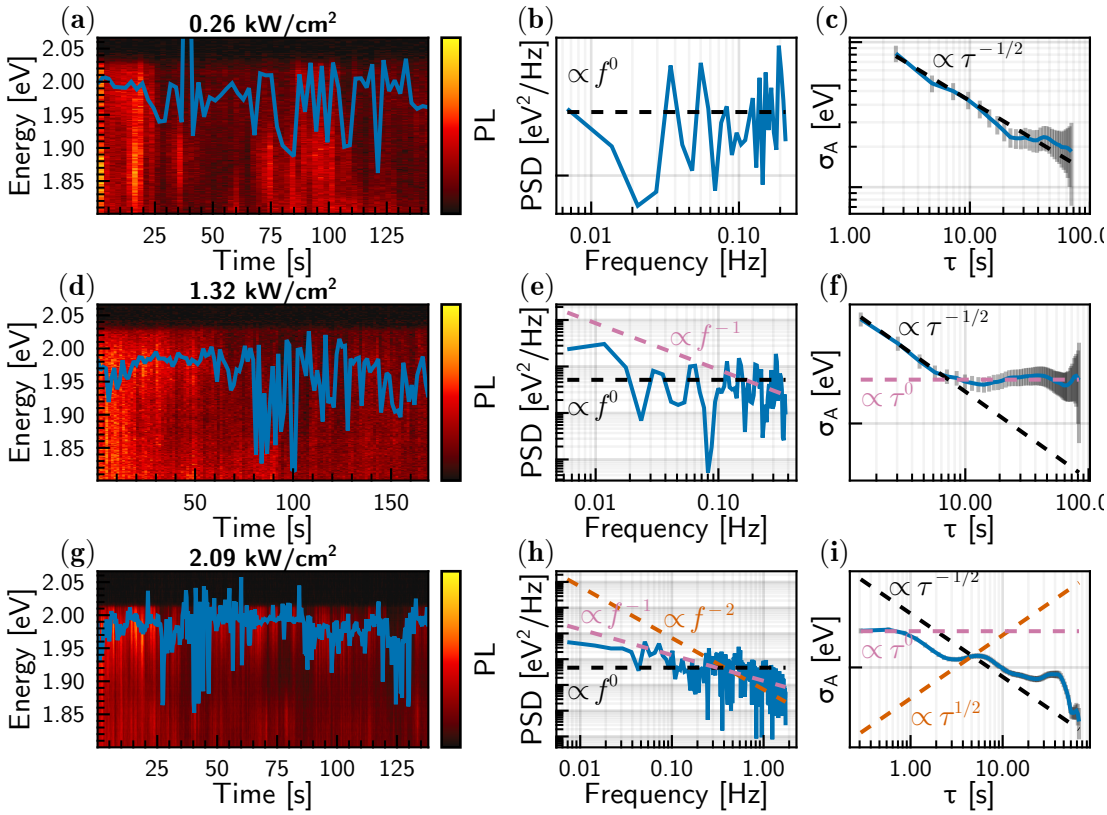

(j)

ZPL [eV]	Peak sep. [eV]	Ampl. 1	Ampl. 2	Γ_1 [eV]	Γ_2 [eV]	filt. [eV]
1.98	0.04	0.170	0.9	0.5	0.05	0.1

Figure 5.23: (**a**), (**d**), and (**g**) Photoluminescence dynamics of diffraction limited spots. Excitation intensities were respectively 0.26 kW/cm^2, 1.32 kW/cm^2 and 2.09 kW/cm^2, all at 2.09 eV. Each spectrum was fitted using a two-Lorentzian lines model that accounts for the transmission of the setup. Parameters of the model are given in Table (**j**). The resulting zero-phonon line positions are plotted in blue. (**b**), (**e**), and (**h**) Power spectral densities of the zero-phonon lines. Some characteristic power laws are given as a guide to the eye, with the same color code as in Figure 5.20. (**c**), (**f**), and (**i**) Allan deviations of the zero-phonon lines. Characteristic power laws are given as a guide to the eye, using the same color code as in Figure 5.20. Error bars are plotted in light gray. (**j**) Input parameters for Levenberg-Marquardt algorithm used to fit the data. $\Gamma_{1,2}$ are the peaks' respective half width at half maxima. The cutoff energy of the filter can be adjusted within the model to account for small misalignments.

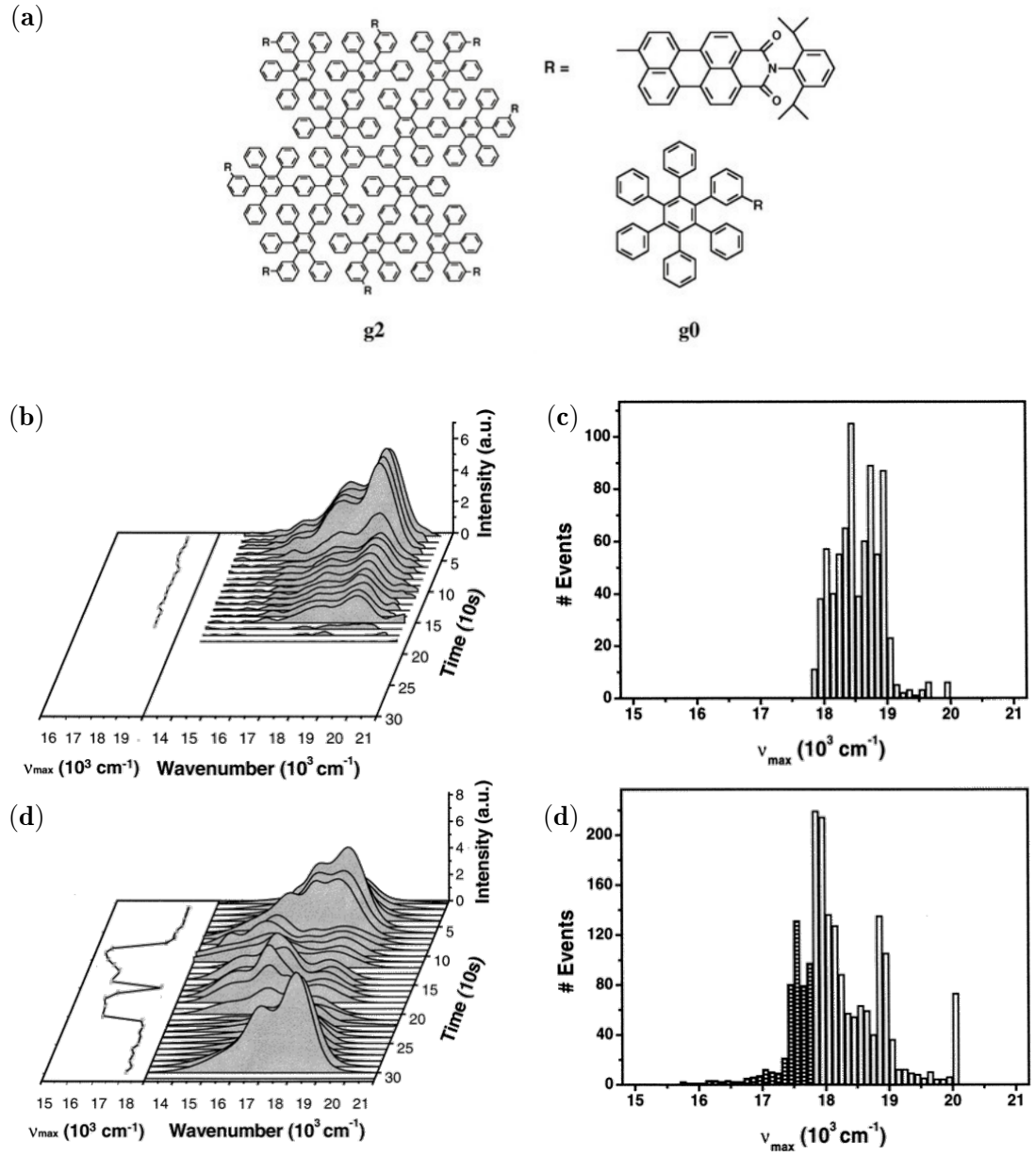

Figure 5.24: (**a**) Molecules studied by Hofkens *et al.* [288]. **g0** is a small dendrimer functionalized with a unique chromophore, while **g2** corresponds to a bigger dendrimer functionalized with eight chromophores. (**b**) Evolution of the emission spectra of **g0** over time. (**c**) Histogram of the positions of the maximum of photoluminescence for **g0**. (**d**) Evolution of the emission spectrum of **g2** over time, featuring discrete jumps towards lower energy regions. (**e**) Histogram of the positions of the maximum of photoluminescence for **g2**. The histogram shows a broader distribution towards lower energies, corresponding to spectra jumps to these regions. Reproduced from Ref. [288].

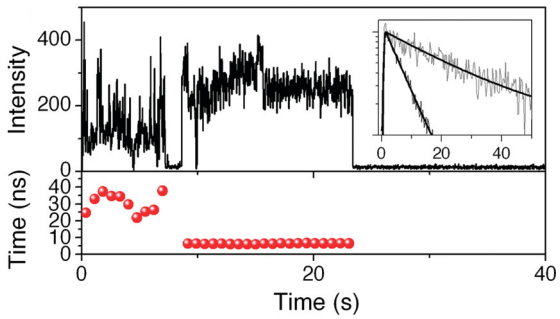

Figure 5.25: Single molecule fluorescence behaviors of two covalently bound cofacial perylenes. The molecule is the same as molecule **2b** in Figure 5.16b. The molecule is excited by a picosecond pulsed 470 nm laser diode, with repetition rate 10 MHz. The measurement is akin to a time-tagged measurement, as described in Chapter 2 (Experimental Methods). This allows recording the evolution of the intensity of the emitter, as well as of the characteristic photoluminescence lifetime. The solid black line is the intensity, while the scatter plot corresponds to the evolution of the fitted fluorescence decay times. Reproduced from Ref. [264].

tra over time similar to the one we observed when the chromophores couple and de-couple. Figure 5.24d shows the wandering dynamics of the emission spectra from such system. As a point of comparison, the emission spectra from a single chromophore is shown in Figure 5.24b. As illustrated by the histograms of the positions of the main emission peak, shown in Figure 5.24c and Figure 5.24e for a single chromophore and for coupling chromophores respectively, the spectrum tends to wander towards the low-energy region when coupling.

Flickering integrated photoluminescence curves are also reported by Odoi *et al.* [289]. In studying,7-bis(3,4,5-tri-methoxyphenyl ethenyl)fluorenone (OFOPV) at the single-site level, they could display red emission due to dimer or larger aggregate formation. Photoluminescence traces originating from red emission are well in accordance with the photoluminescence traces reported in Figure 5.21b. The flickering behavior can be correlated with variations in the photoluminescence lifetime, which is an indicator for excimer emission. Stangl *et al.* [290] report on the study of bichromophoric systems of cofacial oligomers and show how closer-spaced oligomers have a more spread-out, $1/f$-like evolution of the lifetime. More importantly, Yoo *et al.* [264] studied cofacial perylene diimide (PDI) oligomers consisting of two PDIs, corresponding to molecule **2b** in Figure 5.16b on page 167. They report the parallel evolution of integrated photoluminescence and fluorescence lifetime. An example trace is shown in Figure 5.25. The situation when the two PDIs are not coupled, characterized by a short decay time, displays a fairly steady fluorescence rate. In contrast, the coupled state, characterized by longer decay times, shows similar behaviors to the trace we observed.

Honmou *et al.* [291] report on photoluminescence and electroluminescence of individualized polyfluorene chains confined in vertical cylinders of a phase-separated block copolymer. For both excitation methods, zero-phonon line flickering was observed and attributed to excimers, albeit they note the emission of keto defects[5] could also explain it. The former, however, appears to be their favorite explanation. In this scenario, the spectral jumps likely result from local conformational changes of the chains between states allowing aggregates formation from neighboring chains and states that do not.

The reports from the litterature are consistent with our measurements of the dynamics of the excimer-like diffraction-limited spots at the surface of $MAPbBr_3$ perovskites. We observe clear $1/f$ behaviors of both the photoluminescence intensity and the zero-phonon line of these emitters. We think this can be attributed to coupling and de-coupling of excimers, but this needs to be confirmed by further experiments. In particular, we would like to observe the transition between a state where the dynamics is dominated by discrete jumps (random telegraph noise) and one where $1/f$ noise dominates (flickering). Using time-tagged measurements, we also hope to track the evolution of the fluorescence lifetime over time and correlate that to the dynamics of the photoluminescence intensity. In particular, we expect the photoluminescence lifetime to appear longer when the intensity is flickering, which would reproduce the result obtained on covalently-bound excimers.

[5] A keto defect is a local modification of the chemistry of polyfluorene polymers that efficiently traps excitons [292].

Conclusion

The advanced characterization of $C_{96}tBu_8$ and the high purity of our samples allowed us to experiment with the GQD environment to observe its effect on the molecule, as well as developing a new technique to produce flat, millimeter-sized, $MAPbBr_3$ crystals. We investigated the possibility of coupling $C_{96}tBu_8$ to perovskite crystals.

We first observed the formation of films and confirmed that we were able to deposit GQDs at the surface of $MAPbBr_3$ without altering the chemistry of the sample, and with good stability in emission compared to other substrates such as glass. The emission spectra of films are consistent with emission from excimer states in a H-aggregate-like configuration. This study could be extended by going to cryogenic temperature, as emission in excimers with this geometry is known to be mediated by vibronic transitions.

Then, when lowering the density of emitters at the surface of the crystal, we showed that the photophysics of diffraction-limited emitters is consistent with excimer physics. However, we could not investigate the excitation spectra of those emitters because of experimental limitations caused by the photoluminescence of $MAPbBr_3$ overlapping with the signal of the emitters. These limitations may be overcome using more local proping techniques, such as two-photons excitation or near-field collecion. Another route would be to increase the size of the GQDs, *e.g.* using $C_{132}tBu_{12}$, pushing even more to the red region of the photoluminescence, and diminishing the overlap with the tail of the perovskite's photoluminescence spectrum.

In photovoltaics and light-emitting diodes applications, understanding the physics at the interface of perovskites and transport layers is critical to optimizing devices' performances and stability [112]. Our results are a first step towards using graphene quantum dots as a probe in direct, atomically-close, proximity of the crystal. Halide perovskites are known to exhibit processes such as ions migrations [293], which involve moving charges. Since excimer photophysics involves charge transfer, it is possible that the flickering behavior of the photoluminescence that we report would be sensitive to ions migration. Thorough characterization of the flickering in presence of local electric field may thus lead to the realization of an exquisite probe to the local movements of ions at the surface of perovskite crystals.

The reason for the formation of excimers at the surface of perovskites is not completely understood at the time of concluding this chapter. Notably, we do not know if the formation of excimers, even at single-molecule-level dilution ratio of the solution deposited on the substrate, is due to the nature of the substrate. Our group is currently experimenting with substrates with a thin layer of Al_2O_3, deposited by atomic layer deposition techniques. Spin-coating solutions of $C_{96}tBu_8$ on those substrates has so far resulted in photoluminescence raster scans consistent with the presence of films of $C_{96}tBu_8$ on the substrate, with emission spectra similar

to the one we report for films of GQDs on perovskite substrates. The Al_2O_3 substrates can also be capped with a second layer of Al_2O_3 after the GQDs have been deposited, which should allow us to prevent photobleaching of the molecules through interaction with the ambient atmosphere. Comparison of the physics of GQDs on those substrates with the physics on perovskite substrates could provide us with precious hints to the understanding of the latter.

General Conclusion

The study of nano-objects is a research topic at the crossroads of multiple fields and allows the collaboration of researchers with a wide variety of expertise. In this thesis, I focused on the study of halide perovskites, in particular $CsPbBr_3$ nanocrystals, and on graphene quantum dots. Both materials hold great promises because of the possibility of chemical engineering they offer.

In collaboration with Cédric Mayer, we developed a synthesis method for $CsPbBr_3$ nanocrystals. This method allows the synthesis of remarkably well-calibrated nanocrystals at room temperature with soft chemistry. I showed that the optical properties of the nanocrystals, both in solution and in thin films are similar to the properties of $CsPbBr_3$ nanocrystals synthesized using methods already reported in the literature. Moreover, the improved stability of nanocrystal films makes it promising for applications. Since then, Cedric Mayer kept improving the synthesis. In particular, he investigated the role of the amine cation used to slice big polydisperse tens-of-nanometer wide crystals into highly calibrated 10 nm nanocrystals. Early results suggest that a careful choice of amine group allows the synthesis of nanocrystals with a near unity quantum yield in solution. In terms of applications, early results in our collaboration with the group of Johann Bouclé at XLIM suggest that those nanocrystals can be used to build green-emitting LEDs by embedding the nanocrystals in a polymer film.

My contribution to the study of the family of rod-shaped graphene quantum dots intervened after most of the characterizations in solution were already performed. I could however highlight the impressive photoluminescence quantum yield of those objects in solution. I then focused on the study of $C_{96}tBu_8$ at the single-molecule level in a polystyrene matrix. This first demonstrated the high purity of our samples. It also highlighted the good stability of those emitters at room temperature and strengthened some of the theoretical results obtained on that molecule. The low blinking rate could be explained by the low intersystem coupling rate unveiled by a careful study of the second-order correlation function measured on single emitters. This same study also showed that the de-excitation rate of $C_{96}tBu_8$ in the polystyrene matrix is lower than in solution, which could hint at the effects of the matrix on the photophysics of those objects. The environment is expected to influence heavily these atomically-thin objects. Ongoing studies on this family of graphene quantum dots focus on embedding them in other environments, such as molecular crystals or aluminum oxide thin layers.

In the framework of this study, the influence of the environment on the graphene quantum dots has particularly been explored for $MAPbBr_3$ halide perovskite sub-

strates. I showed that $C_{96}tBu_8$ films deposited on that surface present satisfactory stability, as opposed to *e.g.* glass substrate. However, I showed that the quantum dots on the perovskite substrate behave like excimers, with an emission red-shifted and broadened. Reducing the concentration of emitters up to the point where diffraction-limited fluorescence spots were observed on our confocal microscope did not allow us to observe single-photon emission. However, we could observe discrete dynamics in the time domain, such as sudden red-shifts of the main emission peak of the GQD. More advanced characterizations in the time domain showed that the dynamics are dominated by $1/f$ noise. For this thesis, we were limited by the temporal resolution of our spectrometer to study the time dynamics as a function of the energy of emission. Ongoing work on this system focuses on using the two avalanche photodiodes of the Hanbury Brown-Twiss interferometer shielded with band-pass filters to record simultaneously the dynamics in two different regions of the spectrum. We also want to perform experiments with pulsed sources to perform time-tagging experiments and record the fluorescence lifetime as a function of time. This would provide a solid point of comparison with experiments reported in the literature on single-molecule excimers.

A very promising field of application for nano-emitters is the possibility of coupling them to active materials and photonic structures. In that respect, $CsPbBr_3$ nanocrystals are good candidates for embedding in large Si-based photonic structures, as their small size could allow a high degree of flexibility in the shape of the structure compared to bulk perovskites. At the single-object level, both $CsPbBr_3$ nanocrystals and $C_{96}tBu_8$ could benefit from studies of single-objects embedded in photonic cavities. A possible route consists of embedding the emitters in polymer-based photonic structures. Another possible solution is to use matrices such as hexagonal boron nitride. In all cases, this highlights the necessity for a good understanding of the interaction between the emitters and the matrix.

Bibliography

[1] *The Nobel Prize in Chemistry 2023*. URL: https://www.nobelprize.org/prizes/chemistry/2023/summary/ (cited on page 1).

[2] Akihiro Kojima *et al.* 'Organometal Halide Perovskites as Visible-Light Sensitizers for Photovoltaic Cells'. In: *Journal of the American Chemical Society* 131.17 (May 2009), pp. 6050–6051. DOI: 10.1021/ja809598r (cited on pages 1, 13).

[3] Hui-Seon Kim *et al.* 'Lead Iodide Perovskite Sensitized All-Solid-State Submicron Thin Film Mesoscopic Solar Cell with Efficiency Exceeding 9%'. In: *Scientific Reports* 2.1 (Aug. 2012), p. 591. DOI: 10.1038/srep00591 (cited on pages 1, 13).

[4] Kebin Lin *et al.* 'Perovskite Light-Emitting Diodes with External Quantum Efficiency Exceeding 20 per Cent'. In: *Nature* 562.7726 (Oct. 2018), pp. 245–248. DOI: 10.1038/s41586-018-0575-3 (cited on page 1).

[5] Felix Deschler *et al.* 'High Photoluminescence Efficiency and Optically Pumped Lasing in Solution-Processed Mixed Halide Perovskite Semiconductors'. In: *The Journal of Physical Chemistry Letters* 5.8 (Apr. 2014), pp. 1421–1426. DOI: 10.1021/jz5005285 (cited on page 1).

[6] Ferdinand Ledee. 'Cristallisation et fonctionnalisation de pérovskites hybrides halogénées à 2-dimensions pour le photovoltaïque et l'émission de lumière'. PhD thesis. Université Paris Saclay (COmUE), Nov. 2018 (cited on pages 1, 19).

[7] Loredana Protesescu *et al.* 'Nanocrystals of Cesium Lead Halide Perovskites (CsPbX3, X = Cl, Br, and I): Novel Optoelectronic Materials Showing Bright Emission with Wide Color Gamut'. In: *Nano Letters* 15.6 (June 2015), pp. 3692–3696. DOI: 10.1021/nl5048779 (cited on pages 1, 16, 18, 20, 82, 89, 91, 92).

[8] A. Brehier *et al.* 'Strong Exciton-Photon Coupling in a Microcavity Containing Layered Perovskite Semiconductors'. In: *Applied Physics Letters* 89.17 (Oct. 2006), p. 171110. DOI: 10.1063/1.2369533 (cited on page 1).

[9] Paul Bouteyre *et al.* 'Directing Random Lasing Emission Using Cavity Exciton-Polaritons'. In: *Optics Express* 28.26 (Dec. 2020), pp. 39739–39749. DOI: 10.1364/OE.410249 (cited on pages 1, 20).

[10] K. S. Novoselov *et al.* 'Electric Field Effect in Atomically Thin Carbon Films'. In: *Science* 306.5696 (Oct. 2004), pp. 666–669. DOI: 10.1126/science.1102896 (cited on pages 1, 7).

[11] E. Clar. *Polycyclic Hydrocarbons*. Berlin, Heidelberg: Springer, 1964 (cited on pages 1, 26).

[12] C. Toninelli *et al.* 'Single Organic Molecules for Photonic Quantum Technologies'. In: *Nature Materials* 20.12 (Dec. 2021), pp. 1615–1628. DOI: 10.1038/s41563-021-00987-4 (cited on pages 1, 36).

[13] Shen Zhao. 'Propriétés optiques de nanorubans et boites quantiques de graphène'. PhD thesis. Université Paris Saclay (COmUE), Sept. 2018 (cited on pages 1, 33, 73, 127, 133, 135, 137).

[14] Thomas Liu. 'Optical Spectroscopy of Graphene Quantum Dots'. These de Doctorat. université Paris-Saclay, Mar. 2023 (cited on pages 1, 22, 46, 56, 73, 104, 109, 120).

[15] Mark Fox. *Optical Properties of Solids*. 2 ed., (with corr.) Oxford Master Series in Physics Condensed Matter Physics 3. Oxford: Oxford Univ. Press, 2012 (cited on pages 3, 4, 8–10, 12, 23).

[16] Neil W. Ashcroft and N. David Mermin. *Solid State Physics*. Saunders College. 1976 (cited on pages 4, 5, 7).

[17] Peter Y. Yu and Manuel Cardona. 'Electronic Band Structures'. In: *Fundamentals of Semiconductors: Physics and Materials Properties*. Ed. by Peter Y. Yu and Manuel Cardona. Graduate Texts in Physics. Berlin, Heidelberg: Springer, 2010, pp. 17–106. DOI: 10.1007/978-3-642-00710-1_2 (cited on page 5).

[18] James R. Chelikowsky and Marvin L. Cohen. 'Nonlocal Pseudopotential Calculations for the Electronic Structure of Eleven Diamond and Zinc-Blende Semiconductors'. In: *Physical Review B* 14.2 (July 1976), pp. 556–582. DOI: 10.1103/PhysRevB.14.556 (cited on page 5).

[19] Claude Cohen-Tannoudji, Bernard Diu, and Franck Laloë. *Mécanique Quantique*. Company édition CNRS/EDP Sciences. 2018 (cited on pages 6, 125).

[20] Xu Du *et al.* 'Approaching Ballistic Transport in Suspended Graphene'. In: *Nature Nanotechnology* 3.8 (Aug. 2008), pp. 491–495. DOI: 10.1038/nnano.2008.199 (cited on page 7).

[21] Tadao Fukuroi and Toshio Ikeda. 'Electrical Resistivity and Hall Effect of Noble Metals at Very Low Temperatures'. PhD thesis. Tohoku University, 1956, pp. 205–212 (cited on page 7).

[22] J. Frenkel. 'On the Transformation of Light into Heat in Solids. I'. In: *Physical Review* 37.1 (Jan. 1931), pp. 17–44. DOI: 10.1103/PhysRev.37.17 (cited on page 8).

[23] Gregory H. Wannier. 'The Structure of Electronic Excitation Levels in Insulating Crystals'. In: *Physical Review* 52.3 (Aug. 1937), pp. 191–197. DOI: 10.1103/PhysRev.52.191 (cited on page 8).

[24] Alain Aspect *et al. Quantum Optics 1. Lasers*. École Polytechnique (cited on pages 9, 125).

[25] M. D. Sturge. 'Optical Absorption of Gallium Arsenide between 0.6 and 2.75 eV'. In: *Physical Review* 127.3 (Aug. 1962), pp. 768–773. DOI: 10.1103/PhysRev.127.768 (cited on pages 10, 11).

[26] R. J. Elliott. 'Intensity of Optical Absorption by Excitons'. In: *Physical Review* 108.6 (Dec. 1957), pp. 1384–1389. DOI: 10.1103/PhysRev.108.1384 (cited on page 11).

[27] D. D. Sell and P. Lawaetz. 'New Analysis of Direct Exciton Transitions: Application to GaP'. In: *Physical Review Letters* 26.6 (Feb. 1971), pp. 311–314. DOI: 10.1103/PhysRevLett.26.311 (cited on page 11).

[28] Michele Saba *et al.* 'Correlated Electron–Hole Plasma in Organometal Perovskites'. In: *Nature Communications* 5.1 (Sept. 2014), p. 5049. DOI: 10.1038/ncomms6049 (cited on pages 11, 19).

[29] Shivam Singh *et al.* 'Effect of Thermal and Structural Disorder on the Electronic Structure of Hybrid Perovskite Semiconductor CH3NH3PbI3'. In: *The Journal of Physical Chemistry Letters* 7.15 (Aug. 2016), pp. 3014–3021. DOI: 10.1021/acs.jpclett.6b01207 (cited on pages 11, 19).

[30] R. R. Nair *et al.* 'Fine Structure Constant Defines Visual Transparency of Graphene'. In: *Science* 320.5881 (June 2008), pp. 1308–1308. DOI: 10.1126/science.1156965 (cited on pages 11, 12).

[31] Rodney Loudon. *The Quantum Theory of Light*. Third Edition, Third Edition. Oxford, New York: Oxford University Press, Nov. 2000 (cited on pages 12, 125).

[32] A. K. Geim and K. S. Novoselov. 'The Rise of Graphene'. In: *Nature Materials* 6.3 (Mar. 2007), pp. 183–191. DOI: 10.1038/nmat1849 (cited on page 13).

[33] H. L. Wells. 'Über Die Cäsium- Und Kalium-Bleihalogenide'. In: *Zeitschrift für anorganische Chemie* 3.1 (1893), pp. 195–210. DOI: 10.1002/zaac.18930030124 (cited on page 13).

[34] Chr Kn Møller. 'Crystal Structure and Photoconductivity of Cæsium Plumbohalides'. In: *Nature* 182.4647 (Nov. 1958), pp. 1436–1436. DOI: 10.1038/1821436a0 (cited on page 13).

[35] Dieter Weber. 'CH3NH3SnBrxI3-x (x = 0-3), Ein Sn(II)-System Mit Kubischer Perowskitstruktur / CH3NH3SnBrxI3-x(x = 0-3), a Sn(II)-System with Cubic Perovskite Structure'. In: *Zeitschrift für Naturforschung B* 33.8 (Aug. 1978), pp. 862–865. DOI: 10.1515/znb-1978-0809 (cited on page 13).

[36] D. B. Mitzi *et al.* 'Conducting Tin Halides with a Layered Organic-Based Perovskite Structure'. In: *Nature* 369.6480 (June 1994), pp. 467–469. DOI: 10.1038/369467a0 (cited on page 13).

[37] Junke Wang *et al.* 'Halide Homogenization for Low Energy Loss in 2-eV-bandgap Perovskites and Increased Efficiency in All-Perovskite Triple-Junction Solar Cells'. In: *Nature Energy* (Nov. 2023), pp. 1–11. DOI: 10.1038/s41560-023-01406-5 (cited on page 13).

[38] Cheng Liu *et al.* 'Bimolecularly Passivated Interface Enables Efficient and Stable Inverted Perovskite Solar Cells'. In: *Science* 382.6672 (Nov. 2023), pp. 810–815. DOI: 10.1126/science.adk1633 (cited on page 13).

[39] *Best Research-Cell Efficiency Chart*. URL: https://www.nrel.gov/pv/cell-efficiency.html (cited on pages 13, 14, 76).

[40] Cheng Chen *et al.* 'Elucidating the Phase Transitions and Temperature-Dependent Photoluminescence of MAPbBr3 Single Crystal'. In: *Journal of Physics D: Applied Physics* 51.4 (Jan. 2018), p. 045105. DOI: 10.1088/1361-6463/aaa0ed (cited on pages 15, 16).

[41] Y.H. Chang, Chul Hong Park, and Kiyoto Matsuishi. 'First-Principles Study of the Structural and the Electronic Properties of the Lead-Halide-Based Inorganic-Organic Perovskites (CH 3NH 3)PbX 3 and CsPbX 3 (X = Cl, Br, I)'. In: *Journal of the Korean Physical Society* 44 (Apr. 2004), pp. 889–893 (cited on pages 16, 17).

[42] F. Brivio, A.B. Walker, and A. Walsh. 'Structural and Electronic Properties of Hybrid Perovskites for High-Efficiency Thin-Film Photovoltaics from First-Principles'. In: *APL Materials* 1.4 (2013). DOI: 10.1063/1.4824147 (cited on pages 16, 17).

[43] Jacky Even *et al.* 'Importance of Spin–Orbit Coupling in Hybrid Organic / Inorganic Perovskites for Photovoltaic Applications'. In: *The Journal of Physical Chemistry Letters* 4.17 (Sept. 2013), pp. 2999–3005. DOI: 10.1021/jz401532q (cited on pages 16, 17, 143).

[44] Jun Hong Noh *et al.* 'Chemical Management for Colorful, Efficient, and Stable Inorganic–Organic Hybrid Nanostructured Solar Cells'. In: *Nano Letters* 13.4 (Apr. 2013), pp. 1764–1769. DOI: 10.1021/nl400349b (cited on page 15).

[45] Kenichiro Tanaka *et al.* 'Comparative Study on the Excitons in Lead-Halide-Based Perovskite-Type Crystals CH3NH3PbBr3 CH3NH3PbI3'. In: *Solid State Communications* 127.9 (Sept. 2003), pp. 619–623. DOI: 10.1016/S0038-1098(03)00566-0 (cited on pages 18, 19).

[46] Michael A. Becker *et al.* 'Bright Triplet Excitons in Caesium Lead Halide Perovskites'. In: *Nature* 553.7687 (Jan. 2018), pp. 189–193. DOI: 10.1038/nature25147 (cited on pages 18, 22, 91).

[47] Ji-Sang Park *et al.* 'Electronic Structure and Optical Properties of α -CH3NH3PbBr3 Perovskite Single Crystal'. In: *The Journal of Physical Chemistry Letters* 6.21 (Nov. 2015), pp. 4304–4308. DOI: 10.1021/acs.jpclett.5b01699 (cited on page 18).

[48] Soline Boyer-Richard *et al.* 'Symmetry-Based Tight Binding Modeling of Halide Perovskite Semiconductors'. In: *The Journal of Physical Chemistry Letters* 7.19 (Oct. 2016), pp. 3833–3840. DOI: 10.1021/acs.jpclett.6b01749 (cited on page 18).

[49] Qianqian Lin *et al.* 'Electro-Optics of Perovskite Solar Cells'. In: *Nature Photonics* 9.2 (Feb. 2015), pp. 106–112. DOI: 10.1038/nphoton.2014.284 (cited on page 19).

[50] Michal Baranowski and Paulina Plochocka. 'Excitons in Metal-Halide Perovskites'. In: *Advanced Energy Materials* 10.26 (July 2020), p. 1903659. DOI: 10.1002/aenm.201903659 (cited on page 19).

[51] Jenya Tilchin *et al.* 'Hydrogen-like Wannier–Mott Excitons in Single Crystal of Methylammonium Lead Bromide Perovskite'. In: *ACS Nano* 10.6 (June 2016), pp. 6363–6371. DOI: 10.1021/acsnano.6b02734 (cited on page 19).

[52] Michał Baranowski *et al.* 'Giant Fine Structure Splitting of the Bright Exciton in a Bulk MAPbBr3 Single Crystal'. In: *Nano Letters* 19.10 (Oct. 2019), pp. 7054–7061. DOI: 10.1021/acs.nanolett.9b02520 (cited on page 19).

[53] Christoph Wolf, Joo-Sung Kim, and Tae-Woo Lee. 'Structural and Thermal Disorder of Solution-Processed CH3NH3PbBr3 Hybrid Perovskite Thin Films'. In: *ACS Applied Materials & Interfaces* 9.12 (Mar. 2017), pp. 10344–10348. DOI: 10.1021/acsami.6b15694 (cited on page 19).

[54] Arman Mahboubi Soufiani *et al.* 'Polaronic Exciton Binding Energy in Iodide and Bromide Organic-Inorganic Lead Halide Perovskites'. In: *Applied Physics Letters* 107.23 (Dec. 2015), p. 231902. DOI: 10.1063/1.4936418 (cited on page 19).

[55] Jiakai Yan *et al.* 'Advances in the Synthesis of Halide Perovskite Single Crystals for Optoelectronic Applications'. In: *Chemistry of Materials* 35.7 (Apr. 2023), pp. 2683–2712. DOI: 10.1021/acs.chemmater.2c03505 (cited on page 19).

[56] Thomas Campos. 'Study of 2D/3D Perovskites Heterostructures for Solar Cells'. PhD thesis. Université Paris-Saclay, May 2023 (cited on pages 20, 73, 77).

[57] Chun Kiu Ng, Chujie Wang, and Jacek J. Jasieniak. 'Synthetic Evolution of Colloidal Metal Halide Perovskite Nanocrystals'. In: *Langmuir* 35.36 (Sept. 2019), pp. 11609–11628. DOI: 10.1021/acs.langmuir.9b00855 (cited on pages 20, 82).

[58] Javad Shamsi *et al.* 'Metal Halide Perovskite Nanocrystals: Synthesis, Post-Synthesis Modifications, and Their Optical Properties'. In: *Chemical Reviews* 119.5 (Mar. 2019), pp. 3296–3348. DOI: 10.1021/acs.chemrev.8b00644 (cited on pages 20, 82).

[59] Guichuan Xing *et al.* 'Long-Range Balanced Electron- and Hole-Transport Lengths in Organic-Inorganic CH3NH3PbI3'. In: *Science* 342.6156 (Oct. 2013), pp. 344–347. DOI: 10.1126/science.1243167 (cited on page 20).

[60] Samuel D. Stranks *et al.* 'Electron-Hole Diffusion Lengths Exceeding 1 Micrometer in an Organometal Trihalide Perovskite Absorber'. In: *Science* 342.6156 (Oct. 2013), pp. 341–344. DOI: 10.1126/science.1243982 (cited on page 20).

[61] David A. Egger *et al.* 'What Remains Unexplained about the Properties of Halide Perovskites?' In: *Advanced Materials* 30.20 (May 2018), p. 1800691. DOI: 10.1002/adma.201800691 (cited on pages 20, 169).

[62] Michael Grätzel. 'The Light and Shade of Perovskite Solar Cells'. In: *Nature Materials* 13.9 (Sept. 2014), pp. 838–842. DOI: 10.1038/nmat4065 (cited on page 20).

[63] Géraud Delport *et al.* 'Exciton–Exciton Annihilation in Two-Dimensional Halide Perovskites at Room Temperature'. In: *The Journal of Physical Chemistry Letters* 10.17 (Sept. 2019), pp. 5153–5159. DOI: 10.1021/acs.jpclett.9b01595 (cited on page 21).

[64] G. Bastard. *Wave Mechanics Applied to Semiconductor Heterostructures*. Les Ulis: Editions de physique, 1988 (cited on page 20).

[65] Ferdinand Lédée *et al.* 'Fast Growth of Monocrystalline Thin Films of 2D Layered Hybrid Perovskite'. In: *CrystEngComm* 19.19 (May 2017), pp. 2598–2602. DOI: 10.1039/C7CE00240H (cited on pages 20, 72).

[66] Yongping Fu *et al.* 'Broad Wavelength Tunable Robust Lasing from Single-Crystal Nanowires of Cesium Lead Halide Perovskites (CsPbX3, X = Cl, Br, I)'. In: *ACS Nano* 10.8 (Aug. 2016), pp. 7963–7972. DOI: 10.1021/acsnano.6b03916 (cited on page 20).

[67] Muhammad Shoaib *et al.* 'Directional Growth of Ultralong CsPbBr3 Perovskite Nanowires for High-Performance Photodetectors'. In: *Journal of the American Chemical Society* 139.44 (Nov. 2017), pp. 15592–15595. DOI: 10.1021/jacs.7b08818 (cited on page 20).

[68] Joanna M. Urban *et al.* 'Revealing Excitonic Phonon Coupling in (PEA)2 (MA)n-1PbnI3n+1 2D Layered Perovskites'. In: *The Journal of Physical Chemistry Letters* 11.15 (Aug. 2020), pp. 5830–5835. DOI: 10.1021/acs.jpclett.0c01714 (cited on page 22).

[69] Chuanjiang Qin *et al.* 'Triplet Management for Efficient Perovskite Light-Emitting Diodes'. In: *Nature Photonics* 14.2 (Feb. 2020), pp. 70–75. DOI: 10.1038/s41566-019-0545-9 (cited on pages 22, 76, 78, 80, 81, 100, 169).

[70] Chuanjiang Qin *et al.* 'Stable Room-Temperature Continuous-Wave Lasing in Quasi-2D Perovskite Films'. In: *Nature* 585.7823 (Sept. 2020), pp. 53–57. DOI: 10.1038/s41586-020-2621-1 (cited on pages 22, 77, 78, 101).

[71] Ferdinand Lédée *et al.* 'Tetrazine Molecules as an Efficient Electronic Diversion Channel in 2D Organic–Inorganic Perovskites'. In: *Materials Horizons* 8.5 (2021), pp. 1547–1560. DOI: 10.1039/D0MH01904F (cited on pages 22, 143, 169).

[72] Daniel Medina lopez. 'Synthèse et Propriétés Optiques de Nanostructures de Graphène'. These En Préparation. université Paris-Saclay, 2020 (cited on page 22).

[73] Peter W Atkins and Ronald S Friedman. *Molecular Quantum Mechanics*. 4th ed. Oxford University Press, 2004 (cited on pages 23, 25).

[74] Nico R. Verhart, Mathias Müller, and Michel Orrit. 'Spectroscopy of Single Dibenzoterrylene Molecules in Para-Dichlorobenzene'. In: *ChemPhysChem* 17.10 (May 2016), pp. 1524–1529. DOI: 10.1002/cphc.201501087 (cited on page 24).

[75] Michael Kasha. 'Characterization of Electronic Transitions in Complex Molecules'. In: *Discussions of the Faraday Society* 9.0 (Jan. 1950), pp. 14–19. DOI: 10.1039/DF9500900014 (cited on pages 25, 42).

[76] Eric Clar. *The Aromatic Sextet*. Wiley-Interscience. John Wiley and Sons Ltd., 1972 (cited on pages 26, 27).

[77] Leo Gross *et al.* 'Bond-Order Discrimination by Atomic Force Microscopy'. In: *Science* 337.6100 (Sept. 2012), pp. 1326–1329. DOI: 10.1126/science.1225621 (cited on page 27).

[78] Miquel Solà. 'Forty Years of Clar's Aromatic π-Sextet Rule'. In: *Frontiers in Chemistry* 1 (2013) (cited on page 27).

[79] John A. McGuire. 'Growth and Optical Properties of Colloidal Graphene Quantum Dots'. In: *physica status solidi (RRL) – Rapid Research Letters* 10.1 (2016), pp. 91–101. DOI: 10.1002/pssr.201510287 (cited on pages 27, 28, 111).

[80] A. V. Rozhkov and Franco Nori. 'Exact Wave Functions for an Electron on a Graphene Triangular Quantum Dot'. In: *Physical Review B* 81.15 (Apr. 2010), p. 155401. DOI: 10.1103/PhysRevB.81.155401 (cited on pages 28, 29).

[81] Isil Ozfidan *et al.* 'Microscopic Theory of the Optical Properties of Colloidal Graphene Quantum Dots'. In: *Physical Review B* 89.8 (Feb. 2014), p. 085310. DOI: 10.1103/PhysRevB.89.085310 (cited on pages 28, 29).

[82] Stefan Schumacher. 'Photophysics of Graphene Quantum Dots: Insights from Electronic Structure Calculations'. In: *Physical Review B* 83.8 (Feb. 2011), p. 081417. DOI: 10.1103/PhysRevB.83.081417 (cited on pages 28, 29).

[83] Isil Ozfidan *et al.* 'Theory of Optical Properties of Graphene Quantum Dots'. In: *physica status solidi (RRL) – Rapid Research Letters* 10.1 (2016), pp. 102–110. DOI: 10.1002/pssr.201510335 (cited on page 29).

[84] Rico Pohle *et al.* 'Symmetry and Optical Selection Rules in Graphene Quantum Dots'. In: *Physical Review B* 97.11 (Mar. 2018), p. 115404. DOI: 10.1103/PhysRevB.97.115404 (cited on pages 30, 32).

[85] Caterina Cocchi *et al.* 'Anisotropy and Size Effects on the Optical Spectra of Polycyclic Aromatic Hydrocarbons'. In: *The Journal of Physical Chemistry A* 118.33 (Aug. 2014), pp. 6507–6513. DOI: 10.1021/jp503054j (cited on pages 31, 32).

[86] Michael Tinkham. *Group Theory and Quantum Mechanics*. Dover Publications. Dover Books on Chemistry. 2003 (cited on pages 29, 32).

[87] Shahriar N. Khan *et al.* 'Impact of Graphene Quantum Dot Edge Morphologies on Their Optical Properties'. In: *The Journal of Physical Chemistry Letters* 13.25 (June 2022), pp. 5801–5807. DOI: 10.1021/acs.jpclett.2c01036 (cited on page 33).

[88] Jungpil Kim *et al.* 'Distinguishing Zigzag and Armchair Edges on Graphene Nanoribbons by X-ray Photoelectron and Raman Spectroscopies'. In: *ACS Omega* 3.12 (Dec. 2018), pp. 17789–17796. DOI: 10.1021/acsomega.8b02744 (cited on page 32).

[89] H. C. Chung *et al.* 'Exploration of Edge-Dependent Optical Selection Rules for Graphene Nanoribbons'. In: *Optics Express* 19.23 (Nov. 2011), pp. 23350–23363. DOI: 10.1364/OE.19.023350 (cited on page 32).

[90] Ruiqiang Zhang *et al.* 'Size and Refinement Edge-Shape Effects of Graphene Quantum Dots on UV–Visible Absorption'. In: *Journal of Alloys and Compounds* 623 (Feb. 2015), pp. 186–191. DOI: 10.1016/j.jallcom.2014.10.105 (cited on page 32).

[91] M. Wimmer, A. R. Akhmerov, and F. Guinea. 'Robustness of Edge States in Graphene Quantum Dots'. In: *Physical Review B* 82.4 (July 2010), p. 045409. DOI: 10.1103/PhysRevB.82.045409 (cited on page 32).

[92] Jingang Wang *et al.* 'Theoretical Investigations of Optical Origins of Fluorescent Graphene Quantum Dots'. In: *Scientific Reports* 6.1 (Apr. 2016), p. 24850. DOI: 10.1038/srep24850 (cited on page 32).

[93] W. E. Moerner and L. Kador. 'Optical Detection and Spectroscopy of Single Molecules in a Solid'. In: *Physical Review Letters* 62.21 (May 1989), pp. 2535–2538. DOI: 10.1103/PhysRevLett.62.2535 (cited on pages 34, 35).

[94] M. Orrit and J. Bernard. 'Single Pentacene Molecules Detected by Fluorescence Excitation in a P-Terphenyl Crystal'. In: *Physical Review Letters* 65.21 (Nov. 1990), pp. 2716–2719. DOI: 10.1103/PhysRevLett.65.2716 (cited on pages 34, 35).

[95] Th. Basché *et al.* 'Photon Antibunching in the Fluorescence of a Single Dye Molecule Trapped in a Solid'. In: *Physical Review Letters* 69.10 (Sept. 1992), pp. 1516–1519. DOI: 10.1103/PhysRevLett.69.1516 (cited on pages 34, 35).

[96] L. Fleury *et al.* 'Nonclassical Photon Statistics in Single-Molecule Fluorescence at Room Temperature'. In: *Physical Review Letters* 84.6 (Feb. 2000), pp. 1148–1151. DOI: 10.1103/PhysRevLett.84.1148 (cited on pages 34, 35, 136).

[97] B. Sick, B. Hecht, and L. Novotny. 'Orientational Imaging of Single Molecules by Annular Illumination'. In: *Physical Review Letters* 85.21 (Nov. 2000), pp. 4482–4485. DOI: 10.1103/PhysRevLett.85.4482 (cited on pages 34, 35).

[98] F. De Martini. 'Single-Mode Generation of Quantum Photon States by Excited Single Molecules in a Microcavity Trap'. In: *Physical Review Letters* 76.6 (1996), pp. 900–903. DOI: 10.1103/PhysRevLett.76.900 (cited on page 34).

[99] X. Sunney Xie. 'Single-Molecule Spectroscopy and Dynamics at Room Temperature'. In: *Accounts of Chemical Research* 29.12 (Dec. 1996), pp. 598–606. DOI: 10.1021/ar950246m (cited on page 34).

[100] François Treussart *et al.* 'Photon Antibunching in the Fluorescence of a Single Dye Molecule Embedded in a Thin Polymer Film'. In: *Optics Letters* 26.19 (Oct. 2001), pp. 1504–1506. DOI: 10.1364/OL.26.001504 (cited on page 34).

[101] Shimon Weiss. 'Fluorescence Spectroscopy of Single Biomolecules'. In: *Science* 283.5408 (Mar. 1999), pp. 1676–1683. DOI: 10.1126/science.283.5408.1676 (cited on page 34).

[102] Andreas Zürner *et al.* 'Visualizing Single-Molecule Diffusion in Mesoporous Materials'. In: *Nature* 450.7170 (Nov. 2007), pp. 705–708. DOI: 10.1038/nature06398 (cited on page 34).

[103] Clemens Hofmann *et al.* 'Towards Nanoprobes for Conduction in Molecular Crystals: Dibenzoterrylene in Anthracene Crystals'. In: *Chemical Physics*. Molecular Nanoscience 318.1 (Nov. 2005), pp. 1–6. DOI: 10.1016/j.chemphys.2005.02.003 (cited on pages 34, 103).

[104] V. Esteso *et al.* 'Quantum Thermometry with Single Molecules in Nanoprobes'. In: *PRX Quantum* 4.4 (Oct. 2023), p. 040314. DOI: 10.1103/PRXQuantum.4.040314 (cited on page 34).

[105] C. Toninelli *et al.* 'Near-Infrared Single-Photons from Aligned Molecules in Ultrathin Crystalline Films at Room Temperature'. In: *Optics Express* 18.7 (Mar. 2010), pp. 6577–6582. DOI: 10.1364/OE.18.006577 (cited on pages 34, 103).

[106] Claudio Polisseni *et al.* 'Stable, Single-Photon Emitter in a Thin Organic Crystal for Application to Quantum-Photonic Devices'. In: *Optics Express* 24.5 (Mar. 2016), pp. 5615–5627. DOI: 10.1364/OE.24.005615 (cited on page 34).

[107] M. Orrit *et al.* 'Stark Effect on Single Molecules in a Polymer Matrix'. In: *Chemical Physics Letters* 196.6 (Aug. 1992), pp. 595–600. DOI: 10.1016/0009-2614(92)86000-8 (cited on page 34).

[108] Kevin G. Schädler *et al.* 'Electrical Control of Lifetime-Limited Quantum Emitters Using 2D Materials'. In: *Nano Letters* 19.6 (June 2019), pp. 3789–3795. DOI: 10.1021/acs.nanolett.9b00916 (cited on page 34).

[109] Amin Moradi *et al.* 'Matrix-Induced Linear Stark Effect of Single Dibenzoterrylene Molecules in 2,3-Dibromonaphthalene Crystal'. In: *ChemPhysChem* 20.1 (Jan. 2019), pp. 55–61. DOI: 10.1002/cphc.201800937 (cited on page 34).

[110] Maja Colautti *et al.* 'Laser-Induced Frequency Tuning of Fourier-Limited Single-Molecule Emitters'. In: *ACS Nano* 14.10 (Oct. 2020), pp. 13584–13592. DOI: 10.1021/acsnano.0c05620 (cited on pages 34, 103).

[111] Rocco Duquennoy *et al.* 'Real-Time Two-Photon Interference from Distinct Molecules on the Same Chip'. In: *Optica* 9.7 (July 2022), pp. 731–737. DOI: 10.1364/OPTICA.452317 (cited on page 36).

[112] Philip Schulz, David Cahen, and Antoine Kahn. 'Halide Perovskites: Is It All about the Interfaces?' In: *Chemical Reviews* 119.5 (Mar. 2019), pp. 3349–3417. DOI: 10.1021/acs.chemrev.8b00558 (cited on pages 37, 184).

[113] *FS5 User Guide*. Tech. rep. 4. Edinburgh Instruments Ltd, 2019 (cited on page 40).

[114] Thomas G. Mayerhöfer, Susanne Pahlow, and Jürgen Popp. 'The Bouguer-Beer-Lambert Law: Shining Light on the Obscure'. In: *ChemPhysChem* 21.18 (2020), pp. 2029–2046. DOI: 10.1002/cphc.202000464 (cited on page 42).

[115] 'Instrumentation for Fluorescence Spectroscopy'. In: *Principles of Fluorescence Spectroscopy*. Ed. by Joseph R. Lakowicz. Boston, MA: Springer US, 2006, pp. 27–61. DOI: 10.1007/978-0-387-46312-4_2 (cited on page 42).

[116] Thomas Liu *et al.* 'Vibronic Effect and Influence of Aggregation on the Photophysics of Graphene Quantum Dots'. In: *Nanoscale* 14.10 (Mar. 2022), pp. 3826–3833. DOI: 10.1039/D1NR08279E (cited on pages 43, 111, 120).

[117] Michael Wahl. *Time-Correlated Single Photon Counting*. Tech. rep. PicoQuant GmbH (cited on page 44).

[118] Arnold A. Gaertner, Howard W. Yoon, and Thomas A. Germer. 'Chapter 3 - Dispersive Methods'. In: *Experimental Methods in the Physical Sciences*. Ed. by Thomas A. Germer, Joanne C. Zwinkels, and Benjamin K. Tsai. Vol. 46. Spectrophotometry. Academic Press, Jan. 2014, pp. 67–95. DOI: 10.1016/B978-0-12-386022-4.00003-0 (cited on page 55).

[119] Chen-How Huang, Yung-Hsiang Wen, and Yi-Wei Liu. 'Measuring the Second Order Correlation Function and the Coherence Time Using Random Phase Modulation'. In: *Optics Express* 24.4 (Feb. 2016), pp. 4278–4288. DOI: 10.1364/OE.24.004278 (cited on page 60).

[120] Christian Kurtsiefer *et al.* 'The Breakdown Flash of Silicon Avalanche Photodiodes-Back Door for Eavesdropper Attacks?' In: *Journal of Modern Optics* (Nov. 2001). DOI: 10.1080/09500340108240905 (cited on page 62).

[121] Max T. Otten. 'High-Angle Annular Dark-Field Imaging on a Tem/Stem System'. In: *Journal of Electron Microscopy Technique* 17.2 (1991), pp. 221–230. DOI: 10.1002/jemt.1060170209 (cited on page 62).

[122] Stefania Cacovich *et al.* 'Light-Induced Passivation in Triple Cation Mixed Halide Perovskites: Interplay between Transport Properties and Surface Chemistry'. In: *ACS Applied Materials & Interfaces* 12.31 (Aug. 2020), pp. 34784–34794. DOI: 10.1021/acsami.0c06844 (cited on pages 65, 150).

[123] Jonathan Mooney and Patanjali Kambhampati. 'Get the Basics Right: Jacobian Conversion of Wavelength and Energy Scales for Quantitative Analysis of Emission Spectra'. In: *The Journal of Physical Chemistry Letters* 4.19 (Oct. 2013), pp. 3316–3318. DOI: 10.1021/jz401508t (cited on page 65).

[124] Jonathan Mooney and Patanjali Kambhampati. 'Correction to "Get the Basics Right: Jacobian Conversion of Wavelength and Energy Scales for Quantitative Analysis of Emission Spectra"'. In: *The Journal of Physical Chemistry Letters* 5.20 (Oct. 2014), pp. 3497–3497. DOI: 10.1021/jz502066v (cited on page 66).

[125] D. V. O'Connor, W. R. Ware, and J. C. Andre. 'Deconvolution of Fluorescence Decay Curves. A Critical Comparison of Techniques'. In: *The Journal of Physical Chemistry* 83.10 (May 1979), pp. 1333–1343. DOI: 10.1021/j100473a019 (cited on page 66).

[126] Michael Maus *et al.* 'An Experimental Comparison of the Maximum Likelihood Estimation and Nonlinear Least-Squares Fluorescence Lifetime Analysis of Single Molecules'. In: *Analytical Chemistry* 73.9 (May 2001), pp. 2078–2086. DOI: 10.1021/ac000877g (cited on page 66).

[127] Richard McElreath. *Statistical Rethinking*. 2nd ed. Chapman \& Hall/CRC Texts in Statistical Science. Chapman \& Hall/CRC, 2020 (cited on page 66).

[128] Joseph R. Lakowicz. 'Time-Domain Lifetime Measurements'. In: *Principles of Fluorescence Spectroscopy*. Boston, MA: Springer US, 2006, pp. 97–155. DOI: 10.1007/978-0-387-46312-4_4 (cited on pages 67, 111).

[129] Amiram Grinvald and Izchak, Steinberg. 'On the Analysis of Fluorescence Decay Kinetics by the Method of Least-Squares'. In: *Analytical Biochemistry* 59.2 (June 1974), pp. 583–598. DOI: 10.1016/0003-2697(74)90312-1 (cited on page 67).

[130] Michael Wahl *et al.* 'Fast Calculation of Fluorescence Correlation Data with Asynchronous Time-Correlated Single-Photon Counting'. In: *Optics Express* 11.26 (Dec. 2003), pp. 3583–3591. DOI: 10.1364/OE.11.003583 (cited on page 68).

[131] Jan M. Binder *et al.* 'Qudi: A Modular Python Suite for Experiment Control and Data Processing'. In: *SoftwareX* 6 (Jan. 2017), pp. 85–90. DOI: 10.1016/j.softx.2017.02.001 (cited on page 69).

[132] Jeff Bezanson *et al.* 'Julia: A Fresh Approach to Numerical Computing'. In: *SIAM Review* 59.1 (Jan. 2017), pp. 65–98. DOI: 10.1137/141000671 (cited on page 69).

[133] George Datseris *et al.* 'DrWatson: The Perfect Sidekick for Your Scientific Inquiries'. In: *Journal of Open Source Software* 5.54 (Oct. 2020), p. 2673. DOI: 10.21105/joss.02673 (cited on page 69).

[134] Milan Bouchet-Valat and Bogumił Kamiński. 'DataFrames.Jl: Flexible and Fast Tabular Data in Julia'. In: *Journal of Statistical Software* 107 (Sept. 2023), pp. 1–32. DOI: 10.18637/jss.v107.i04 (cited on page 69).

[135] Simon Danisch and Julius Krumbiegel. 'Makie.Jl: Flexible High-Performance Data Visualization for Julia'. In: *Journal of Open Source Software* 6.65 (2021), p. 3349. DOI: 10.21105/joss.03349 (cited on page 69).

[136] Inkscape Project. *Inkscape* (cited on page 69).

[137] Alvise Vianello. *ComponentLibrary* (cited on page 69).

[138] *Spin Coating: Complete Guide to Theory and Techniques*. URL: https://web.archive.org/web/20230517035930/https://www.ossila.com/en-eu/pages/spin-coating (cited on page 71).

[139] Alfred G. Emslie, Francis T. Bonner, and Leslie G. Peck. 'Flow of a Viscous Liquid on a Rotating Disk'. In: *Journal of Applied Physics* 29.5 (June 2004), pp. 858–862. DOI: 10.1063/1.1723300 (cited on page 71).

[140] Dietrich Meyerhofer. 'Characteristics of Resist Films Produced by Spinning'. In: *Journal of Applied Physics* 49.7 (Aug. 2008), pp. 3993–3997. DOI: 10.1063/1.325357 (cited on page 71).

[141] Christopher B. Walsh and Elias I. Franses. 'Ultrathin PMMA Films Spin-Coated from Toluene Solutions'. In: *Thin Solid Films* 429.1 (Apr. 2003), pp. 71–76. DOI: 10.1016/S0040-6090(03)00031-2 (cited on page 71).

[142] Joseph R. Lakowicz, ed. *Principles of Fluorescence Spectroscopy*. Boston, MA: Springer US, 2006 (cited on page 73).

[143] Shuji Nakamura, Masayuki Senoh Masayuki Senoh, and Takashi Mukai Takashi Mukai. 'P-GaN/N-InGaN/N-GaN Double-Heterostructure Blue-Light-Emitting Diodes'. In: *Japanese Journal of Applied Physics* 32.1A (Jan. 1993), p. L8. DOI: 10.1143/JJAP.32.L8 (cited on page 75).

[144] Matthias Auf der Maur *et al.* 'Efficiency Drop in Green InGaN/GaN Light Emitting Diodes: The Role of Random Alloy Fluctuations'. In: *Physical Review Letters* 116.2 (Jan. 2016), p. 027401. DOI: 10.1103/PhysRevLett.116.027401 (cited on page 75).

[145] Kirill A. Bulashevich, Alexey V. Kulik, and Sergey Yu. Karpov. 'Optimal Ways of Colour Mixing for High-Quality White-Light LED Sources'. In: *physica status solidi (a)* 212.5 (2015), pp. 914–919. DOI: 10.1002/pssa.201431576 (cited on page 75).

[146] Dario Schiavon *et al.* 'Wavelength-Dependent Determination of the Recombination Rate Coefficients in Single-Quantum-Well GaInN/GaN Light Emitting Diodes'. In: *physica status solidi (b)* 250.2 (2013), pp. 283–290. DOI: 10.1002/pssb.201248286 (cited on page 75).

[147] *Strategies For Creating Efficient, Beautiful Whites - News*. URL: https://compoundsemiconductor.net/article-gen/96572 (cited on page 75).

[148] Daniel S.P. Tanner *et al.* 'Polar (In,Ga)N/GaN Quantum Wells: Revisiting the Impact of Carrier Localization on the "Green Gap" Problem'. In: *Physical Review Applied* 13.4 (Apr. 2020), p. 044068. DOI: 10.1103/PhysRevApplied.13.044068 (cited on page 75).

[149] Jeffrey Y. Tsao *et al.* 'Toward Smart and Ultra-efficient Solid-State Lighting'. In: *Advanced Optical Materials* 2.9 (2014), pp. 809–836. DOI: 10.1002/adom.201400131 (cited on page 76).

[150] Yang Mei *et al.* 'Quantum Dot Vertical-Cavity Surface-Emitting Lasers Covering the 'Green Gap''. In: *Light: Science & Applications* 6.1 (Jan. 2017), e16199–e16199. DOI: 10.1038/lsa.2016.199 (cited on page 76).

[151] Jae Choul Yu *et al.* 'High-Performance Perovskite Light-Emitting Diodes via Morphological Control of Perovskite Films'. In: *Nanoscale* 8.13 (2016), pp. 7036–7042. DOI: 10.1039/C5NR05604G (cited on page 76).

[152] Lucie McGovern *et al.* 'Grain Size Influences Activation Energy and Migration Pathways in MAPbBr3 Perovskite Solar Cells'. In: *The Journal of Physical Chemistry Letters* 12.9 (Mar. 2021), pp. 2423–2428. DOI: 10.1021/acs.jpclett.1c00205 (cited on page 76).

[153] Chenglian Zhu *et al.* 'Room-Temperature, Highly Pure Single-Photon Sources from All-Inorganic Lead Halide Perovskite Quantum Dots'. In: *Nano Letters* 22.9 (May 2022), pp. 3751–3760. DOI: 10.1021/acs.nanolett.2c00756 (cited on pages 76, 82).

[154] Chen Hu *et al.* 'Discovery of a New Intermediate Enables One-Step Deposition of High-Quality Perovskite Films via Solvent Engineering'. In: *Solar RRL* 5.4 (2021), p. 2000712. DOI: 10.1002/solr.202000712 (cited on page 80).

[155] Xinjian Geng *et al.* 'Transient Energy-Resolved Photoluminescence Study of Excitons and Free Carriers on FAPbBr3 and FAPbBr3/SnO2 Interfaces'. In: *The Journal of Physical Chemistry C* 127.6 (Feb. 2023), pp. 3085–3092. DOI: 10.1021/acs.jpcc.2c07931 (cited on page 80).

[156] Constantinos C. Stoumpos *et al.* 'Crystal Growth of the Perovskite Semiconductor CsPbBr3: A New Material for High-Energy Radiation Detection'. In: *Crystal Growth & Design* 13.7 (July 2013), pp. 2722–2727. DOI: 10.1021/cg400645t (cited on pages 81, 89).

[157] Dmitry N. Dirin *et al.* 'Solution-Grown CsPbBr3 Perovskite Single Crystals for Photon Detection'. In: *Chemistry of Materials* 28.23 (Dec. 2016), pp. 8470–8474. DOI: 10.1021/acs.chemmater.6b04298 (cited on pages 81, 89).

[158] Gabriele Rainò *et al.* 'Superfluorescence from Lead Halide Perovskite Quantum Dot Superlattices'. In: *Nature* 563.7733 (Nov. 2018), pp. 671–675. DOI: 10.1038/s41586-018-0683-0 (cited on page 82).

[159] Sergii Yakunin *et al.* 'Low-Threshold Amplified Spontaneous Emission and Lasing from Colloidal Nanocrystals of Caesium Lead Halide Perovskites'. In: *Nature Communications* 6.1 (Aug. 2015), p. 8056. DOI: 10.1038/ncomms9056 (cited on pages 82, 101).

[160] Xiaoming Li *et al.* 'CsPbX3 Quantum Dots for Lighting and Displays: Room-Temperature Synthesis, Photoluminescence Superiorities, Underlying Origins and White Light-Emitting Diodes'. In: *Advanced Functional Materials* 26.15 (2016), pp. 2435–2445. DOI: 10.1002/adfm.201600109 (cited on pages 82, 89, 91).

[161] Song Wei *et al.* 'Homogeneous Synthesis and Electroluminescence Device of Highly Luminescent CsPbBr3 Perovskite Nanocrystals'. In: *Inorganic Chemistry* 56.5 (Mar. 2017), pp. 2596–2601. DOI: 10.1021/acs.inorgchem.6b02763 (cited on pages 82, 91).

[162] Cédric R. Mayer *et al.* 'Synthesis of Highly Calibrated CsPbBr3 Nanocrystal Perovskites by Soft Chemistry'. In: *Chemical Communications* 58.40 (May 2022), pp. 5960–5963. DOI: 10.1039/D2CC01028C (cited on pages 82, 100).

[163] Rafael C. Gonzalez and Richard E. Woods. *Digital Image Processing*. 2. ed., internat. ed. Upper Saddle River, NJ: Prentice-Hall, 2002 (cited on page 84).

[164] William H. Press. *Numerical Recipes 3rd Edition: The Art of Scientific Computing*. Cambridge University Press, Sept. 2007 (cited on page 84).

[165] J. Calabrese *et al.* 'Preparation and Characterization of Layered Lead Halide Compounds'. In: *Journal of the American Chemical Society* 113.6 (Mar. 1991), pp. 2328–2330. DOI: 10.1021/ja00006a076 (cited on page 87).

[166] R. J. Hill. 'Refinement of the Structure of Orthorhombic PbO (Massicot) by Rietveld Analysis of Neutron Powder Diffraction Data'. In: *Acta Crystallographica Section C* 41.9 (1985), pp. 1281–1284. DOI: 10.1107/S0108270185007454 (cited on page 87).

[167] Hanleem Lee *et al.* 'Design of Chemically Stable Organic Perovskite Quantum Dots for Micropatterned Light-Emitting Diodes through Kinetic Control of a Cross-Linkable Ligand System'. In: *Advanced Materials* 33.23 (2021), p. 2007855. DOI: 10.1002/adma.202007855 (cited on pages 87, 150).

[168] Bo Chen *et al.* 'Imperfections and Their Passivation in Halide Perovskite Solar Cells'. In: *Chemical Society Reviews* 48.14 (2019), pp. 3842–3867. DOI: 10.1039/C8CS00853A (cited on page 88).

[169] James M. Ball and Annamaria Petrozza. 'Defects in Perovskite-Halides and Their Effects in Solar Cells'. In: *Nature Energy* 1.11 (Oct. 2016), pp. 1–13. DOI: 10.1038/nenergy.2016.149 (cited on page 88).

[170] Weixin Huang, Yuanxing Wang, and Subila K. Balakrishnan. 'Controllable Transformation between 3D and 2D Perovskites through Cation Exchange'. In: *Chemical Communications* 54.57 (July 2018), pp. 7944–7947. DOI: 10.1039/C8CC04261F (cited on page 88).

[171] Guadalupe Garcia-Arellano *et al.* 'Unexpected Anisotropy of the Electron and Hole Landé G-Factors in Perovskite CH3NH3PbI3 Polycrystalline Films'. In: *Nanomaterials* 12.9 (Jan. 2022), p. 1399. DOI: 10.3390/nano12091399 (cited on page 89).

[172] Chun Kiu Ng *et al.* 'Scalable Synthesis of Colloidal CsPbBr3 Perovskite Nanocrystals with High Reaction Yields through Solvent and Ligand Engineering'. In: *Nanoscale* 12.8 (Feb. 2020), pp. 4859–4867. DOI: 10.1039/C9NR10726F (cited on page 89).

[173] Jiaoxian Yu *et al.* 'Perovskite CsPbBr 3 Crystals: Growth and Applications'. In: *Journal of Materials Chemistry C* 8.19 (2020), pp. 6326–6341. DOI: 10.1039/D0TC00922A (cited on page 89).

[174] Giovanni Mannino *et al.* 'Temperature-Dependent Optical Band Gap in $CsPbBr_3$, $MAPbBr_3$, and $FAPbBr_3$ Single Crystals'. In: *The Journal of Physical Chemistry Letters* 11.7 (Apr. 2020), pp. 2490–2496. DOI: 10.1021/acs.jpclett.0c00295 (cited on page 91).

[175] Mohamed-Raouf Amara *et al.* 'Spectral Fingerprint of Quantum Confinement in Single CsPbBr3 Nanocrystals'. In: *Nano Letters* 23.8 (Apr. 2023), pp. 3607–3613. DOI: 10.1021/acs.nanolett.3c00793 (cited on page 91).

[176] Gabriele Rainò *et al.* 'Ultra-Narrow Room-Temperature Emission from Single CsPbBr3 Perovskite Quantum Dots'. In: *Nature Communications* 13.1 (May 2022), p. 2587. DOI: 10.1038/s41467-022-30016-0 (cited on page 91).

[177] Goutam Ghosh *et al.* 'Influence of Shape on the Carrier Relaxation Dynamics of CsPbBr 3 Perovskite Nanocrystals'. In: *Physical Chemistry Chemical Physics* 21.35 (2019), pp. 19318–19326. DOI: 10.1039/C9CP03386F (cited on page 91).

[178] Francesco Di Stasio *et al.* 'Near-Unity Photoluminescence Quantum Yield in CsPbBr3 Nanocrystal Solid-State Films via Postsynthesis Treatment with Lead Bromide'. In: *Chemistry of Materials* 29.18 (Sept. 2017), pp. 7663–7667. DOI: 10.1021/acs.chemmater.7b02834 (cited on page 92).

[179] Yanqing Zu *et al.* 'Ultra-Stable CsPbBr 3 Nanocrystals with near-Unity Photoluminescence Quantum Yield via Postsynthetic Surface Engineering'. In: *Journal of Materials Chemistry A* 7.45 (2019), pp. 26116–26122. DOI: 10.1039/C9TA08421E (cited on page 92).

[180] Lin Yang *et al.* 'Poly(Vinylidene Fluoride)-Passivated CsPbBr 3 Perovskite Quantum Dots with near-Unity Photoluminescence Quantum Yield and Superior Stability'. In: *Journal of Materials Chemistry C* 9.6 (2021), pp. 1983–1991. DOI: 10.1039/D0TC05103A (cited on page 92).

[181] Qixuan Zhong *et al.* 'L-Type Ligand-Assisted Acid-Free Synthesis of CsPbBr3 Nanocrystals with Near-Unity Photoluminescence Quantum Yield and High Stability'. In: *Nano Letters* 19.6 (June 2019), pp. 4151–4157. DOI: 10.1021/acs.nanolett.9b01666 (cited on page 92).

[182] V. G. Vasavi Dutt *et al.* 'Year-Long Stability and Near-Unity Photoluminescence Quantum Yield of CsPbBr3 Perovskite Nanocrystals by Benzoic Acid Post-treatment'. In: *The Journal of Physical Chemistry C* 126.22 (June 2022), pp. 9502–9508. DOI: 10.1021/acs.jpcc.2c01467 (cited on page 92).

[183] Hiba Diab *et al.* 'Impact of Reabsorption on the Emission Spectra and Recombination Dynamics of Hybrid Perovskite Single Crystals'. In: *The Journal of Physical Chemistry Letters* 8.13 (July 2017), pp. 2977–2983. DOI: 10.1021/acs.jpclett.7b00998 (cited on page 93).

[184] Dong Liang *et al.* 'Color-Pure Violet-Light-Emitting Diodes Based on Layered Lead Halide Perovskite Nanoplates'. In: *ACS Nano* 10.7 (July 2016), pp. 6897–6904. DOI: 10.1021/acsnano.6b02683 (cited on page 99).

[185] Chaoyang Ge *et al.* 'Centimeter-Scale 2D Perovskite (PEA)2PbBr4 Single Crystal Plates Grown by a Seeded Solution Method for Photodetectors'. In: *RSC Advances* 9.29 (May 2019), pp. 16779–16783. DOI: 10.1039/C9RA01415B (cited on page 99).

[186] Yue Wang *et al.* 'All-Inorganic Colloidal Perovskite Quantum Dots: A New Class of Lasing Materials with Favorable Characteristics'. In: *Advanced Materials* 27.44 (2015), pp. 7101–7108. DOI: 10.1002/adma.201503573 (cited on page 101).

[187] Jun Pan *et al.* 'Air-Stable Surface-Passivated Perovskite Quantum Dots for Ultra-Robust, Single- and Two-Photon-Induced Amplified Spontaneous Emission'. In: *The Journal of Physical Chemistry Letters* 6.24 (Dec. 2015), pp. 5027–5033. DOI: 10.1021/acs.jpclett.5b02460 (cited on page 101).

[188] Yue Wang *et al.* 'Solution-Processed Low Threshold Vertical Cavity Surface Emitting Lasers from All-Inorganic Perovskite Nanocrystals'. In: *Advanced Functional Materials* 27.13 (Feb. 2017), p. 1605088. DOI: 10.1002/adfm.201605088 (cited on page 101).

[189] Chun-Ying Huang *et al.* 'CsPbBr3 Perovskite Quantum Dot Vertical Cavity Lasers with Low Threshold and High Stability'. In: *ACS Photonics* 4.9 (Sept. 2017), pp. 2281–2289. DOI: 10.1021/acsphotonics.7b00520 (cited on page 101).

[190] Deng-Gui Zhang *et al.* 'Investigation of Random Lasing from All-Inorganic Halide Perovskite Quantum Dots Prepared under Ambient Conditions'. In: *Nanoscale* (Feb. 2021). DOI: 10.1039/D0NR08326G (cited on page 101).

[191] Lei Wang *et al.* 'Ultralow-Threshold and Color-Tunable Continuous-Wave Lasing at Room-Temperature from In Situ Fabricated Perovskite Quantum Dots'. In: *The Journal of Physical Chemistry Letters* 10.12 (June 2019), pp. 3248–3253. DOI: 10.1021/acs.jpclett.9b00658 (cited on page 101).

[192] Zhengzheng Liu *et al.* 'Subwavelength-Polarized Quasi-Two-Dimensional Perovskite Single-Mode Nanolaser'. In: *ACS Nano* (Apr. 2021). DOI: 10.1021/acsnano.0c10647 (cited on page 101).

[193] Meili Li *et al.* 'Amplified Spontaneous Emission Based on 2D Ruddlesden–Popper Perovskites'. In: *Advanced Functional Materials* 28.17 (2018), p. 1707006. DOI: 10.1002/adfm.201707006 (cited on page 101).

[194] Hongbo Zhang *et al.* 'Room-Temperature Continuous-Wave Vertical-Cavity Surface-Emitting Lasers Based on 2D Layered Organic–Inorganic Hybrid Perovskites'. In: *APL Materials* 9.7 (July 2021), p. 071106. DOI: 10.1063/5.0052458 (cited on page 101).

[195] Quang-Huy Do *et al.* 'Fabrication of Green Light-Emitting Diodes Using CsPbBr3 Perovskite Nanocrystals Embedded in Polymer Matrices'. In: *8ème Journées Pérovskites Halogénées (JPH2023)*. May 2023 (cited on page 102).

[196] Elisa Riccardi *et al.* 'Ultrasensitive Photoresponse of Graphene Quantum Dots in the Coulomb Blockade Regime to THz Radiation'. In: *Nano Letters* 20.7 (July 2020), pp. 5408–5414. DOI: 10.1021/acs.nanolett.0c01800 (cited on page 103).

[197] Aurélien A. L. Nicolet *et al.* 'Single Dibenzoterrylene Molecules in an Anthracene Crystal: Main Insertion Sites'. In: *ChemPhysChem* 8.13 (Sept. 2007), pp. 1929–1936. DOI: 10.1002/cphc.200700340 (cited on page 103).

[198] J. Bernard *et al.* 'Photon Bunching in the Fluorescence from Single Molecules: A Probe for Intersystem Crossing'. In: *The Journal of Chemical Physics* 98.2 (Jan. 1993), pp. 850–859. DOI: 10.1063/1.464249 (cited on pages 103, 125, 136).

[199] J.-B. Trebbia *et al.* 'Efficient Generation of near Infra-Red Single Photons from the Zero-Phonon Line of a Single Molecule'. In: *Optics Express* 17.26 (Dec. 2009), pp. 23986–23991. DOI: 10.1364/OE.17.023986 (cited on page 103).

[200] Ghulam Murtaza *et al.* 'Efficient Room-Temperature Molecular Single-Photon Sources for Quantum Key Distribution'. In: *Optics Express* 31.6 (Mar. 2023), pp. 9437–9447. DOI: 10.1364/OE.476440 (cited on pages 103, 137).

[201] Jian Zhang *et al.* 'Contacting Individual Graphene Nanoribbons Using Carbon Nanotube Electrodes'. In: *Nature Electronics* 6.8 (Aug. 2023), pp. 572–581. DOI: 10.1038/s41928-023-00991-3 (cited on page 103).

[202] Min-Ken Li *et al.* 'Electroluminescence from Single-Walled Carbon Nanotubes with Quantum Defects'. In: *ACS Nano* 16.8 (Aug. 2022), pp. 11742–11754. DOI: 10.1021/acsnano.2c03083 (cited on page 103).

[203] Mitchell Bacon, Siobhan J. Bradley, and Thomas Nann. 'Graphene Quantum Dots'. In: *Particle & Particle Systems Characterization* 31.4 (2014), pp. 415–428. DOI: 10.1002/ppsc.201300252 (cited on page 103).

[204] Gabriela Borin Barin *et al.* 'Surface-Synthesized Graphene Nanoribbons for Room Temperature Switching Devices: Substrate Transfer and Ex Situ Characterization'. In: *ACS Applied Nano Materials* 2.4 (Apr. 2019), pp. 2184–2192. DOI: 10.1021/acsanm.9b00151 (cited on page 103).

[205] Daniel Medina-Lopez *et al.* 'Interplay of Structure and Photophysics of Individualized Rod-Shaped Graphene Quantum Dots with up to 132 Sp^2 Carbon Atoms'. In: *Nature Communications* 14.1 (Aug. 2023), p. 4728. DOI: 10.1038/s41467-023-40376-w (cited on pages 104, 109, 110, 114, 138, 167, 168).

[206] R. Rieger and K. Müllen. 'Forever Young: Polycyclic Aromatic Hydrocarbons as Model Cases for Structural and Optical Studies'. In: *Journal of Physical Organic Chemistry* 23.4 (2010), pp. 315–325. DOI: 10.1002/poc.1644 (cited on page 108).

[207] Andre Neumann *et al.* 'Accidental Contamination of Substrates and Polymer Films by Organic Quantum Emitters'. In: *Nano Letters* 19.5 (May 2019), pp. 3207–3213. DOI: 10.1021/acs.nanolett.9b00712 (cited on pages 111, 120).

[208] Douglas Magde, Roger Wong, and Paul G. Seybold. 'Fluorescence Quantum Yields and Their Relation to Lifetimes of Rhodamine 6G and Fluorescein in Nine Solvents: Improved Absolute Standards for Quantum Yields'. In: *Photochemistry and Photobiology* 75.4 (Apr. 2002), pp. 327–334. DOI: 10.1562/0031-8655(2002)075<0327:fqyatr>2.0.co;2 (cited on page 114).

[209] L. Fleury *et al.* 'Single Molecule Spectra of an Impurity Found in N-Hexadecane and Polyethylene'. In: *Molecular Crystals and Liquid Crystals Science and Technology. Section A. Molecular Crystals and Liquid Crystals* 283.1 (June 1996), pp. 81–87. DOI: 10.1080/10587259608037868 (cited on page 120).

[210] Vijay Tripathi, Panyala Linga Reddy, and Leela S. Panchakarla. 'Photoluminescence with Peaked Structure: Inherent to Nanoparticles or Resulting From Impurities in Sample Vial Caps?' In: *ChemPhysChem* 22.12 (2021), pp. 1167–1169. DOI: 10.1002/cphc.202100110 (cited on page 120).

[211] Freddy T. Rabouw *et al.* 'Non-Blinking Single-Photon Emitters in Silica'. In: *Scientific Reports* 6.1 (Feb. 2016), p. 21187. DOI: 10.1038/srep21187 (cited on page 120).

[212] Thomas Liu *et al.* 'Vibronic Fingerprints in the Luminescence of Graphene Quantum Dots at Cryogenic Temperature'. In: *The Journal of Chemical Physics* 156.10 (Mar. 2022), p. 104302. DOI: 10.1063/5.0083282 (cited on page 120).

[213] R Thul and M Falcke. 'Waiting Time Distributions for Clusters of Complex Molecules'. In: *Europhysics Letters (EPL)* 79.3 (Aug. 2007), p. 38003. DOI: 10.1209/0295-5075/79/38003 (cited on page 129).

[214] Haw Yang, Hao Li, and Tao Liu. 'Photobleaching Statistics in Single-Molecule on-/off-Time Distributions'. In: *Journal of Chemical Physics* 151.17 (Nov. 2019). DOI: 10.1063/1.5126500 (cited on page 129).

[215] Jianshu Cao. 'Single Molecule Waiting Time Distribution Functions in Quantum Processes'. In: *The Journal of Chemical Physics* 114.12 (Mar. 2001), pp. 5137–5140. DOI: 10.1063/1.1342217 (cited on page 129).

[216] Rogier Verberk and Michel Orrit. 'Photon Statistics in the Fluorescence of Single Molecules and Nanocrystals: Correlation Functions versus Distributions of on- and off-Times'. In: *The Journal of Chemical Physics* 119.4 (July 2003), pp. 2214–2222. DOI: 10.1063/1.1582848 (cited on page 129).

[217] Serge Reynaud. 'La fluorescence de résonance : Etude par la méthode de l'atome habillé'. In: *Annales de Physique* 8 (1983), pp. 315–370. DOI: 10.1051/anphys/198308080315 (cited on page 130).

[218] Michele Celebrano *et al.* 'Single-Molecule Imaging by Optical Absorption'. In: *Nature Photonics* 5.2 (Feb. 2011), pp. 95–98. DOI: 10.1038/nphoton.2010.290 (cited on page 133).

[219] Fabien Vialla *et al.* 'Chirality Dependence of the Absorption Cross Section of Carbon Nanotubes'. In: *Physical Review Letters* 111.13 (Sept. 2013), p. 137402. DOI: 10.1103/PhysRevLett.111.137402 (cited on page 133).

[220] Weston Thatcher Borden *et al.* 'Dioxygen: What Makes This Triplet Diradical Kinetically Persistent?' In: *Journal of the American Chemical Society* 139.26 (July 2017), pp. 9010–9018. DOI: 10.1021/jacs.7b04232 (cited on page 136).

[221] Th Basché, S. Kummer, and C. Bräuchle. 'Direct Spectroscopic Observation of Quantum Jumps of a Single Molecule'. In: *Nature* 373.6510 (Jan. 1995), pp. 132–134. DOI: 10.1038/373132a0 (cited on page 136).

[222] Marco Pirotta *et al.* 'Single Molecule Spectroscopy. Fluorescence-lifetime Measurements of Pentacene in p-Terphenyl'. In: *Chemical Physics Letters* 208.5-6 (June 1993), pp. 379–384. DOI: 10.1016/0009-2614(93)87159-Z (cited on page 136).

[223] Qiang Chen *et al.* 'Dibenzo[Hi,St]Ovalene as Highly Luminescent Nanographene: Efficient Synthesis via Photochemical Cyclodehydroiodination, Optoelectronic Properties, and Single-Molecule Spectroscopy'. In: *Journal of the American Chemical Society* 141.41 (Oct. 2019), pp. 16439–16449. DOI: 10.1021/jacs.9b08320 (cited on page 136).

[224] Lukas Novotny and Bert Hecht. *Principles of Nano-Optics*. 2nd ed. Cambridge: Cambridge University Press, 2012 (cited on page 136).

[225] B. C. Buchler *et al.* 'Measuring the Quantum Efficiency of the Optical Emission of Single Radiating Dipoles Using a Scanning Mirror'. In: *Physical Review Letters* 95.6 (Aug. 2005), p. 063003. DOI: 10.1103/PhysRevLett.95.063003 (cited on page 137).

[226] Hugo Levy-Falk *et al.* 'Investigation of Rod-Shaped Single-Graphene Quantum Dot'. In: *physica status solidi (b)* 260.12 (2023), p. 2300310. DOI: 10.1002/pssb.202300310 (cited on page 138).

[227] Elisa M. Miller *et al.* 'Substrate-Controlled Band Positions in CH3NH3PbI3 Perovskite Films'. In: *Physical Chemistry Chemical Physics* 16.40 (Sept. 2014), pp. 22122–22130. DOI: 10.1039/C4CP03533J (cited on page 142).

[228] Jungwook Choi, Hanyu Zhang, and Jong Hyun Choi. 'Modulating Optoelectronic Properties of Two-Dimensional Transition Metal Dichalcogenide Semiconductors by Photoinduced Charge Transfer'. In: *ACS Nano* 10.1 (Jan. 2016), pp. 1671–1680. DOI: 10.1021/acsnano.5b07457 (cited on page 142).

[229] Kin Fai Mak and Jie Shan. 'Opportunities and Challenges of Interlayer Exciton Control and Manipulation'. In: *Nature Nanotechnology* 13.11 (Nov. 2018), pp. 974–976. DOI: 10.1038/s41565-018-0301-1 (cited on page 142).

[230] H. Fang *et al.* 'Strong Interlayer Coupling in van Der Waals Heterostructures Built from Single-Layer Chalcogenides'. In: *Proceedings of the National Academy of Sciences* 111.17 (Apr. 2014), pp. 6198–6202. DOI: 10.1073/pnas.1405435111 (cited on page 142).

[231] Zhihui Chen *et al.* 'Transient Reflection Spectroscopy on Ultrafast Interlayer Charge Transfer Processes in a MoS_2 /WSe_2 van Der Waals Heterojunction'. In: *The Journal of Physical Chemistry C* 125.48 (Dec. 2021), pp. 26575–26582. DOI: 10.1021/acs.jpcc.1c07143 (cited on page 142).

[232] Yingying Chen *et al.* 'Robust Interlayer Coupling in Two-Dimensional Perovskite/Monolayer Transition Metal Dichalcogenide Heterostructures'. In: *ACS Nano* 14.8 (Aug. 2020), pp. 10258–10264. DOI: 10.1021/acsnano.0c03624 (cited on page 142).

[233] M. Karpińska *et al.* 'Interlayer Excitons in MoSe2/2D Perovskite Hybrid Heterostructures – the Interplay between Charge and Energy Transfer'. In: *Nanoscale* 14.22 (June 2022), pp. 8085–8095. DOI: 10.1039/D2NR00877G (cited on page 142).

[234] Shuxia Tao *et al.* 'Absolute Energy Level Positions in Tin- and Lead-Based Halide Perovskites'. In: *Nature Communications* 10.1 (June 2019), p. 2560. DOI: 10.1038/s41467-019-10468-7 (cited on page 143).

[235] Thomas M. Brenner *et al.* 'Hybrid Organic—Inorganic Perovskites: Low-Cost Semiconductors with Intriguing Charge-Transport Properties'. In: *Nature Reviews Materials* 1.1 (Jan. 2016), pp. 1–16. DOI: 10.1038/natrevmats.2015.7 (cited on page 143).

[236] Wei Han *et al.* 'Spin Transport and Relaxation in Graphene'. In: *Journal of Magnetism and Magnetic Materials* 324.4 (Feb. 2012), pp. 369–381. DOI: 10.1016/j.jmmm.2011.08.001 (cited on page 143).

[237] Daniel Huertas-Hernando, F. Guinea, and Arne Brataas. 'Spin-Orbit Coupling in Curved Graphene, Fullerenes, Nanotubes, and Nanotube Caps'. In: *Physical Review B* 74.15 (Oct. 2006), p. 155426. DOI: 10.1103/PhysRevB.74.155426 (cited on page 143).

[238] Björn Trauzettel *et al.* 'Spin Qubits in Graphene Quantum Dots'. In: *Nature Physics* 3.3 (Mar. 2007), pp. 192–196. DOI: 10.1038/nphys544 (cited on page 143).

[239] Pramod Ghising, Chandan Biswas, and Young Hee Lee. 'Graphene Spin Valves for Spin Logic Devices'. In: *Advanced Materials* 35.23 (2023), p. 2209137. DOI: 10.1002/adma.202209137 (cited on page 143).

[240] Shen Zhao *et al.* 'Single Photon Emission from Graphene Quantum Dots at Room Temperature'. In: *Nature Communications* 9.1 (Aug. 2018), p. 3470. DOI: 10.1038/s41467-018-05888-w (cited on page 144).

[241] Mark Fox and Mark Fox. *Optical Properties of Solids*. Second Edition, Second Edition. Oxford Master Series in Physics. Oxford, New York: Oxford University Press, Mar. 2010 (cited on page 144).

[242] Van Dong Pham *et al.* 'Electronic Interaction between Nitrogen-Doped Graphene and Porphyrin Molecules'. In: *ACS Nano* 8.9 (Sept. 2014), pp. 9403–9409. DOI: 10.1021/nn503753e (cited on pages 144, 169).

[243] Solène Béchu *et al.* 'Photoemission Spectroscopy Characterization of Halide Perovskites'. In: *Advanced Energy Materials* 10.26 (2020), p. 1904007. DOI: 10.1002/aenm.201904007 (cited on page 146).

[244] Guillaume Vidon *et al.* 'The Impact of X-Ray Radiation on Chemical and Optical Properties of Triple-Cation Lead Halide Perovskite: From the Surface to the Bulk'. In: *Advanced Functional Materials* 33.45 (2023), p. 2304730. DOI: 10.1002/adfm.202304730 (cited on page 149).

[245] Stefania Cacovich *et al.* 'In-Depth Chemical and Optoelectronic Analysis of Triple-Cation Perovskite Thin Films by Combining XPS Profiling and PL Imaging'. In: *ACS Applied Materials & Interfaces* 14.30 (Aug. 2022), pp. 34228–34237. DOI: 10.1021/acsami.1c22286 (cited on page 150).

[246] M. Kasha, H. R. Rawls, and M. Ashraf El-Bayoumi. 'The exciton model in molecular spectroscopy'. In: *Pure and Applied Chemistry* 11.3-4 (Jan. 1965), pp. 371–392. DOI: 10.1351/pac196511030371 (cited on page 154).

[247] Nicholas J. Hestand and Frank C. Spano. 'Expanded Theory of H- and J-Molecular Aggregates: The Effects of Vibronic Coupling and Intermolecular Charge Transfer'. In: *Chemical Reviews* (Apr. 2018). DOI: 10.1021/acs.chemrev.7b00581 (cited on pages 154–156, 158).

[248] Wei Wang *et al.* 'Dynamic $\Pi - \pi$ Stacked Molecular Assemblies Emit from Green to Red Colors'. In: *Nano Letters* 3.4 (Apr. 2003), pp. 455–458. DOI: 10.1021/nl025976j (cited on pages 156–159).

[249] V. Czikklely, H.D. Forsterling, and H. Kuhn. 'Extended Dipole Model for Aggregates of Dye Molecules'. In: *Chemical Physics Letters* 6.3 (Aug. 1970), pp. 207–210. DOI: 10.1016/0009-2614(70)80220-2 (cited on page 157).

[250] Andrzej Witkowski and William Moffitt. 'Electronic Spectra of Dimers: Derivation of the Fundamental Vibronic Equation'. In: *The Journal of Chemical Physics* 33.3 (1960), pp. 872–875. DOI: 10.1063/1.1731278 (cited on page 157).

[251] Robert L. Fulton and Martin Gouterman. 'Vibronic Coupling. I. Mathematical Treatment for Two Electronic States'. In: *The Journal of Chemical Physics* 35.3 (Sept. 1961), pp. 1059–1071. DOI: 10.1063/1.1701181 (cited on page 157).

[252] R. E. Merrifield. 'Vibronic States of Dimers'. In: *Radiation Research* 20.1 (Sept. 1963), p. 154. DOI: 10.2307/3571343 (cited on page 157).

[253] R. E. Merrifield. 'Ionized States in a One-Dimensional Molecular Crystal'. In: *The Journal of Chemical Physics* 34.5 (1961), pp. 1835–1839. DOI: 10.1063/1.1701086 (cited on page 157).

[254] Frank Würthner *et al.* 'Perylene Bisimide Dye Assemblies as Archetype Functional Supramolecular Materials'. In: *Chemical Reviews* 116.3 (Feb. 2016), pp. 962–1052. DOI: 10.1021/acs.chemrev.5b00188 (cited on page 158).

[255] April L. Bialas and Frank C. Spano. 'A Holstein–Peierls Approach to Excimer Spectra: The Evolution from Vibronically Structured to Unstructured Emission'. In: *The Journal of Physical Chemistry C* 126.8 (Mar. 2022), pp. 4067–4081. DOI: 10.1021/acs.jpcc.1c10255 (cited on page 158).

[256] Jovan M. Giaimo *et al.* 'Excited Singlet States of Covalently Bound, Cofacial Dimers and Trimers of Perylene-3,4:9,10-Bis(Dicarboximide)s'. In: *The Journal of Physical Chemistry A* 112.11 (Mar. 2008), pp. 2322–2330. DOI: 10.1021/jp710847q (cited on pages 158, 166, 167).

[257] Sara Wirsing *et al.* 'Excited-State Dynamics in Perylene-Based Organic Semiconductor Thin Films: Theory Meets Experiment'. In: *The Journal of Physical Chemistry C* 123.45 (Nov. 2019), pp. 27561–27572. DOI: 10.1021/acs.jpcc.9b07511 (cited on page 158).

[258] Eric A. Margulies *et al.* 'Excimer Formation in Cofacial and Slip-Stacked Perylene-3,4:9,10-Bis(Dicarboximide) Dimers on a Redox-Inactive Triptycene Scaffold'. In: *Physical Chemistry Chemical Physics* 16.43 (Oct. 2014), pp. 23735–23742. DOI: 10.1039/C4CP03107E (cited on page 158).

[259] Y. F. Huang *et al.* 'Aggregate versus Excimer Emissions from Poly(2,5-Di- *n* -Octyloxy-1,4-Phenylenevinylene)'. In: *The Journal of Physical Chemistry C* 111.14 (Apr. 2007), pp. 5533–5540. DOI: 10.1021/jp067751t (cited on page 158).

[260] Hanna Traeger *et al.* 'Folded Perylene Diimide Loops as Mechanoresponsive Motifs'. In: *Angewandte Chemie International Edition* 60.29 (2021), pp. 16191–16199. DOI: 10.1002/anie.202105219 (cited on page 158).

[261] Reinhold F. Fink *et al.* 'Exciton Trapping in π-Conjugated Materials: A Quantum-Chemistry-Based Protocol Applied to Perylene Bisimide Dye Aggregates'. In: *Journal of the American Chemical Society* 130.39 (Oct. 2008), pp. 12858–12859. DOI: 10.1021/ja804331b (cited on page 158).

[262] Woojae Kim *et al.* 'Solvent-Modulated Charge-Transfer Resonance Enhancement in the Excimer State of a Bay-Substituted Perylene Bisimide Cyclophane'. In: *The Journal of Physical Chemistry Letters* 10.8 (Apr. 2019), pp. 1919–1927. DOI: 10.1021/acs.jpclett.9b00357 (cited on page 158).

[263] Minjung Son *et al.* 'Spectroscopic Demonstration of Exciton Dynamics and Excimer Formation in a Sterically Controlled Perylene Bisimide Dimer Aggregate'. In: *The Journal of Physical Chemistry Letters* 5.20 (Oct. 2014), pp. 3601–3607. DOI: 10.1021/jz501953a (cited on page 158).

[264] Hyejin Yoo *et al.* 'Excimer Formation Dynamics of Intramolecular π-Stacked Perylenediimides Probed by Single-Molecule Fluorescence Spectroscopy'. In: *Journal of the American Chemical Society* 132.11 (Mar. 2010), pp. 3939–3944. DOI: 10.1021/ja910724x (cited on pages 158, 182).

[265] Andrzej Molski. 'Statistics of the Bleaching Number and the Bleaching Time in Single-Molecule Fluorescence Spectroscopy'. In: *The Journal of Chemical Physics* 114.3 (Jan. 2001), pp. 1142–1147. DOI: 10.1063/1.1333760 (cited on pages 160, 161).

[266] Edwin K. L. Yeow *et al.* 'Characterizing the Fluorescence Intermittency and Photobleaching Kinetics of Dye Molecules Immobilized on a Glass Surface'. In: *The Journal of Physical Chemistry A* 110.5 (Feb. 2006), pp. 1726–1734. DOI: 10.1021/jp055496r (cited on page 161).

[267] Rob Zondervan *et al.* 'Photobleaching of Rhodamine 6G in Poly(Vinyl Alcohol) at the Ensemble and Single-Molecule Levels'. In: *The Journal of Physical Chemistry A* 108.10 (Mar. 2004), pp. 1657–1665. DOI: 10.1021/jp037222e (cited on page 161).

[268] Liming Ying and X. Sunney Xie. 'Fluorescence Spectroscopy, Exciton Dynamics, and Photochemistry of Single Allophycocyanin Trimers'. In: *The Journal of Physical Chemistry B* 102.50 (Dec. 1998), pp. 10399–10409. DOI: 10.1021/jp983227d (cited on page 161).

[269] W. Lukosz and R. E. Kunz. 'Light Emission by Magnetic and Electric Dipoles Close to a Plane Interface. I. Total Radiated Power'. In: *JOSA* 67.12 (Dec. 1977), pp. 1607–1615. DOI: 10.1364/JOSA.67.001607 (cited on page 163).

[270] Nina Sultanova, S. Kasarova, and I. Nikolov. 'Dispersion Properties of Optical Polymers'. In: *ACTA PHYSICA POLONICA A* 116 (Oct. 2009), pp. 585–587. DOI: 10.12693/APhysPolA.116.585 (cited on page 163).

[271] 'Phase Noise and Frequency Stability'. In: *Phase Noise and Frequency Stability in Oscillators*. Ed. by Enrico Rubiola. The Cambridge RF and Microwave Engineering Series. Cambridge: Cambridge University Press, 2008, pp. 1–34. DOI: 10.1017/CBO9780511812798.005 (cited on page 172).

[272] Joseph W. Goodman. *Statistical Optics*. Wiley, Feb. 1985 (cited on page 172).

[273] Norbert Wiener. 'Generalized Harmonic Analysis'. In: *Acta Mathematica* 55.none (Jan. 1930), pp. 117–258. DOI: 10.1007/BF02546511 (cited on page 172).

[274] A. Khintchine. 'Korrelationstheorie der stationären stochastischen Prozesse'. In: *Mathematische Annalen* 109.1 (Dec. 1934), pp. 604–615. DOI: 10.1007/BF01449156 (cited on page 172).

[275] P. Welch. 'The Use of Fast Fourier Transform for the Estimation of Power Spectra: A Method Based on Time Averaging over Short, Modified Periodograms'. In: *IEEE Transactions on Audio and Electroacoustics* 15.2 (June 1967), pp. 70–73. DOI: 10.1109/TAU.1967.1161901 (cited on page 173).

[276] D.W. Allan. 'Statistics of Atomic Frequency Standards'. In: *Proceedings of the IEEE* 54.2 (1966), pp. 221–230. DOI: 10.1109/PROC.1966.4634 (cited on page 173).

[277] J A Barnes *et al.* 'Characterization of Frequency Stability'. In: *IEEE Transactions on Instrumentation and Measurement* IM-20.2 (1971), pp. 105–120 (cited on page 173).

[278] D.A. Howe, D.U. Allan, and J.A. Barnes. 'Properties of Signal Sources and Measurement Methods'. In: *Thirty Fifth Annual Frequency Control Symposium*. IEEE, 1981, pp. 669–716. DOI: 10.1109/FREQ.1981.200541 (cited on page 173).

[279] Jaejin Lee *et al.* 'Characterization of Noise in a Single-Molecule Fluorescence Signal'. In: *The Journal of Physical Chemistry B* 126.6 (Feb. 2022), pp. 1160–1167. DOI: 10.1021/acs.jpcb.1c08621 (cited on pages 174, 176).

[280] Nien Fan Zhang. 'Allan Variance of Time Series Models for Measurement Data'. In: *Metrologia* 45.5 (Sept. 2008), p. 549. DOI: 10.1088/0026-1394/45/5/009 (cited on page 174).

[281] '1/f Noise and Random Telegraph Noise'. In: *Electronic Noise and Fluctuations in Solids*. Ed. by Sh. Kogan. Cambridge: Cambridge University Press, 1996, pp. 203–286. DOI: 10.1017/CBO9780511551666.009 (cited on page 174).

[282] K. S. Ralls and R. A. Buhrman. 'Defect Interactions and Noise in Metallic Nanoconstrictions'. In: *Physical Review Letters* 60.23 (June 1988), pp. 2434–2437. DOI: 10.1103/PhysRevLett.60.2434 (cited on page 176).

[283] K. S. Ralls *et al.* 'Discrete Resistance Switching in Submicrometer Silicon Inversion Layers: Individual Interface Traps and Low-Frequency (1/f?) Noise'. In: *Physical Review Letters* 52.3 (Jan. 1984), pp. 228–231. DOI: 10.1103/PhysRevLett.52.228 (cited on page 176).

[284] T. G. M. Kleinpenning and A. H. De Kuijper. 'Relation between Variance and Sample Duration of 1/ f Noise Signals'. In: *Journal of Applied Physics* 63.1 (Jan. 1988), pp. 43–45. DOI: 10.1063/1.340460 (cited on page 176).

[285] Ferdinand Grüneis. '1/f Noise under Drift and Thermal Agitation in Semiconductor Materials'. In: *Physica A: Statistical Mechanics and its Applications* 593 (May 2022), p. 126917. DOI: 10.1016/j.physa.2022.126917 (cited on pages 176, 177).

[286] C. T. Rogers and R. A. Buhrman. 'Composition of $\frac{1}{f}$ Noise in Metal-Insulator-Metal Tunnel Junctions'. In: *Physical Review Letters* 53.13 (Sept. 1984), pp. 1272–1275. DOI: 10.1103/PhysRevLett.53.1272 (cited on page 176).

[287] K. S. Ralls and R. A. Buhrman. 'Microscopic Study of 1/f Noise in Metal Nanobridges'. In: *Physical Review B* 44.11 (Sept. 1991), pp. 5800–5817. DOI: 10.1103/PhysRevB.44.5800 (cited on page 176).

[288] Johan Hofkens *et al.* 'Probing Photophysical Processes in Individual Multichromophoric Dendrimers by Single-Molecule Spectroscopy'. In: *Journal of the American Chemical Society* 122.38 (Sept. 2000), pp. 9278–9288. DOI: 10.1021/ja0012570 (cited on pages 179, 181).

[289] Michael Y. Odoi *et al.* 'Single-Molecule Studies of a Model Fluorenone'. In: *ChemPhysChem* 8.10 (2007), pp. 1481–1486. DOI: 10.1002/cphc.200700133 (cited on page 182).

[290] Thomas Stangl *et al.* 'Temporal Fluctuations in Excimer-Like Interactions between π-Conjugated Chromophores'. In: *The Journal of Physical Chemistry Letters* 6.8 (Apr. 2015), pp. 1321–1326. DOI: 10.1021/acs.jpclett.5b00328 (cited on page 182).

[291] Yoshihiro Honmou *et al.* 'Single-Molecule Electroluminescence and Photoluminescence of Polyfluorene Unveils the Photophysics behind the Green Emission Band'. In: *Nature Communications* 5.1 (Aug. 2014), p. 4666. DOI: 10.1038/ncomms5666 (cited on page 183).

[292] Emil J. W List *et al.* 'The Role of Keto Defect Sites for the Emission Properties of Polyfluorene-Type Materials'. In: *Synthetic Metals*. Proceedings of the Fifth International Topical Conference on Optical Probes of Conjugated Polymers and Organic and Inorganic Nanostructures 139.3 (Oct. 2003), pp. 759–763. DOI: 10.1016/S0379-6779(03)00249-2 (cited on page 183).

[293] David A. Egger, Andrew M. Rappe, and Leeor Kronik. 'Hybrid Organic–Inorganic Perovskites on the Move'. In: *Accounts of Chemical Research* 49.3 (Mar. 2016), pp. 573–581. DOI: 10.1021/acs.accounts.5b00540 (cited on page 184).

Résumé en Français

Ce travail se concentre sur la spectroscopie optique de deux classes de matériaux en utilisant la microscopie de fluorescence à température ambiante.

Tout d'abord, les pérovskites halogénées, une classe de semi-conducteurs qui ont connu un regain d'intérêt au cours des dix dernières années en raison de leurs propriétés optoélectroniques exceptionnelles, ce qui en fait une plate-forme prometteuse pour les applications photovoltaïques, mais aussi pour l'émission de lumière dans les diodes, les lasers et les dispositifs quantiques. Ces matériaux cristallins sont constitués d'octaèdres dont les sommets sont partagés. Un ion métallique est positionné au centre, souvent du plomb, et des ions halogénures aux sommets : Cl, Br ou I. Un cation complète la structure. Il est soit organique, par exemple le méthylammonium (MA) ou le formamidinium, soit inorganique, par exemple le césium. Dans le contexte de l'émission de lumière, les pérovskites halogénées constituent un excellent choix pour résoudre le problème du *green gap*, c'est-à-dire le manque d'émetteurs efficaces dans la région verte du spectre optique, en raison de la possibilité d'ajuster leur bande interdite grâce à un choix éclairé de l'halogénure lors de la synthèse. De plus, comme la synthèse se fait à température ambiante et implique des étapes de chimie simples, ils sont prometteurs pour les applications industrielles. La synthèse et la caractérisation de nanocristaux de $CsPbBr_3$ émettant dans la région verte du spectre optique à l'aide d'une nouvelle méthode basée sur la précipitation est rapportée. En particulier, la calibration élevé et la bonne stabilité des nanocristaux sont mis en évidence.

La deuxième partie de cette étude porte sur les boîtes quantiques de graphène. Ces objets de faible dimension permettent d'ouvrir la bande interdite du graphène, ce qui les rend fluorescents. Ces émetteurs sont prometteurs parce que leur structure atomiquement fine et leur accordabilité les rendent aptes à réaliser des nanocapteurs. En s'appuyant sur la relation structure-propriétés récemment étudiée des boîtes quantiques de graphène rectangulaires, une étude approfondie au niveau de l'objet unique de ces boîtes quantiques hautement fluorescentes avec 96 atomes de carbone sp^2 est rapportée. L'excellente pureté des échantillons a été mise en évidence. L'étude de la dynamique temporelle de ces émetteurs de photons uniques dans une matrice de polystyrène a permis d'estimer les temps caractéristiques de la dynamique transitoire des boîtes quantiques.

Enfin, la troisième partie rapporte l'étude des boîtes quantiques de graphène sur une surface de pérovskite. La surface des pérovskites présente un intérêt particulier pour la réalisation de dispositifs avec ces semi-conducteurs, ce qui en fait un terrain de jeu intéressant pour l'utilisation des boîtes quantiques de graphène. À cette fin,

les boîtes quantiques ont été déposés sur la surface de monocristaux millimétriques de $MAPbBr_3$.

- En tant que films minces déposés sur la pérovskite, les boîtes quantiques de graphène présentent une photophysique compatible avec la formation d'excimères.
- Lorsque la concentration de boîtes quantiques sur la surface est réduite, des taches limitées par la diffraction sont observées. L'étude de la photoluminescence dans le domaine temporel révèle des sauts entre des états discrets du système.
- L'étude dans le domaine des fréquences de l'intensité de la photoluminescence de ces émetteurs limités par la diffraction est dominée par le bruit en 1/f, ce qui contraste fortement avec la dynamique stable, dominée par le bruit de grenaille, des émetteurs uniques lorsqu'ils sont étudiés dans une matrice de polystyrène.

Nous avons donc observé la formation d'excimères à la surface de perovskite hybrides halogénées. La compréhension de la dynamique temporelle de la photophysique de ces aggrégats pourraient mener à une compréhension plus fine de la surface des perovskites.